THESES

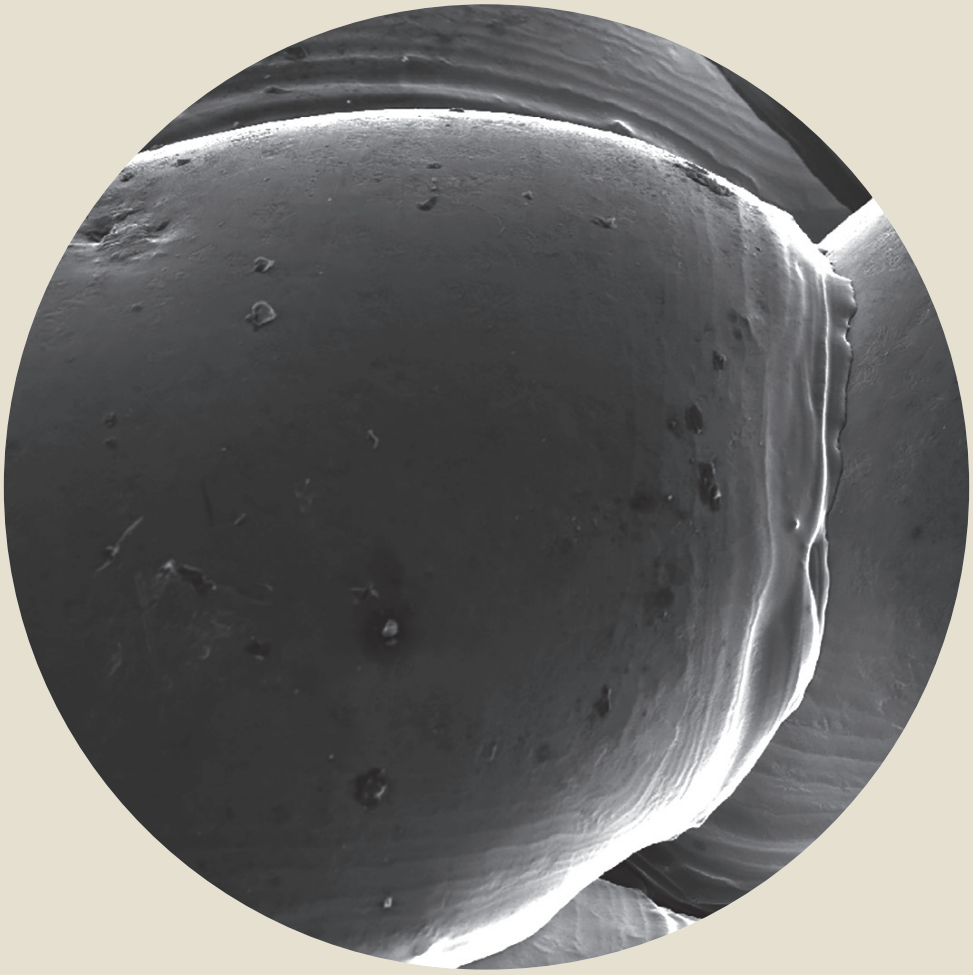

21

Maschinenbau
Lehrstuhl für
Umformtechnik
und Gießereiwesen

Benjamin Himmel

Material Jetting of Aluminium

Analysis of a Novel Additive Manufacturing Process

TUM.University Press

Schriftenreihe Umformtechnik und Gießereiwesen

Lehrstuhl für Umformtechnik und Gießereiwesen
Fakultät für Maschinenwesen
Technische Universität München

Material Jetting of Aluminium

Analysis of a Novel Additive Manufacturing Process

Benjamin Himmel

Vollständiger Abdruck der von der Fakultät für Maschinenwesen
der Technischen Universität München zur Erlangung des akademischen
Grades eines Doktor-Ingenieurs (Dr.-Ing.) genehmigten Dissertation.

Vorsitzender:

Prof. Dr.-Ing. Gunter Reinhart

Prüfer der Dissertation:

1. Prof. Dr.-Ing. Wolfram Volk
2. Prof. Dr. rer. nat. Tim C. Lüth

Die Dissertation wurde am 28.05.2019 bei der Technischen
Universität München eingereicht und durch die Fakultät für
Maschinenwesen am 04.12.2019 angenommen.

The German National Library has registered this publication in the
German National Bibliography. Detailed bibliographic data are available
on the Internet at https://portal.dnb.de.

Imprint

Series: Schriftenreihe Umformtechnik und Gießereiwesen
Editor: Lehrstuhl für Umformtechnik und Gießereiwesen (utg),
TUM Department of Mechanical Engineering, Technical University of Munich

Layout design and typesetting: Benjamin Himmel
Layoutguidelines for cover design: Designbuero Josef Grillmeier, Munich
Cover design: Caroline Ennemoser
Cover illustration: Benjamin Himmel

TUM.University Press
Technical University of Munich
Arcisstrasse 21
80333 Munich

ISSN: 2569-4928
DOI: 10.14459/2020md1488686
ISSN printed edition: 2364-6942
ISBN printed edition: 978-3-95884-049-2

www.tum.de

Danksagung

Diese Arbeit entstand während meiner Tätigkeit als wissenschaftlicher Mitarbeiter am Lehrstuhl für Umformtechnik und Gießereiwesen (utg) der Technischen Universität München. Meinem Doktorvater, Prof. Wolfram Volk, Ordinarius des Lehrstuhls, möchte ich im Besonderen danken für die Möglichkeit an diesem außergewöhnlichen Thema zu arbeiten, für das mir entgegengebrachte Vertrauen und die damit verbundenen Freiheiten bei der Bearbeitung. Es sind nicht zuletzt diese Freiheiten, die die Zeit am Lehrstuhl zu einem großen Gewinn für die persönliche und fachliche Entwicklung machen.

Prof. Tim C. Lüth, Ordinarius des Lehrstuhls für Mikrotechnik und Medizingerätetechnik der Technischen Universität München, danke ich zum einen für die Übernahme des Korreferats und zum anderen für die gute Zusammenarbeit mit seinem Team im gemeinsamen Kooperationsprojekt. Hierbei geht mein besonderer Dank auch an Franz Irlinger und Dominik Rumschöttel für die wohlwollende und freundschaftliche Zusammenarbeit.

Ich bedanke mich auch bei den Mitarbeiterinnen und Mitarbeitern des Lehrstuhls utg, die mich tatkräftig unterstützten und von denen viele zu Freunden geworden sind. Ihretwegen wird mir die Zeit am utg immer in guter Erinnerung bleiben. Besonders hervorheben möchte ich dabei Robert Ramakrishnan, der mich als Student motivierte an den Lehrstuhl zu gehen und mir seitdem ein guter Freund und Mentor ist. Außerdem möchte ich noch Tim Mittler und Georg Baumgartner nennen. Mit ihnen hatte ich als Bürokollegen unzählige, intensive Gespräche über persönliche wie fachliche Themen, die sowohl mich als auch diese Arbeit prägten. Beide wurden zu guten Freunden. Weiter danke ich auch den Studenten, die mich bei der Bearbeitung des Promotionsprojektes unterstützt haben und ohne deren Hilfe es in diesem Umfang nicht möglich gewesen wäre.

Tausend Dank an meine Eltern Heidrun und Claus-Otto Griebel, für ihre fortwährende Unterstützung in sämtlichen Lebenslagen, ohne die ich es nie bis hier geschafft hätte. Meiner Mutter möchte ich diese Arbeit widmen, da sie mir die Neugierde zeigte und das Vertrauen in mich selbst gab, das notwendig war, um die Dissertation erfolgreich zu beenden. Sie verstarb, viel zu jung, nur wenige Monate vor dem Rigorosum.

Abschließend danke ich meiner Frau Anne. Sie schenkte mir während der Zeit am utg zwei großartige Kinder. Das hat zwar die Fertigstellung der Arbeit nicht unbedingt beschleunigt, aber dafür kann ich heute nicht nur stolz sein meine Promotion erfolgreich beendet zu haben, sondern

auch darauf, eine wunderbare Familie zu haben. Außerdem danke ich Anne für ihre große Unterstützung beim Schreiben der Arbeit, nicht nur moralisch, sondern auch als unermüdliche Lektorin und wertvolle Diskussionspartnerin.

München, im Februar 2020 *Benjamin Himmel*

Für meine Mama

Executive Summary

Additive manufacturing methods have become an integral part of 21st century production technology. A majority of the most recent developments focused on the industrial production of metal parts by additive methods. Even though laser and powder based methods such as selective laser melting are already capable of fabricating high quality parts in an industrial environment, their application in volume production is limited by the elevated cost of raw material and low build rates. The common way to increase build rates of those machines is by adding more laser sources to a single machine, but as laser sources and laser optics are costly parts, this also increases the machine cost significantly.

Material jetting processes are additive manufacturing methods that directly print build material on an empty platform. Their advantage in terms of cost and speed is that individual printing nozzles are comparably cheap and therefore build rates can be multiplied, by using print heads with a high number of nozzles, without dramatically increasing machine cost. Today, those methods are only commercialised for polymers, while the developments for metals are just starting.

This thesis contributes to the fundamental understanding of material jetting of aluminium by analysing the correlations between thermal conditions, alloy composition and macroscopic part properties as well as microstructure formation. A prototypic printing machine, capable of printing small test parts, was developed and installed. Samples fabricated under a variation of process parameters and alloy compositions were analysed to determine microstructure, relative density and mechanical properties. Additionally, a novel method to simulate the temperature field developing throughout the printing process, was implemented and used to give insight into local thermal conditions during build-up. Furthermore, an industrial printing process with higher deposition rates was virtually modelled to predict the effects of a wider range of process parameters on local conditions.

Results show that material jetting of aluminium is able to produce parts with a density over 99 % and mechanical properties superior or comparable to cast parts of the same alloys. Droplet spreading and inter droplet bonding depend on the alloy composition and consequently on the microstructure development during solidification. The behaviour of different alloys varies significantly and cannot be described by models currently used, which assume that remelting of previously printed droplets is necessary for the formation of metallic bonds. In any case

the part's temperature needs to be close to the alloy's solidus temperature during the printing process to obtain the desired part properties. However, temperatures must not get too high, since then an undesired large volume melts during droplet deposition and the geometric shape is lost. Therefore, it is a challenging task to control the process, according to the printed geometry, in a way that local temperatures stay inside the process window. The present work contributes to the fundamental knowledge needed to design an industrial material jetting process of aluminium that meets the requirements to produce high quality metal parts.

Kurzbeschreibung

Additive Fertigungsverfahren sind ein fester Bestandteil der Produktionstechnik des 21ten Jahrhunderts geworden. Die Entwicklungen der letzten Jahre in diesem Bereich fokussieren sich auf die additive Fertigung von Metallbauteilen. Dabei sind die Laser und Pulver basierten Methoden, wie das *Selective Laser Melting* am weitesten verbreitet und auch bereits am weitesten hinsichtlich einer Industrialisierung entwickelt. Auch wenn mit diesen Verfahren bereits hochqualitative Bauteile in einer industriellen Umgebung gefertigt werden können, ist ihre Anwendung für größere Stückzahlen limitiert durch die hohen Kosten des Ausgangsmaterials und die geringen Baugeschwindigkeiten der Maschinen. Um eine höhere Baugeschwindigkeit zu erreichen, werden derzeit Anlagen mit mehreren Laserquellen angeboten. Da die Laserquellen kostenintensive Bauteile sind, steigt mit zunehmender Anzahl der Maschinenpreis ebenfalls deutlich an. Bei einer anderen Art der additiven Fertigungsprozesse, wird das Baumaterial direkt von einem Druckkopf auf eine Bauplattform gedruckt. Diese Verfahren nennen sich *Material Jetting* Prozesse und ihre Vorteile hinsichtlich Kosten und Baugeschwindigkeit sind, dass einzelne Druckdüsen vergleichsweise günstig sind und daher Druckköpfe mit einer Vielzahl an Düsen gefertigt werden können. Damit lassen sich hohe Aufbauraten erzielen, ohne eine deutliche Steigerung im Maschinenpreis. Diese Verfahren wurden bereits für Polymere kommerzialisiert, während die Entwicklungen für das *Material Jetting* von Metallen noch in ihren Anfängen sind.

Diese Arbeit trägt zum grundlegenden Verständnis des *Material Jetting* von Aluminiumlegierungen bei, indem sie die Auswirkungen der lokalen thermischen Bedingungen und der Legierungszusammensetzung auf die makroskopischen und mikroskopischen Bauteileigenschaften systematisch analysiert. Dazu wurde eine Prototypenanlage entwickelt, die in der Lage ist kleine Versuchsbauteile zu drucken. Unter variierten Prozessbedingungen und Legierungszusammensetzungen konnten Proben gefertigt werden, welche anschließend hinsichtlich ihrer Mikrostruktur, ihrer relativen Dichte und ihrer mechanischen Eigenschaften untersucht wurden. Zusätzlich präsentiert diese Arbeit eine neue Methode, um die lokalen thermischen Bedingungen während des Aufbaus von Bauteilen im *Material Jetting* Prozess zu simulieren. Diese Simulationsmethode wurde verwendet, um die Bedingungen während der durchgeführten Experimente zu berechnen. Weiterhin ermöglicht die Simulationsmethode die Modellierung und Analyse eines industriellen *Material Jetting* Prozesses mit höheren Druckfrequenzen und geringeren Tropfendurchmessern im Vergleich zur Prototypenanlage.

Die Ergebnisse zeigen, dass dieses Fertigungsverfahren den Aufbau von Bauteilen aus Aluminiumlegierungen mit einer relativen Dichte von über 99 % und mit mechanischen Festigkeiten oberhalb der gegossenen Referenz ermöglicht. Das Fließen des Tropfens beim Aufprall und die Anbindung an benachbartes Material sind stark von der Legierungszusammensetzung und der Mikrostruktur abhängig, welche sich während der raschen Erstarrung bildet. Das Verhalten unterschiedlicher Legierung variiert mitunter deutlich und kann nicht durch bereits veröffentlichte Modelle erklärt werden. Diese Modelle nehmen an, dass es erforderlich ist das benachbarte Material durch die Überhitzung des Tropfens aufzuschmelzen, um eine metallische Bindung zu bilden. Diese Annahme konnte nicht bestätigt werden. Für die meisten Legierungen ist es notwendig das Bauteil während des Druckprozesses lokal auf eine Temperatur nahe der Solidustemperatur zu bringen, um eine metallische Bindung zum aufgebrachten Tropfen zu ermöglichen. Wählt man die Temperatur zu hoch, so schmilzt zu viel Material auf und die erwünschte Geometrie des Teils geht verloren. Daher ist es eine Herausforderung den Prozess so zu steuern, dass die Temperatur beim Aufbau beliebiger Geometrien jederzeit im erforderlichen Prozessfenster bleibt. Die Ergebnisse dieser Arbeit tragen zum erforderlichen Verständnis bei, um einen solchen industriellen *Material Jetting* Prozess für Aluminiumlegierungen zu entwerfen, welcher hochqualitative Bauteile mit beliebigen Geometrien aufbauen kann.

Contents

List of Symbols

Symbol	SI Unit	Meaning
A	m^2	Area
Bo	-	Bond number
c	$J\,kg^{-1}\,K^{-1}$	Specific heat capacity
c	-	Concentration
C	-	Constant
d	mm	Diameter
D	$m^2\,s^{-1}$	Diffusion coefficient
f	Hz	Printing frequency
fs	-	Fraction solid
g	$m\,s^{-2}$	Gravitational constant
G	$K\,m^{-1}$	Gibb's free energy
h	m	'Solidified' layer height
k	-	Distribution coefficient
l	m	Length
L	$J\,kg^{-1}$	Specific heat of fusion
m	-	Slope of liquidus temperature in phase diagram
n	-	Number
Oh	-	Ohnesorge number
p	bar	Pressure
Pr	-	Prandtl number
St	-	Stefan number
T	°C	Temperature
t	s	Time
v	$m\,s^{-1}$	Velocity
V	m^3	Volume
We	-	Weber number
α	$W\,m^{-2}\,K^{-1}$	Heat transfer coefficient
Γ	$K\,m$	Gibbs-Thomson coefficient
ΔT	°C	Temperature difference
η	$Pa\,s$	Dynamic viscosity
θ	°	Contact angle

θ^*	°	Apparent contact angle
λ	$W\,m^{-1}\,K^{-1}$	Thermal conductivity
ρ	$kg\,m^{-3}$	Density
ρ_{rel}	-	Relative density
σ	$N\,m^{-1}$	Surface tension

Index	**Meaning**
0	Initial
abs	Absolute stability
adj	Adjacent
c, c1, c2	Contact
con	Constitutional undercooling
d	Dynamic
DCP	Dendrite coherency point
drop	Droplet
env	Environment
f	Flow arrest
liq	Liquidus
lv	Liquid-vapour
m	Mean
metal	Metal
ml	Monolayer
O_2	Oxygen
period	Period between two droplets
ph	Print head
pulse	Droplet ejection pulse
rel	Relative
s	Substrate sheet
sf	Solidification
sl	Solid-liquid
so	Start of oxidation
sol	Solidus
subs	Substrate
sv	Solid-vapour
total	Total
x,y,z	Coordinate directions

List of Abbreviations

Abbreviation	**Meaning**
AlN	Aluminium Nitride
AM	Additive Manufacturing
BJT	Binder Jetting
BN	Boron Nitride
BPM	Ballistic Particle Manufacturing
CAD	Computer-Aided Design
CNC	Computerised Numerical Control
DCP	Dendrite Coherency Point
DED	Direct Energy Deposition
DMD	Direct Metal Deposition
DMLS	Direct Metal Laser Sintering
DoD	Drop on Demand
EDX	Energy Dispersive X-ray Spectroscopy
FDM	Fused Deposition Modelling
FEM	Finite Element Method
FFF	Fused Filament Fabrication
GP I	Guinier-Preston-Zones I
GP II	Guinier-Preston-Zones II
LENS	Laser Engineered Net Shaping
LOM	Laminated Object Modelling
MDDM	Micro Droplet Deposition Manufacturing
MEX	Material extrusion
MHD	Magneto-hydrodynamic
MJT	Material jetting (with metals)
NDM	Net Droplet-based Manufacturing
PBF	Powder bed fusion
PLC	Programmable logic controller
PTFE	Polytetrafluoroethylene
SEM	Scanning electron microscope
SHL	Sheet lamination
SLA	Stereolithography

SLM	Selective Laser Melting
SLS	Selective Laser Sintering
SSS	Supersaturated Solid Solution
utg	Institute for metal forming and casting
VOF	Volume-of-Fluid method
WAAM	Wire+Arc Additive Manufacturing

1 Introduction

Additive manufacturing (AM) is one of the most important developments for the production industry in the last 25 years. This technology, which has become popular in the mainstream press as *3D Printing*, is defined as a process of joining materials to make objects from 3D model data, as opposed to subtractive manufacturing methods such as milling. AM processes are usually performed layer upon layer and can be divided into several distinctly different processes. Fabricating parts in a layer-by-layer fashion is possible by extruding, jetting, photo-curing, laminating or fusing materials. The latest edition of the Wohler's Report (2018), which is also referred to as the *bible of 3D printing*, focuses on metal additive manufacturing as the currently fastest growing branch of AM industry. According to it, AM system sales increased by almost 80 % in 2017 with an estimated 1768 machines sold compared to 983 in 2016. Five years earlier in 2012, only 200 machines were sold throughout the year. By far the greatest share of those systems are machines for a powder bed fusion process. In this process, metal powder is selectively fused in the powder bed by a focused laser or electron beam. Even though this technology has rapidly developed into the metal AM process with the highest flexibility, distribution and technological readiness on the market, its further application in higher volume production is limited by the elevated cost for both, machines and raw material (Ngo et al., 2018). Machine prices are driven by expensive beam sources, beam scanners and the costly metal powder of high quality. Build rates of the machines are low compared to conventional manufacturing processes and the currently chosen way of machine designers to increase build rates, is integrating multiple beam sources. As mentioned before, that also increases machine prices significantly.

Another AM process for metals with a potentially higher build rate and moderate machine prices is the binder jetting process that selectively applies binder from multiple printing nozzles on a metal powder bed to create organically bound green parts. These have to be sintered or infiltrated in a second process step to create a fully metallic part. Apart from the disadvantage of a complex and design limiting multi-step process, this technology still uses metal powders as raw material. An AM process that completely avoids the use of metal powders and beam sources is the material jetting process, where build material is directly deposited through printing nozzles on the build platform. While material jetting processes for polymers have already been successfully commercialised, the development of the metal process and its commercialisation are just starting.

This thesis focuses on the analysis of droplet-droplet bonding in material jetting processes of aluminium alloys and how a process should be controlled to obtain sound metal parts. This is especially challenging in the case of material jetting, as all quality features of the part – i.e. mechanical strength, porosity, surface quality and geometrical accuracy – are defined during droplet deposition. The most important physical quantity that controls droplet spreading and bonding to adjacent material is the temperature of the droplet itself and even more important that of the adjacent material. The latter is a result of the printed geometry and process parameters, i.e. droplet size, printing frequency and build platform temperature. Therefore, one has to carefully control process parameters according to the printed geometry in order to obtain a sound part with uniform properties. Currently, in published literature, there is scarce information on how printed part quality develops for different aluminium alloys under certain thermal conditions and even less information is available on how to efficiently simulate a material jetting process with metals to predict local temperature evolution. Both are essential to design an industrial manufacturing process, which yields high quality metal parts. This work contributes to this knowledge by presenting a novel simulation method for the process of interest and by systematically analysing the influences of thermal conditions and oxidation on the mechanical properties, porosity and microstructure formation of printed parts.

2 State of the Art

First this chapter will give a brief overview of existing metal AM processes and their classification, then the process material jetting is explained in detail including current technical realisations. Subsequently, the state of the art in simulation methods for this process is described. Finally, the chapter presents knowledge on the topics needed to discuss the obtained experimental results, like the formation of metallic bonds, the rapid solidification of aluminium alloys and the oxidation behaviour of aluminium.

2.1 Additive Manufacturing for Metals

A series of international standards deal with additive manufacturing: ISO 17296-2,3,4 and ISO/ASTM 52900. Even though the latest version of ISO/ASTM 52900 is still in the draft status, it will be referred to in this work. It defines the term 'additive manufacturing' (AM) or in German 'Additive Fertigung' as:

> Process of joining materials to make parts from 3D model data, usually layer upon layer, as opposed to subtractive manufacturing and formative manufacturing methodologies.

The commercialisation of AM started in 1987 with stereolithography from 3D Systems. In this process, thin layers of ultraviolet light-sensitive liquid polymers are solidified using a laser beam. Four years later, in 1991, three AM process to create polymer parts were introduced, including fused deposition modelling from Stratasys, solid ground curing from Cubital and laminated object manufacturing from Helisys. Selective laser sintering (SLS), the first powder bed process, became available from DTM in 1992. The company Solingen commercialised direct shell production casting in 1993, which uses inkjet printing to deposit binder on a ceramic powder to fabricate investment-casting shells. This process was based on the patents from Massachusetts Institute of Technology (MIT), which described the consolidation of a powder bed by binder jetting. One year after, ModelMaker from Solidscape was introduced, which was the first material jetting (MJT) process on the market. ModelMaker deposits wax droplets using an inkjet print head. In 1996, Fraunhofer ILT filed the patent application 'shaped body especially prototype or replacement part production', the basic patent for selective laser melting, which became the most relevant AM process to directly fabricate metal parts. Since 2000, an

increasing amount of processes and machines are coming into the market each year and AM is currently evolving from rapid prototyping to series production. (Meiners et al., 1998; Wohlers and Campbell, 2017)

2.1.1 Overview and Classification

All AM processes have in common, that they build parts by adding elements or layers according to a digital model. They do not need any geometry-specific tools and are characterised by minimal design limitations compared to conventional manufacturing processes like milling, casting or forming. The principle of AM is shown in figure 2.1: starting point is a digital model that normally derives from a computer-aided design (CAD) or from measurement data of an existing part. This digital model is divided into layers, which are separately built and fused to form a physical part during the AM process.

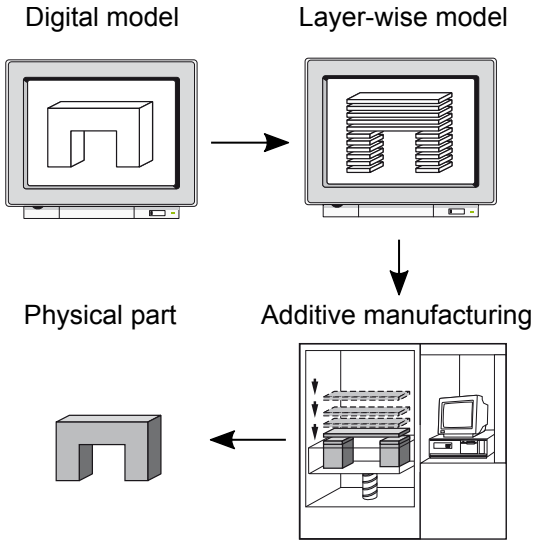

Figure 2.1: Principle of AM processes: The digital model is divided into layers that are then separately built and fused in the AM machine to form a physical part. According to Gebhardt (2013)

Additive manufacturing methods today are available for a multitude of different materials including building materials like concrete (Lim et al., 2012), foods like chocolate (Hao et al., 2010) and even living cells (Melchels et al., 2012). The amount of different processes is just as large as the number of materials that can be processed in AM. This chapter is limited to additive manufacturing methods directly processing metallic materials in the AM machine. In contrast, indirect methods create models or moulds that are used in conventional non-additive processes afterwards. Examples are printed sand moulds for sand casting and wax or plastic models

for investment casting. Table 2.1 gives an overview of the process categories defined in ISO 17296-2, common proprietary names, their suitability to process metals and whether parts can be manufactured in a single step or not. ISO/ASTM 52900 differs between single-step processes, where the basic geometric shape and the basic material properties are achieved simultaneously in one operation and multi-step processes, where typically a first step forms the basic geometry and one or more following steps consolidate the parts to obtain the desired material properties.

Table 2.1: Overview of AM processes defined by ISO 17296-2, common names, their suitability to process metals and whether they are single step processes for the production of metal parts.

Name according to ISO 17296-2	**Common name(s)**	**Metal**	**Single-step**
VAT photopolymerisation	SLA	No	-
Powder bed fusion (PBF)	SLM DMLS	Yes	Yes
Binder jetting (BJT)	3D Printing	Yes	No
Directed energy deposition (DED)	LENS DMD WAAM	Yes	Yes
Material extrusion (MEX)	FDM FFF	Yes	No
Sheet lamination (SHL)	LOM	Yes	Yes
Material jetting (MJT)	BPM MagnetoJet MDDM NDM	Yes	Yes

As there are no metal processes in the category VAT photopolymerisation, it will not be explained in more detail.

Probably the best known representatives to produce metal parts belong to the category powder bed fusion: fusing metal particles by laser beam is commercialised under several trademarks: e.g. ‘Selective Laser Melting’ (SLM), ‘Direct Metal Laser Sintering’ (DMLS), ‘LaserCUSING’ or ‘Laser Metal Fusion’. This process uses one or more lasers to locally melt metal powder in a powder bed. That way a solid metal layer is welded on the build platform. After each layer, the build platform is lowered and a recoating device spreads a new layer of powder. An alternative, whose patents are held by the company ARCAM AB (Mölndal/Göteborg, Sweden), uses an electron beam instead of a laser beam to melt and fuse the powder. An advantage of the electron beam is the larger penetration depth, whereas a high vacuum is necessary resulting in a more

massive and expensive machine design. Figure 2.2 shows a schema of this category. (Gebhardt, 2013; Zäh and Lutzmann, 2010)

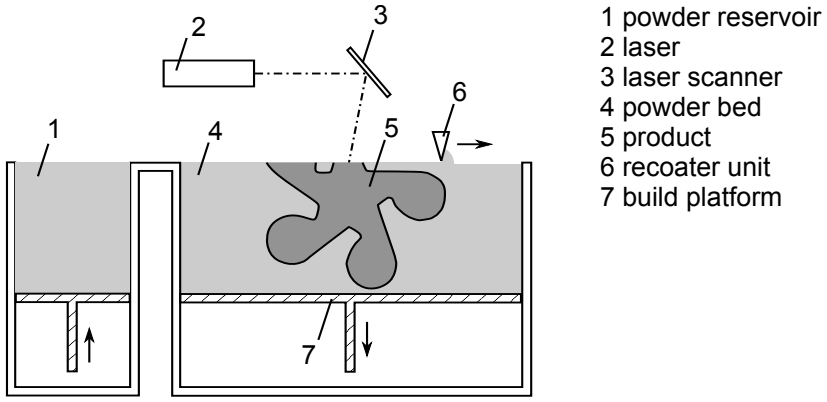

Figure 2.2: Schema of powder bed fusion processes. An energy beam (e.g. laser) selectively consolidates powder in a powder bed layer by layer. According to ISO 17296-2

Another category broadly used and commonly known is binder jetting. The process name '3D printing' used by several companies, who commercialised such processes, will be used in its narrow sense for processes, where a binder is selectively suspended through a printing system on the surface of the powder bed. The binder locally joins the powder particles inside a layer to each other and to the layers below. Figure 2.3 shows a schema of the category BJT. One process uses organic resins printed through conventionally piezoelectric print heads for normal ink. The resin hardens right after printing and bonds the metal particles to form a green part that has sufficient strength to be removed from the powder bed. After printing the green part is moved to two successive process steps: debinding and sintering. In the first step a great share of the resin is removed thermally or chemically and during sintering, the metal particles fuse together to form a solid metal part. Usually fully dense parts can not be produced that way, as a certain porosity remains, which needs to be infiltrated to obtain dense parts. (Agarwal et al., 2002; Desktop Metal Inc., 2018; Gebhardt, 2013)

A process of the same category, which is only described in a scientific publication (Sohn and Yang, 2005) and a patent (US6238614B1), directly prints molten solder (Sn-Pb alloy) as a binder in the powder-bed. The method is called 'Selective Infiltration Manufacturing' in the cited patent. No information is given to successive process steps or properties of the parts produced that way, neither to the application of those parts.

The last category of the aforementioned, with a high degree of commercialisation, is direct energy deposition. In the processes 'laser engineered net shaping' (LENS) or 'direct metal

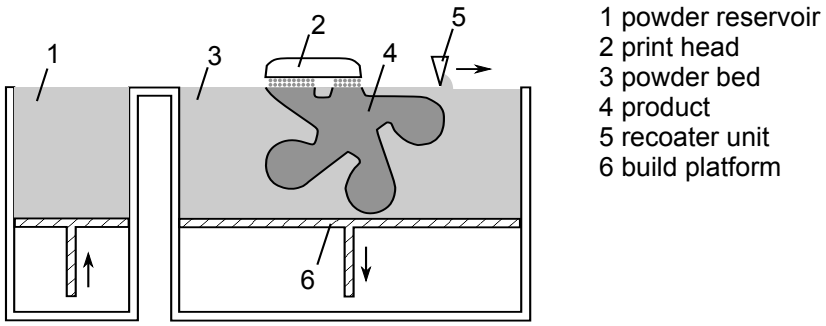

Figure 2.3: Schema of binder jetting processes. A print head selectively deposits binder in a powder bed that locally consolidates the particles. According to ISO 17296-2

deposition' (DMD) the material is supplied by metal powder which is blown into a melt pool established by a laser beam. The powder is transported by a stream of inert gas through nozzles arranged radially around the laser beam. The powder fuses with the existing material inside the melt pool and by moving the substrate relative to the laser beam, parts are successively built. An example setup is depicted in figure 2.4. This build-up welding device is usually installed in a machine, which is similar to a CNC portal milling machine with five axes. As no support material is used in this process, five axes are necessary to create parts with overhanging features. Common applications use this method to add functionality to conventionally manufactured parts or for repair purposes of worn parts. (Atwood et al., 1998; DMG MORI, 2018; Gebhardt, 2013)

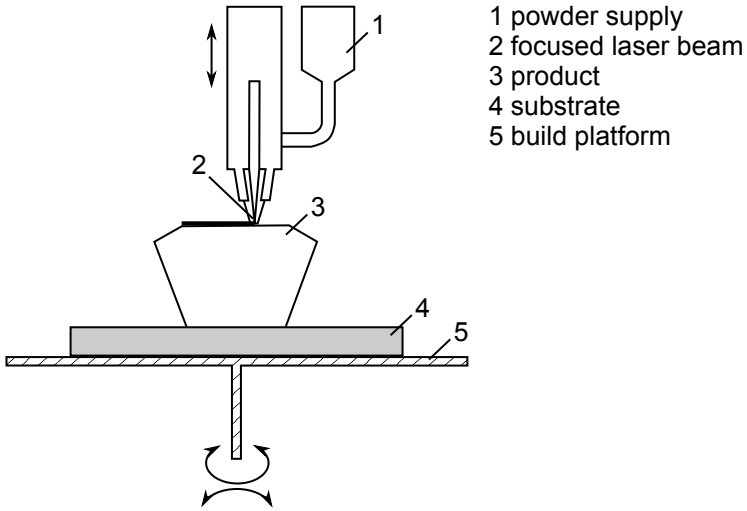

Figure 2.4: Schema of direct energy deposition processes. A focused energy beam (e.g. laser) locally welds material to the product. Material is fed to the melt pool by wire or powder as shown here. According to ISO 17296-2

A similar process uses conventional filler wire and an electric arc as energy source (Karunakaran et al., 2000). It is called 'wire+arc additive manufacturing' (WAAM) and is developed by

Cranfield University in Great Britain. The main advantage of this process is the utilisation of conventional welding equipment and materials, which are fully developed, easy available and cost-efficient. The welding head is manipulated by a robot, or similar to the DMD process, in a five axes portal machine. Taminger and Hafley (2003, 2006) report a process that uses an electron beam instead of the electric arc to supply energy, while material is added via wire.

Cold gas dynamic spray or cold spray is a process conventionally used for coatings, which can also be used to additively build parts. In this processes metal particles are accelerated to high velocities by a supersonic carrier gas stream. When the particles impact on the substrate they will fuse with it by intense local plastic deformation. The resolution of this process is limited by the spot size of the deposition nozzle, which is commonly greater than 1 mm. Therefore, in most application this method is combined with a milling device to obtain accurate shapes. (Sova et al., 2013)

Figure 2.5 shows a schema of the well-known material extrusion process for polymers 'fused deposition modeling' (FDM). Based on it, a process for fabricating metal parts was developed: A thermoplastic filament filled with a high amount of metallic particles is heated and extruded through a nozzle. Due to the elevated temperature the thermoplastic fuses with the surrounding material before it hardens by cooling. As in most other AM processes the build-up is layer by layer and support structures or a support material can be used to create three-dimensional parts. The part created is a green part, that needs to be consolidated in a second process step. Just as in 3D Printing with organic binders, a debinding and a sintering process are necessary to create metal parts. (Desktop Metal Inc., 2018; Geiger et al., 1994; Gonzalez-Gutierrez et al., 2017; G. Wu et al., 1999)

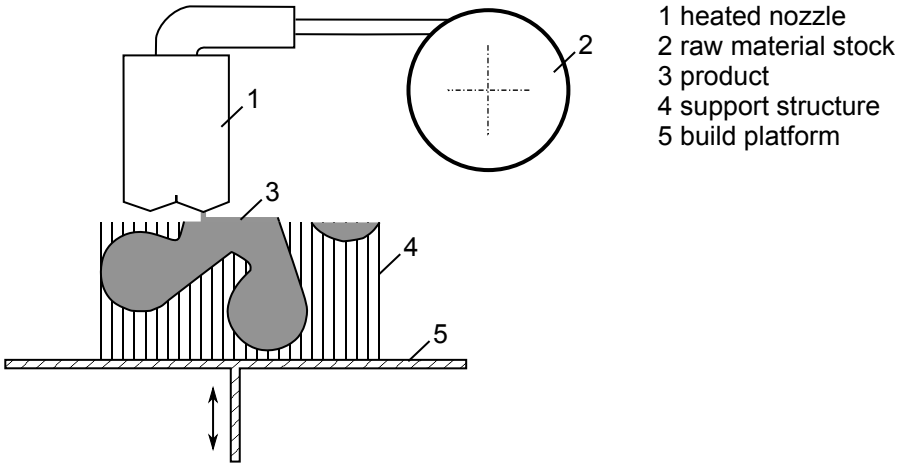

Figure 2.5: Schema of material extrusion processes. A filament from the feed stock is extruded through a heated nozzle and deposited on the product. According to ISO 17296-2

Another method similar to FDM directly extrudes metal in a semi-solid state. To obtain the semi-solid state, an alloy is held at a temperature between solidus and liquidus temperature and constantly stirred. Through a nozzle the material is then pressed on a substrate just as it is done for thermoplastic materials in FDM. (Finke and Feenstra, 2002; Rice, 2000)

In the category sheet lamination, metal foil or sheet metals are used as a feedstock. They are cut to the desired layer shape, stacked upon the existing part and fused with it. Bonding is achieved by several methods: adhesives (Gebhardt, 2013), diffusion welding (Yi et al., 2004) or ultrasonic welding (Friel and Harris, 2013). The shaping of each layer is done by laser cutting or milling.

Processes of the category material jetting differ from the extrusion processes as there is no contact between the material supply and the part being built. This gives the opportunity to use several parallel operating nozzles. The material deposition is no longer vector-based but raster-based. The complete layer is run over by the print head and single droplets are deposited on the desired coordinates, as it is done in ink-jet printing. This basically enables a significant higher material flow rate compared to vector-based methods, as there are no restrictions to the number of nozzles. Figure 2.6 shows the differences for an example layer.

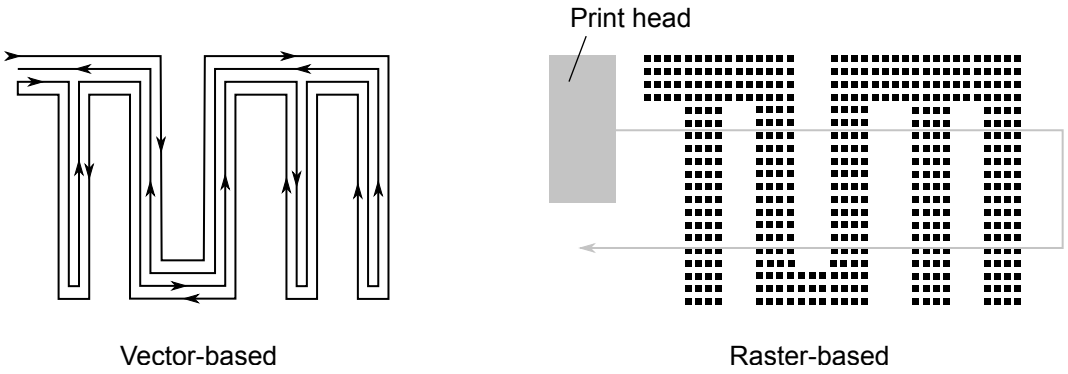

Figure 2.6: Comparison of vector-based and raster-based methods to deposit one layer.

One commercialised method of this category is ‘NanoParticle Jetting’ by the company XJet (Rehovot, Israel). It prints a liquid suspension containing small particles of the build or support material through a piezoelectric ink-jet print head directly on the build platform. This platform is heated and a part of the fluid evaporates immediately after impact. A secondary heat input by an infrared heater sinters the particles partly together. In each layer, the complete build platform is covered with either build or support material. That way a green part is produced, which needs to be consolidated by sintering as it was already described for other processes. (Gothait et al., 2015; Xjet, 2018)

The only single-step process of the category material jetting deposits directly molten metal droplets on a build platform to fabricate metal parts.

2.1.2 Material Jetting of Metal

This thesis focusses on the material jetting (MJT) process of metal, which is presented in detail in the following section. First, the process procedure is described, then the most important technical realisations are presented and finally published knowledge on the mechanisms of droplet bonding are explained. Several names were given to this process but none of them has established itself yet. Throughout this work the term 'material jetting of metal' will be used for all realisations. As abbreviation MJT is used for the processing of metal, even though in its general meaning this term also includes polymer processes.

Description of Process Procedure

In MJT an equipment called print head ejects droplets of molten metal. The material in the print head is heated at least to liquidus temperature. The droplets are deposited on a build platform or on the already deposited material, which will be called substrate in the following. The substrate has a temperature below or only slightly above the material's solidus temperature. Incoming droplets bond with the substrate and solidify upon deposition. In this manner a desired part is deposited droplet by droplet. Figure 2.7 shows the principle procedure of MJT processes.

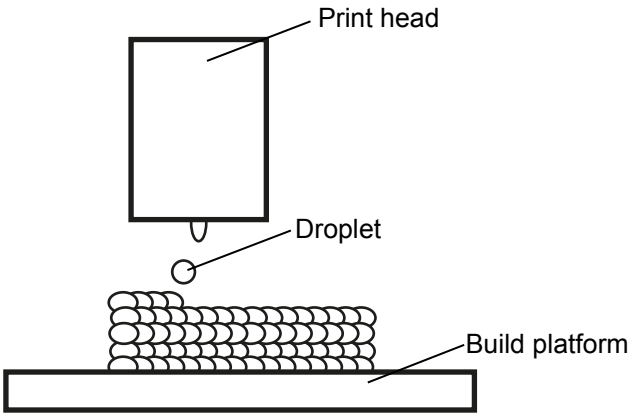

Figure 2.7: Principle procedure of MJT processes: A print head ejects molten metal droplets, which are deposited on a build platform, where they bond with the existing material.

In almost all realisations the substrate and/or the print head are positioned in three linear axes to control the location of droplet deposition and the distance between print head and part surface

(Pham and Gault, 1998). An alternative method was published by Orme and Smith (1999), where the droplets are electrically charged and deflected by electro-magnetic fields.

To build overhanging features, with an angle of more than 40° against the build platform, in a three axes setup, support material is necessary. In comparable methods to process plastics or wax, support materials are used that can be removed due to their mechanical brittleness, their low melting point or their chemical solubility (Gebhardt, 2013). For MJT of metal, there is not yet a publication concerning suitable support materials. But due to the high surface tension of metals, overhangs up to 40° against the build platform can be build without using support material (Zhang et al., 2017). Figure 2.8 illustrates this possibility with zigzag columns.

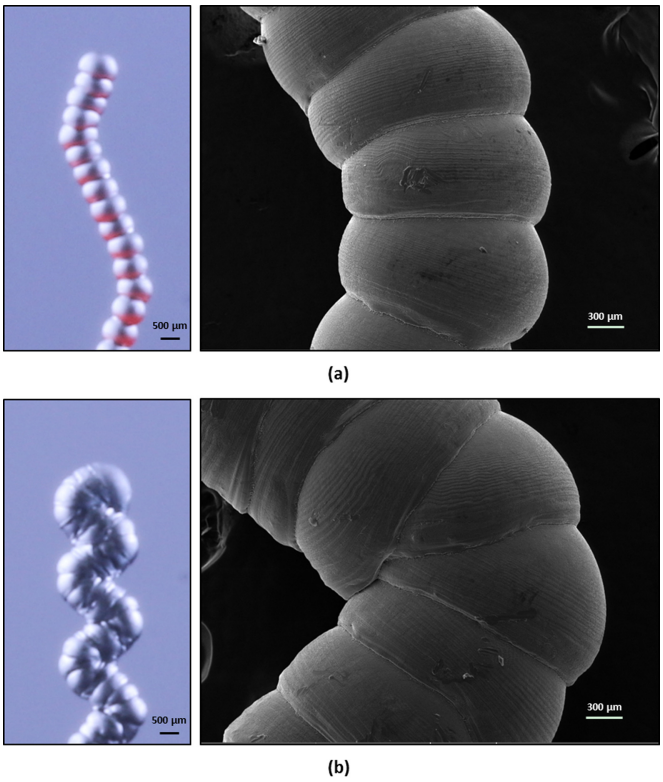

Figure 2.8: Zigzag columns build by MJT of aluminium. Reprinted from Zhang et al. (2017), page 22, ©2017, with permission from Elsevier.

Methods for droplet ejection

Existing methods to deliver droplets for an MJT process can be divided into two categories: 'continuous-jet' and 'drop-on-demand' (DoD) systems (Heinzl and Hertz, 1958). In 'continuous-jet' methods, fluid is continuously jetted from a nozzle. The jet disintegrates to a train of droplets according to Rayleigh (1878). To stabilise the disintegration into regular droplets of a constant size, a small excitation in an appropriate frequency is necessary. The

droplets are usually electrically charged and deflected in electric fields. The deflection can have two purposes: To control the direction of flight and therefore the location of deposition on the platform and/or to deflect undesired droplets in a gutter (Heinzl and Hertz, 1958; Orme and Smith, 1999). An advantage of those methods is the high delivery rate. Orme and Smith (1999) presented a setup to eject droplets of pure aluminium with a diameter of 189 µm at a rate of 24 kHz. Figure 2.9 shows the principle of a 'continuous-jet' print head.

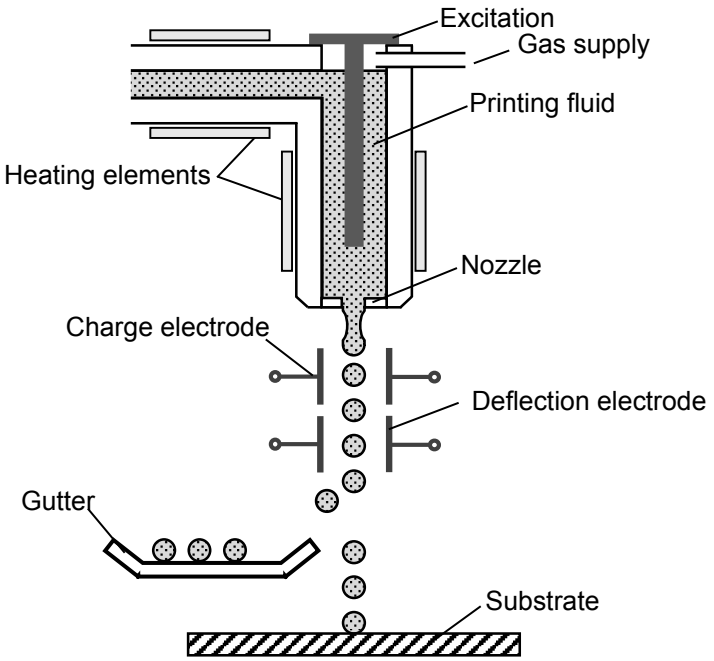

Figure 2.9: Principle of a 'continuous-jet' print head: A fluid is forced through the nozzle by a constant gas back pressure. Supported by the vibration excitation the jet quickly disintegrates to a train of droplets, which are charged and deflected in electric fields.

However, most published realisations of MJT are based on DoD methods. By several mechanisms a pulsed force on the molten metal inside the reservoir is created. The bottom of the reservoir is closed by a nozzle, which is small enough to avoid dripping due to surface tension and capillary pressure. The pulsed forces induce a pressure at the nozzle entrance that ejects a small amount of fluid through the nozzle. Figure 2.10 shows the principles of DoD print heads with different actuations: A gas pressure pulse can be applied to the surface of the molten metal to create a pressure pulse at the nozzle entrance, which cause a droplet ejection (Rumschoettel et al., 2017). Alternatively a piezoelectric or electromagnetic actuator can be used to apply the necessary force (Lee et al., 2008; Zhong et al., 2014). Those actuators need to be thermally decoupled by a transmitter rod from the liquid metal as they can not withstand the high temperatures. Piezoelectric ceramics, which are commonly used for DoD print heads working at room temperature like ink-jet print heads, loose their piezoelectric effect at temper-

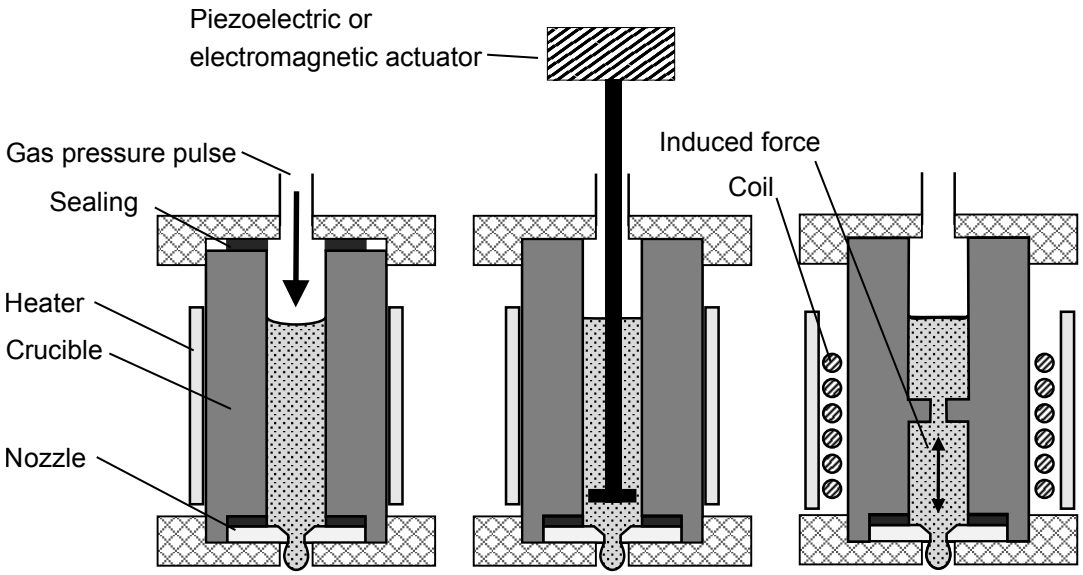

Figure 2.10: Principle of 'drop-on-demand' print heads with pneumatic actuation (left), piezoelectric or electromagnetic actuation (centre) and magneto-hydrodynamic actuation (right).

atures above the curie-temperature (< 350 °C) (Uchino, 2017). Another contactless method is the magneto-hydrodynamic principle (MHD). A pulsed magnetic field is induced by an external coil surrounding the crucible. The induced eddy currents interact with the magnetic field and create an axial Lorentz force, which can be used to eject a droplet. (S. Vader et al., 2016)

Another method, which also uses Lorentz forces, creates the magnetic field and the electric current separately. A constant magnetic field is created by a permanent magnet or an electromagnet. A current pulse between two electrodes that are in contact with the molten metal interacts with the magnetic field and applies a Lorentz force on the melt, which is perpendicular to the magnetic field and the electric current according to the right-hand rule. (Sachs et al., 2017; Suter et al., 2012)

A special form was developed by Harnisch (2009) to print solder: A ferromagnetic piston is balanced by two external coils to float in the molten metal above the nozzle plate. The lost heat from the coil is used to melt the solder inside the crucible. By varying the coil currents the piston is moved axially to generate the desired pressure for droplet ejection.

The StarJet system is a pneumatically driven system that can be operated in DoD mode as well as in continuous mode. Scientists at the University of Freiburg (Freiburg, Germany) are still working on this method. Its special feature is the nozzle with star-shaped bypass channels surrounding the nozzle orifice (see figure 2.11). The bypass channels are narrow enough not to

be wet by the molten metal, which therefore has only little contact with the nozzle material. A constant gas flow through the bypass channels induces the droplet break-up when liquid enters the nozzle. That way this system delivers a continuous train of equally sized droplets at a constant rate by only applying a constant gas pressure on the molten metal. When applying pressure pulses, the print head can also be operated in DoD mode. The challenge for this system is to fabricate a nozzle chip from a material that is inert to aluminium melt at the high temperatures necessary. (Gerdes et al., 2017; Tropmann et al., 2012)

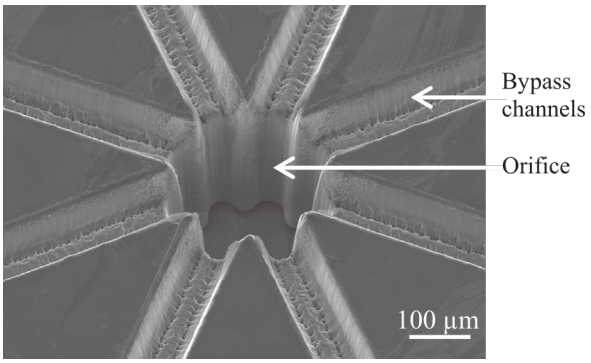

Figure 2.11: SEM view of a Star-Jet nozzle with the nozzle orifice and the star-shaped bypass channels. (Gerdes et al., 2017) ©2017 IEEE

Technical Realisations of MJT

So far there is only one MJT system commercialised and available on the market: A technology called 'MagnetoJet' is developed and distributed by the company Vader Systems, LLC (New York, USA). The print head is based on the MHD principle and is patented in the US (S. Vader and Z. Vader, 2015). It ejects droplets with a size of 50 to 500 µm at a frequency of 40 to 1000 Hz. A wire feeder, as it is used in welding equipment, supplies the print head with an aluminium wire that is used as raw material. After entering the print head, the wire is molten under inert gas and flows into the ejection chamber, where MHD forces are induced by the surrounding coil. All parts being in contact with molten aluminium are made from boron nitride. The print head is embedded in a heated housing, which is purged by inert gas. An opening below the nozzle allows the droplet to escape together with the inert gas. All other components, e.g. the build platform are not enclosed in a housing, so one can assume, that there is no controlled atmosphere around the parts during build-up. Figure 2.12 shows the setup. (Karampelas et al., 2017; Sukhotskiy et al., 2018; Vader Systems, 2018)

A patent research reveals that there are current developments in other companies on that topic too: Desktop Metal Inc. (Burlington, USA) plans to bring two AM systems to produce metal parts on the market: The studio system, which extrudes a metal particle enriched filament (MEX) and

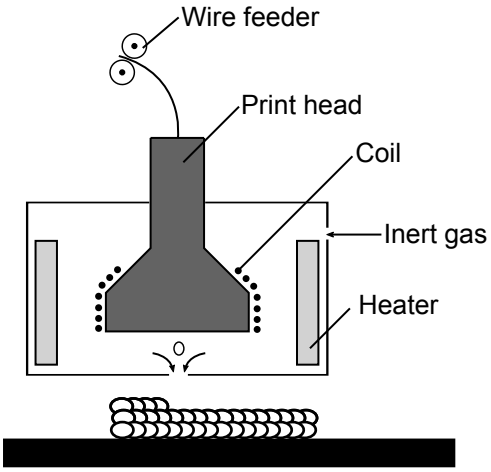

Figure 2.12: Schema of the setup commercialised by Vader Systems, LLC: A wire feeder provides aluminium wire to the print head, where it is molten. A coil provides a pulsed magnetic field that induces Lorentz forces in the liquid metal. The forces eject droplets from the nozzle. The print head is contained in a heated housing purged by inert gas.

the production system, which prints organic binder on a metal powder bed (PBF). Both methods create green parts that needs to be consolidated in additional process steps (Desktop Metal Inc., 2018). But Desktop Metal Inc. is also working on a MJT process with molten metals according to their three recent patent applications on that topic (Myerberg, Fulop et al., 2017; Myerberg, Natchurivalapil Rappai James et al., 2017; Sachs et al., 2017). Two other companies that published patent applications on MJT are Robert Bosch GmbH (Stuttgart, Germany) and OCE Technologies B.V. (Venlo, Netherlands) (Rheiter and Rasa, 2015; Voehringer et al., 2017).

At the universities Jiaotong University and Northwestern Polytechnical University in Xi'an, China, two very similar setups are used for research purposes. In their publications a total of three different print heads are presented: two mechanical systems using a coupling rod that reaches into the melt close to the nozzle entrance and is connected to either a piezoelectric actuator (Luo et al., 2014) or an electromagnetic vibration exciter (Zhong et al., 2014) and a simple pneumatic drive (Zuo et al., 2015). Droplets are deposited from a stationary print head on the build platform, which can be manipulated by three linear motion stages. The characteristic of all those systems is that they are completely enclosed in a vacuum-tight chamber. This chamber is evacuated and purged with inert gas several times before starting the experiments, which leads to a oxygen content of less than 5 ppm (Chao et al., 2012; Zuo et al., 2015). Figure 2.13 shows a schema of those systems.

A scientific group at the University of Toronto, Canada, published several articles on metal droplet generation for solder, tin and aluminium in the years 2000 to 2009. A pneumatic

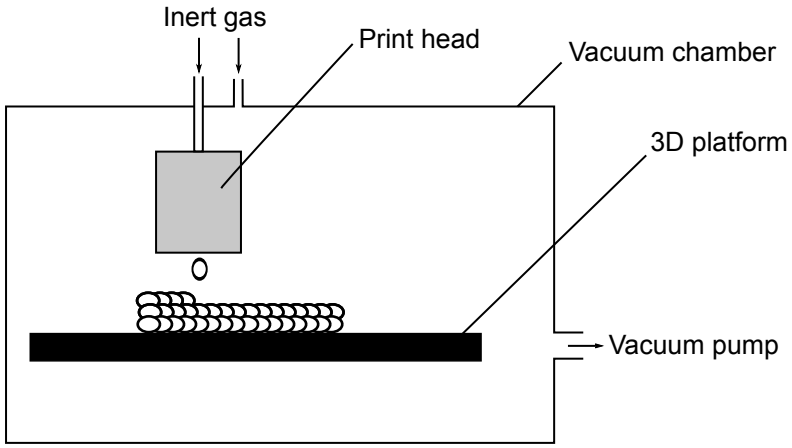

Figure 2.13: Schema of the setup at Jiaotong University and Northwestern Polytechnical University in Xi'an. The complete setup is enclosed in a vacuum chamber that is evacuated and purged by inert gas before the experiments.

actuation is used to eject droplets. The rest of the setup is comparable to that shown in figure 2.13 except that the print head is outside the chamber and oxygen concentration is 35 ppm. Moreover, the build platform can only be moved in a plane by two axes, so the distance between print head and build platform remains constant. (Cheng et al., 2005; Fang et al., 2009)

The only MJT system with a continuous-jet print head was developed and run at the University of California-Irvine, USA. Droplets are ejected at a high speed of $10.9\,\mathrm{m\,s^{-1}}$. They are charged electrically after separation from the jet and can be deflected by electric fields to reach the desired location on the build platform. Due to the high speed, the flight distance between print head and substrate is 50 cm to enable a sufficient lateral deflection. Despite that possibility of deflection, all three-dimensional parts from the publications are built using a motion stage to manipulate the build platform. The complete apparatus is evacuated and purged by nitrogen to maintain oxygen concentrations of 35 ppm. (Liu and Orme, 2001; Orme and Smith, 1999)

2.2 Process Simulation of Material Jetting of Metal

Several publications focus on the coupled fluid motion, heat transfer and solidification phenomena, which occur when molten droplets impinge a solid substrate at a temperature below the solidus temperature of the droplet. Zhao et al. (1996a,b) published a mathematical formulation of the problem without solidification that they solved by a finite element approach with a remeshing criteria to avoid excessive distortion of the elements. In the second paper, the authors compare their simulated results with experimental results of ink and tin droplets on a quartz plate. They find good agreement with the model in the early stages of spreading, which are controlled by

the inertial of the droplet. In the late stage of spreading, the effect of wetting at the contact line becomes dominant and the model fails to accurately predict the droplet shape, as they do not model the wetting correctly. Pasandideh-Fard et al. (2002) use a fixed grid discretisation and a volume-of-fluid method that tracks the free liquid surface, to solve the governing equation for fluid motion, heat transfer and solidification. A cell size of 50 to 70 µm was necessary to find valid results for the impingement of a tin droplet with 2.7 mm diameter. They successfully compare numeric results with experimental results of a tin droplet deposited on a steel substrate at high Weber numbers (final splash diameter ≫ final splash height). Fang et al. (2009) present an analytic model for the 1-D temperature field of a growing column created by the successive deposition of droplets on a fixed position. They compare measured temperatures in experiments with an aluminium alloy to their prediction and find a fairly good conformity. H. Li et al. (2012) model fluid motion, heat transfer and solidification in three dimensions during the successive deposition of three aluminium droplets on a moving substrate. The software Flow 3D with the volume-of-fluid method is used to solve the problem. Time step is 1×10^{-9} s and the grid has a spacing of 75 µm in all three dimensions. Validation experiments are carried out with pure aluminium. The resulting geometry is compared qualitatively with images taken by a scanning electron microscope (SEM). In an almost identical publication of the same working group, the authors compare a simulated line of five droplets qualitatively with SEM images of experiments with Al7075 (H.-p. Li et al., 2014).

Only two publications address the prediction of a global thermal field during the build-up of a part consisting of more than one thousand droplets: Chao et al. (2013) present a model based on the software ANSYS, which neglects fluid motion and approximates each droplet as a cuboid brick represented by a single cell. The equations are solved with the finite-element-method (FEM). The ‘element birth’ and ‘death’ capabilities of ANSYS are used to implement the successive deposition of material. When an element is ‘killed’ its conductivity is multiplied by a factor close to zero and its mass is set to zero. At the start of the simulation, all cells are ‘killed’ and for each droplet deposition, the corresponding element is set ‘alive’. In a later publication the authors present good agreement with temperature curves measured in experiments with Al7075 and they calculate thermal stresses based on the same model (Chao et al., 2016).

2.3 Formation of Metallic Bonds

In the process of MJT, liquid metal droplets fall on (semi) solid material of the same kind. To be able to produce parts with comparable properties to conventionally manufactured ones in a single step, it is necessary that metallic bonds are formed directly after contact. This chapter

presents the published knowledge on this topic. The first part comprises information gained in the field of MJT while the second and third part shows information on comparable processes.

2.3.1 Droplet-Droplet Bonds in Material Jetting of Metal

An often cited model to estimate the temperature in the contact zone between a droplet and the substrate for short times after contact is the model of semi-infinite bodies. Droplet in this context always relates to the liquid droplet just arriving, while substrate is the already deposited material, which comes into contact with the droplet. When two semi-infinite bodies with different temperatures come into contact without thermal resistance, their temperature profiles can be calculated analytically. In this case the contact temperature, which describes the local temperature in both bodies next to the contact zone, is independent of time and can be calculated to (Polifke and Kopitz, 2009):

$$T_{c1} = \frac{T_{subs}\sqrt{\rho_{subs}c_{subs}\lambda_{subs}} + T_{drop}\sqrt{\rho_{drop}c_{drop}\lambda_{drop}}}{\sqrt{\rho_{subs}c_{subs}\lambda_{subs}} + \sqrt{\rho_{drop}c_{drop}\lambda_{drop}}} \qquad \text{(Equation 2.1)}$$

T: Temperature
ρ: Density
c: Specific heat capacity
λ: Thermal conductivity
$_{c1,subs,drop}$: Evaluated at contact, substrate, droplet

Fang et al. (2009) use the contact temperature T_{c1} as a criteria to decide if remelting of the substrate occurs or not. It is assumed that remelting occurs when the contact temperature is higher than the alloy's solidus temperature $T_{c1} > T_{sol}$. The assumption is successfully validated by comparing the outer appearance of columns formed by droplet deposition at the same position. The alloy A380 (AlSi9Cu3(Fe)) is used in these experiments.

Also Chao et al. (2013) employ this model to define three regions dependent on the solidus T_{sol} and liquidus temperature T_{liq} of the alloy:

$T_{c1} < T_{sol}$ I: No remelting and therefore no metallic bonds form
$T_{sol} < T_{c1} < T_{liq}$ II: Remelting with formation of metallic bonds
$T_{c1} > T_{liq}$ III: 'Over-remelting', printed parts loose their shape

To validate those assumptions, blocks and columns are printed from aluminium 7075 with different substrate and droplet temperatures. Outer appearance and micro-sections are compared. It should be noted that all shown combinations of temperatures are within the region II but still all three states are found: insufficient bonding, satisfying bonds and loss of shape. So one can conclude that, at least for aluminium 7075, those regions are not adequate to predict part quality.

Aziz and Chandra (2000) deposit droplets of molten tin with a diameter of 2 to 3 mm on a steel platform. The surface temperature below the droplets is recorded by a fast-responding thermocouple. The authors find that the temperatures estimated by T_{c1} (Equation 2.1) are lower than the measured temperatures. They conclude that liquid convection inside the droplet during spreading on the substrate invalidates the assumption of a semi-infinite body described by ρ, c and λ. Instead they propose to use a semi-infinite body for the substrate and a constant temperature boundary condition for the droplet as fluid convection supplies the interface with 'fresh' melt during impact of the droplet. To find an analytical solution, it is necessary to introduce a heat transfer coefficient α between droplet and substrate. Now the temperature inside the semi-infinite body next to the interface can be estimated to (Polifke and Kopitz, 2009):

$$T_{c2} = T_{drop} - (T_{drop} - T_{subs}) \left[\exp\left(\frac{\alpha^2 t}{\lambda_{subs} \rho_{subs} c_{subs}} \right) \operatorname{erfc}\left(\frac{\alpha \sqrt{t}}{\sqrt{\lambda_{subs} \rho_{subs} c_{subs}}} \right) \right] \quad \text{(Equation 2.2)}$$

T: Temperature
t: Time
ρ: Density
c: Specific heat capacity
λ: Thermal conductivity
α: Heat transfer coefficient
$_{c2,subs,drop}$: Evaluated at contact, substrate, droplet

Aziz and Chandra (2000) determine α by fitting (Equation 2.2) to their experimental data and obtain values from 2×10^5 to 1×10^6 W m^{-2} K^{-1} dependent on the conditions.

S. P. Wang et al. (1998) provide a model of one-dimensional heat conduction in a semi-infinite substrate covered by a layer with a finite height. Phase change with super-cooling and overheating is included in the model. At the interface a heat transfer coefficient is introduced and the problem is numerically solved for several different material combinations. The criteria for remelting of

the substrate by the applied layer is presented graphically in figure 2.14. Also S. P. Wang et al. (1998) assume that remelting is necessary to obtain metallic bonds between substrate and layer.

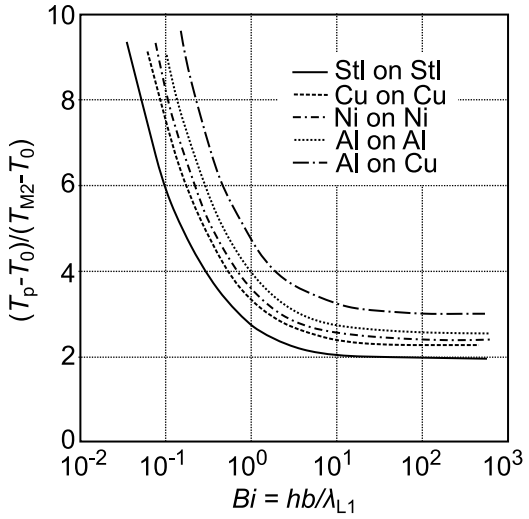

Figure 2.14: Operational map for substrate remelting after contact with a finite layer. With the layer height b, the heat transfer coefficient h, initial temperatures of substrate T_0 and layer T_p, the fusion temperature of the substrate T_{M2} and the heat conductivity of the layer λ_{L1}. According to S. P. Wang et al. (1998)

2.3.2 Compound Casting

Compound casting is defined as the production of a part consisting of two different metals of which one at least is cast in a mould, which is at least partly formed by the compound partner. This compound partner was either produced by casting in a preceding step and is already (partly) solidified or it was produced in a different manner and placed in the mould. (Lange, 1998)

According to Ißleib et al. (1995) there are two basic requirements for the formation of metallic bonds between compound partners:

- The materials needs to be free of disturbing non-metallic atoms or molecules on the surface.
- At least one of the materials needs to be in the molten or thixotropic state for a certain time, because the technical roughness of solid parts does not allow the partners to approach close enough for a physical contact of the atoms.

Lange (1998) states that, to satisfy the second requirement, it is necessary that the contact temperature is above the solidus temperature of one of the partners. To estimate the contact temperature the model of semi-infinite bodies T_{c1} (Equation 2.1) is employed.

Bobzin (2013) distinguishes five mechanisms of bonding between metallic compound partners as shown in figure 2.15:

- Mechanical interlocking: Bonds created by a surface structure with undercuts that are filled by the compound partner.
- Diffusion: Mutual solubility of the metals enables diffusion in each other creating a diffusion zone in the interface. This zone compensates the chemical composition, lattice structure and residual stresses of the partners.
- Pseudo-diffusion: When high energies (e.g. kinetic) are present when partners come into contact, atoms of one partner may be brought inside the others lattice, where they remain even though no solubility is given.
- Adhesion: Partners without solubility and chemical reactivity are merely bond by van-der-Waals forces between atoms and molecules on the surfaces.
- Chemical compound: A chemical reaction of the partners creates an interface layer consisting of intermetallic phases or oxides for example. This layer comprises usually several atom layers. The properties of the layer are decisive for the properties of the part.

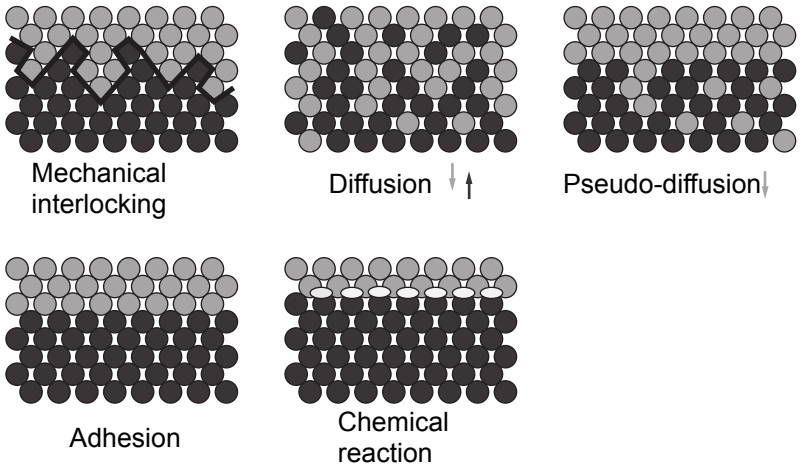

Figure 2.15: Mechanisms of bonding between metallic partners. (Bobzin, 2013)

For compound casting of an aluminium alloy onto a rolled aluminium sheet, Papis et al. (2008) suggest to coat the metal sheet with tin prior to casting, which improves the wetting behaviour.

Otherwise the wetting of the metal sheet's surface by the melt is insufficient. In contrast to that Nerl et al. (2014) show metallic bonds without surface treatment in a continuous compound casting process of two aluminium alloys. The process is characterised by casting both alloys in a single tool in immediate sequence. Heugenhauser (2018) studies a casting process that forms aluminium compound strips by casting pure aluminium on a preheated strip of AlSn25 or Al 7075. He states that the crucial condition to form a sound metallic bond is the removal of the thick oxide layer, which formed during preheating of the substrate. To remove this layer it is necessary to melt the substrate below the oxide layer, so it can be displaced and fractured by the melt flow on top of it.

2.3.3 Soldering and Brazing

According to ISO 857-2 soldering and brazing are defined as:

> Joining processes in which a molten filler material is used that has a lower liquidus temperature than the solidus temperature of the parent material(s), which wets the surfaces of the heated parent material(s) and which, during or after heating, is drawn into (or, if pre-placed, is retained in) the narrow gap between the components being joined.

Soldering is a process using a filler metal with a liquidus temperature below 450 °C, while brazing uses one with a liquidus temperature above 450 °C. As aluminium alloys in technical applications are usually joined by brazing, the following will concentrate on this process.

The bonding process is based mainly on cohesion forces resulting from mutual diffusion of alloy elements. Generally, atomic bonds between parent metal and filler metal are created by four processes (Matthes et al., 2003):

- Diffusion of atoms from the parent metal into the molten filler metal and formation of a solid solution in the subsequent solidification.
- Diffusion of atoms from the molten filler metal into the solid parent metal under formation of a solid solution.
- Mutual diffusion of atoms from the filler metal and the parent metal under formation of intermetallic compounds.
- Adhesion (diffusion-free bonds).

To enable those processes, an intermediate contact of atoms on the surface of parent metal and molten filler metal is necessary. Therefore, the correct preparation of the parts for brazing is of particular importance. In the case of aluminium alloy as parent material the oxide layer on the surface needs to removed before brazing. It is first grounded then remaining grease is removed by organic solvents and then the surface is strained by straining agents containing HF and HNO_3. As a thin oxide layer will form immediately when the virgin metal gets into contact with oxygen, a flux is used to remove existing oxides and protect the surface against oxidation until it is covered with molten filler metal. To fill the assembly gap between joint partners, wetting of the filler metal on the parent material needs to be sufficiently good (contact angle < 30°). (Bobzin, 2013; Matthes et al., 2003)

2.3.4 Wetting

As just mentioned, a necessary condition to obtain metallic bonds is, that the substrate is properly wetted by the molten metal. In this section the basics of wetting are explained with a focus on molten materials.

Basics of Wetting

To describe the wetting of a solid by a liquid quantitatively, usually the contact angle is given. This can be illustrated by a sessile drop on a flat surface as shown in figure 2.16. The angle present between solid and liquid in the point where the three phases liquid, solid and surrounding gas meet, is called contact angle. Young (1805) was first to deal with it and established the relationship between the contact angle and the surface energies between the phases:

$$\cos\theta = \frac{\sigma_{sv} - \sigma_{sl}}{\sigma_{lv}} \qquad \text{(Equation 2.3)}$$

θ: Contact angle

σ: Surface energy or tension

$_{sv,\ sl,\ lv}$: Solid-vapour, solid-liquid, liquid-vapour

As shown in figure 2.16 a small contact angle corresponds to a good wetting. While σ_{lv} is a measurable value usually called surface tension σ, the quantities σ_{sv} and σ_{sl} can only be determined as the difference $\sigma_{sv} - \sigma_{sl}$. The higher the interactions between solid and liquid, the smaller the value of σ_{sl}. Good wetting with small contact angles is present, when reaction occur

between liquid and solid, like the formation of intermetallic phases or dissolution. (Bobzin, 2013; John, 1981)

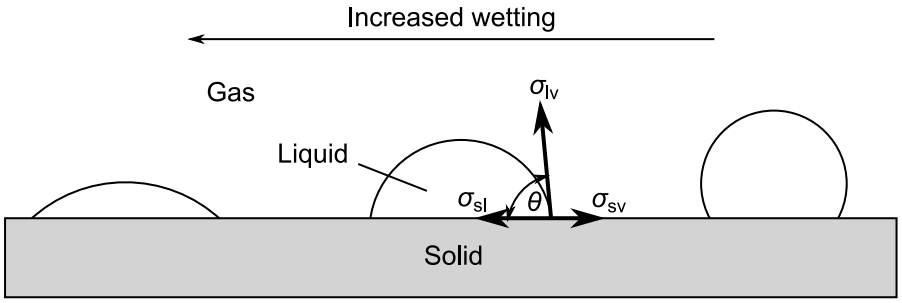

Figure 2.16: Illustration of the contact angle with a sessile drop on a flat surface.

Molten Droplet Deposition

Young's Equation (Equation 2.3) and the theory behind it are only valid for the equilibrium state. That means the droplet is at rest and no thermal gradient is present. According to this a molten droplet on a solid of the same material can never be in equilibrium state. Schiaffino and Sonin (1997a,b,c) published a series of articles on this problem and the following summarises their assumptions:

After impact, the droplet spreads under inertia or capillary forces, dependent on the Weber number We. The Weber number measures the relative importance of inertia compared to surface tension and is defined by (Haenlein, 1931; Weber, 1931):

$$We = \frac{\rho v^2 l}{\sigma} \qquad \text{(Equation 2.4)}$$

We: Weber number
ρ: Density of the liquid
v: Velocity of the droplet
σ: Surface energy or surface tension
l: Characteristic length, usually diameter

During spreading, the advancing contact line is arrested by solidification close to the contact line. The local 'contact angle' θ_{sf} is called solidification angle and decreases with an increased substrate temperature T_{subs}. The contact line arrests in much shorter time than the bulk solidification time for low or medium Weber numbers, when the post-solidification height is not small compared to the diameter of the contact line. In this case the liquid above the frozen footprint continues to oscillate until the motion is damped by viscous effects. When gravitational effects

can be neglected (small Bond number), the liquid forms a spherical cap on top of the frozen footprint. The Bond number is defined by (Suter, 2012):

$$Bo = \frac{\rho g l^2}{\sigma} \qquad \text{(Equation 2.5)}$$

Bo: Bond number
ρ: Density of the liquid
g: Gravitational constant
l: Characteristic length, usually diameter
σ: Surface energy or tension

This results in a macroscopic shape with an apparent contact angle θ^* between the droplet and the substrate. Figure 2.17 illustrates this behaviour. For low Weber numbers this apparent contact angle can be estimated by empirical correlation (Schiaffino and Sonin, 1997c):

$$\theta^* = \frac{9}{16}\frac{C}{St}\left(\sqrt{1 + 19\left(\frac{St}{C}\right)^2} - 1\right) \qquad \text{(Equation 2.6)}$$

θ^*: Apparent contact angle
C: Material constant
St: Stefan number

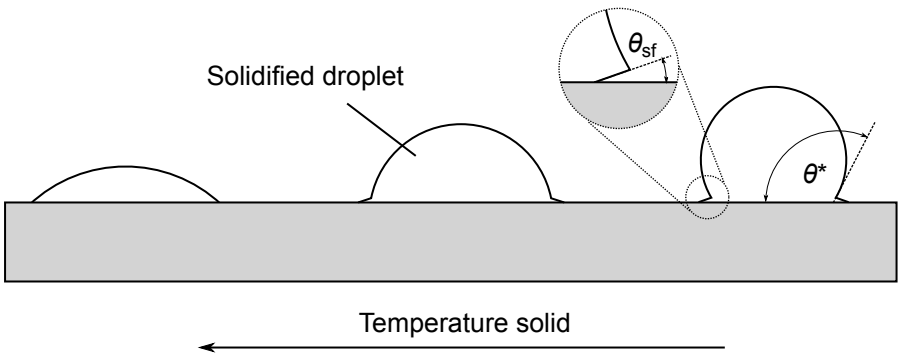

Figure 2.17: Post-solidification shape of droplets depending on the substrate temperature.

The Stefan number St is a dimensionless quantity that compares sensible heat to latent heat. It is defined as (Šarler, 1995):

$$St = \frac{c(T_{\mathrm{sol}} - T_{\mathrm{subs}})}{L} \qquad \text{(Equation 2.7)}$$

St: Stefan number
c: Specific heat capacity
T: Temperature
L: Specific latent heat of fusion
$_{\mathrm{sol,subs}}$: Solidus and substrate

For mercury and water they found good agreements between their experimental results and their estimations (Equation 2.6) with $C = 0.216$ for mercury and $C = 1.331$ for water.

Another series of publications from authors at the Swiss Federal Institute of Technology (ETH, Zurich, Switzerland) take a closer look on heat transfer and fluid dynamics of solder droplets deposited on a flat substrate and of a pile-up consisting of two droplets deposited on the same position. For the MJT process the results of the pile-up are more relevant, as the interaction with the build platform is only important for the first layer and also highly dependent on the materials. The main findings are that the spreading of the second droplet is higher for smaller Stefan numbers. This is in good agreement with (Equation 2.6). They also find that the spreading increases with an increased droplet velocity (here presented as the Weber number). This is basically also in agreement with the model of Schiaffino and Sonin (1997c) as for higher Weber numbers the velocity of spreading is higher and therefore the droplet spreads further before the contact line is arrested by solidification. However, the final shape of a two droplet pile-up is far more dependant on the Stefan number than on the Weber number as can be seen in figure 2.18. (Haferl and Poulikakos, 2002, 2003)

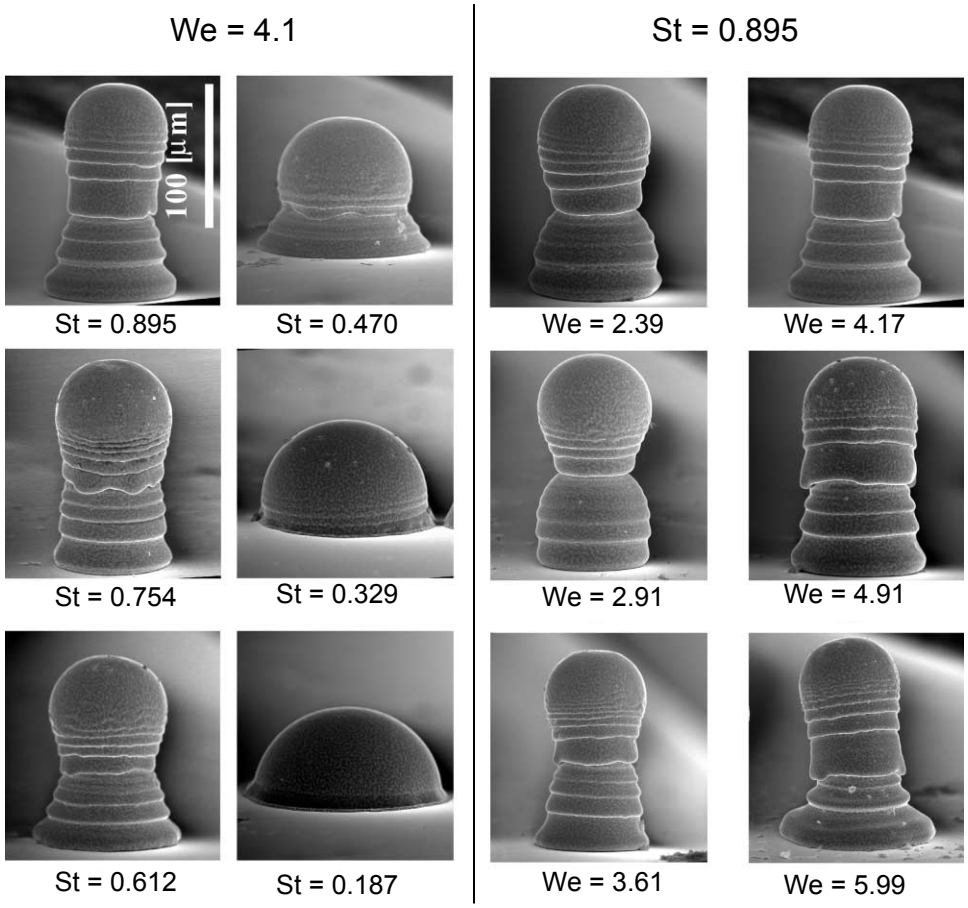

Figure 2.18: SEM pictures of pile-up of two solder droplets deposited at the same position for different Stefan and Weber numbers. The effect of the Stefan number on the final shape is significantly higher than the effect of the Weber number. Reprinted from Haferl and Poulikakos (2003), page 547, ©(2013), with permission from Elsevier.

2.4 Aluminium and its Alloys

This work focuses on an additive manufacturing method for aluminium alloys, therefore a general overview on aluminium is given: Compared to other metals, aluminium is a rather young material. It is produced on a technical scale only since 1886, less than 150 years ago. In this time the amount of aluminium produced for technical purposes increased to over 44 million tons per year in 2011. For different applications a wide range of alloys was developed based on the main alloying elements: silicon, copper, magnesium and zinc. (Bundesverband der Deutschen Gießerei-Industrie, 2013; Kammer, 2002)

Aluminium is mainly used owing to its low density and its high thermal and electric conductivity. Table 2.2 presents the most relevant physical properties for this study of pure aluminium. The density change on melting is 7 %. Values reported for the surface tension are valid for oxygen saturated melt, the effect of oxidation on the surface tension is explained in more detail in section 2.7.

Binary compositions of silicon, copper and magnesium were studied in this work but valuable results were only obtained for silicon and copper. Therefore, AlSi and AlCu alloys are described in more detail below.

Table 2.2: Overview of the most important physical properties of pure aluminium. [a] Values relate to oxygen saturated liquid Al. (Mills, 2002)

T/°C	ρ/kg m^{-3}	c/J kg^{-1} K^{-1}	λ/W m^{-1} K^{-1}	η/mPa s	σ/mN m^{-1}
25	2702	905	237	-	-
100	2685	945	240	-	-
200	2662	990	238	-	-
300	2640	1030	233	-	-
400	2617	1070	228	-	-
500	2594	1100	222	-	-
600	2571	1150	215	-	-
660.2	2558	1180	211	-	-
660.2	2380	1180	91	1.11	871[a]
700	2366	1180	92	1.049	865[a]
800	2331	1180	96	0.93	849[a]

2.4.1 Aluminium-Silicon

Silicon is the most common addition to aluminium alloys, to which it imparts fluidity and good mechanical properties. With aluminium it forms a simple eutectic phase system, which is shown in figure 2.19. The eutectic temperature is generally accepted as 577 °C and the most probable composition of the eutectic point is 12.5 wt.%, though values between 11.7 to 14.5 wt.% have been reported, as the structure close the eutectic composition is more influenced by the cooling rate, than the silicon content. In the equilibrium state, the solid solubility of silicon in α-aluminium is 1.65 wt.% at the eutectic temperature and decreases below 0.01 wt.% at room temperature. (Mondolfo, 1976)

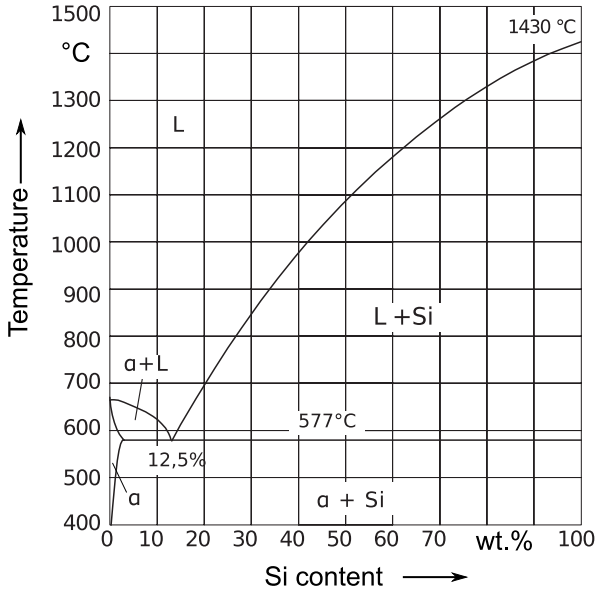

Figure 2.19: Aluminium-Silicon phase diagram. The system is a simple eutectic one with an eutectic composition of 12.5 wt.%Si at 577 °C. According to (Kammer, 2002)

When a hypo-eutectic alloy (Si content < 12.5 wt.%) is cooled slowly, to ensure thermodynamic equilibrium conditions, solidification starts once the temperature is below the corresponding liquidus temperature. In case of aluminium-silicon alloys, this temperature falls from 660 °C for pure aluminium to 577 °C for the eutectic composition. During primary solidification α-aluminium grows in dendritic crystals. Due to the limited solubility of silicon in α-aluminium the remaining melt is enriched with silicon until the eutectic composition is reached at the eutectic temperature. The remaining melt will then solidify in a coupled growth to form the eutectic phase. Coupled growth means that α-aluminium and silicon crystals grow simultaneously into the melt with short diffusion distances between both phases creating the fine polyphase distribution typical for eutectic alloys. Note that even though the term ‘eutectic phase’ is commonly used, it

does actually not describe a single phase but two individual phases distributed in a characteristic manner. If the silicon concentration is above the eutectic composition (hyper-eutectic), primary silicon will grow in polyhedral crystals during the primary solidification instead of α-aluminium. Figure 2.20 shows the characteristic microstructure of hypo-, hyper- and eutectic compositions. (Bührig-Polaczek et al., 2013; Hellawell, 1970)

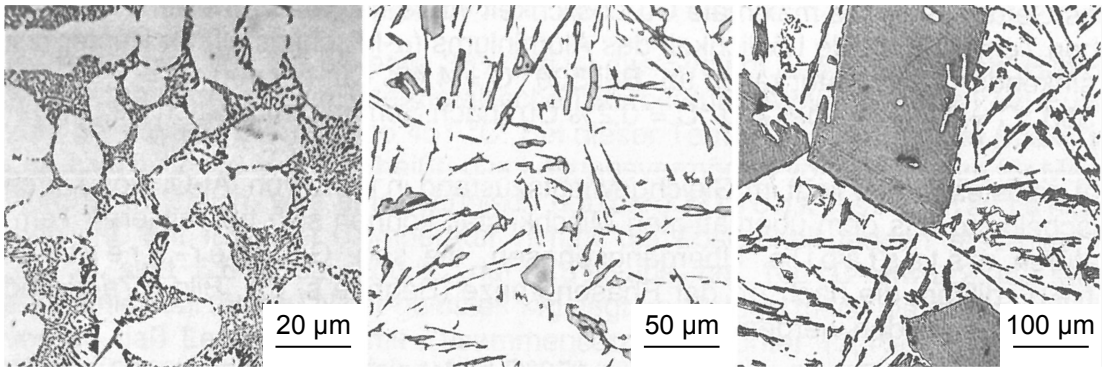

Figure 2.20: Microstructure of aluminium-silicon alloys: Left: Hypo-eutectic microstructure with dendrites of α-aluminium solid solution in white and modified eutectic between dendrites. Middle: Normal eutectic alloy with coarse flake morphology of silicon. Right: Hyper-eutectic alloy with primary silicon in polyhedral shape and coarse eutectic with flake morphology of silicon. According to (Kammer, 2002)

The structure of the eutectic coupled growth can have several forms depending on the presence of elements like sodium, strontium or antimony, the solidification velocity v_{sf} and the thermal gradient ∇T during solidification. The presence of sodium or strontium hinders the growth of the silicon particles, which results in a fibrous and significantly finer eutectic microstructure known as modified eutectic. Figure 2.21 compares the modified and the unmodified eutectic in Al-Si alloys. In alloys without sodium, strontium or antimony the silicon crystallises in the flaky form shown in figure 2.21 when v_{sf} is in the order of 1 to 100 µm s^{-1}. For high rates of solidification above 0.2 to 1 mm s^{-1}, as they occur in chill or pressure die casting, a transition in microstructure to a fibrous form of silicon in the eutectic phase occurs. Even though the mechanisms of formation for the fibrous silicon in a modified eutectic and for the fibrous silicon in a rapidly solidified eutectic are different, their appearance in micrographs, as well as their effects on the mechanical properties are similar. (Justi, 1971; Khan and Elliott, 1996; Makhlouf and Guthy, 2001; Steent and Hellawell, 1972)

Rapid solidification has another effect on the eutectic reaction: The eutectic temperature is depressed and the eutectic composition is shifted to higher silicon contents. For sufficiently high cooling rates the limit of primary solubility of silicon in α-aluminium can be extended to almost the eutectic composition (Bose and Kumar, 1973; Murray and McAlister, 1984). The

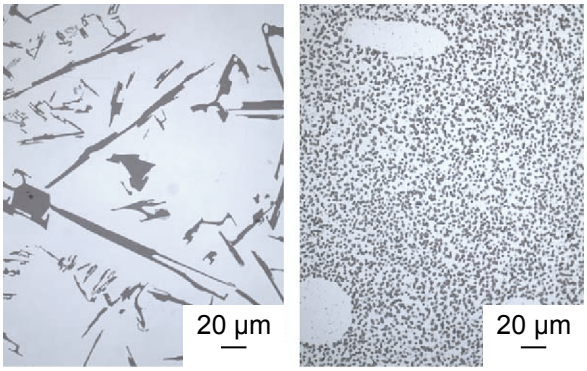

Figure 2.21: Comparison of normal and modified Al-Si eutectic: Flake structure of silicon in normal eutectic (left) and fibrous structure of silicon in modified eutectic (right). According to (Dahle et al., 2005)

microstructure of a rapidly solidified alloy with an eutectic composition therefore shows primary α-aluminium dendrites like in hypo-eutectic alloys. Figure 2.22 shows the micrographs of two unmodified eutectic alloys. While the slowly cooled sample does not show primary dendrites and a flaky silicon, the chill cast sample shows primary α-dendrites and a fibrous silicon. Elliott and Glenister (1980) studied undercooling of the eutectic reaction and proposed the relationship $\Delta T = 2.24 v_{\mathrm{sf}}^{0.25}$ for low velocities ($v_{\mathrm{sf}} < 50$ to $100\,\mu\mathrm{m\,s^{-1}}$) and $\Delta T = 0.8 v_{\mathrm{sf}}^{0.25}$ for high velocities, with ΔT in K and v_{sf} in $\mu\mathrm{m\,s^{-1}}$. Those findings are only valid for the flake morphology, which changes to the fibrous morphology at a critical solidification rate. Khan and Elliott (1996) present a drop in undercooling, when the silicon structure changes from flake to fibrous type caused by rapid cooling, so undercooling is in the range of 2 to 20 K for any case.

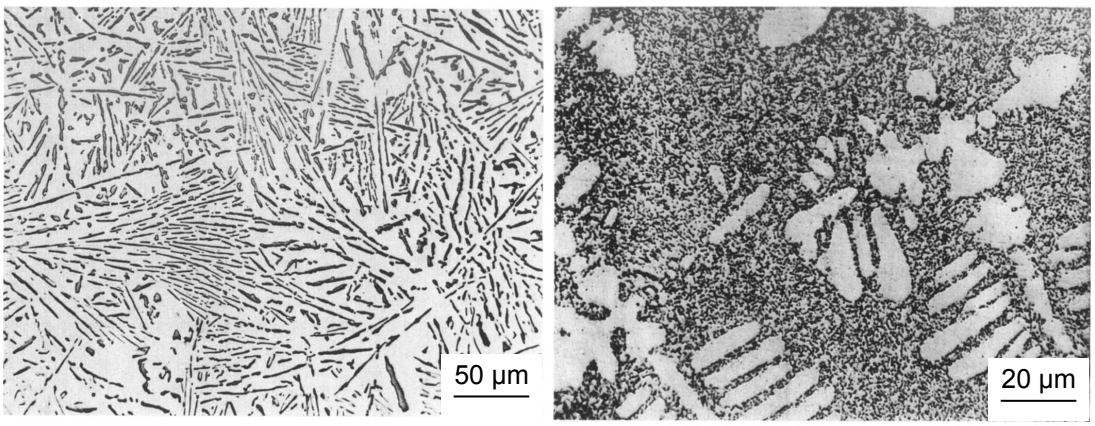

Figure 2.22: Effect of solidification rate on Al-Si eutectic: Flake morphology in slowly cooled sample (left) and fibrous morphology with primary dendrites in chill cast sample (right). (Hellawell, 1970)

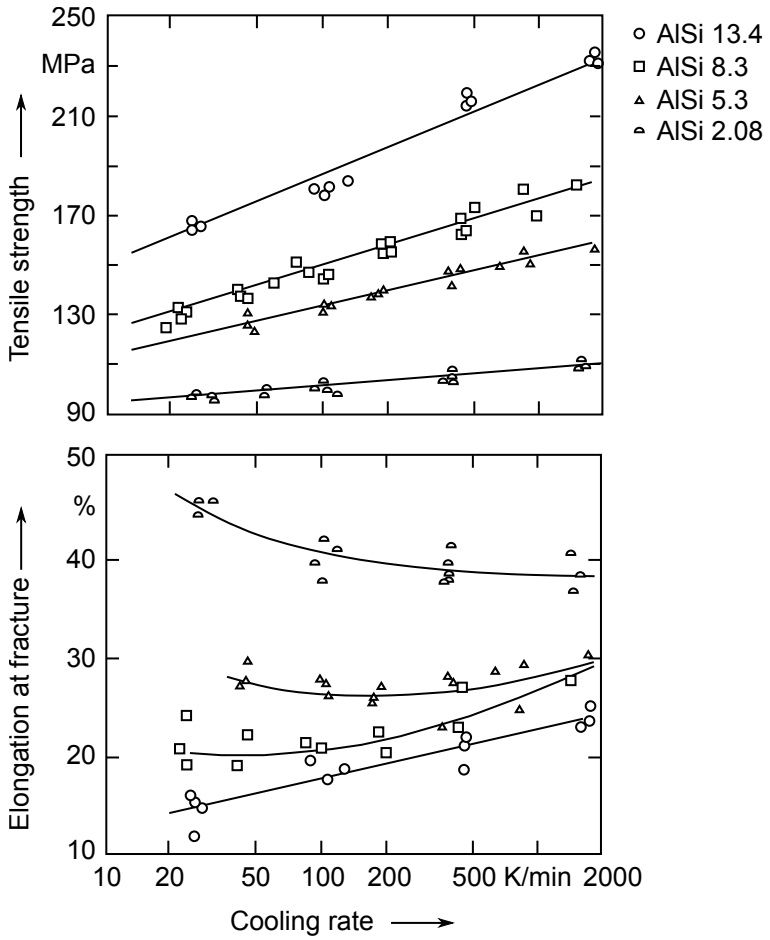

Figure 2.23: Effect of cooling rate on ultimate tensile strength and elongation at fracture for Al-Si alloys. Both properties increase more for alloys with a higher silicon content. According to Pek (1987)

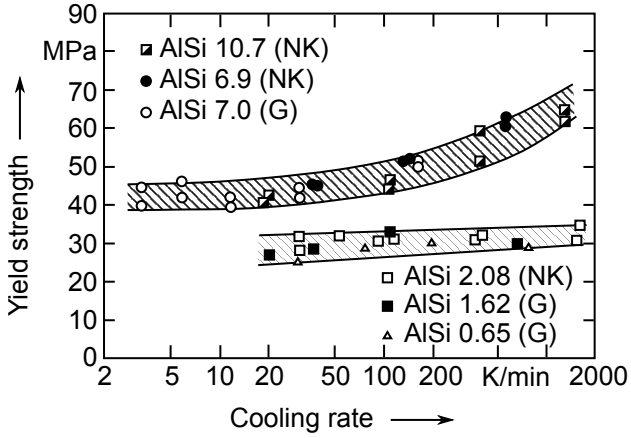

Figure 2.24: Effect of cooling rate on 0.2 % offset yield strength for Al-Si alloys. For high cooling rates and alloys containing at least 7 wt.%Si the yield strength increases with the cooling rate. In all other cases no effect is visible. According to Pek (1987)

Pek (1987) examines the influence of solidification rate on the mechanical properties of binary Al-Si alloys without chemical modification. Figure 2.23 shows the effects of cooling rate on ultimate tensile strength and elongation at fracture. The increase in tensile strength is higher for alloys with a high silicon content, which can be explained by a fine eutectic phase. The effect of rapid solidification is stronger for the eutectic than for the primary dendrites, therefore an alloy with more eutectic phase is more sensitive to high cooling rates. Same is true for the elongation at fracture: while it increases with cooling rate for alloys with 13.4 wt.%Si and 8.3 wt.%Si, it is hardly affected by the cooling rate for alloys with 5.3 wt.%Si and 2.08 wt.%Si. Figure 2.24 shows the influence of cooling rate on the 0.2 % offset yield strength. Only for cooling rates above 100 $\mathrm{K\,min^{-1}}$ and only for alloys containing more than 7 wt.%Si an effect is visible: the yield strength increases progressively with the cooling rate.

Müller (1996) shows that, similar to unmodified alloys, also modified alloys show a finer eutectic phase when cooled at higher rates.

2.4.2 Aluminium-Copper

Between 0 wt.% and 53 wt.% aluminium and copper form a simple eutectic phase diagram with α-aluminium and the intermetallic Al_2Cu called θ-phase. Figure 2.25 shows the phase diagram in that range. Industrial relevant compositions of aluminium alloys are in the range of the solid solubility in α-Al below 5 wt.%. The solubility of Cu in α-Al reduces dramatically from 5.7 wt.% at the eutectic temperature 548.2 °C to 0.05 wt.% at room temperature. (Bundesverband der Deutschen Gießerei-Industrie, 2013; Murray and McAlister, 1984)

This circumstance can be used for precipitation hardening: After homogenisation close to the eutectic temperature, the material is quenched and then age hardened. Samples analysed in this work were also heat-treated during build-up. To be able to understand the resulting microstructure and mechanical properties, the precipitation hardening of Al-Cu alloys is described in detail:

Depending on the supersaturation of α-Al, the temperature and the time of age hardening five structures can form:

- Supersaturated Solid Solution (SSS)
- Guinier-Preston-Zones I (GP I)
- Guinier-Preston-Zones II (GP II) or θ″

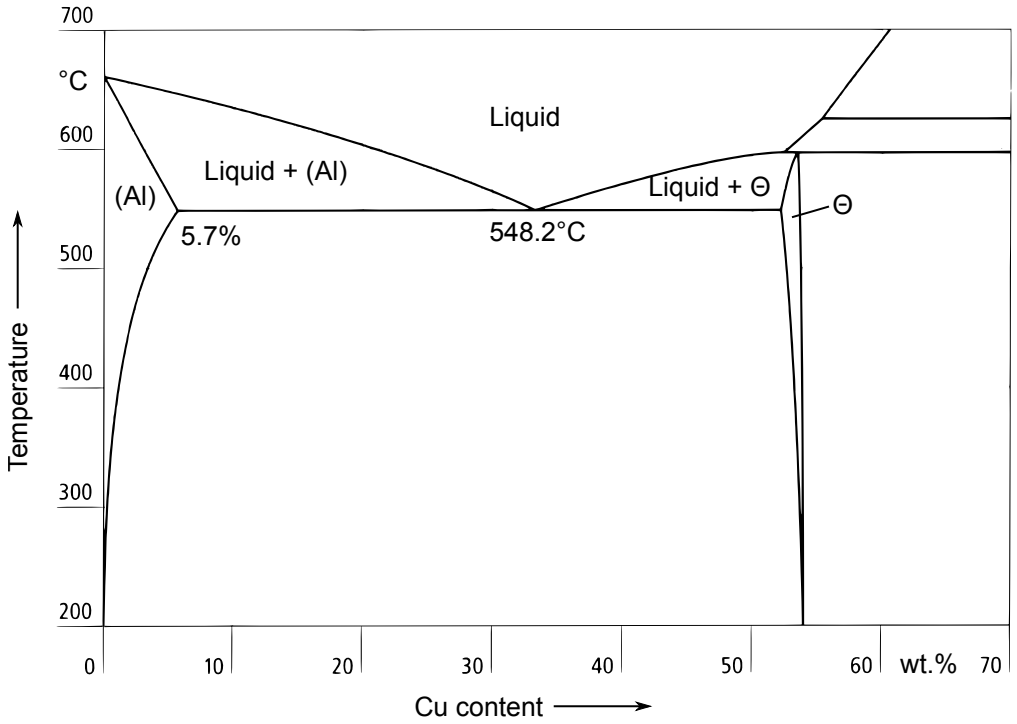

Figure 2.25: Aluminium-copper phase diagram for 0 to 53 wt.%. Simple eutectic of α solid solution and intermetallic θ-phase. According to Bundesverband der Deutschen Gießerei-Industrie (2013)

- θ′-phase
- θ-phase

They generally form in the order above, though depending on the temperature history during hardening, not all of them necessarily appear. Nevertheless, they will not coexist but each form will replace the predecessor. GP I-zones will rapidly form from SSS even at subzero temperatures. They consist most probably of single atom layers of pure copper in the [100] planes of the Al matrix. Their diameter grows depending on the temperature to several hundred angstrom. GP I-zones are fully coherent with the parent matrix. When aged at 100 to 200 °C GP II-zones will start to replace GP I-zones. There is disagreement about the exact structure of GP II-zones. The consensus is that they are coherent to the matrix and that they have a disk shape, like GP I, but are several atom layers thick (20 to 100 Å) with a greater diameter of 400 to 1500 Å. θ′-phase forms after GP II-zones when ageing longer times at 100 to 200 °C or directly from GP I-zones or SSS when ageing above 200 °C. It is a precursor to the stable θ-phase, but still shows partly coherency to the Al-matrix. Again there is disagreement about the exact structure, but θ′ is generally seen as a definite phase. Finally at temperatures above 300 °C the stable θ-phase (Al_2Cu) occurs, which has a tetragonal lattice and is incoherent to the Al-matrix. (Franz, 1957; Mondolfo, 1976; Murray and McAlister, 1984)

As GP I-zones will form even at room temperature, copper additions to aluminium increase the strength and hardness of the alloy significantly, even without a heat treatment. But applying a heat treatment can increase the strength by almost factor two, followed by a loss of strength and hardness, when the alloy is aged to long (or at temperatures being too high). This correlates to the structures mentioned above: The presence of SSS, GP I- and GP II-zones increase the strength significantly. They will form more likely for higher copper contents and therefore alloys with a copper content close to the maximum solid solubility show the highest values. Then the formation of θ' will still increase strength and hardness until a certain amount before their values start to decrease for longer ageing times. Finally when the intermetallic θ-phase forms, the material fails brittle at low tensile stresses. Ductility is preserved during natural ageing close to room temperature but will successively decrease during artificial ageing at elevated temperatures. (Bundesverband der Deutschen Gießerei-Industrie, 2013; Franz, 1957)

2.5 Rapid Solidification

The formation of solid crystals in metallic melts will generally include two diffusion processes: thermal diffusion of latent heat formed during solidification and chemical diffusion of alloy elements, as the solid solubility is commonly smaller than the liquid solubility. The process is therefore highly dependent on the solidification rate. But phase diagrams as they were presented earlier are only valid for equilibrium conditions that means at infinitesimal small rates of solidification. The MJT process is characterised by high rates of solidification and therefore equilibrium phase diagrams can only be used to derive tendencies and basic correlations. Table 2.3 shows the hierarchy of non-equilibrium that is followed by an increasing solidification rate. (Sahm et al., 1986)

In the first regime, at solidification velocities $\approx 1\,\mathrm{nm\,s^{-1}}$, metal will freeze in full equilibrium without thermal or chemical gradients. The phase diagram is fully applicable. In the second regime at rates $\approx 1\,\mu\mathrm{m\,s^{-1}}$, the phase diagram is only valid locally at the solidification front. In the third regime ($\approx 1\,\mathrm{mm\,s^{-1}}$) stable phases can not nucleate or grow fast enough, so the metastable phase diagram can be used to describe the local conditions at the interface. Finally, at rates of $\approx 1\,\mathrm{m\,s^{-1}}$ diffusion is mostly suppressed and conditions at the solidification front can not be described by a phase diagram. (Sahm, 1999)

Common technical processes are taking place in the second and third regime, where a local stable or metastable equilibrium is present at the solidification front. Prominent examples are macrosegregation for the second regime and white cast iron for the third. In white cast iron, the

Table 2.3: Hierarchy of non-equilibrium states for increasing solidification rates. According to (Sahm et al., 1986; Sahm, 1999)

Solidification rate	Conditions at the solid-liquid interface
$\approx 1\,\mathrm{nm\,s^{-1}}$	Full diffusional equilibrium • No chemical potential gradients (composition of phases is uniform) • No temperature gradients • Lever rule in phase diagram is valid
$\approx 1\,\mathrm{\mu m\,s^{-1}}$	Local interface equilibrium • Phase diagram gives composition and temperatures only at liquid-solid interface • Corrections made for interface curvature (Gibbs-Thomson effect)
$\approx 1\,\mathrm{mm\,s^{-1}}$	Metastable local interface equilibrium • Stable phase can not nucleate or grow sufficiently fast • Metastable phase diagram gives the interface conditions
$\approx 1\,\mathrm{m\,s^{-1}}$	Interfacial non-equilibrium • Phase diagram fails at interface • Chemical potentials are not equal at interface

nucleation and growth of graphite is suppressed by the rate of solidification and the metastable phase cementite forms.

Figure 2.26 illustrates how rapid solidification influences the phase diagram of binary alloys: Solid solubility is increased and the liquid temperature is decreased. Therefore, the solidification range also decreases. Also the eutectic point is affected: it shifts to higher concentrations of the alloy element and to lower temperatures. In the extreme case the solidification range is reduced to a line and a degenerated eutectic phase diagram results, which is shown by the dash-dotted line in the figure. (Kurz and Trivedi, 1991; Sahm, 1999)

Maybe the technically most relevant effect of the solidification rate is the change in solidification morphology shown in figure 2.27. For a given thermal gradient, which is usually small for metals, and increasing solidification rate, the morphology of the solidification front changes from planar to cellular at v_{con} then to dendritic. For even higher rates the morphology changes back to cellular and finally planar for rates higher than the absolute stability v_{abs}. (Sahm, 1999)

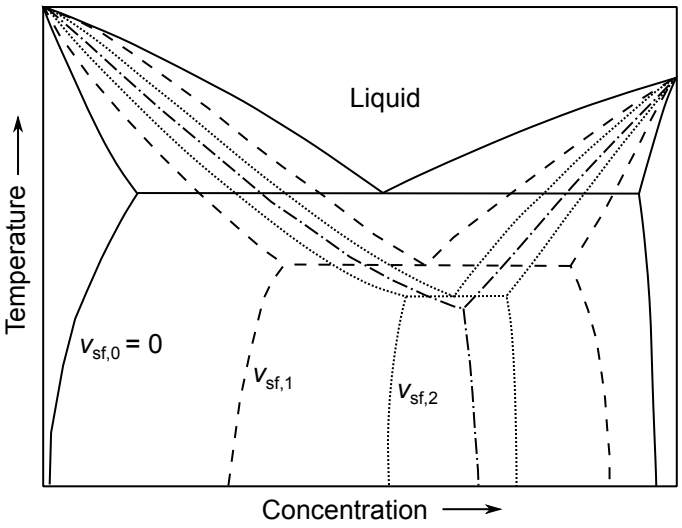

Figure 2.26: Schematic binary phase diagram for different growth rates v_{sf}. Rapid solidification suppresses the eutectic temperature and shifts it to higher concentrations. Also the solid solubility increases. $v_{sf,0} < v_{sf,1} < v_{sf,2}$. According to (Kurz and Trivedi, 1991)

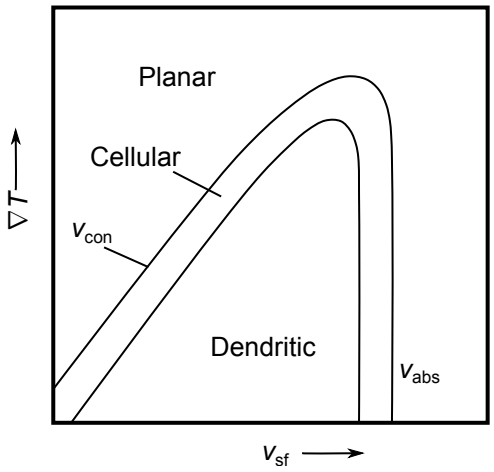

Figure 2.27: Qualitative effect of solidification rate and thermal gradient on the morphology: for a given thermal gradient the morphology changes from planar to cellular/dendritic and back with increasing solidification rate. According to (Sahm, 1999)

The rate for the onset of diffuse crystal growth (cellular or dendritic) v_{con} can be explained by the concept of constitutional undercooling shown in figure 2.28. A crystal of a binary alloy with limited solubility in the solid state grows in positive z-direction. Here the distribution coefficient $k = c_{sol}/c_{liq}$ is smaller than unity. As the crystal grows, solute will pile up ahead of the interface when the excess solute is rejected from the solid phase. The solute concentration will decrease exponentially in z-direction according to solute diffusion in the liquid phase. As the liquidus temperature changes with solute concentration in the melt according to the phase diagram, the negative gradient in solute concentration can be transformed into a positive gradient in liquidus temperature. Now depending on the thermal gradient and the solidification rate, the local temperature in the melt ahead of the interface can be lower than the local liquidus temperature. In this case the melt is constitutionally undercooled. When a small perturbation arises in the interface it will steepen the local concentration gradient and consequently the local constitutional undercooling. Therefore, the perturbation is stabilised and grows preferably, which leads to a diffuse growth. (Kurz and Fisher, 1992)

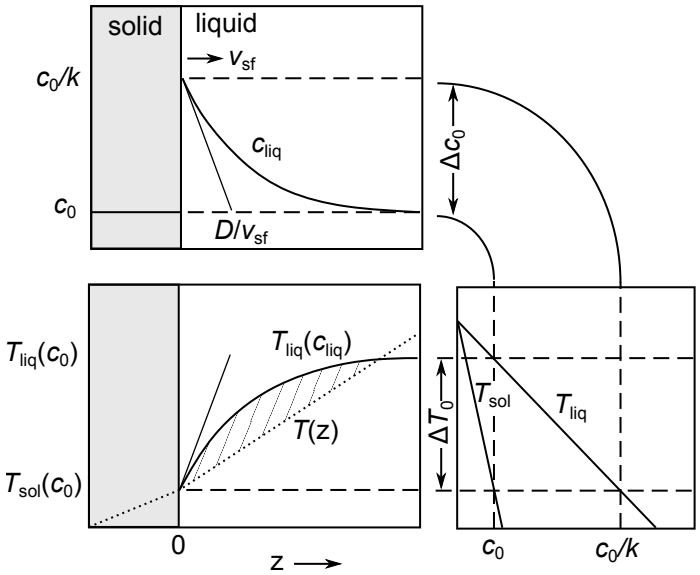

Figure 2.28: Constitutional undercooling in alloys: The solute pile up ahead of the solidification front creates a gradient in the liquidus temperature. If the melt temperature falls below that local liquidus temperature, it is constitutinal undercooled. According to (Kurz and Fisher, 1992)

The gradient of c_{liq} close to the interface can be derived from a mass flow balance at the interface according to (Equation 2.8). The interface becomes unstable once the gradient of solute concentration is greater than the thermal gradient. So the critical solidification rate can be calculated according to (Equation 2.9). To derive the equation for the upper boundary of the diffuse solidification v_{abs}, more complex models and mathematics are necessary. So the

explanation here will be limited to a qualitative description: With increasing rate of solidification, the isolines of solute concentration ahead of the diffuse solidification front will adapt closer to the interfaces shape. Finally, when the isolines exactly follow the interface shape, the constitutional undercooling is equal along the interface and perturbations are no longer stabilised by it. Now the surface tension between liquid and solid, which is present in any case, will try to minimise the interface area and a planar growth becomes stable. This absolute stability limit can be calculated by (Equation 2.10). (Sahm, 1999)

$$\frac{dc_{\mathrm{liq}}}{dz} = -\frac{v_{\mathrm{sf}}}{D}\Delta c_0 \qquad \text{(Equation 2.8)}$$

c_{liq}: Local solute concentration in melt
Δc_0: Difference in solubility solid/liquid
v_{sf}: Velocity of solidification front
D: Diffusion coefficient of solute in melt

$$v_{\mathrm{con}} = -\frac{\nabla T}{m}\frac{D}{\Delta c_0} = \nabla T\frac{D}{\Delta T_0} \qquad \text{(Equation 2.9)}$$

v_{con}: Critical solidification rate for constitutional undercooling
∇T: Thermal gradient
m: Slope of liquidus temperature in phase diagram
D: Diffusion coefficient of solute in melt
Δc_0: Difference in solubility solid/liquid
ΔT_0: Solidification range

$$v_{\mathrm{abs}} = \frac{D\Delta T_0}{k\Gamma} \qquad \text{(Equation 2.10)}$$

D: Diffusion coefficient of solute in melt
ΔT_0: Solidification range
k: Distribution coefficient
Γ: Gibbs-Thomson coefficient [1]

[1] The Gibbs-Thomson coefficient measures the surface tension at the solid-liquid interface and is in the order of 10^{-7} K m

2.6 Dendrite Coherency Point

The dendrite coherency point (DCP) describes the state of a solidifying alloy when growing dendrites come into contact and form a coherent network. At this point solidifying metal behaves rather as a solid than a liquid. To understand the droplet spreading after deposition in MJT, it is necessary to understand the dendrite coherency. The DCP is characterised by the temperature and the fraction solid of dendrite coherency T_{DCP}, fs_{DCP}. Thermal analysis can be used to detect the DCP, as the dendrites can not grow any longer in their preferred direction, which effects the thermal gradient. Also at DCP the materials viscosity increases steeply, which can be detected by a rheometer (Arnberg et al., 1993; Djurdjevic et al., 2012). The DCP is commonly used in casting simulations to describe the transistion between liquid-like and solid-like behaviour during mould filling (Stefanescu, 2002).

The DCP depends on dendrite growth velocity as well as grain size, which both depend on the cooling rate (Malekan and Shabestari, 2009). Therefore, fs_{DCP} is not always monotonically dependent on the cooling rate: Arnberg et al. (1993) show that for the alloy 355 (AlSi5Cu1Mg) the fraction solid reduces from 15 to 10 % when the cooling rate is increased from 0.1 to 3 $\mathrm{K\,s^{-1}}$. On the other hand, Ghoncheh and Shabestari (2015) present data for Al 2024 (AlCu4Mg1): For cooling rates between 0.4 to 1.1 $\mathrm{K\,s^{-1}}$ the fraction solid at DCP increases from 11 to 29 %, but for cooling rates higher than that fs_{DCP} decreases to 7 % at 17 $\mathrm{K\,s^{-1}}$. In a recent publication Malekan et al. (2016) study the alloys ADC12 (AlSi10Cu2Fe) and the dependency of DCP on the cooling rate: when the cooling rate was increased from 1.2 to 7.2 $\mathrm{K\,s^{-1}}$, then fs_{DCP} increased from 8 to 19 %.

2.7 Oxidation of Aluminium Alloys

As mentioned earlier, oxide layers are disturbing the formation of metallic bonds. This section presents published knowledge on the formation of oxide layers on aluminium with a focus on the initial oxidation as it is most relevant for MJT. The affinity of a metal to form a metal oxide can be measured by the Gibb's free energy of formation ΔG. The higher the negative value of ΔG the more likely a metal oxide will be formed. Aluminium has one of the highest affinities to oxygen of all common metals. At 1000 K only Ba, Be, Ce, Ca, Gd, Mg and Y have a higher value of ΔG amongst the more common metals. (Reed, 1971)

Common sources for the oxygen necessary to form alumina (aluminium oxide) are air and water:

$$4\,Al + 3\,O_2 \longrightarrow 2\,Al_2O_3$$
$$2\,Al + 3\,H_2O \longrightarrow Al_2O_3 + 3\,H_2$$

Alumina appears in many different structures, but three of them are of particular interest: an amorphous and two crystalline (γ and α) structure. The amorphous alumina is completely dense and provides the protective character on solid aluminium. At higher temperatures (500 to 700 °C) it transforms into γ-alumina which is a cubic spinel. On liquid aluminium γ-alumina is directly formed and no amorphous structures are present. At even higher temperatures (750 °C in dry air (Impey et al., 1988); 900 °C (Thiele, 1962)) γ-alumina transform to the α-type which is a hexagonal lattice with a 24 % higher density compared to the cubic γ. This transformation induces cracks in the oxide layer and the rate of oxidation increases significantly. This effect is known as break away oxidation. (Ostermann, 2014; Thiele, 1962)

Bachrach et al. (1978) analyse the initial oxide formation on an aluminium single crystal and assume a three step model for initial oxidation: first oxygen is adsorbed to the surface, then incorporated below it and finally alumina forms. The authors also find evidence that the initial oxide grows in islands. This is supported by the work of Gartland (1977). As both works show that adsorption and oxide formation is depending on the crystals orientation one can expect island-like growth on a polycrystalline surface in any case. Stucki et al. (1987) studied the oxidation on polycrystalline solid and liquid of high purity aluminium by Auger electron spectroscopy and determine the exposure necessary to form one monolayer of aluminium oxide on the surface. The point of monolayer formation is characterised by a reduction in oxide formation rate, as islands can rapidly grow radial without diffusion, but further growth can only take place if oxygen or aluminium diffuses through the oxide layer. For solid aluminium at room temperature they obtain an exposure for monolayer formation of 1.33×10^{-4} mbar s and for liquid aluminium 3.99×10^{-3} mbar s, which is 30 times higher than for the solid state. They discuss that on solid Al, the oxygen is adsorbed on the surface (up to 2.66×10^{-5} mbar s) before it starts to form aluminium oxides. In contrast, the authors could not measure adsorbed oxygen on the liquid surface and therefore state, that it is immediately incorporated in the liquid until a certain exposure (1.33×10^{-3} mbar s) before the first oxide islands form.

Oxidation of Al-Mg alloys

Magnesium additions to aluminium melt are of special interest, as Mg is a very common alloying element for aluminium and has a great effect on the oxidation behaviour: Thiele (1962) reports a drastic increase in oxides mass of an Al-Mg alloy compared to pure aluminium and also to Al-Si alloys as figure 2.29 shows. Additions of Be to Al-Mg melts can protect them from break away oxidation with Be contents as little as 0.0001 % as they form preferable BeO coatings on the melt, which protect it from further oxidation. However, if seeds of crystalline metal oxides are added to the melt, they counteract the protective action of Be additions completely. (Cochran et al., 1977)

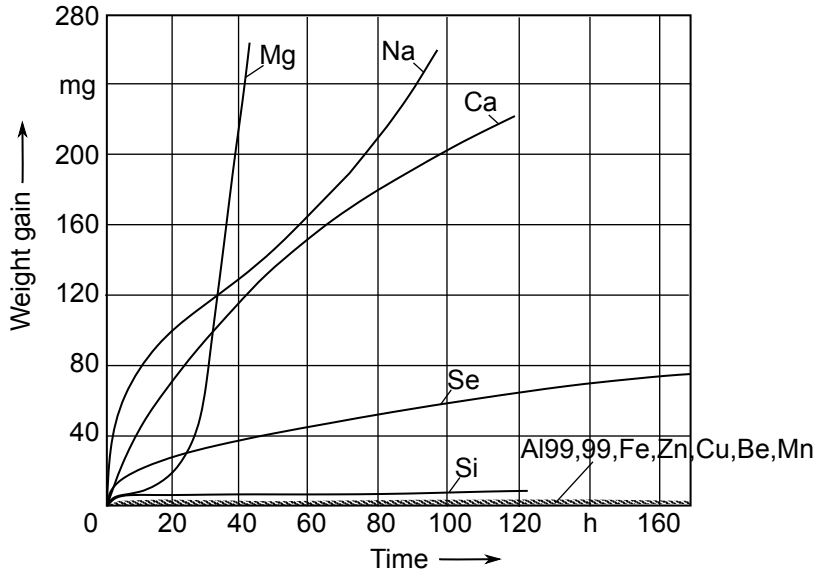

Figure 2.29: Effect of alloy elements on the oxidation of aluminium at 700 °C. Each additions is 1 atom-%. Rate of oxidation increases significantly for additions of Mg, Na und Ca. According to (Thiele, 1962)

Effect on the Surface Tension

An alumina film on the aluminium melt also effects the surface tension. For a droplet surface covered completely with alumina consistent values of $0.85\,\mathrm{N\,m^{-1}}$ are reported in literature (Goumiri and Joud, 1982; Molina et al., 2007). For values of a 'pure' aluminium surface the data is inconsistent, as it is technically almost impossible to create an oxide free aluminium melt surface. A recent publications obtains a value for an oxide-free aluminium of $0.95\,\mathrm{N\,m^{-1}}$ (Molina et al., 2007).

Effect on the Wetting Behaviour

Several studies examine the contact angle between aluminium melt and aluminium nitride (AlN) and boron nitride (BN). Their results allow the following conclusion:

When the melt surface is covered with alumina the melt does not wet the ceramic and high contact angles between 140° and 160° are reported. At temperatures above 800 °C Al_2O is formed on the melt's surface, which is gaseous and volatile. Now clean aluminium comes in direct contact with the substrate and contact angles are reduced to values below 90°. This is also consistent with the results of Ho and S.-T. Wu (1998) who adapted the sessile drop method to deposit droplets from a syringe instead of melting them from a solid aluminium part. In comparison to existing data they measure smaller contact angles between aluminium and AlN of 110° at 800 °C. (Chiaramonte and Rosenthal, 1991; Impey et al., 1988)

2.8 Summary and Conclusion

Material jetting of metal is a promising technology to additively manufacture parts from aluminium alloys. It is currently on the verge of commercialisation. As described in this chapter, there is already some published knowledge on print heads for high melting metals, the behaviour of metal droplets impinging on a flat surface and on the numerical description of the behaviour of a liquid droplet spreading and solidifying on a substrate of the same kind. However, there is very little published knowledge on the effect of process parameters on resulting macroscopic part properties. One of the few publications on macroscopic part properties by Chao et al. (2013) presents four cuboids fabricated under different thermal conditions. According to the quality prediction by the semi-infinite-model presented in the same publication, all four should yield good results with a well defined geometry and a low porosity as the contact temperature T_{c1} is between T_{sol} and T_{liq}. But exactly the opposite is true: The sample printed at the lowest temperatures shows a great amount of pores, while the sample printed at the highest temperatures looses its geometry almost completely. There clearly is a lack of information on how thermal conditions influence the MJT process, which is of great importance as the local temperatures during droplet deposition have a major effect on the resulting macroscopic part properties.

3 Objectives and Structure of Thesis

The scope of this work is to contribute to the basic knowledge needed to design an industrial MJT process for aluminium alloys. It focuses on the droplet-droplet bonding process, which is crucial to the quality of printed parts. The quality can be described by two basic criteria: geometrical accuracy and material soundness. This work focuses on the latter, which means in the case of MJT: mechanical strength and porosity.

Tensile tests and relative density measurements were conducted to quantify their dependency on the main process parameters, i.e. alloy composition, thermal conditions, oxygen concentration in the printing atmosphere and Weber number of the droplets. The results are supported by the analysis of micrographs and fractured surface by optical microscopy and scanning electron microscopy (SEM). To be able to fabricate specimens for the aforementioned analysis, it was first necessary to develop and install a prototypic printing machine. It was developed in cooperation with the Institute of Micro Technology and Medical Device Technology at the Technical University of Munich. It consists of a print head, a printing environment with controlled oxygen concentration, a heated build platform, a 3D-motion stage able to move the build platform and finally a programmable logic controller (PLC) to automate the build process based on a G-code script, similar to scripts used in computerised numerical control (CNC) machining.

A particular feature of additive manufacturing processes is, that quantities like the temperature are changing on small scales in both time and space. This makes those quantities difficult or impossible to access by conventional measurement methods. To overcome this hurdle, a simulation method for MJT was developed and used in this work to gain more insight into the manufacturing process of the analysed specimens. It is further used to extrapolate to conditions occurring in an industrial process with smaller droplets deposited at a higher frequency compared to the prototypic machine used here.

Figure 3.1 gives an overview of the content and structure of the present work. In Chapter 4 the experimental and simulation methods are described, including the prototypic machine used to fabricate specimens under a variation of process parameters. To analyse the process, Chapter 5 compares simulation results with the analysis of printed specimens. A fundamental understanding of droplet-droplet bonding can be derived from these results taking into account the already published knowledge presented in chapter 2. Finally the simulation model is adapted to predict conditions in a notional industrial process. In combination with the experimental results, basic knowledge that supports the design an industrial MJT process for aluminium is presented in chapter 6.

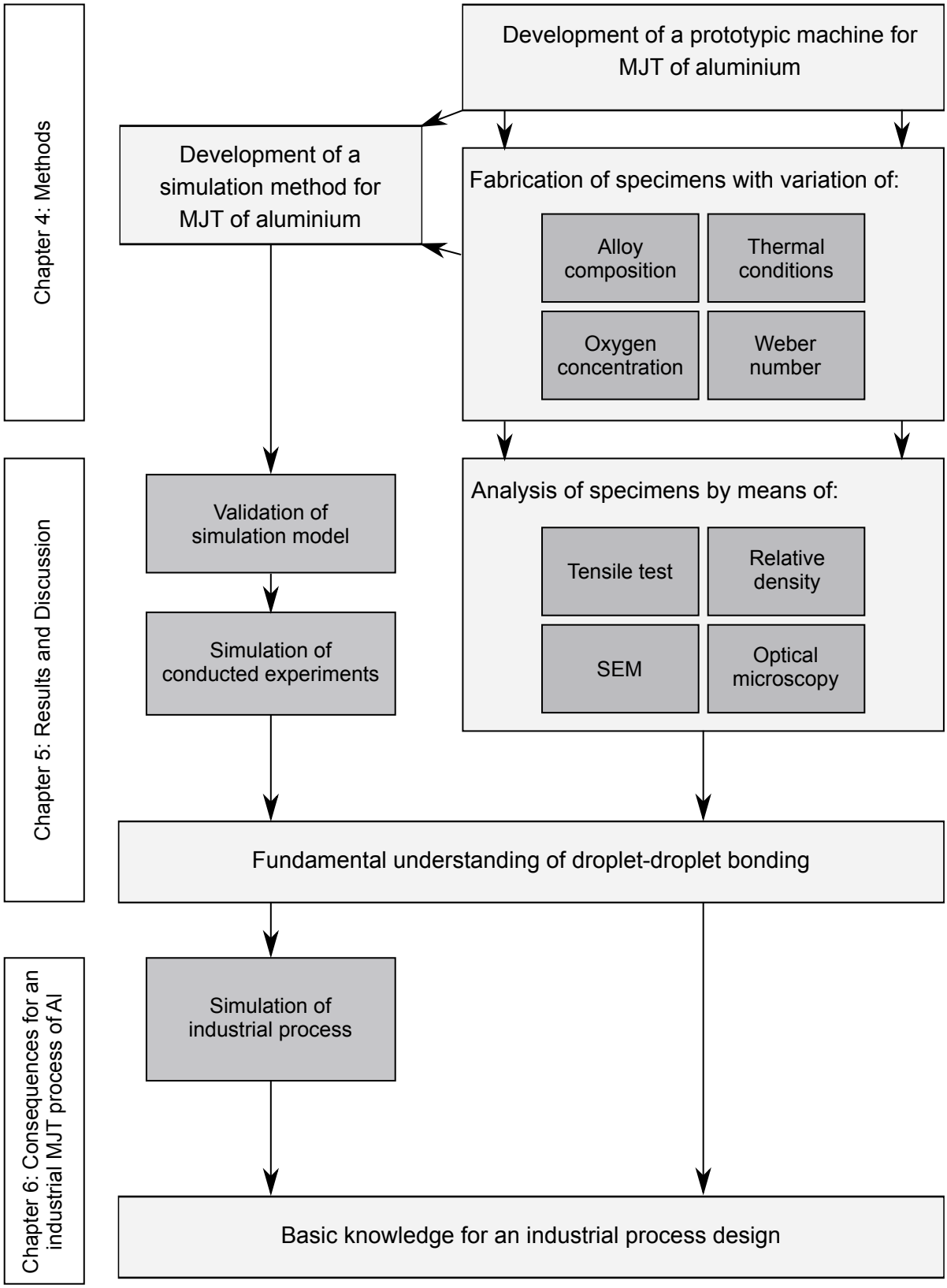

Figure 3.1: Overview of content and structure of the present work.

4 Methods

During the research project this thesis is based on, a prototype printing machine for material jetting of aluminium was designed in cooperation with the Institute of Micro Technology and Medical Device Technology at the Technical University of Munich. This chapter will first describe the machine itself, then the experiments that were conducted and finally a novel simulation model, used to gain inside into the local conditions of the conducted experiments.

4.1 Prototype Printing Machine

Figure 4.1 shows the CAD model of the mechanical parts of the printer and a picture of the complete setup. The motion stage assembly and the printing chamber are mounted in the machine frame, which is assembled from aluminium profiles. The print head is integrated in the printing chamber's lid and therefore stationary. The picture also shows the pneumatic plate with the valves and flowmeters, the nitrogen supply and the visualisation of the programmable logic controller (PLC). The main components are described in detail in the following sections.

4.1.1 Motion Stage Assembly

The printer's XY stage is arranged in an 'H-Bot' configuration that is shown in figure 4.2. Two rail guides in y-direction carry the two rail guides in x-direction on four carriages. The base plate of the printer is attached to four carriages on the rail guides in x-direction. The toothed belt starts and ends at the base plate, where it is held by belt tensioners. Four return pulleys turn the belt by 90° to be in parallel with the y-direction. Attached to the y-direction rails, two motor pulleys and two free turning pulleys complete the H-shape. If only one motor is turning while the other one stands still, the base plate moves in the directions m1 or m2, which have an angle of 45° to the x- and y-axis. To transform the motor axis system to the machine axis system a simple rotation of 45° is sufficient.

The advantage of this configuration is that both motors are stationary and do not move with the base plate. Therefore, the accelerated mass is lower and higher dynamics can be achieved. The linear stage for the z-direction is designed for lower dynamics and is therefore light. It is

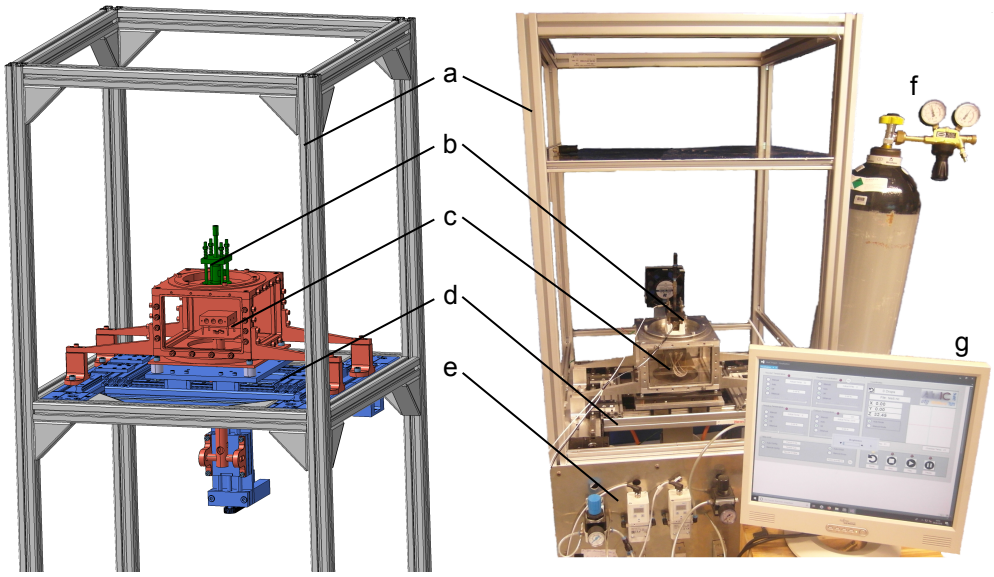

Figure 4.1: Overview of the prototype printing machine: The motion stage assembly (d) and the printing chamber (c) are fixed in the aluminium frame (a). The print head (b) is mounted in the chamber's lid. The picture also shows the pneumatic actuation (e), the nitrogen supply (f) and the visualisation of the machine control (g).

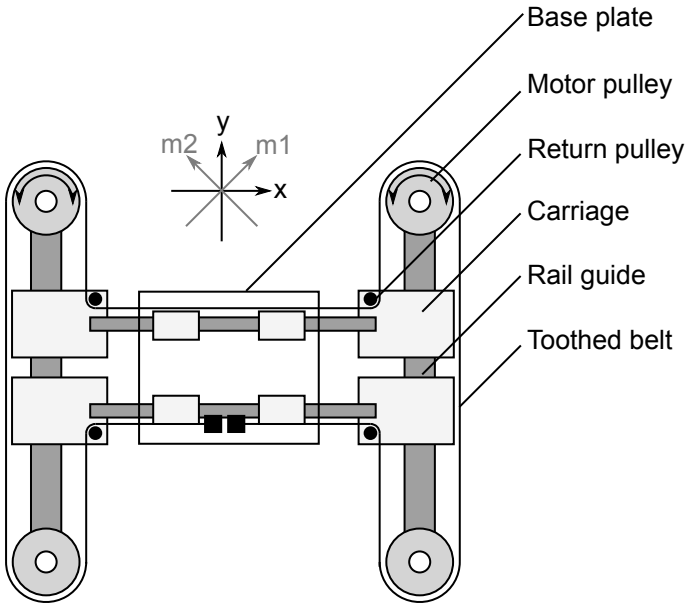

Figure 4.2: Sketch of 'H-Bot' configuration of the XY motion stage: The base plate is mounted on carriages on rail guides to be able to move in x- and y-direction. A toothed belt is attached to the base plate and is guided by six return pulleys and two motor pulleys in a shape, which resembles the letter 'H'. Each motor moves the base plate in a direction 45° to the x- and y-axis when operated individually (m1, m2).

attached to the base plate and consists of lead screw linear stage driven by a stepper motor. More detail on the motion stages is given in table 4.1

Table 4.1: Overview of the most important components of the motion stage.

Part	Type	Manufacturer
Rail guide (x,y)	Linear Guide Rail PS 4-15	item Industrietechnik GmbH, Solingen, Germany
Carriage (x,y)	Bearing Carriage PS 4-15	item Industrietechnik GmbH, Solingen, Germany
Motor pulley	Timing-Belt Reverse Unit 8 40 R25	item Industrietechnik GmbH, Solingen, Germany
Return pulley	Timing-Belt Counter-Reverse Unit 8 R25	item Industrietechnik GmbH, Solingen, Germany
Toothed belt	Timing Belt R25 T10	item Industrietechnik GmbH, Solingen, Germany
Linear stage (z)	drylin SHT-12-AWM-100	igus GmbH, Köln, Germany
Servomotor (x,y)	AM8111-1F20-0000	Beckhoff Automation GmbH & Co. KG, Verl, Germany
Gearbox (x,y)	AG2250-+PLE40-M02-20-1B1-AM811x	Beckhoff Automation GmbH & Co. KG, Verl, Germany
Stepper motor (z)	AS1020-0120	Beckhoff Automation GmbH & Co. KG, Verl, Germany

4.1.2 Printing Chamber

A middle section of the printing chamber is shown in figure 4.3. It can be divided into two parts: a stationary and a moving part. The latter consist of the base plate, which is driven by the XY stage and the lifting rod that carries the heated build platform. For heating the platform three heat cartridges (hotrod 10x60, Hotset GmbH, Lüdenscheid, Germany) are fitted in the boreholes, which can be seen in the figure. A thermocouple (type K, class I) is used to control the temperature of the build platform. It is fitted in a borehole between two heat cartridges (not shown in the figure). To isolate the build platform from the lifting rod, it is attached by four thin-walled spacer tubes made from stainless steel. The lifting rod is guided by two sliding bearings (H4FM-2528-21, igus GmbH, Köln, Germany), which are pressed in a bearing block connected to the base plate. On the bottom the lifting rod is mounted to the linear stage. The complete lifting rod is hollow and contains the cables of heat cartridges and thermocouple. An

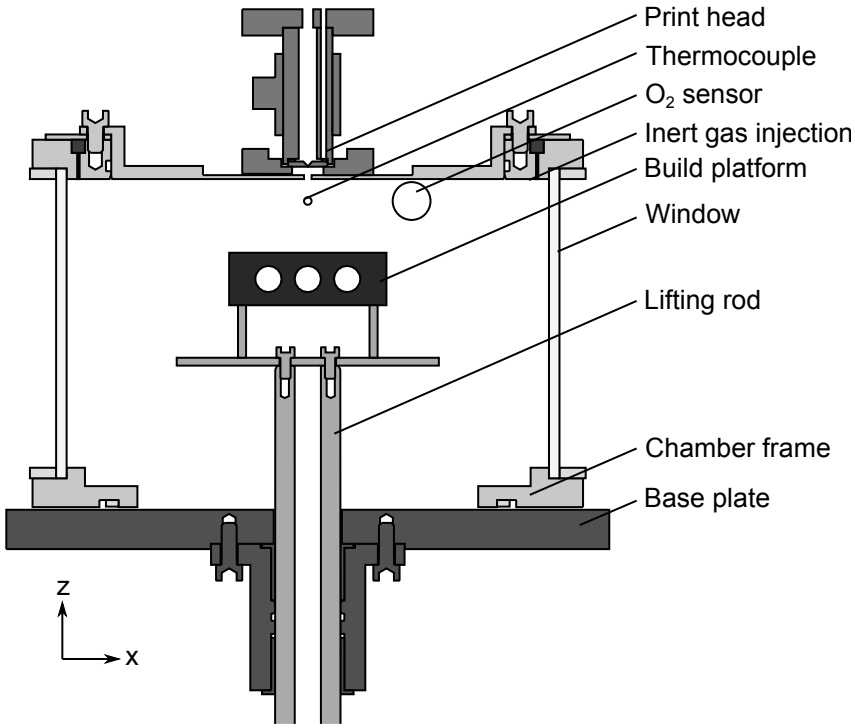

Figure 4.3: Middle section of the printing chamber. The base plate is connected to the XY stage and carries the build platform with the lifting rod. The chamber frame is stationary and fixed to the machine frame. Three glass windows enable optical access to the process. The top lid contains the print head and is surrounded by the inert gas injection.

O-ring between the two sliding bearings and high temperature silicone injected in the hollow rod after installing the cables, provide sealing to separate the inert atmosphere inside the printing chamber from the environment.

The stationary part is based on the chamber frame made from aluminium, which is fixed on the machine frame. An O-ring sealing is pressed into a groove in the bottom of the chamber frame. This O-ring is in contact with the moving base plate. To minimise friction and wear the base plate is coated with Polytetrafluoroethylene (PTFE). Three sides of the chamber frame are closed by glass windows and the forth side is closed by the back plate. In the back plate a thermocouple (type K, class I) and an oxygen sensor (S0-D0-001, SENSORE Electronic GmbH, Klosterneuburg, Austria) are fitted. The top is closed by a lid containing the print head. Surrounding the lid, the chamber frame contains the inert gas injection. Through 12 circular arranged holes nitrogen is blown into the chamber.

The pneumatic plan of the inert gas supply is shown in figure 4.4. A gas bottle with nitrogen (purity 99.999 %) supplies inert gas to the setup. The electronic pressure regulator (VPPE 3-1-1, Festo AG & Co KG, Esslingen, Germany) in combination with a flow restrictor enables

the machine control to set a desired inert gas flow, which is visualised by the flowmeter. The pressure regulator works from 0 to 6 bar and the restrictor is designed to create a gas flow between 0 to 1 $m^3\,h^{-1}$. A closed-loop control is implemented in the PLC to maintain a desired oxygen concentration in the printing chamber's atmosphere by adjusting the inert gas flow accordingly.

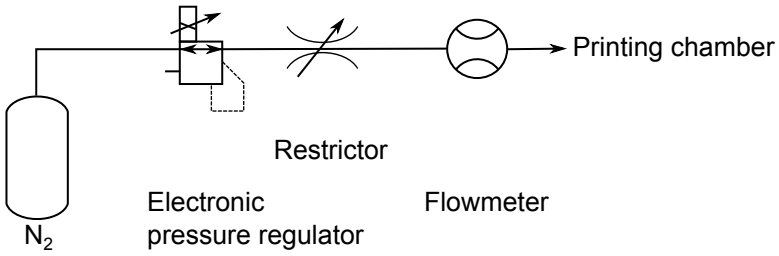

Figure 4.4: Pneumatic plan of inert gas supply: An electronic pressure regulator and a flow restrictor enable the PLC to set a desired gas flow between 0 to 1 $m^3\,h^{-1}$, which is visualised by the flowmeter.

4.1.3 Print Head

Figure 4.5 shows a middle section of the CAD model and a photo of the print head. Four bolts with nuts and springs clamp together the top plate, the crucible, the bottom plate, the lid of the printing chamber and all components in between. The lid of the printing chamber is not shown completely here (see figure 4.3). The crucible is centred in both the top and the bottom plate. It needs to withstand the aluminium melt, the high temperatures in an oxidising environment and it needs to be resistant to thermal shock to allow fast heating and cooling of the setup. Therefore, a sintered silicon nitride ceramic (SN-TC, FCT Ingenieurkeramik GmbH, Frankenblick, Germany) is used for the crucible. The top plate, the gas adaptor, bolts, springs and nuts are made from stainless steel (1.4301 or 1.4305). The bottom plate needs to thermally isolate the nozzle plate from the printing chamber and is therefore made from calcium silicate (Calcast CC 350, SILICA GmbH, Mettmann, Germany). To improve inert gas flow at the nozzle orifice, a vent is machined in the bottom of the plate, to allow inert gas to flow from the chamber to the nozzle and escape through the vent. This is shown in more detail in section 4.3.7. A heating coil (hotspring Mini, Hotset GmbH, Lüdenscheid, Germany) with a power of 268 W, surrounds the crucible and can heat it to a maximum temperature of 750 °C. Sealings made from graphite paper are placed between top plate and crucible as well as between crucible and nozzle plate. The nozzle plate is centred in a pocket in the crucible and is made from an aluminium nitride/boron nitride mixed ceramic (Shapal Hi-M Soft, Tokuyama Corporation, Tokyo, Japan).

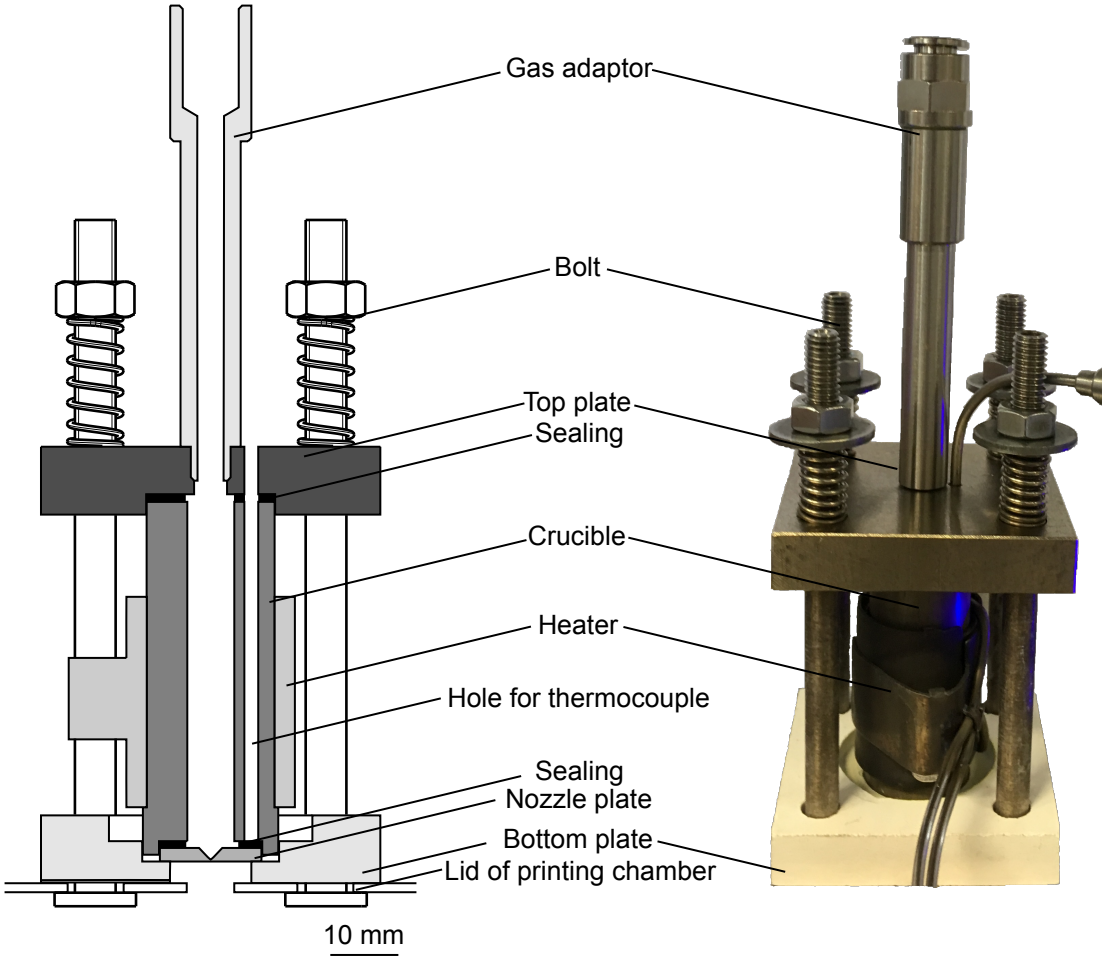

Figure 4.5: Middle section of CAD model (left) and picture (right) of the print head. The crucible, which contains the molten aluminium, is clamped between the top and the bottom plate by four bolts. On the bottom it is closed by the nozzle plate and on the top it is closed by the gas adaptor. A heater surrounding the crucible is controlled to set a desired temperature that is measured by a thermocouple plugged into a hole through the top plate and the crucible.

The advantage of this ceramic is that it can be machined by conventional tools in the sintered state. It has a bending strength of 300 MPa, is resistant to thermal shock and molten aluminium. Figure 4.6 shows the drawing and a picture of the orifice after machining.

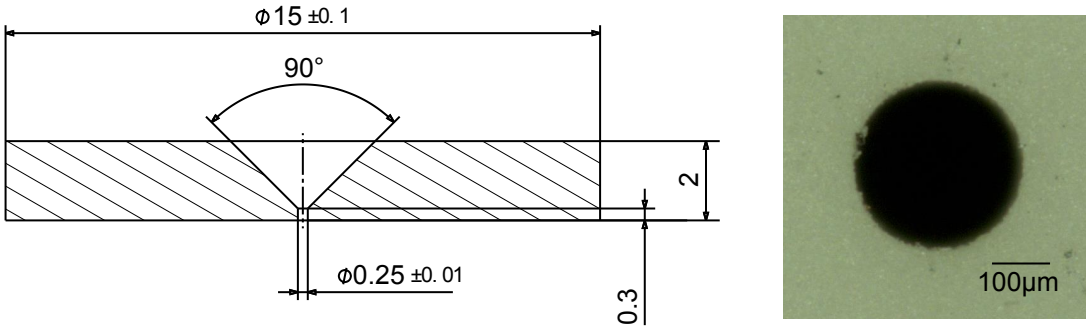

Figure 4.6: Drawing (left) and picture (right) of the nozzle plate. The picture shows the orifice on the bottom site after machining.

The pneumatic layout to create the pressure pulse used to eject droplets is shown in figure 4.7. The gas is taken from the same bottle used to purge the printing chamber. An electronic pressure regulator (VPPE 3-1-1, Festo AG & Co KG, Esslingen, Germany) is used to set the desired amplitude of pressure. A fast switching 2/2-way valve (MHJ 9, Festo AG & Co KG, Esslingen, Germany) creates a pressure pulse with a minimum length of 1.2 ms. The pressure pulse runs through a hose made from PTFE to the print head where it provides the energy for droplet ejection. To avoid reflections of the pressure pulse between melt and valve, which would cause multiple droplets to be ejected, the wave has to be terminated. For that purpose a restrictor open to the environment is placed close to the print head. The opening diameter is just big enough to terminate the wave after one reflection on the surface of the melt completely.

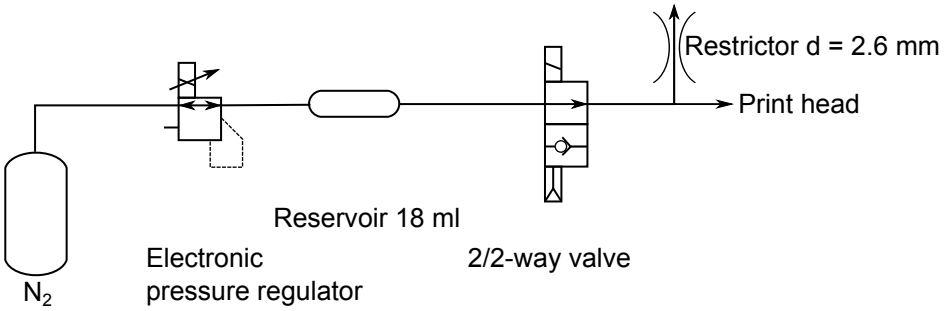

Figure 4.7: Pneumatic layout to supply pressure pulses to the print head: A pressure regulator sets the desired pressure amplitude for the pulses. The reservoir is designed to contain the gas needed for a single pulse without a significant pressure drop. A fast switching 2/2-way valve creates the pulse, which runs through the hose to the print head. Close to the print head an opening terminates the pressure pulse and suppresses multiple reflections in the hose.

4.1.4 Machine Control

To operate the printing machine, a programmable logic controller (PLC) based on the modular I/O-system EtherCAT (Beckhoff Automation GmbH, Verl, Germany) is employed. It consists of an EtherCAT coupler and a number of EtherCAT terminals for several functions. Figure 4.8 shows a screenshot of the user interface. It comprises following core elements:

- Close-loop controller for the temperature of the print head, the temperature of the build platform and the oxygen concentration in the printing chamber
- Manual control for the valve to eject droplets
- Player to run the machine automatically by G-code scripts

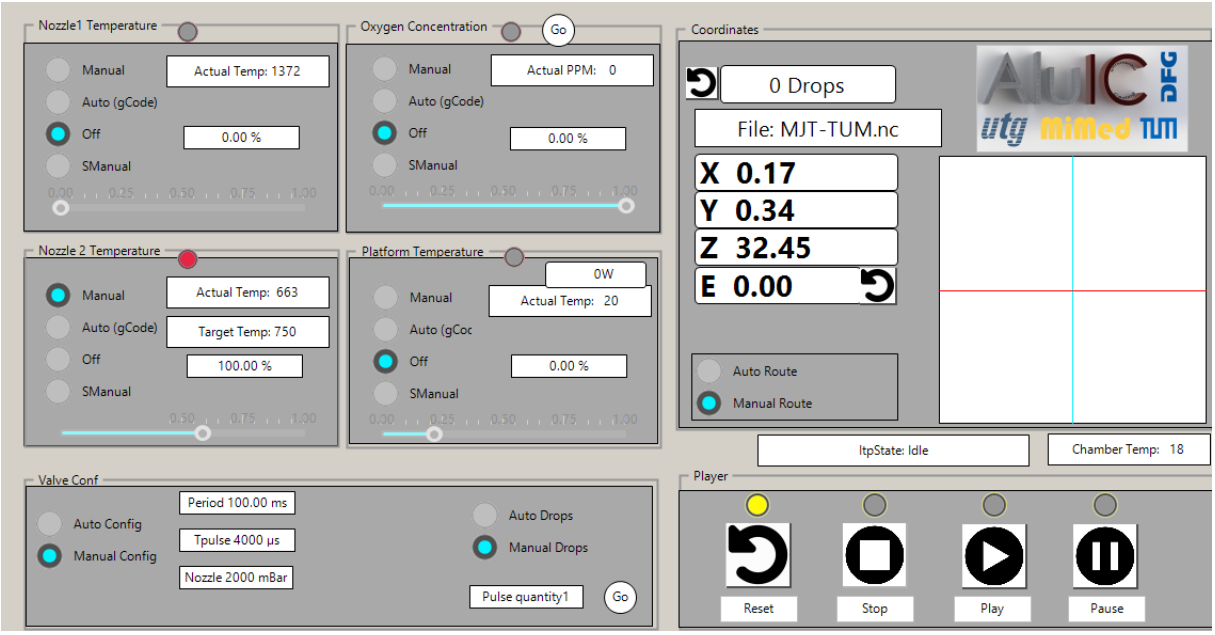

Figure 4.8: User interface of machine control consisting of the core elements: closed-loop controller for temperatures and oxygen concentration, a manual control to eject droplets and a player to run G-code scripts.

The set value of the close-loop controllers can be either given by the user or by the G-code script. Alternatively the controller can be switched off and the actuating variable is set manually between 0 to 100 %. The parameters to eject droplets are the time between two droplets t_{period}, the time the fast switching valve is opened t_{pulse} and the pressure amplitude p_{pulse} that is given to the pressure regulator. All parameters can be either set manually or by the G-code script. When a droplet should be ejected manually, a number of droplets can be entered that are ejected in a series according to the parameters after the trigger button 'Go' is pressed. The player is

used to load a G-code script, which can then be started, stopped and paused. After a change in the set temperatures, a G-code command can be given, to pause the machine, until the measured temperatures are within ±10 °C of the set temperatures. A visualisation shows the current position of the motion stages and counts the number of droplets.

4.2 Alloys

Six different aluminium alloys were used for the presented studies. The reference material for most of the experiments was an eutectic aluminium-silicon alloy AlSi12 (4047A). To examine the influence of the silicon content it is compared to AlSi5 (4043A) and to Al99.5Ti (1450). Additionally the effects of aluminium-copper and aluminium-magnesium were examined with AlMg3 (5754), AlMg5Cr (5356) and AlCu5. The latter was prepared by melting pure aluminium (Al99.9) and dissolving pure copper (Cu-ETP) in it. The other five alloys can be obtained as filler metals for welding in various wire diameters, whereas no binary aluminium-copper alloys are available as filler metal. The norm ISO 18273 standardises filler metals for welding and the numbers given in parentheses always refer to that norm. The material is inserted in the crucible after heating and purging with inert gas, therefore it needs to fit through the bore in the top plate. A maximum diameter of 4 mm is possible, so the AlCu5 was first cast into a block and then rods with a cross section of 3 mm × 3 mm were cut from it. Suppliers and forms of all materials are summarised in table 4.2. As the tests with AlMg alloys failed owing to excessive oxidation (see section 5.3.2), those materials are not further described.

Table 4.2: Overview of the alloys used in the presented studies, with supply form and supplier.

Alloys	Grade	Form	Supplier
AlSi12	4047A	wire coil d = 0.8 mm	Drahtwerke ELISENTAL W. Erdmann GmbH & Co, Neuenrade, Germany
AlSi5	4043A	rod d = 2.0 mm	voestalpine Böhler Welding GmbH, Düsseldorf, Germany
Al99.5Ti	1450	rod d = 1.6 mm	VDB-Schweißtechnik, Dormagen, Germany
AlMg3	5754	rod d = 3.2 mm	VDB-Schweißtechnik, Dormagen, Germany
AlMg5Cr	5356	rod d = 3.2 mm	VDB-Schweißtechnik, Dormagen, Germany
AlCu5	-	cast block, cut into rods 3 mm x 3 mm	-

The chemical composition of all alloys was tested by an optical emission spectrometer (Foundry-Master, Worldwide Analytical Systems AG, Uedem, Germany). The results are presented in table 4.3 compared to the norm ISO 18273.

Thermal properties used throughout the work for those alloys are summarised in table 4.4. Al99.5Ti is considered to be pure aluminium. For AlCu5 data from the technical alloys EN AW 2024 (AlCu4Mg1) is used. For the aluminium-silicon alloys the METALS model was used to estimate the necessary properties. All data as well as the model are described by Mills (2002).

Table 4.3: Chemical Analysis (meas.) of used materials compared to the norm ISO 18273. AlCu5 was not produced according to any norm. All numers in wt.%.

	Si	Fe	Cu	Mn	Mg	Cr	Zn	Ti	Be
AlSi12 (norm)	11-13	<0.6	<0.3	<0.15	<0.1	-	<0.2	<0.15	<0.0003
AlSi12 (meas.)	13	0.16	0.006	0.005	0.001	<0.0003	<0.001	0.021	<0.0001
Al99.5Ti (norm)	<0.25	<0.4	<0.05	<0.05	<0.05	-	<0.07	0.1-0.2	<0.0003
Al99.5Ti (meas.)	0.05	0.13	0.006	<0.001	<0.0001	<0.0004	<0.002	0.106	<0.0001
AlSi5 (norm)	4.5-6	<0.6	<0.3	<0.15	<0.2	-	<0.1	<0.15	<0.0003
AlSi5 (meas.)	5.38	0.14	0.019	<0.001	<0.0001	<0.0003	<0.001	0.008	<0.0001
AlCu5 (meas.)	0.04	0.03	5.25	<0.001	<0.0001	<0.003	<0.001	0.002	<0.0001

Table 4.4: Thermal properties of alloys used in this study. According to Mills (2002)

Property	Unit	Al99.5Ti	AlCu5	AlSi5	AlSi12
Liquidus temperature: T_{liq}	°C	660	632	632	577
Solidus temperatur: T_{sol}	°C	660	538	577	577
Thermal conductivity at T_{liq}: λ_{liq}	$W\,m^{-1}\,K^{-1}$	91	86	85	77
Thermal conductivity at T_{sol}: λ_{sol}	$W\,m^{-1}\,K^{-1}$	208	188	210	207
Specific heat capacity at T_{liq}: c_{liq}	$J\,kg^{-1}\,K^{-1}$	1180	1140	1169	1155
Specific heat capacity at T_{sol}: c_{sol}	$J\,kg^{-1}\,K^{-1}$	1180	1100	1126	1101
Density at T_{liq}: ρ_{liq}	$kg\,m^{-3}$	2380	2500	2388	2401
Density at T_{sol}: ρ_{sol}	$kg\,m^{-3}$	2557	2674	2641	2613
Heat of fusion	$kJ\,kg^{-1}$	397	366	389	426

4.3 Experimental Procedure

Different experimental setups were used throughout the studies to print specimens for tensile tests and micrographs, to record single droplets with a high speed camera and to measure the cooling of single droplets with a pyrometer. The setups and the procedures are described in the following sections.

4.3.1 Blocks for Tensile Tests and Micrographs

Each experiment starts with the job preparation that ensures comparable conditions for every run. Afterwards, the G-code script is started and the printing process is then running automatically. All steps done after the block was build, are summarised in the post process.

Job Preparation

Before every run, the print head is taken from the machine and disassembled completely to remove remaining material and slag from a previous test run. The nozzle is checked for clogging and eventually cleaned by pressurised air. All seals are replaced in case they were damaged in the previous run or while disassembling. Then the components are reassembled and clamped by the springs. A nickle sheet (50 mm × 50 mm × 1 mm) serves as a carrier plate. Before every run that nickle sheet is sanded with 1200 grit paper until it is metallic bright and then placed on the build platform.

After the print head is mounted in the printing chamber, the heaters of build platform and print head are started in manual mode and set to the temperatures for the first layer. The inert gas supply is set to maximum flow until the oxygen concentration in the chamber can be detected by the sensor (< 1000 ppm). Then the close-loop controller is activated and set to the desired value of oxygen concentration.

When the print head temperature and oxygen concentration are reached, material is fed through the gas adaptor manually. Once the crucible is filled, the gas hose is connected to the gas adaptor and the printer is ready to operate.

Build Process

Once the job preparation is finished, the G-code player is started and the automatic build process begins. The dimensions of one printed block were chosen to make full use of the material that fits into a crucible filled to the maximum and to be able to machine a tensile test specimen similar to the smallest one standardised in DIN 50125. Each layer is deposited the same way, following the path shown in figure 4.9. The path shows the relative movement of the print head as seen from the build platform. This point of view is easier to interpret, even though the platform is moving, not the print head. After reaching the start position, a short movement without droplet ejection in positive y and in negative x directions ensures that no backlash appears during droplet deposition. Then, during constant movement, the droplet ejection is activated for 32 mm. The movement is stopped a few millimetre after droplet ejection is finished, to make sure no effects of acceleration can be seen in the parts. After an offset of 1 mm in y-direction the second line is deposited in opposite x-direction. Deposition is now started 0.5 mm earlier than the last line ended. This alternating offset in x-direction allows to print two lines closer to each other resulting in a higher density. Velocity during printing is set to 5.5 mm s^{-1} and the period time is 200 ms, so the distance between two droplet ejections is 1.1 mm. That way, five lines are printed until one layer is finished. Then the platform is lowered by 0.8 mm and moved to the start position before the next layer is deposited. A total of eight layers is printed for one block. All geometric parameter were set in a way to ensure planar layers with a maximum density and a constant distance between nozzle and part.

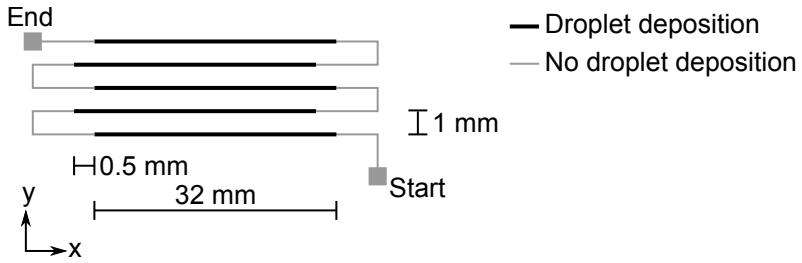

Figure 4.9: Path of the print head relative to the platform during deposition of a single layer while printing a block for tensile tests and micrographs. Five lines are printed in alternating directions with a distance between the lines of 1 mm. Each line is 32 mm long. Ending of one line and starting of the next line are shifted for 0.5 mm.

It was desired to achieve a certain amount of bonding between droplets and carrier plate to avoid deformation induced by thermal contraction but bonding should also not be too high, to enable part removal without damaging the carrier plate or the printed specimen. This is only possible for certain platform and droplet temperatures. Therefore, the first layer is always printed with $T_{\mathrm{plat}} = 450\,^{\circ}\mathrm{C}$ and $T_{\mathrm{ph}} = 700\,^{\circ}\mathrm{C}$. Before the second layer those temperatures were set to the desired value. The valve parameters pulse time t_{pulse} and pulse pressure p_{pulse} were identified for

each alloy to eject a volume between 0.8 to 0.9 mm^3 with a velocity of approximately 2.7 $m\,s^{-1}$ at each pulse. This corresponds to a droplet diameter of 1.15 to 1.2 mm for a single ideal spherical droplet. The parameters were also adjusted to ensure stable operation conditions, so the velocity criteria is not always exactly met.

Three test series were carried out: a full factorial variation of alloys, the platform temperature T_{plat} and the print head temperature T_{ph}, a one factor variation of oxygen concentration in the build chamber c_{O_2} and a full factorial variation of droplet ejection pressure p_{pulse} and T_{plat} on two stages. Table 4.5 gives an overview of the process parameters that were used in the test series of temperature variations. Tables 4.6 and 4.7 show the parameters for the variation of oxygen concentration and variation of Weber number. In the case of p_{pulse} variation, the valve opening time t_{pulse} was adjusted to maintain a constant droplet size at higher droplet velocities.

Table 4.5: Parameter settings for the test series of temperature variations.

Alloy	T_{plat} in °C	T_{ph} in °C	t_{pulse} in ms	p_{pulse} in bar	c_{O_2} in ppm
AlSi12	300,350,400,450,500	650,700,750	7	1.2	20
AlSi5	450,500,550	700,750	6.3	1	20
Al99.5Ti	580,600,620	750	6.0	0.9	20
AlCu5	500,550	700,750	11.5	1.5	20

Table 4.6: Parameter settings for the test series of oxygen concentration variations.

Alloy	T_{plat} in °C	T_{ph} in °C	t_{pulse} in ms	p_{pulse} in bar	c_{O_2} in ppm
AlSi12	500	650	7	1.2	20,60,100,140,200,350

Table 4.7: Parameter settings for the test series of droplet velocity variations. t_{pulse} is adjusted to maintain a constant droplet size.

Alloy	T_{plat} in °C	T_{ph} in °C	t_{pulse} in ms	p_{pulse} in bar	c_{O_2} in ppm
AlSi12	300,500	700	4, 3.3, 2.3	2, 3, 5	20

Post Process

For AlSi12, AlSi5 and Al99.5Ti the cooling after printing is uncontrolled on the building platform or after removing the nickle plate. As AlCu5 shows precipitation hardening the cooling history has an effect on the tensile properties. Therefore, it was cooled by pressurised air from an air gun at 6 bar, directly after printing.

After cooling, the blocks are removed from the nickle sheet and either machined to tensile specimens or cut diagonal to prepare micrographs. Figure 4.10 shows a printed block from AlSi12 with the cutting plane for micrographs on the left and a machined tensile specimen on the right. The amount of pores is higher between lines and layers as it is in the middle of a line or a layer, a diagonal cutting plane for the micrographs is therefore necessary to get a representative image. Simulation results (see section 5.2.1) show that local thermal conditions do not differ significantly in x-,y- and z-directions during the experiments. Consequently, microstructure is expected to be independent of the cutting plane. Tensile specimens were machined from the centre of the block.

Figure 4.10: Printed block of AlSi12 (left) and tensile specimen (right). A white dotted line shows the cutting plane for the micrographs.

4.3.2 Tensile Tests

As already mentioned, tensile test specimens are machined from the printed blocks. The print head does not contain sufficient material to print a block big enough to machine a specimen according to DIN 50125, which is based on the international standard ISO 6892-1. According to those standards, a machined specimen with a circular cross section needs to have a minimum diameter of 4 mm and a minimum initial gauge length of 20 mm. For this study a specimen was designed with a diameter of 3 mm and an initial gauge length of 15 mm. The technical drawing is shown in figure 4.11.

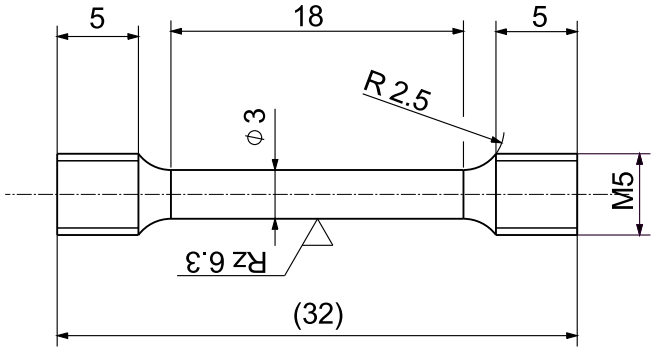

Figure 4.11: Drawing of tensile test specimen. It has a circular cross section with a diameter of 3 mm, a parallel length of 18 mm and M5 threads.

All tensile tests are performed in a universal testing machine (1484, Zwick GmbH & Co. KG, Ulm, Germany). The test setup is according to ISO 6892-1 with a constant strain rate of $2.5 \times 10^{-4}\,\mathrm{s}^{-1}$. Elongation is measured with an extensometer (Makro, Zwick GmbH & Co. KG, Ulm, Germany) directly on the specimen's surface. The recorded stress and strain data is evaluated for ultimate tensile strength R_m, 0.2 % offset yield strength $R_{\mathrm{p}0.2}$ and uniform elongation A_u. To determine $R_{\mathrm{p}0.2}$, the elastic modulus E is necessary and as the initial gauge length is smaller than requested by the standard, it is assumed that measuring uncertainties are greater than deviation of E between different samples. Therefore, a constant elastic modulus of 70 GPa is assumed.

4.3.3 Preparation of Micrographs

Printed blocks were cut diagonal as shown in figure 4.10 and then embedded under reduced pressure of −0.6 bar relative to environment. After hardening of the resin they were grounded and polished step-wise to a final polishing step with a colloidal SiO_2 suspension containing 0.04 µm particles (OP-S, Struers GmbH, Willich, Germany). Specimens of the alloy AlCu5 were additionally etched in two steps, first with sodium hydroxide solution (2%), then with a mixed solution of sodium hydroxide (1%) and potassium permanganate (4%).

4.3.4 Density Evaluation from Micrographs

According to VDI 3405-2 the density of additively built metal parts by means of beam melting, can be measured by image analyses of micrographs. As there is no standard for MJT yet, the VDI 3405-2 is used instead. Images of the micrographs covering the whole specimen are made by a light microscope (Axioplan 2, Carl-Zeiss Micro-Imaging GmbH, Göttingen, Germany) with a resolution of $7.5\,\mu\mathrm{m\,px}^{-1}$. The open source software Fiji is used for the image analyses. First the picture is cropped to cut away the boarders that do not show printed metal but embedding material. Then the colour image is converted to an 8-bit grey-scale image. Next, the image is segmented to separate pore from material. To do so, Fiji uses the isodata algorithm of Ridler and Calvard (1978). A filter is applied to ignore all pores smaller than two pixels. The steps are visualised in figure 4.12. Now the relative density can be calculated by dividing the number of pixels representing metal, by the total number of pixels:

$$\rho_{\text{rel}} = \frac{n_{\text{metal}}}{n_{\text{total}}} \qquad \text{(Equation 4.1)}$$

ρ_{rel}: Density
n_{metal}: Number of pixels representing metal
n_{total}: Total number of pixels

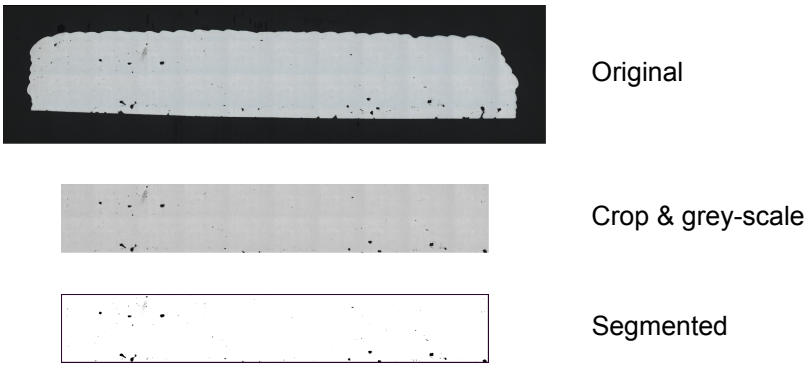

Figure 4.12: Steps of image analysis to measure the relative density. First the image is cropped to show only material, then it is converted to an 8-bit grey-scale and segmented by the isodata algorithm.

4.3.5 High-speed Camera Records

To evaluate the droplet characteristics, a high-speed camera records images of ejected droplets in flight. Figure 4.13 shows a schema of the experimental setup. Through the two opposite glass windows of the printing chamber, the droplet can be observed in flight by a high-speed camera (MotionBlitz EoSens mini2, Mikrotron GmbH, Unterschleißheim, Germany) and a LED backlight (M450LP1, Thorlabs GmbH, Dachau, Germany). Pictures are recorded at a speed of 5000 frames per second with a shutter time of approximately 20 µs. With the used objective (LM50TC, Kowa Optimed Deutschland GmbH, Düsseldorf, Germany) droplets can be observed for approximately 10 mm depending on the exact position of the camera. To calibrate the length of each pixel in the images, a caliper opened exactly 2 mm is held in the beam path at the same position at which the droplets will be ejected, and a picture is taken by the camera. By counting pixels between the calipers legs in the picture, the length of one pixel can be calculated. This value is determined at the beginning of every test run and is about 17.5 µm.

A script for the software Matlab (The MathWorks Inc., Natick, MA, USA) automatically evaluates the recorded images. To do so, two pictures are given to the function. One when the main droplet is fully visible and one showing the main droplet just before leaving the recorded area.

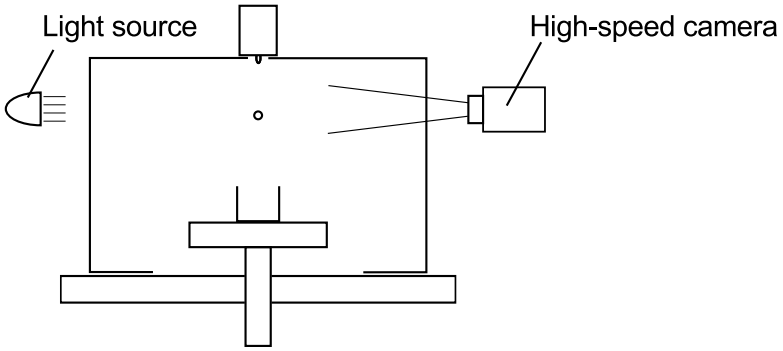

Figure 4.13: Schema of experimental setup to evaluate droplet characteristics: Through two glass windows the droplet in flight is observed by a high-speed camera and illuminated by a LED backlight.

The image is then segmented in fore- and background by a threshold grey value, which is set by the user. The closed area which is closest to the bottom of the image is assumed to be the main droplet and its centre of area is calculated in both images. The distance travelled between both images can be calculated using the pixel length from the calibration and the time between both images known by the frame rate and the image number. Figure 4.14 shows an image as it is taken by the high-speed camera and the processed result from the Matlab-script with the droplet's centre of area.

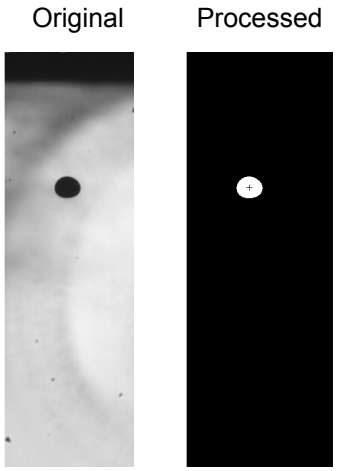

Figure 4.14: An image taken by the high-speed camera and the result after processing it with the Matlab-script. A threshold grey value is used to segment the image in fore- and background. The droplet's centre of area is calculated and shown by a cross.

4.3.6 Pyrometer Measurements

The main purpose of this setup was to validate the simulation described in section 4.4. Unfortunately it was not possible to measure temperatures with the pyrometer directly for several reasons: The emissivity of aluminium and its alloys is very low and depends on the surface structure (Wen and Mudawar, 2006). Test on conventionally cast blocks showed, that the emissivity changes significantly during solidification. Figure 4.15 compares the temperatures measured by a thermocouple and measured by a pyrometer with a constant set emissivity of 0.435 during the solidification of a conventionally cast AlSi12 surface. The emissivity value was calibrated at room temperature and is valid as soon as the material is fully solidified. It is not valid for liquid aluminium and changes during solidification, when the surface structure changes owing to the microstructure of the solid material and owing to oxidation.

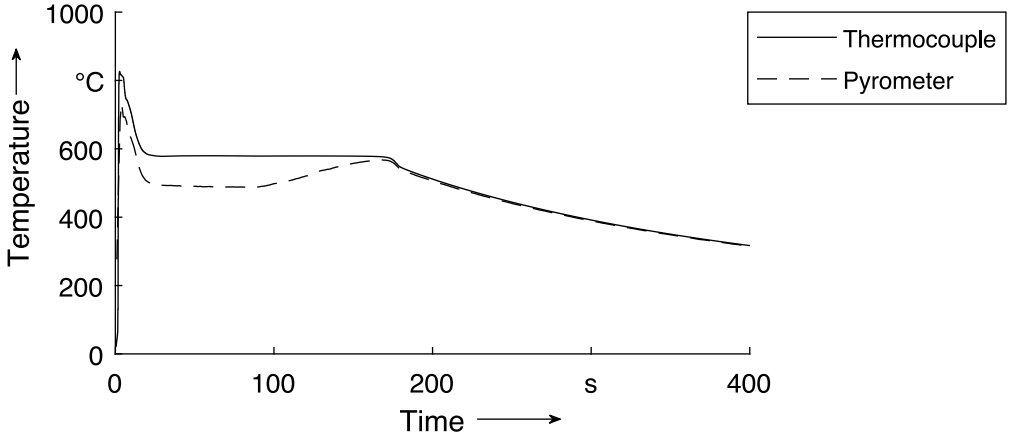

Figure 4.15: Comparison of temperatures measured by thermocouple and pyrometer during solidification of conventionally cast AlSi12. The emissivity was set constantly to 0.435. While temperatures are equal after solidification, they differ before and during solidification.

Another reason is, that the droplet is small compared to the detector of the pyrometer. Thus, a significant amount of background radiation is measured, especially from the build platform. Finally, the angle between metal surface and pyrometer is also affecting the measured radiation (Lax and Pirani, 1929). As the droplets have a high curvature and are moving relative to the pyrometer, this angle is permanently changing.

Despite the described challenges to measure temperatures directly, it was possible to determine the solidification time from the pyrometer signal. The experimental setup for this purpose is shown in figure 4.16. A pyrometer (CTvideo3M, Optris GmbH, Berlin, Germany) with a spectral range of 2.3 µm and a 300:1 optic (CF-vario, Optris GmbH, Berlin, Germany) is

focused to measure the droplets just after deposition. Sensor values are recorded at a frequency of 1000 Hz. In the acquisition software, the emissivity is set to a minimal value of 0.1 to ensure a maximal sensitivity. To determine the start and end of solidification, the first derivative of the temperature curve is formed and its minima are evaluated. Figure 4.17 shows the raw pyrometer signal for the measured temperature and its derivative. The minima in the derivative mark the onset and the end of solidification.

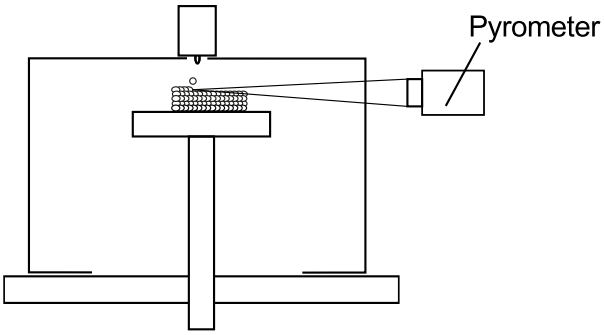

Figure 4.16: Schema of experimental setup to determine the droplet solidification time by a pyrometer measurement.

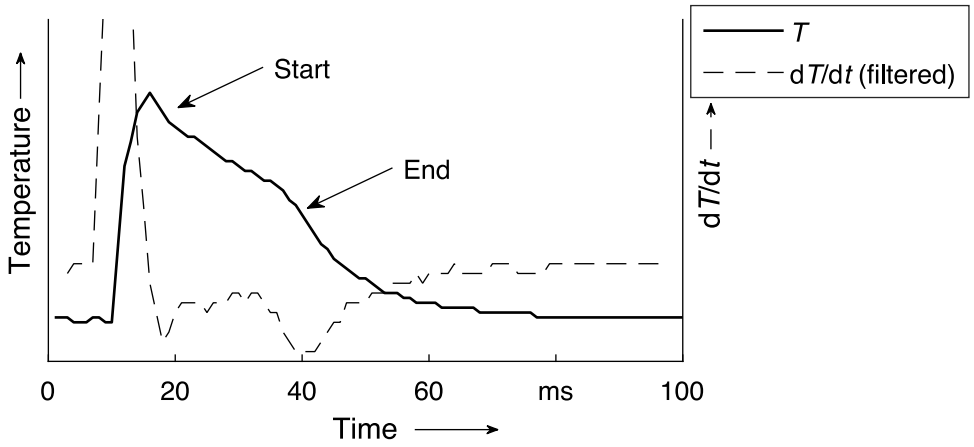

Figure 4.17: Evaluation of solidification time from pyrometer signal: The derivative of the pyrometer signal shows minima for the onset and the end of solidification.

To validate the simulation, a cuboid block with $32 \times 5 \times 8$ droplets is printed with the parameters summarised in table 4.8 at two different platform temperatures. The solidification times of all 32 droplets in the first line of the sixth layer were measured. The solidification time is constant for those 32 droplets owing to the fact, that at low deposition frequencies each droplet cools essentially to the platform temperature before the next droplet is deposited. Therefore, an average solidification time is calculated for the complete row.

Table 4.8: Process parameters for validation experiments at two different platform temperatures.

Alloy	T_{plat} in °C	T_{ph} in °C	t_{pulse} in ms	p_{pulse} in bar	c_{O_2} in ppm
AlSi12	400,490	700	7	1.2	20

4.3.7 Oxygen Measurements

The oxygen content in the printing chamber atmosphere is measured only at one position during normal operation, which is shown in figure 4.3. Owing to the high temperatures of print head and build platform, convective gas flow might lead to an inhomogeneous oxygen distribution. Hence, a test series was carried out to measure the oxygen concentration close to the nozzle position in comparison to the normal measurement position. An adaptor, which was fabricated by SLS, allows to install the oxygen sensor at the same position as the nozzle plate in normal operation. For this purpose the adaptor replaces top plate, crucible and heater in the print head. The base plate is maintained to ensure comparable gas flow. As the maximal operating temperature of the sensor is 350 °C, the nozzle temperatures can not be fully simulated by this setup, but it should still reproduce the principle relations. Figure 4.18 compares the setup used for the oxygen measurement at nozzle position with the normal print head setup.

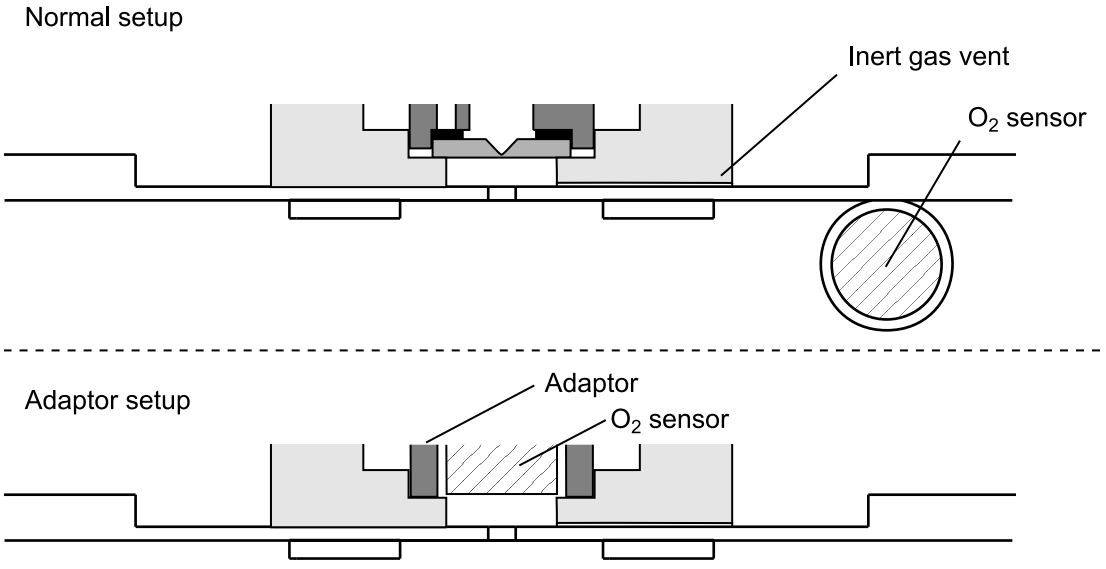

Figure 4.18: Setup to measure oxygen content close to printing nozzle: Instead of the crucible an adaptor is installed that positions the oxygen sensor at the same place as the nozzle in normal operation.

In a first step, the build platform is positioned 10 mm below the printing chamber's lid and is heated to 500 °C. The oxygen sensor is installed at its normal position and the print head is heated to 700 °C. Then the printing chamber is purged with inert gas and the controller for

the oxygen concentration is set to the desired value. After the gas flow controller established a constant value, this value is documented together with the set oxygen concentration.

In the second step, the adaptor together with the sensor is installed at the print head and the opening in the build chamber is sealed. Now the chamber is purged again manually with an inert gas flow corresponding to the values documented in the first step. Build platform position and temperature are identical. Once the value measured by the oxygen sensor becomes constant, it is documented. This procedure was necessary, as only a single oxygen sensor was available.

4.3.8 Inert Gas Injection for Print Head Nozzle

Aluminium-magnesium alloys could not be printed with the conventional print head design, owing to nozzle clogging by oxidation. Therefore, a gas injection was designed that delivers inert gas directly to the printing nozzle. The inert gas injection replaces the bottom plate of the print head as shown in figure 4.19. The part was additively built from 1.4404 stainless steel in SLM process at AMCM GmbH (Starnberg, Germany). A fitting at the top of the part allows inert gas to be bled into the cavity, where it flows along the side walls and exits through a ring nozzle pointing upwards. Simulation of gas flow, show that the gas hits the printing nozzle, flows radially inwards and forms a concentric stream around the orifice. The open area is designed to generate a flow velocity of $1\,\mathrm{m\,s^{-1}}$ at a flow rate of $0.25\,\mathrm{m^3\,h^{-1}}$. A ceramic inlay between crucible and inert gas injection and a ceramic ring between printing chamber lid and inert gas injection provide heat insulation of the crucible. Both ceramic parts were made from calcium silicate (Calcast CC 350, SILICA GmbH, Mettmann, Germany). The oxygen adaptor for the oxygen measurements at nozzle position is also compatible with the inert gas injection.

4.4 Simulation Model

The process MJT is characterised by incrementally adding material to a part being built. Those increments are small in time and spatial dimensions. Thus, physical quantities like local temperatures are hard or impossible to access by conventional measurement techniques. So it is essential to establish simulation methods that yield the possibility to look into the process and obtain full access to the physical quantities of interest. For the evaluation of experimental results it is essential to know, whether local temperatures change during build-up and to what extent. A new method to simulate the temperature field on the scale of full parts consisting of

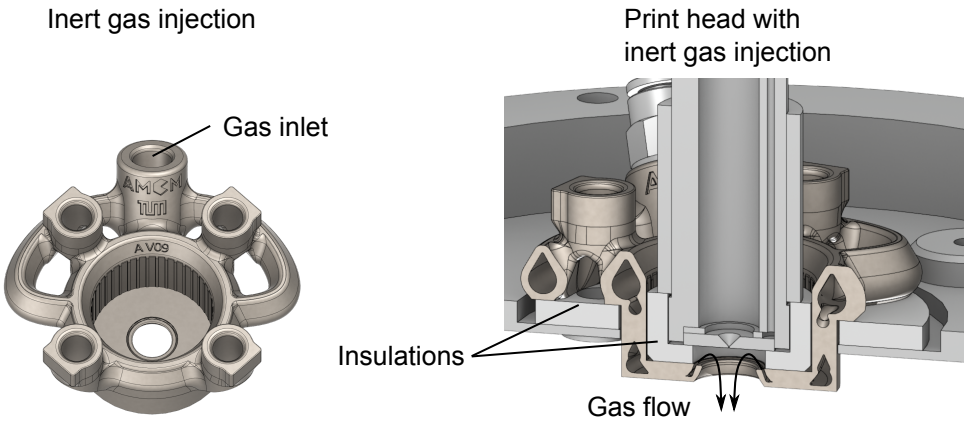

Figure 4.19: Rendering of inert gas injection alone and built in the print head. Inert gas enters through a fitting, flows through the side walls and exits through a ring nozzle pointing upward to the printing nozzle.

several thousand droplets was developed and is presented in the following sections. The method was already published in the journal Production Engineering (Himmel et al., 2018).

As shown in section 2.2 spatial and time resolution needs to be very small (1×10^{-9} s and 50 µm) to obtain valid results for the fluid motion of deposited droplets. Therefore, fluid motion has to be neglected to simulate the thermal field of a part consisting of several thousand droplets with an acceptable effort. This is valid for the macroscopic thermal field, as according to Schiaffino and Sonin (1997a) the bulk solidification time of a droplet is at least one order of magnitude greater than the spreading time (for aluminium alloys at temperatures and droplet sizes occurring in MJT). The only method of such kind already published, is based on the software ANSYS (ANSYS Inc., Canonsburg, PA, USA) and the finite-element-method (FEM) (Chao et al., 2013). Using a FEM solver to simulate the MJT process yields some difficulties for the model setup: During printing process, the shape of the part and the boundary surfaces are changing with each droplet being deposited. For every droplet a separate simulation run has to be started with adapted conditions and adapted boundaries. Doing that for a part consisting of several thousand droplets is inefficient and difficult to implement automatically for arbitrary geometries.

The following sections present a novel method based on the software Flow 3D (FlowScience Inc., Santa Fe, NM, USA), which uses the Finite-Difference-Method (FDM) to solve the governing equations in time and space. A special method called ‘volume of fluid’ (VOF) is used by Flow 3D to describe the fluid’s free surface and the boundary conditions at this surface. This method defines a step function F that is unity at any point occupied by fluid and zero otherwise. The value of F in a cell represents the fractional volume of fluid in that cell. Accordingly, each cell with an F value between one and zero contains a fluid surface. The surface normal can

be computed by calculating the derivatives of F in space. A detailed description of the VOF method was published by Hirt and Nichols (1981). As the fluid surface is evaluated in every time step, this method is ideal to use for MJT, where the material's surface changes over time.

4.4.1 Subroutine

To efficiently simulate the MJT process, the initialisation of individual droplets needs to be done automatically while the solver is running. For this purpose a subroutine was developed that reads the time t_{next} and the coordinates for each droplet deposition from an ASCII-file and initialises fluid with the desired temperature T_{drop} in the desired cells at the correct time step. This subroutine was compiled directly into the solver's executable and is called in each solver iteration. Figure 4.20 shows the flow chart of this subroutine. When the current simulation time t gets greater or equal to t_{next}, the subroutine continues by reading the next line of the input ASCII-file, which contains the time t_{next} for the following droplet and the x,y,z-coordinates for the current droplet. Each droplet is represented by a cuboid with $n_{\mathrm{x}} \times n_{\mathrm{y}} \times n_{\mathrm{z}}$ cells and the coordinates describe the corner in positive x-, y- and z-direction. Next, the routine identifies the cells corresponding to the coordinates and the given size of the cuboid and fills them with fluid ($F = 1$). Finally the solvers routine to evaluate the cells' internal energy is called and the subroutine ends. The parameters T_{drop}, n_{x}, n_{y} and n_{z} are stored in the input deck of the solver (.prepin file) and can be read by the subroutine. As the solver will reevaluate the free surface in the following time step, all boundary conditions are automatically updated. This subroutine yields the possibility to simulate the build-up process of a part consisting of an arbitrary amount of droplets in a single simulation run.

According to the literature the crucial parameter controlling the spreading and bonding behaviour of a droplet on a substrate (carrier plate or previously printed droplet) is its temperature. So a relevant result is the surface temperature that an arriving droplet 'sees' when it is deposited. Therefore, the subroutine calculates the average temperatures of the cells next to a new droplet in x-,y- and z-direction just before it is initialised. Those temperatures are called adjacent temperatures $T_{\mathrm{adj,x}}$, $T_{\mathrm{adj,y}}$ and $T_{\mathrm{adj,z}}$. They are calculated by the subroutine and written in a result file in ASCII format. Figure 4.21 depicts where the temperatures are evaluated at the time of droplet arrival.

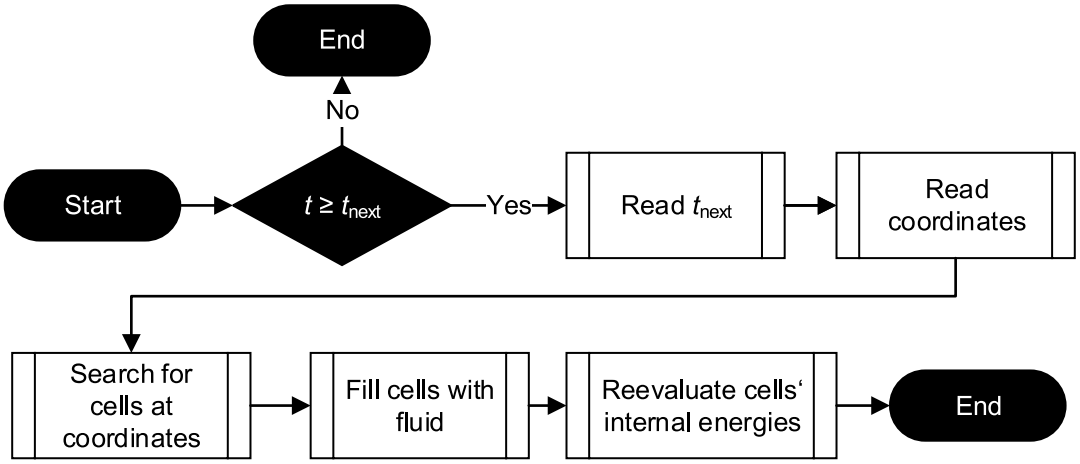

Figure 4.20: Flowchart of subroutine that automates the build-up process. The routine initialises droplets of the desired temperature in the correct time step at the desired position. Reprinted by permission from Springer Nature: Himmel et al. (2018), ©2018

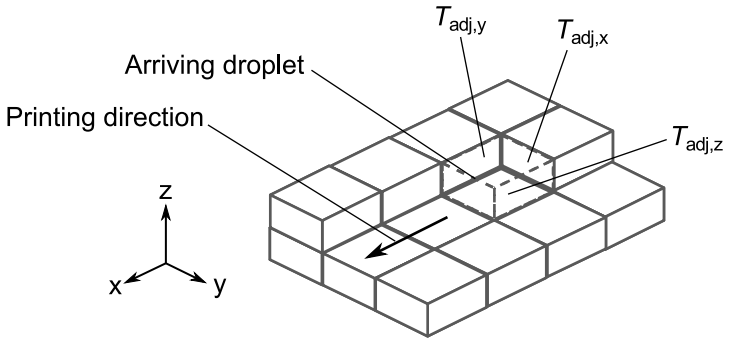

Figure 4.21: Evaluation of adjacent temperatures. The adjacent temperatures $T_{adj,x/y/z}$ of an arriving droplet are evaluated on the faces of neighbour droplets just before the droplet is initialised.

4.4.2 Model Setup

According to the samples produced for the experimental studies in this work, a simple cuboid geometry is used to study the influences of process parameters on the thermal field during a build-up process. Figure 4.22 shows the model setup for the parameter study. A nickle sheet (60 mm × 60 mm × 1 mm) serves as the carrier plate. A constant temperature boundary condition is applied to the surface of this sheet in negative z-direction with a heat transfer coefficient to the nickle sheet of $\alpha_s = 200\,\mathrm{W\,m^{-2}\,K^{-1}}$. To obtain this value a thermocouple was welded to the surface of the nickle sheet. Then the nickle sheet was brought into contact to the preheated build platform (500 °C). Assuming that the nickle sheet acts as a block capacity, the heat transfer coefficient between build platform and carrier plate can be calculated from the measured heating curve according to the relation $\tau = \rho c V/(\alpha A_c)$, where τ is the time constant and ρ, c, V, A_c are the density, specific heat capacity, volume and contact area (Polifke and Kopitz, 2009). Between the environment with a constant temperature $T_{env} = 100\,°C$ and the nickle sheet as well as the printed droplets a heat transfer coefficient of $\alpha_{env} = 20\,\mathrm{W\,m^{-2}\,K^{-1}}$ is used. This value was estimated for free convection and radiation of a horizontal plate according to (Polifke and Kopitz, 2009). The environmental temperature is measured in the experimental setup by a thermocouple in the printing chamber. It ranges from 60 to 160 °C depending on the temperature of the build platform and the printing time. As the influence of heat transfer to the environment is small owing to the small heat transfer coefficient, the value was set independent to the platform temperature to a constant average value of 100 °C.

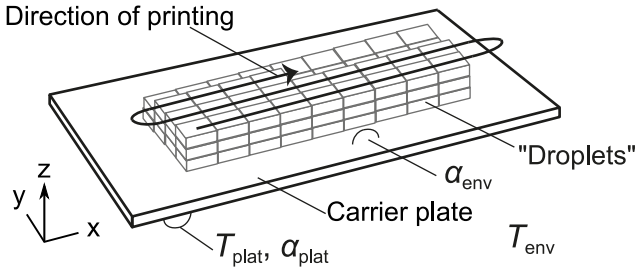

Figure 4.22: Model setup for the simulation study showing the order of droplet deposition and boundary conditions. According to Himmel et al. (2018)

Droplets are represented by a brick with 1.2 mm × 1.2 mm × 0.6 mm, which corresponds approximately the dimensions of a deposited droplet in the experiments. Droplets are deposited on the platform in alternating direction as indicated by the arrow. Each layer starts at the same position in the lower left corner. A delay of 1 s after each line and 7 s after each layer is considered. Those times were measured in the experiment and rounded to a full second.

Material properties are taken from the literature and were presented in table 4.4 in section 4.2. For numerical simulations a solidification interval of 5 K was introduced for AlSi12 ($T_{\mathrm{liq}} = 582\,^{\circ}\mathrm{C}$) and Al99.5Ti ($T_{\mathrm{liq}} = 665\,^{\circ}\mathrm{C}$), as a certain range of latent heat release is necessary for numerical stability. This is also physically valid, as only a high purity alloy with exact composition can really show a solidification point instead of a solidification range. In this study technical alloys are used, which contain impurities and will not exactly have the eutectic composition.

The computational mesh is a regular mesh with a cell size of 0.3 mm in all three dimensions. Consequently, each droplet is represented by $4 \times 4 \times 2 = 32$ cells. Equations for the temperature field are solved implicit with a maximum time step of $t_{\mathrm{period}}/20 = 10\,\mathrm{ms}$.

5 Results and Discussion

This chapter will first show the analysis of droplet characteristics as this will be necessary to further understand the details of all presented results. Next, the variation of thermal conditions, oxygen concentration and Weber number are presented and discussed separately. The variation of alloy composition is integrated in the variation of thermal conditions. In the final section 'Understanding the Droplet Deposition' all gathered results and the already published knowledge are brought together, to give an extensive view on the deposition of a single droplet.

5.1 Droplet Characteristics

Even though the droplet generation process is not the scope of this work, it is essential, for the interpretation of the final results, to understand the characteristics of the flying droplets. Hence, they were analysed based on high-speed camera records.

Results

Figure 5.1 shows a recorded sequence of a single droplet ejection. The times are given relative to the first image. Each pressure pulse ejects a series of smaller droplets that are moving in the same direction with almost the same velocity. They tend to coalesce to form bigger droplets as can be seen by the last two droplets in the sequence. After coalescence the formed droplet is oscillating as shown by the first droplet in the first image of the sequence. The last image was recorded 17 ms after the first one and shows a trailing satellite droplet, which is significantly smaller and also slower than the main droplet train. This satellite also tends to deviate in the direction of travel. As all of the droplets in the main train will arrive in the same position at almost the same time, they instantly coalesce to one droplet on the substrate. Thus, in the whole text outside of this section, 'droplet' describes the material ejected by one pressure pulse that forms one droplet on the substrate. Small satellites will not always coalesce with the main droplet, as they arrive in a different location or as they are already solidified upon arrival.

The recorded image sequences are used to calculate the droplet velocity. Figure 5.2 presents the measured droplet velocity against the set pressure at the inlet of the solenoid valve (see Figure 4.7). For sufficiently high pressures, the velocity follows an almost linear dependency. At pressures above 2.5 bar the ejected material could not be analysed properly for valve opening

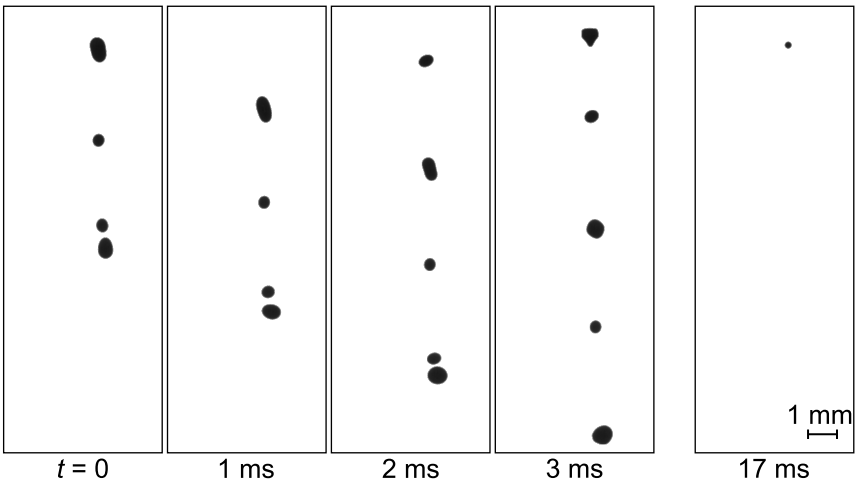

Figure 5.1: Sequence of single droplet ejection recorded by the high-speed camera. Each pressure pulse ejects a series of droplets flying in the same direction with the same velocity and occasionally trailing satellites that are significantly smaller and slower.

times of 6 ms. Thus, a second series with a valve opening time of 3 ms time was measured. In this series no results were obtained at pressures below 2 bar. Generally, the opening times do not have a significant effect on the droplet velocity, only on the ejected volume.

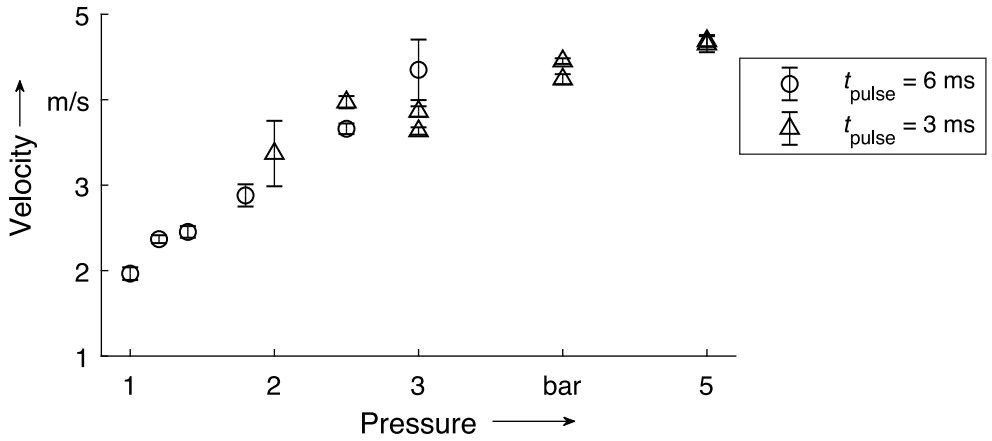

Figure 5.2: Droplet velocity against pulse pressure as evaluated from high-speed camera records. The droplet velocity increases almost linearly with the pressure.

Each point in the plot represents the mean value of 20 droplet ejected in one sequence at 10 Hz. The error bars represent two standard deviations of these 20 droplets. Apart from the extreme configurations, the deviation inside one sequence is small, but there are clearly deviations between individual sequences, which were measured on different days.

In the rest of this thesis, results of droplet velocity variations are presented against the droplet Weber number. It is calculate from the measured velocity according to (Equation 2.4) with the

density of AlSi12 according to table 2.2, the droplet diameter of 1.18 mm as characteristic length and the surface tension of pure aluminium of 0.871 $\mathrm{N\,m^{-1}}$ according to Mills (2002).

Discussion

The whole train of droplets, which is ejected by a single pressure pulse, extends over a range of approximately 12 ms for the parameters used in most test setups. The major part of the ejected volume is contained in the first, bigger droplets over a time of 4 ms. According to Schiaffino and Sonin (1997a) the characteristic spreading time of a droplet is in the order of $d_{\mathrm{drop}}/(2v_{\mathrm{drop}})$. In this case, with a droplet velocity of 2 $\mathrm{m\,s^{-1}}$ and a droplet diameter of 1.2 mm the spreading time would be in the order of 0.3 ms and therefore one order of magnitude faster than the time of droplet arrival. The droplet spreading process of this droplet train will therefore differ significantly from the spreading process of a single droplet of the same size.

To understand how the fragmentation of the fluid volume in several subdroplets instead of one single droplet affects the process of droplet impingement, one needs to image the ideal case of a fluid on a flat substrate without solidification. A continuous stream of small droplets with short distances between each other is feeding a bigger droplet that spreads on the substrate. Now as seen from the bigger droplet forming on the substrate, a continuous supply of fluid would force the droplet to spread further and further. In that case, the spreading time is not any longer $d_{\mathrm{drop}}/(2v_{\mathrm{drop}})$, but the time of small droplet arrival. It can be assumed that the fragmentation of droplets in the experiments essentially increases spreading time by a factor of ten.

Another observation of the droplet characteristic is that satellites with low velocities and small diameters follow the main train of droplets. They are still visible in the final product as they usually do not fuse with the main droplet. The satellites will reduce density and accuracy of the final part. Figure 5.3 shows a SEM image of an AlSi12 droplet with a satellite on the surface and another one in the interface at the bottom.

To estimate the cooling of droplets during flight the loss of heat due to convection was estimated according to Polifke and Kopitz (2009). The assumptions for this estimation are as follows: A droplet of a constant temperature of 700 °C is flying for a distance of 8 mm through nitrogen at 1 bar and 100 °C with a velocity of 5 $\mathrm{m\,s^{-1}}$. The size of a droplet is calculated by the assumption that the main volume of one ejection is distributed in three droplets having a diameter of 0.8 mm. Material properties for aluminium are taken from table 4.4 and properties for nitrogen are taken from VDI (2013). The heat loss owing to radiation can be estimated to be less than 2 °C with an emissivity of the droplet of 0.1 according to Mills (2002) and the surface of three droplets with a diameter of 0.8 mm. The environment is assumed to be infinite compared to the droplet and

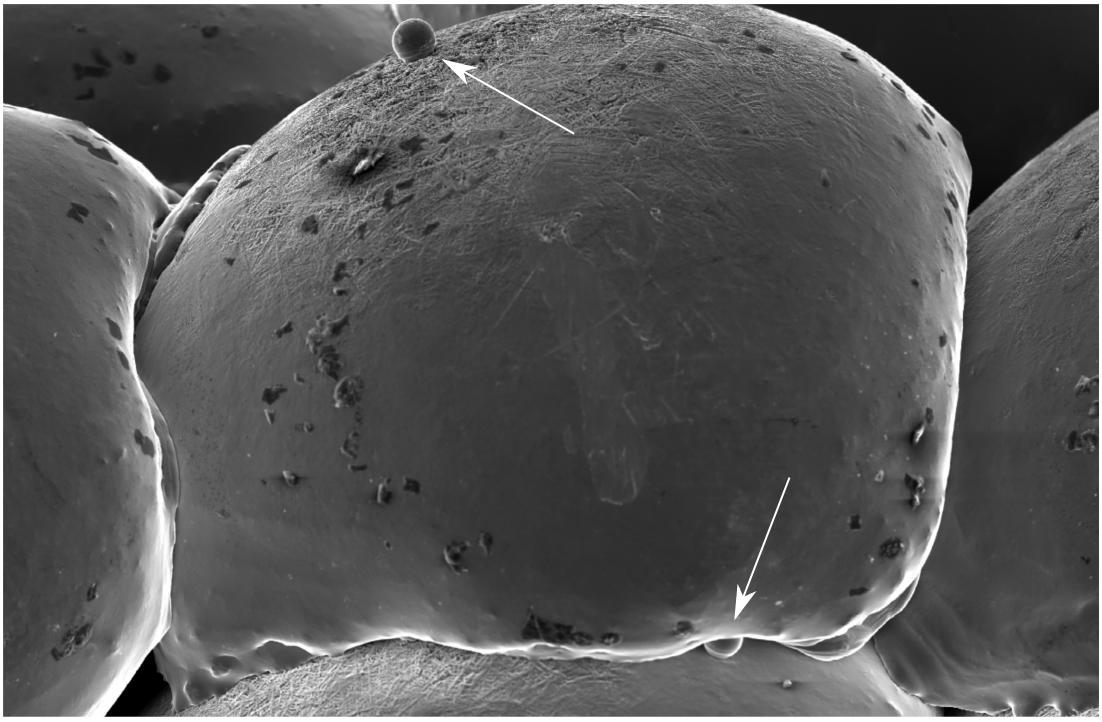

Figure 5.3: SEM images of AlSi12 droplet with satellites highlighted by white arrows. T_{subs} = 435 °C

has a temperature of 100 °C. Even though all estimations are rough, most of them are worst-case assumptions and one could hardly expect a droplet cooling of more than 10 °C. Accordingly, throughout the presentation of the results as well as in the discussion, the droplet temperature upon deposition is assumed to equal to the print head temperature ($T_{\mathrm{drop}} = T_{\mathrm{ph}}$).

5.2 Variation of Thermal Conditions

The variation of thermal conditions, mainly the substrate temperature, is the most important influence factor on the droplet-droplet bonding. It is most intensively studied throughout this work. First, the simulation results are analysed to see if the condition inside one specimen can be considered homogeneous and isotropic. Then the experimental results and their interpretation for the alloys AlSi12, AlSi5, AlCu5 and Al99.5Ti are presented.

5.2.1 Simulation Model of Laboratory Setup

After the validation of the simulation model against measured data, the influences of the main process parameters are presented and discussed.

Validation of Simulation Model

Simulations according to the experimental setup described in section 4.3.6 are performed. To compare the simulated solidification time to the measured values, the result 'local solidification time' provided by Flow3D for each cell is used. It measures the time that passed between liquidus and solidus temperature in the cell during cooling. The measurement method to obtain these values experimentally is described in section 4.3.6. Figure 5.4 compares the average simulated values of all cells representing the 32 droplets of the first line in the sixth layer with the average measured solidification time obtained from experiments. The results show a good agreement between simulation and experiment. Therefore, the simulation is capable to determine the influences of process parameters despite the simple setup, rough estimations of droplet shape and the neglect of fluid motion. It cannot clearly be stated, where validity limits of the chosen simulation setup are, but once the droplet shape is significantly influenced by the temperatures it might not be valid anymore. This is the case, if adjacent material is still liquid, when a new droplet arrives, because then it will fuse with the existing material in the liquid state and probably result in a significantly different shape compared to that defined in the model setup.

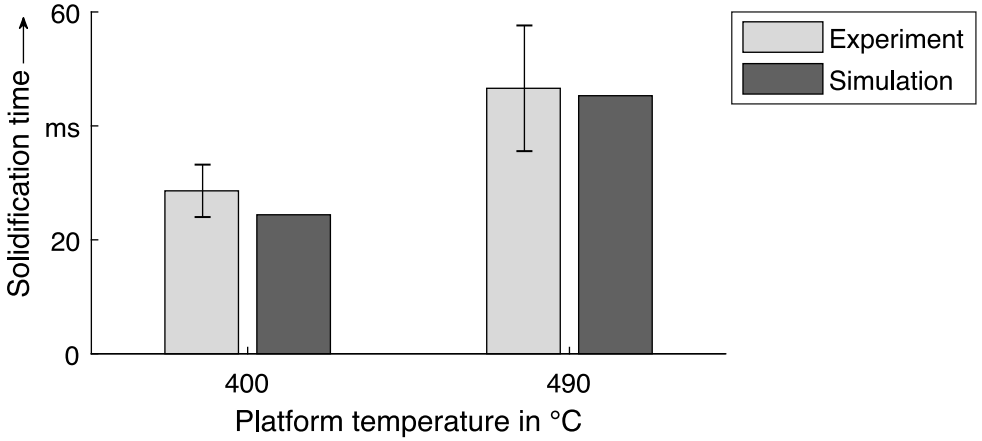

Figure 5.4: Simulation validation: Measured solidification times compared to simulated values. The error bars show two standard deviations of the measured values. The simulation correlates well with the measured solidification times. Reprinted with permission from Springer Nature: Himmel et al. (2018), ©2018

Simulation Results

To analyse local thermal conditions during the experiments, simulations of the build-up of similar cuboid blocks were performed. The cuboids consist of $32 \times 5 \times 8$ droplets (38.4 mm × 6 mm × 4.8 mm). Two factors were varied in the experiments: platform temperature T_{plat} and droplet temperature T_{drop}. A full factorial design with 12 setups was simulated: T_{plat} =

300, 400, 500, 550 °C and T_{drop} = 650, 700, 750 °C. The printing frequency is 5 Hz. The alloy for the presented results is AlSi12.

Figure 5.5 shows $T_{adj,x}$ and $T_{adj,z}$ for the complete build job with the highest (T_{plat} = 550 °C, T_{drop} = 750 °C) and lowest (T_{plat} = 300 °C, T_{drop} = 650 °C) temperature combination. $T_{adj,y}$ will always be between $T_{adj,x}$ and $T_{adj,z}$, as the adjacent temperatures are controlled by the cooling time. Hence, the temperatures in y-direction are not shown in the plots to improve clarity. While in the 'cold' setup temperatures slowly increase, they slowly decrease in the 'hot' setup. The mean value of adjacent temperatures is always some degree higher than the platform temperature. Within each layer, temperatures are rising from the first to the last line.

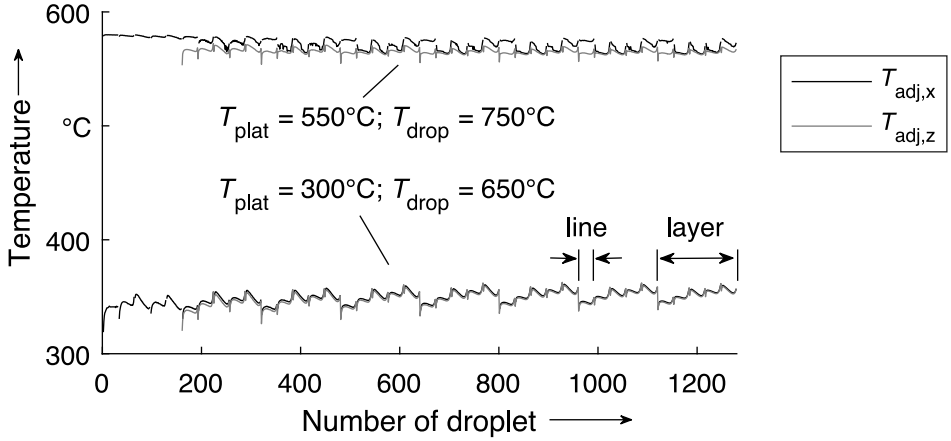

Figure 5.5: Simulated adjacent temperatures for a complete build job in the laboratory model. Comparison of $T_{adj,x}$ and $T_{adj,z}$ of the highest and lowest temperature combination.

To discuss the experimental results, it is helpful to know the mean adjacent temperatures within one specimen and also the maximum deviation from this mean. As the experimental evaluation does not consider the first layer and also not the beginning and ending of each line, the mean values and maximum spread values are calculated without the first layer and without the first and last three droplets of each line.

Figure 5.6 presents the difference between the mean adjacent temperature and the platform temperature $T_{adj,m} - T_{plat}$ on the left and the maximum spread ΔT_{adj} on the right, depending on the platform and droplet temperatures. $T_{adj,m} - T_{plat}$ decreases from 50 °C at low platform temperatures to 15 °C at high platform temperatures. Droplet temperature has only a small effect on both results compared with the platform temperature. The maximum variation of adjacent temperatures in one cuboid decreases with the platform temperature until 500 °C and increases for 550 °C.

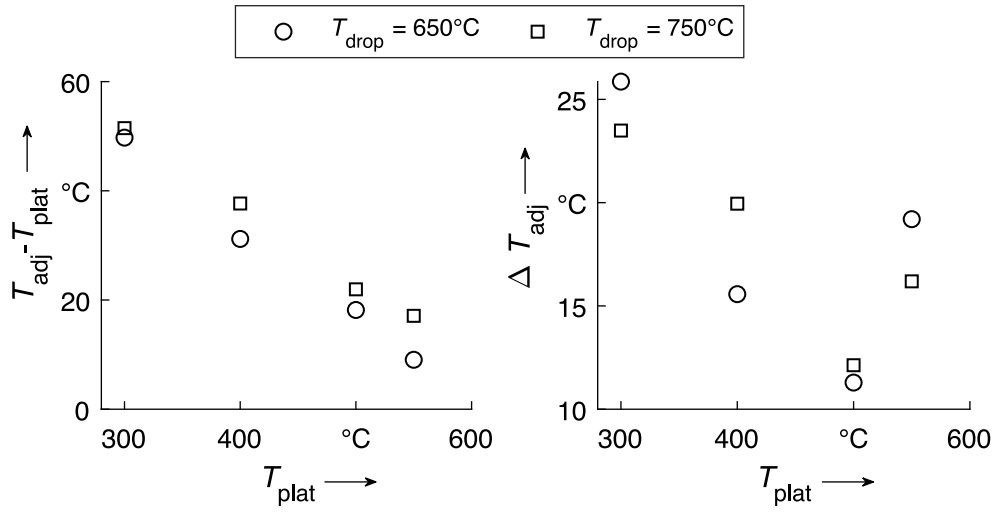

Figure 5.6: Effect of platform and droplet temperature on difference between mean adjacent and platform temperatures $T_{adj,m} - T_{plat}$ (left) as well as maximum adjacent temperature difference ΔT_{adj} (right).

Discussion of Simulation Results

The small increase respectively decrease of the mean temperatures throughout the printing process, shown in figure 5.5, can be explained by the low coefficient of heat transfer between nickle plate and build platform (200 W m^{-1} K^{-1}): For low platform temperatures, heat convection to the surrounding gas is low and the system therefore heats up, as not enough heat can be transferred to the build platform. For high platform temperatures a significant amount of heat can be transferred to the gas by convection and so the system cools when the surface of the cuboid grows. Nevertheless, those effects are small as the mean layer temperatures in x-direction decrease by about 10 °C for the 'hottest' setup and increase by the same amount for the 'coldest' setup.

The temperature evolution within one layer can be explained by the influence of two parameters: The size of the contact area of each droplet to adjacent material and the time that passed since the deposition of this adjacent material. The first droplet of each layer has only contact with one neighbour, the remaining droplets of the first line and the first droplets of the following lines have contact with two neighbours and all other droplets of one layer have contact with three neighbours. A greater contact area to solid material leads to higher cooling rates.

As each layer is build in the same sequence, the time that has passed since the deposition of adjacent droplets in z-direction is constant. Still, the first droplet in each layer will fall on the coldest material and will transfer heat to it and the surrounding material. In consequence, the

successive droplets fall on preheated material and the temperatures $T_{adj,z}$ show a steep increase at the beginning of each layer.

The explanation for the difference between platform and substrate temperature is straight forward: At high platform temperatures, the heat can mainly be transferred to the cold surrounding gas. Hence, less heat is conducted to the build platform and the temperature difference between part and platform becomes small.

Owing to a high latent heat of fusion, the greatest share of heat is transferred from the droplet to already build material in the freezing range of the alloy (577 to 582 °C). And as the temperature variations within one build job ΔT_{adj} are caused by cooling during pause times and heating during printing times, the variations are high, when the platform is significantly colder than the solidus temperature. At 550 °C the first line of each layer remains liquid during printing, as adjacent temperatures are still above solidus temperatures. At the same time the adjacent droplets in z-direction in the first line are comparably cold owing to the period without printing between two layers. Thus, ΔT_{adj} increases as soon as droplets do not fully solidify between two depositions. In this case we expect those droplets to merge to a coherent line.

For the experiments we can conclude that:

- All adjacent temperatures for all droplets of one cuboid are within ±15 °C, when the first layer and the beginning and ending of each line are ignored. This is valid, as the borders of the cuboids are not taken into account in the experimental evaluation.
- The mean adjacent temperatures are some degree higher than the build platform temperature. This deviation will be considered during the experimental evaluation. Evaluation of printed specimens will be presented against T_{subs} instead of T_{plat}, with $T_{subs} = T_{adj,m}$.
- The droplet temperature has only little effect on the adjacent temperatures.

5.2.2 AlSi12

The eutectic alloy AlSi12 was most intensively studied though out this work, as it yielded analysable results over the greatest range of parameters. Results for this alloy were obtained by the analysis of microstructure, SEM images, evaluation of relative density and tensile tests. Some of the results of AlSi12 were already published in the Rapid Prototyping Journal (Himmel et al., 2019).

Results

Figure 5.7 shows images taken from a cuboid printed at $T_{\text{subs}} = 520\,°\text{C}$ and one printed at $T_{\text{subs}} = 565\,°\text{C}$. While droplets solidify individually at 520 °C, they merge to line-wise solidification at $T_{\text{subs}} = 565\,°\text{C}$. That matches well with the prediction of the simulation model.

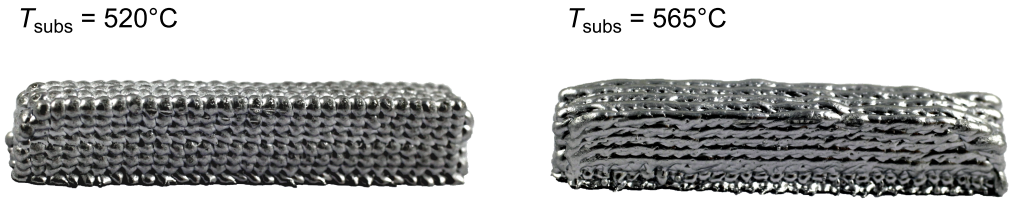

Figure 5.7: Images of cuboids printed at $T_{\text{subs}} = 520\,°\text{C}$ and 565 °C. While droplets solidify individually up to $T_{\text{subs}} = 520\,°\text{C}$, they merge to continuous lines at $T_{\text{subs}} = 565\,°\text{C}$.

To analyse the droplet shape and microstructure in printed parts, images of micrographs made by optical microscope and images of the surface made by a scanning electron microscope (SEM) are presented. To describe the circumstances, droplets will be labelled ‘first’ and ‘second’, meaning that the first droplet was deposited earlier than the second droplet. The surface and microstructure of each droplet changes from the surface, where the droplet comes into contact with already printed material and the free surface, where the droplet is only in contact with the surrounding gas. Those directions will be called ‘bottom’ and ‘top’. In figure 5.10 the labels are shown in the figure representative of all following figures.

Figure 5.8 shows a SEM image of AlSi12 printed at a substrate temperature of 350 °C. Apart from some impurities, the surface of the droplet is free of any structure in the bottom and shows dendrite tips at the top. A macroscopic contact angle greater than 90° is visible, but on both sides a ‘foot’ close to the neighbour droplet can be seen. The contact angle of this ‘foot’ is about 90° as shown in magnification.

To study the effect of the substrate temperature, figure 5.9 shows the same details for a part printed at $T_{\text{subs}} = 520\,°\text{C}$. The amount of surface with a dendritic structure on the top is greater compared to figure 5.8. The ‘foot’ at the contact line disappears and the macroscopic contact angle is equal to the microscopic one, both approximately 90°.

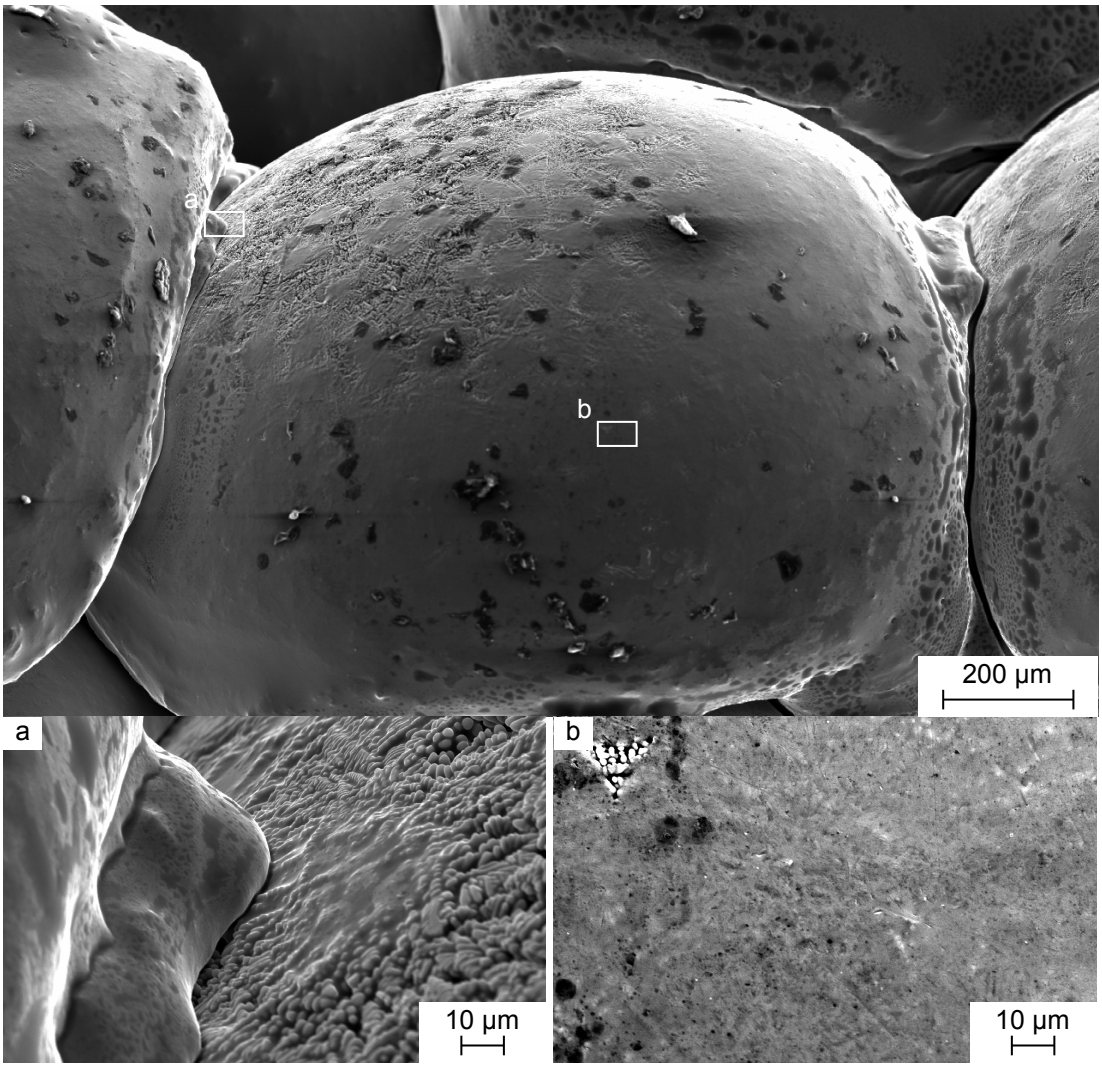

Figure 5.8: SEM images of an AlSi12 droplet at $T_{\mathrm{subs}} = 350\,^{\circ}\mathrm{C}$ *Droplet overview and magnifications of the contact area (a) and unstructured part of the surface (b).* $T_{\mathrm{drop}} = 700\,^{\circ}\mathrm{C}$

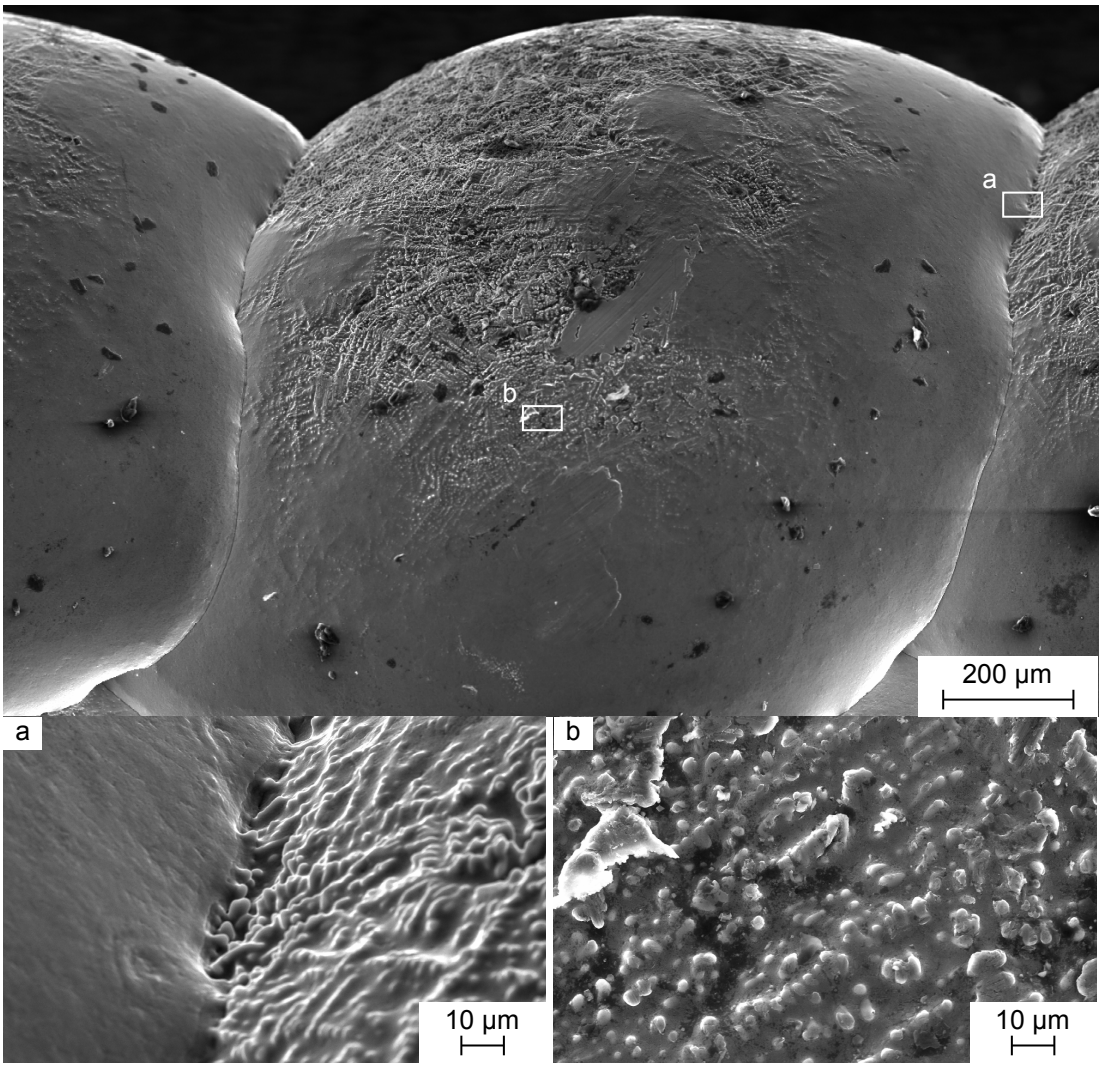

Figure 5.9: SEM images of an AlSi12 droplet at 520 °C substrate temperature: Droplet overview and magnifications of the contact area (a) and part of the surface (b). $T_{\mathrm{drop}} = 700\,^{\circ}\mathrm{C}$

Figures 5.10 and 5.11 show micrographs close to a droplet-droplet boundary of AlSi12 specimen for the variation of T_{drop} and T_{subs}. In all cases a highly dendritic structure is apparent. Each droplet shows a gradient in the fineness of the microstructure: At the bottom, where it first comes into contact with a neighbour droplet a fine structure is formed, which gradually gets coarser to the top, where the solidification ends. All images show the two extremes in each droplet: the top of the first droplet in the lower left corner of the image and the bottom of the second droplet in the upper right corner. While the droplet temperature does not show an effect, the substrate temperature changes the microstructure significantly. For lower substrate temperatures the dendritic structure is much finer, especially in the bottom. In the case of $T_{subs} = 350\,°C$ even a globular structure appears close to the interface. Lower substrate temperatures also yield a finer eutectic phase: While at 520 °C silicon and α-aluminium can still be resolved at the given resolution, the eutectic phase appears as a single tone of grey for 350 °C.

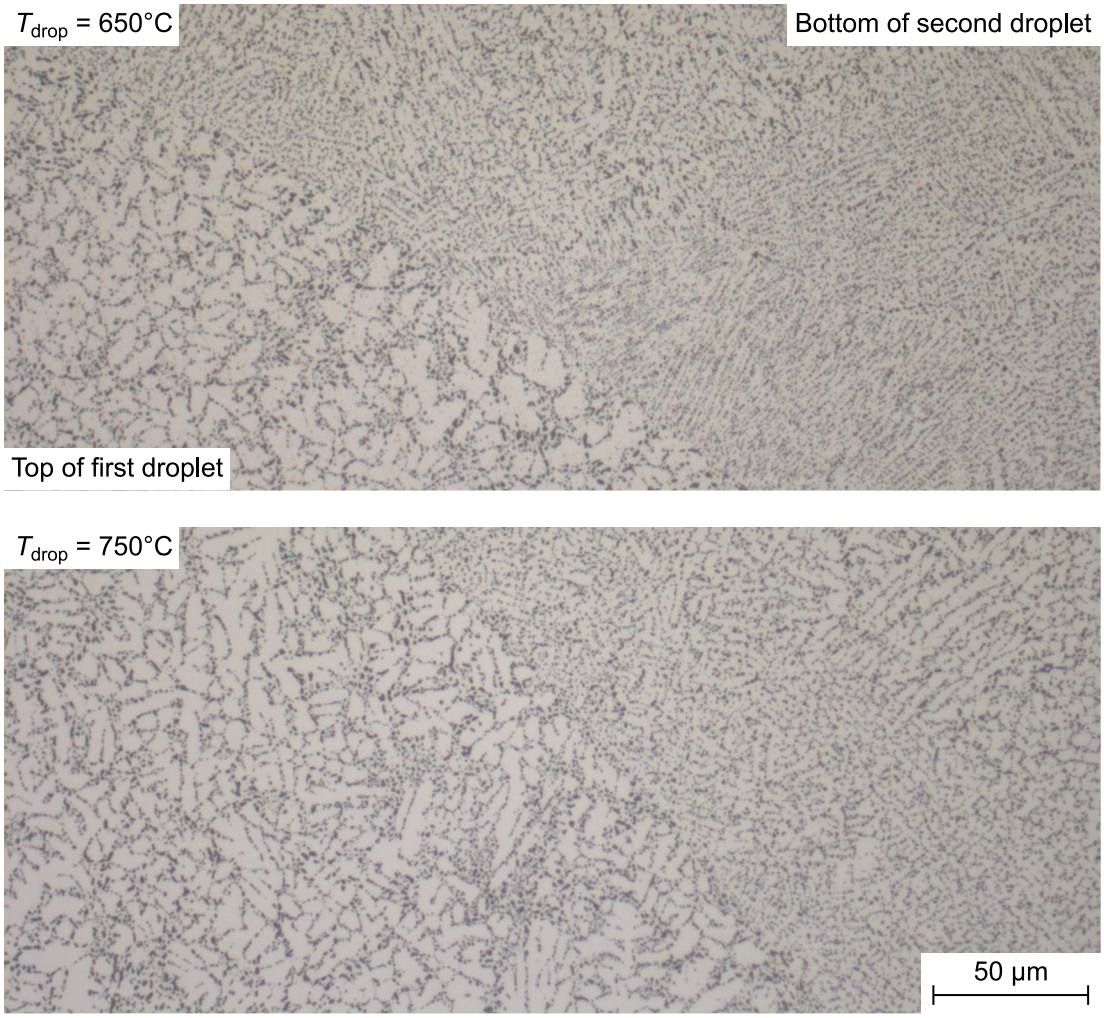

Figure 5.10: Micrographs of a droplet-droplet interface for AlSi12 at different droplet temperatures: Hardly any visible effect of droplet temperature. $T_{subs} = 435\,°C$

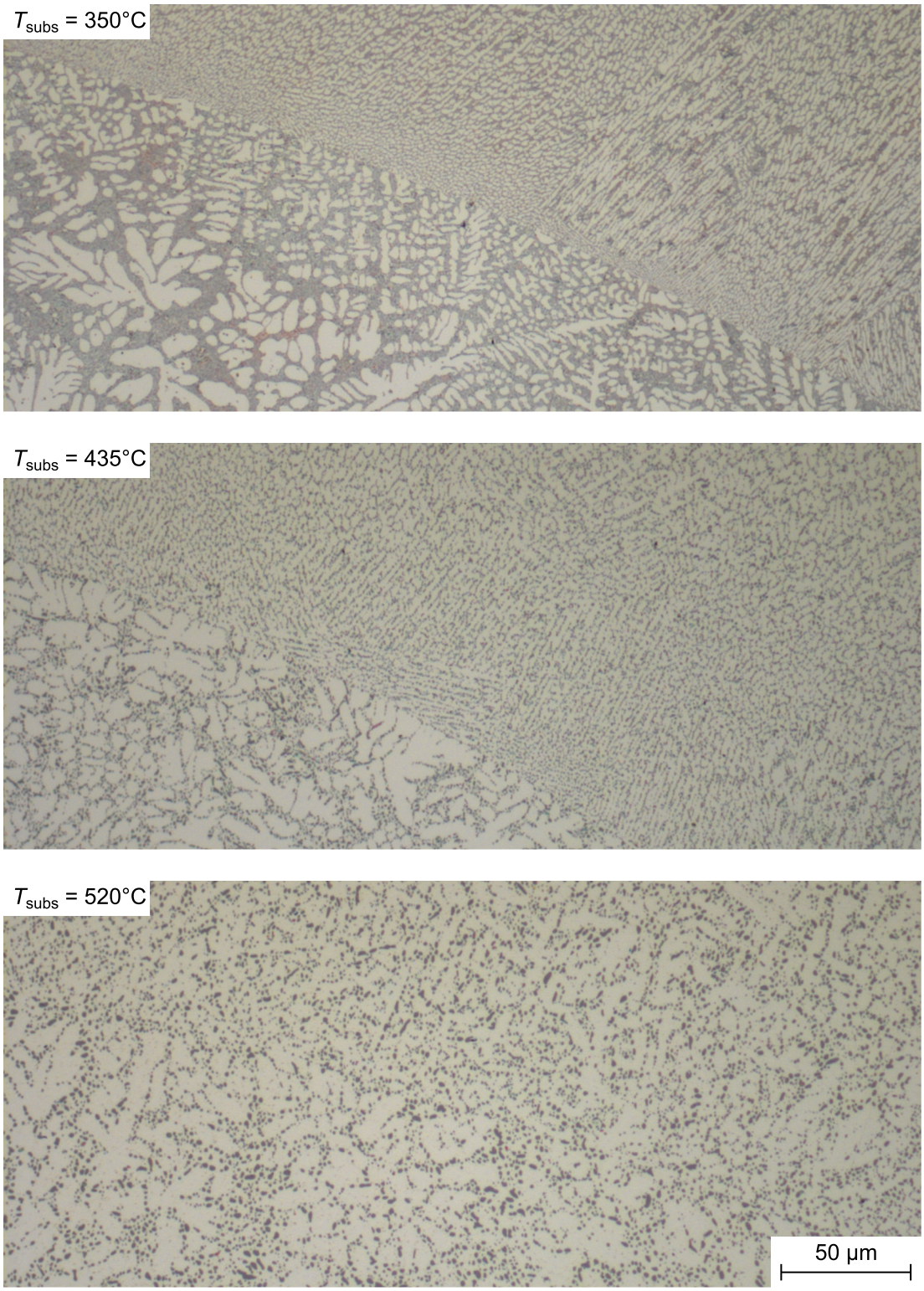

Figure 5.11: Micrographs of a droplet-droplet interface for AlSi12 at different substrate temperatures: The interface is visible owing to the sudden change in the microstructure. Lower substrate temperatures result in a higher gradient in microstructure and an overall finer eutectic phase. T_{drop} = 700 °C

As mentioned in section 2.3.4 the thermal conditions during droplet impact influence the spreading and the post solidification shape of each droplet. Therefore, they also affect the amount and size of pores that remain between adjacent droplets. As an example, figure 5.12 shows two low magnified micrographs at different substrate temperatures. Bigger pores are located in the corners between three or more droplets and occasionally smaller pores are visible inside droplets. The size and amount of pores between droplets is reduced with a higher substrate temperature. That observation is generally true for all materials.

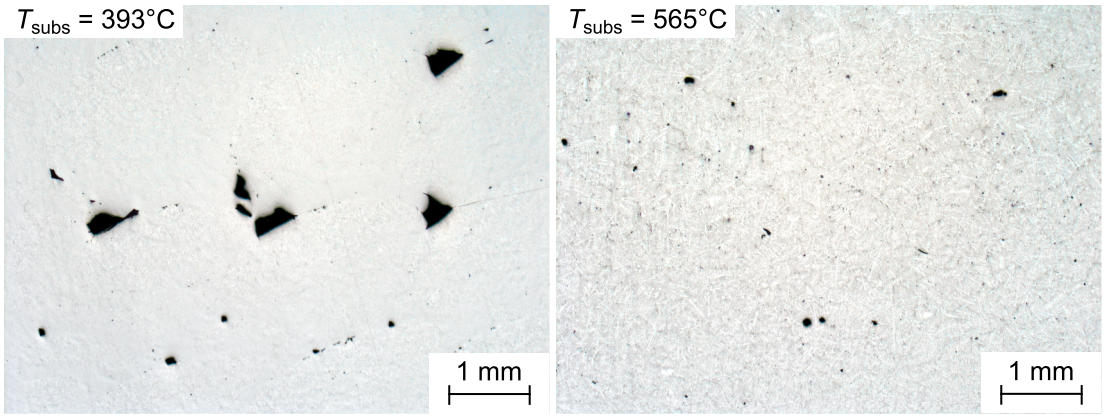

Figure 5.12: Micrographs showing the pores inside printed AlSi12: greater pores are mainly situated between three or more droplets and only seldom inside a droplet. Amount and size of pores reduce with a rising substrate temperature. T_{drop} = 700 °C

Figure 5.13 presents the relative densities for AlSi12 against the variation of substrate temperature and droplet temperature. The scatter of the data is comparably high, but nevertheless an increased density with an increased substrate temperature can be observed. The droplet temperature, on the other hand, has no significant effect. Relative densities between 93 and 99 % were measured. The highest value is measured in the case, that droplets fuse to coherent lines (see figure 5.7).

The results of tensile test evaluation uniform elongation, 0.2% offset yield strength and tensile strength, are presented in Figure 5.14. Owing to a high experimental effort, in most cases less than ten tensile specimens were tested under the same condition and in some cases even less than five. Moreover, the scatter of the data is high and it is therefore not presented by a mean value and a standard deviation but by individual measured values instead. A cast reference was produced by casting a block of 50 mm × 30 mm × 90 mm in an open steel die at room temperature. Specimens with the same dimensions as those manufactured from printed material were machined and tested. The cast reference results are presented as two grey dash-dot lines,

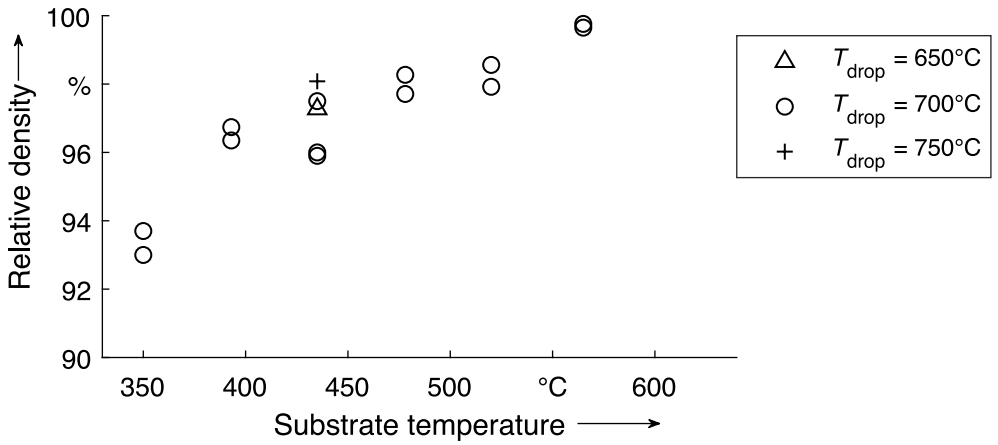

Figure 5.13: Relative density of printed AlSi12 against substrate temperature for droplet temperatures of 650 °C, 700 °C and 750 °C. While the substrate temperature increases the relative density significantly, the droplet temperature has no clear effect.

with one line at a standard deviation below the mean and one line at a standard deviation above the mean.

The elongation increases significantly with an increased substrate temperature from values below 1 % to values of 12 %. For a substrate temperature of 520 °C the uniform elongation is comparable to the cast reference. The droplet temperatures do not show a significant effect on the elongation, only in the case of T_{subs} = 520 °C a minor effect is noticeable. The yield strength decreases linearly from about 140 to 100 MPa with the substrate temperature. The lowest values are still slightly higher than the cast reference with a mean of 87 MPa. And the ultimate tensile strength is more or less stable over the whole range, but the scatter of the data decreases for higher substrate temperatures. No effect of the droplet temperature on either the yield strength or the uniform elongation is visible. Among all testes alloys, only for AlSi12 it was possible to machine tensile specimens from cuboids printed at the lowest tested substrate temperature. No specimens were made for substrate temperatures below 350 °C as the elongation was already close to zero.

Discussion

Tensile specimens could be evaluated for all tested conditions, so the lower boundary for T_{subs} was not reached. Figure 5.15 shows representative stress-strain curves of tensile specimens made from AlSi12 at different substrate temperatures.

First the cast reference is compared to the specimen printed at T_{subs} = 565 °C: The printed specimen has superior mechanical properties and even a higher elongation owing to the fact,

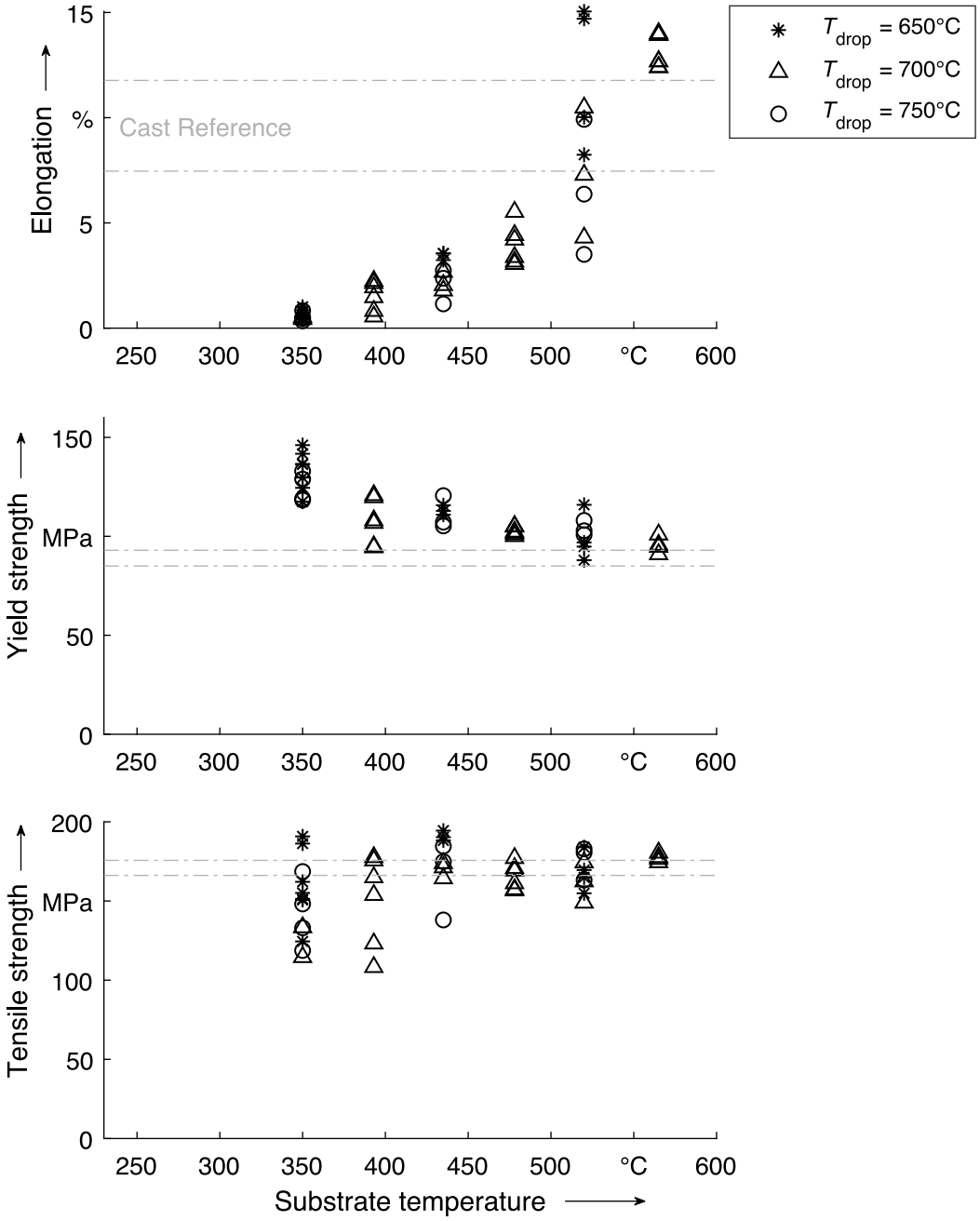

Figure 5.14: Tensile properties of printed AlSi12: The elongation increases significantly with the substrate temperature. The 0.2% offset yield strength decreases linearly with the substrate temperature and the ultimate tensile strength remains almost constant. The data scatter reduces with an increased substrate temperature. Cast reference shows the range of two standard deviations.

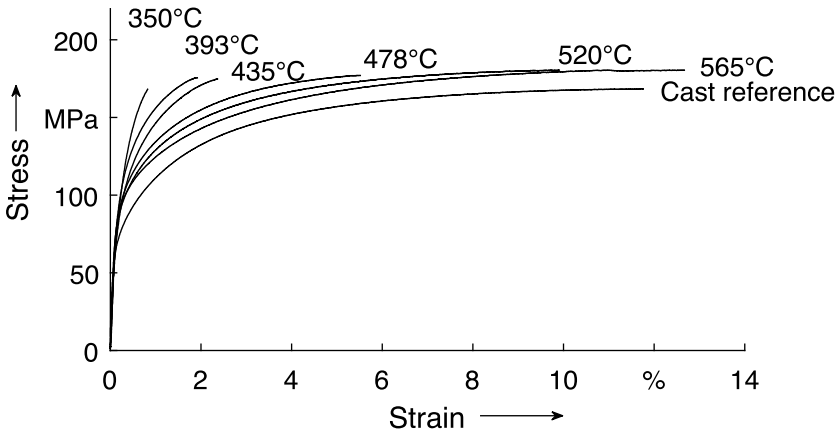

Figure 5.15: Stress-strain curves of AlSi12 for different substrate temperatures. With decreased substrate temperature the yield strength increases and the elongation decreases, while the ultimate tensile strength stays approximately constant.

that at the given conditions, the droplets will merge to form a line in the printing direction. As the tensile specimens are also tested in printing direction, there is essentially no limiting porosity, but the material benefits from the higher cooling rate and a finer eutectic phase, respectively. For lower substrate temperatures, the elongation reduces and the yield strength increases. That can be explained by two opposite effects: The size and amount of pores between individual droplets increases, but also the solidification rate increases and so the fineness of the eutectic phase (and also of the dendrites). A finer microstructure improves yield strength, elongation and ultimate tensile strength of Al-Si alloys. As the eutectic phase is much harder than the α-phase it bears the main part of the load and is therefore crucial to the mechanical properties. Moreover, the eutectic phase is sensitive to the solidification rate, so an alloy with a higher amount of eutectic phase will also be more sensitive to the solidification rate (Baumgartner, 2019; Pek, 1987). To summarise, the increased solidification rate induced by a cold substrate should improve all mechanical properties. But the pores between droplets have sharp edges at the droplet interfaces and serve as crack-initiators reducing the possible elongation. Consequently, the ultimate tensile strength remains constant over the substrate temperature.

Especially the elongation data at $T_{\text{subs}} = 520\,°\text{C}$ shows a significant amount of scatter. When pores are responsible for crack initiation, then a single critical pore can lead to low elongation values. If a high amount of pores is present, a critical one will always be in the tested volume and the scatter is low. For higher substrate temperatures the amount of pores is reduced and some specimens will and others will not contain a critical pore and thus, the scatter increases.

Figure 5.16 compares SEM images taken from the fractured surfaces of specimens fabricated at $T_{\text{subs}} = 350\,°\text{C}$ and $520\,°\text{C}$. At the lower substrate temperature the droplet shape is clearly

visible and great parts of each droplet surface were not in contact with the neighbour droplet before fracture. In the centre of each droplet a fractured area is visible that indicates the area, which was in contact with the neighbour droplet. Probably not even 50 % of the area shows fracture marks and the real stress inside the material is therefore significantly underestimated by the macroscopic evaluation in a tensile test. Samples fabricated at $T_{\mathrm{subs}} = 520\,^{\circ}\mathrm{C}$ show a continuous fractured area without droplet-droplet interfaces over great parts, even though there are still some droplet interfaces visible. In contrast to the specimen printed at 350 °C those droplet interfaces have a rough surface, which means that they were also bound. The fact that the crack followed the droplet-droplet interface can have several reasons: The droplets may not have bound properly and the interface itself is an imperfection in the material. Another option would be that residual stresses have build up due to thermal contractions during rapid solidification. But the whole cuboid is held at 520 °C for the complete printing process, which should release residual stresses. The last and most likely option is that the crack propagates close to the interface in the 'first' droplet as the discontinuity in the microstructure at the interface will concentrate the stress.

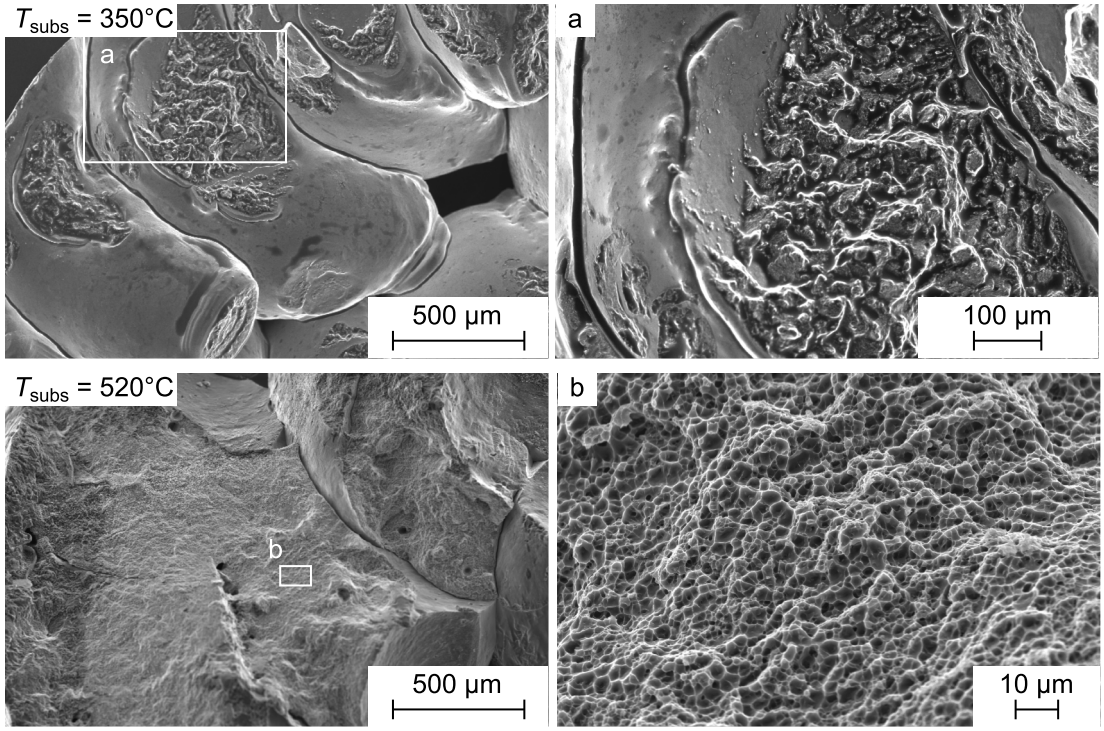

Figure 5.16: SEM images of fracture surfaces comparing tensile specimens printed at $T_{\mathrm{sub}} = 350\,^{\circ}\mathrm{C}$ *and 520 °C: For low substrate temperatures only small parts of the droplet show a fractured surface, while for high temperatures, a great area shows fracture marks.*

5.2.3 AlSi5

Specimens fabricated from the hypo-eutectic alloy AlSi5 were analysed by micrographs, SEM images, tensile tests and density evaluation. The results will be presented and discussed in the following section compared to the eutectic composition.

Results

Figure 5.17 shows the measured relative density of AlSi5. A comparable range of densities is measured but on a significantly smaller range of substrate temperatures compared to AlSi12.

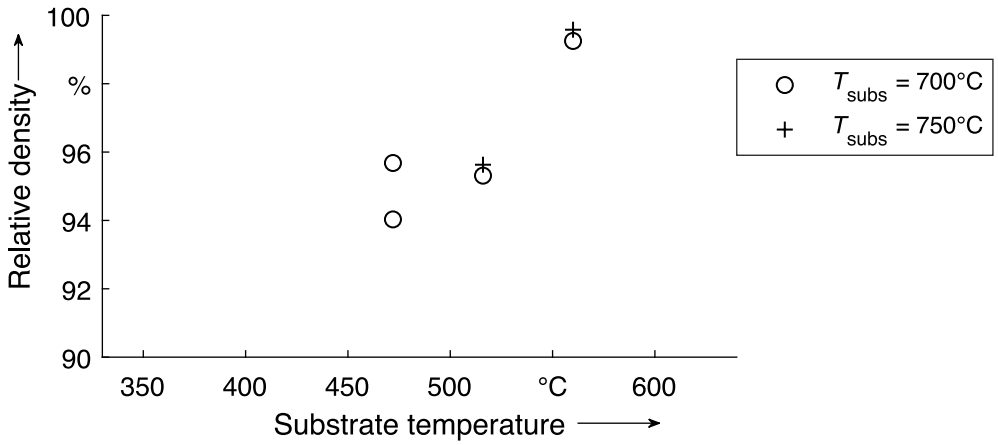

Figure 5.17: Relative density of printed AlSi5 against substrate temperature for droplet temperatures of 700 °C and 750 °C. The substrate temperature increases the relative density significantly.

Figure 5.18 compares the microstructure at the interface of droplets deposited at T_{subs} = 516 °C and 560 °C. The structure at 516 °C is comparable to that of AlSi12 deposited at the same temperature (see figure 5.11): The interface can hardly be seen and the microstructure at the bottom and at the top of each droplet are comparable. But in the case of AlSi5 the amount of α-dendrites is significantly higher. For T_{subs} = 560 °C the interface is clearly visible in the z-direction (between layers), as the microstructure at the top of the first droplet changed and is now mainly consisting of eutectic phase with some coarse silicon particles. There is no visible interface between two droplets in the direction of printing (x-direction). This is only the case for AlSi5 at T_{subs} = 560 °C. For all other configurations, there are no differences between interfaces in x- or z-direction.

Compared to AlSi12, the surface of a droplet from AlSi5 in figure 5.19 has a rougher surface almost without any smooth areas. The magnification of the surface shows a fully dendritic

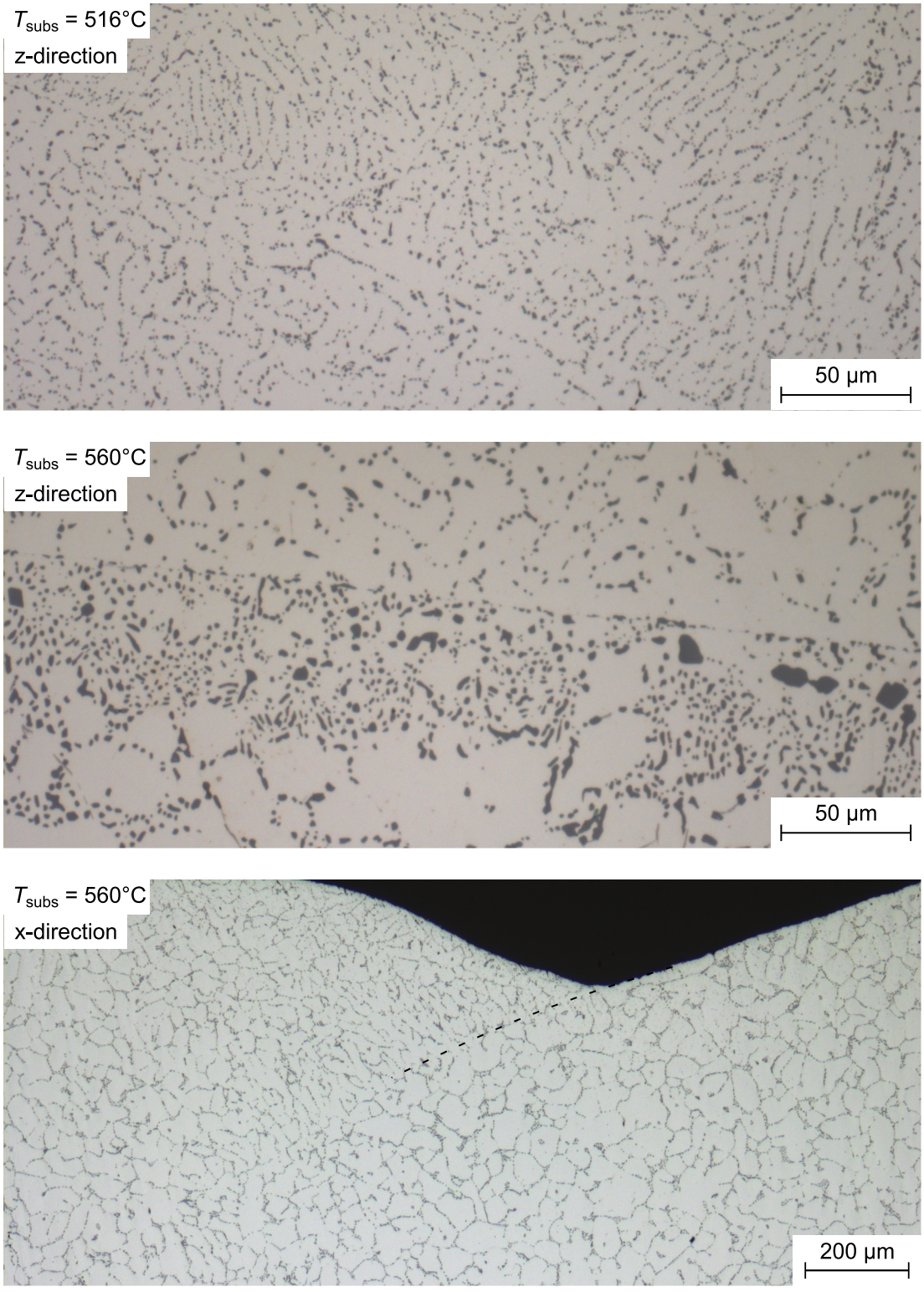

Figure 5.18: Micrographs of a droplet-droplet interface for AlSi5 at different substrate temperatures: At T_{subs} = 516 °C the interface can hardly be seen. At T_{subs} = 560 °C a layer with more silicon phase is apparent in the lower droplet at the interface perpendicular to the printing direction (z). In printing direction (x) no interface is visible. T_{drop} = 700 °C

structure and in comparison to AlSi12 the inter-dendritic spaces appear to be empty. Here again the droplet has a ‘foot’ at the contact line with an contact angle of about 90° and the apparent macroscopic contact angle is greater than that.

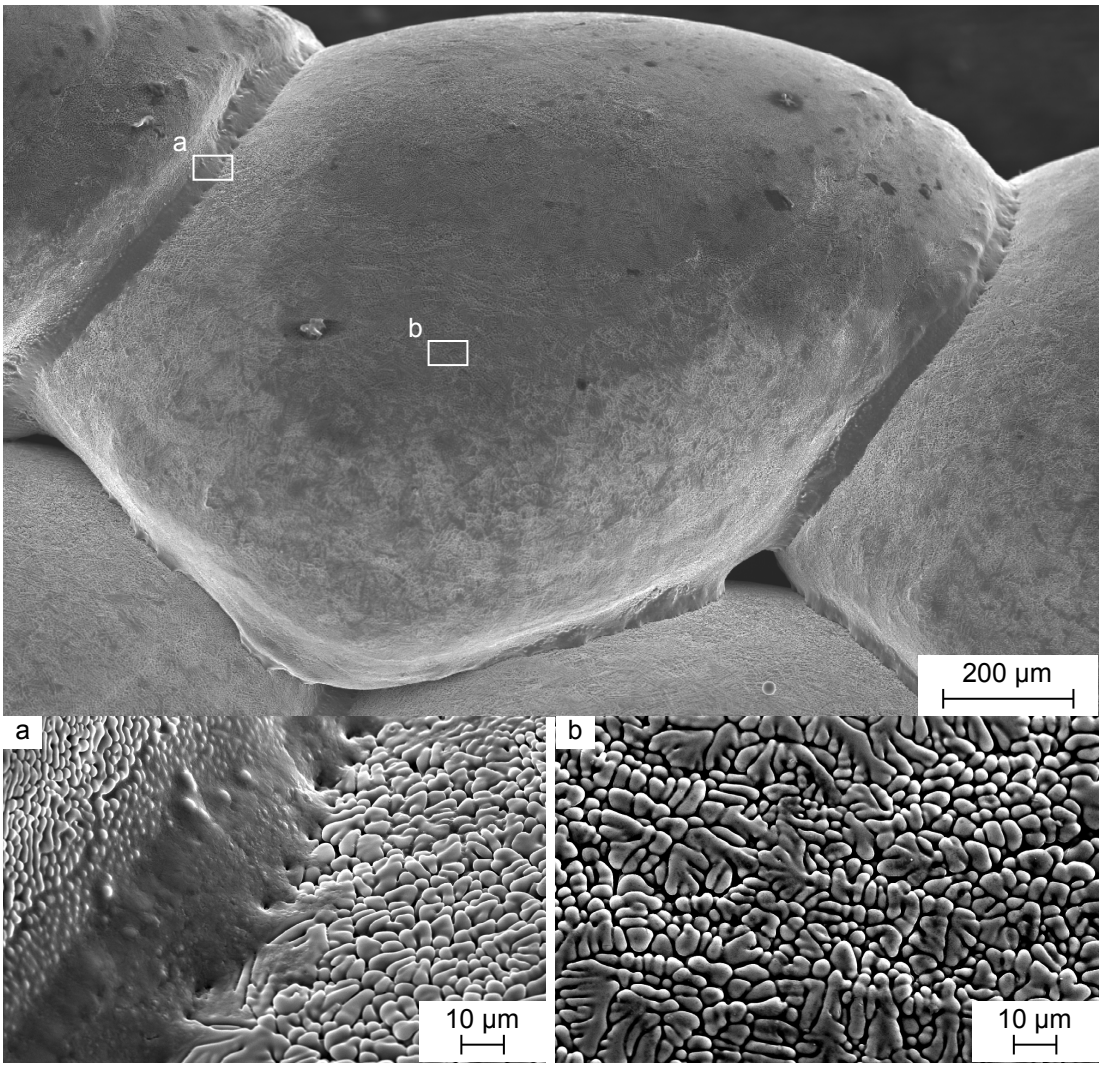

Figure 5.19: SEM images of an AlSi5 droplet at 516 °C substrate temperature: Droplet overview and magnifications of the contact area (a) and part of the surface (b). T_{drop} = 700 °C

Figure 5.20 shows the properties of AlSi5 as measured in the tensile tests. Cuboids fabricated at substrate temperatures below 472 °C could either not be removed from the nickle plate or could not be machined without breaking. Again, the uniform elongation increases with the substrate temperature to values above 15 %, which is more than measured for the cast reference. No effect of the droplet temperature can be seen. Yield strength increases slightly with the substrate temperature and is not affected by the droplet temperature. Still almost all measured values

lie above the mean yield strength of the cast reference. The tensile strength increases with the substrate temperature to values well above the cast reference.

Discussion

For this alloy, specimen could only be fabricated for substrate temperatures of at least 472 °C. In contrast to AlSi12, the yield strength is almost constant over the substrate temperature, which is in agreement with Pek (1987), as this alloy has a low amount of eutectic phase. At higher cooling rates, finer dendrites and a finer eutectic phase form (see figure 5.18). But as the eutectic phase is incoherent, it can not transfer load on a macroscopic scale and the α-phase does not benefit from higher cooling rates.

The relative density increases steeply with the substrate temperature and the uniform elongation increases accordingly. For a material with otherwise constant properties, an increased uniform elongation also yields an increased ultimate tensile strength.

Figure 5.18 shows coarse silicon particles at the 'top' of the 'first' droplet in z-direction. Owing to high solidification rates, the α-dendrites are supersaturated with silicon. At $T_{\mathrm{subs}} = 560\,°\mathrm{C}$ the heat released by the 'second' droplet performs a heat treatment in the 'first' droplet, which results in a precipitation of silicon from α-dendrites and a coarsening of existing particles.

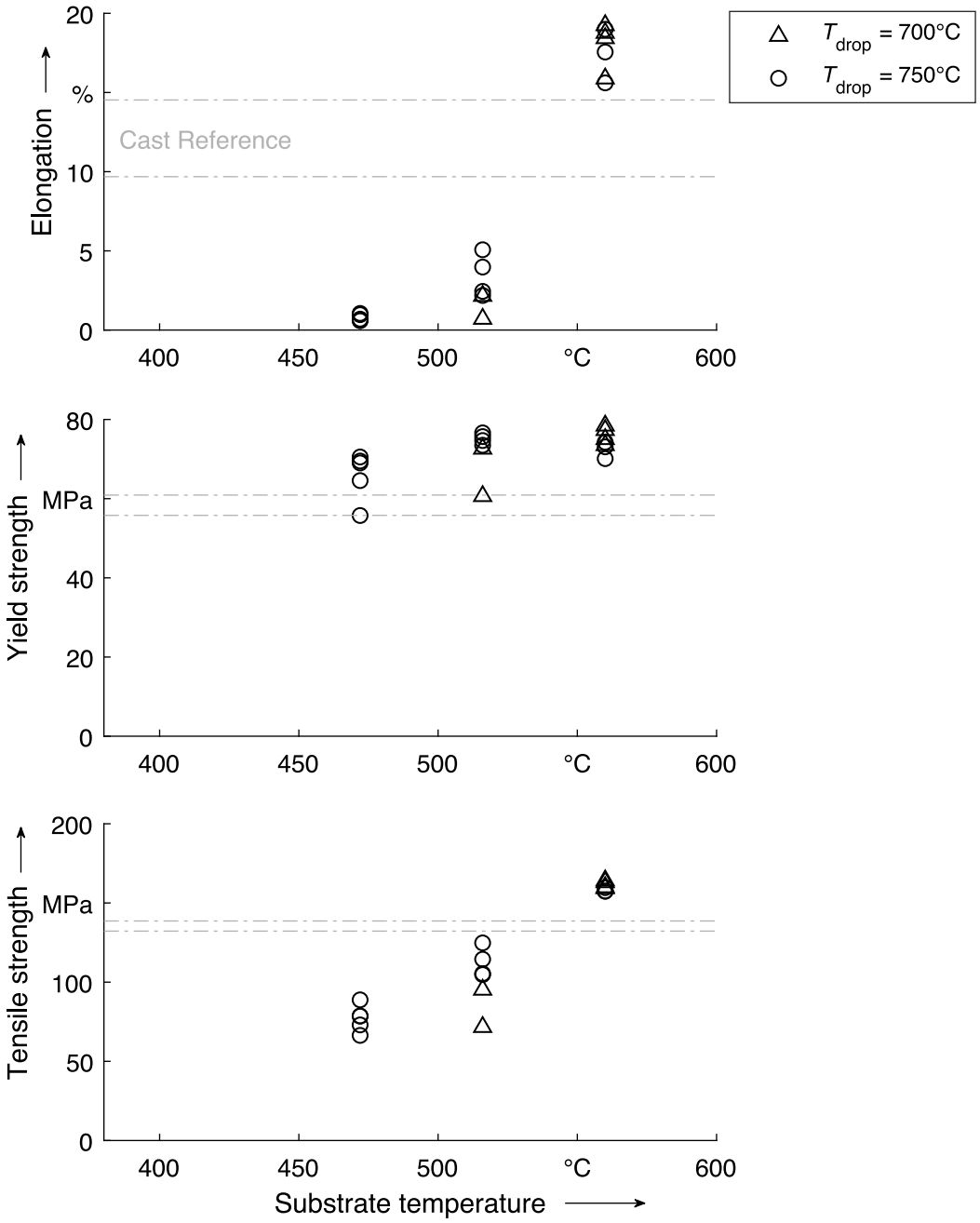

Figure 5.20: Tensile properties of printed AlSi5: The uniform elongation increases significantly with the substrate temperature. The 0.2% offset yield strength shows only a weak dependency on the substrate temperature and the ultimate tensile strength increases with the substrate temperature to values above the cast reference. Cast reference shows the range of two standard deviations.

5.2.4 AlCu5

This section presents micrographs, SEM images, density measurements and tensile test evaluations for the alloy AlCu5. The interpretation of those results is dominated by the state of precipitation hardening caused by the thermal history.

Results

Figure 5.21 presents the relative density. A even greater range of densities (90 to 99 %) compared to AlSi12 and AlSi5 is measured for a variation of the substrate temperature of only 42 °C.

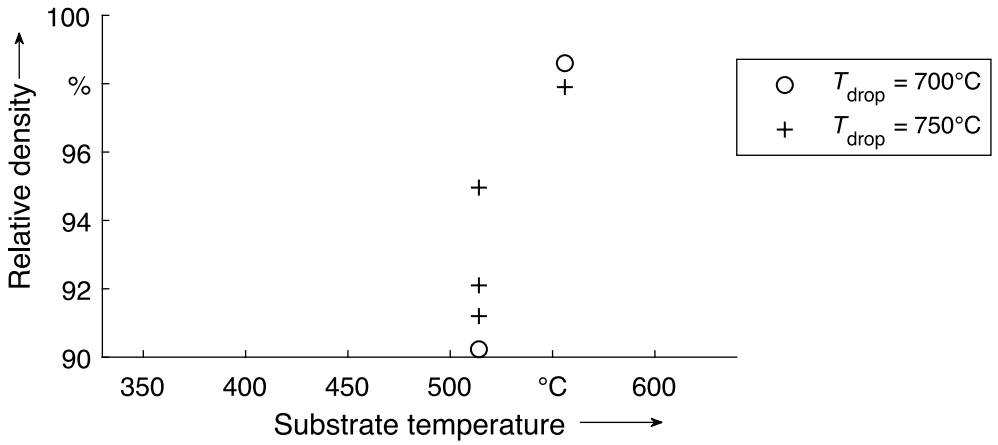

Figure 5.21: Relative density of printed AlCu5 against substrate temperature for droplet temperatures of 700 °C and 750 °C. The substrate temperature increases the relative density significantly.

Figure 5.22 shows two etched micrographs for the alloy AlCu5 printed at a substrate temperature of 514 °C and 556 °C. While for 514 °C the grains share a common grain boundary along the droplet-droplet interface, for a substrate temperature of 556 °C that boundary vanishes in some cases and grains extend over the interface. For lower substrate temperatures the grains are generally smaller and a fine distributed phase is present inside the grains of solid solution. Those particles of a second phase almost disappear for the higher substrate temperatures.

The SEM images in figure 5.23 show a completely smooth surface in the low magnification, but at a higher magnification, a dendritic structure becomes apparent. The macroscopic contact angle is significantly greater than 90° and comparable to AlSi12 at $T_{subs} = 350$ °C (see figure 5.8). Also in this case, a 'foot' forms at the contact line to the previous droplet. The contact line lies far behind the greatest extend of the droplet and is overhung by it.

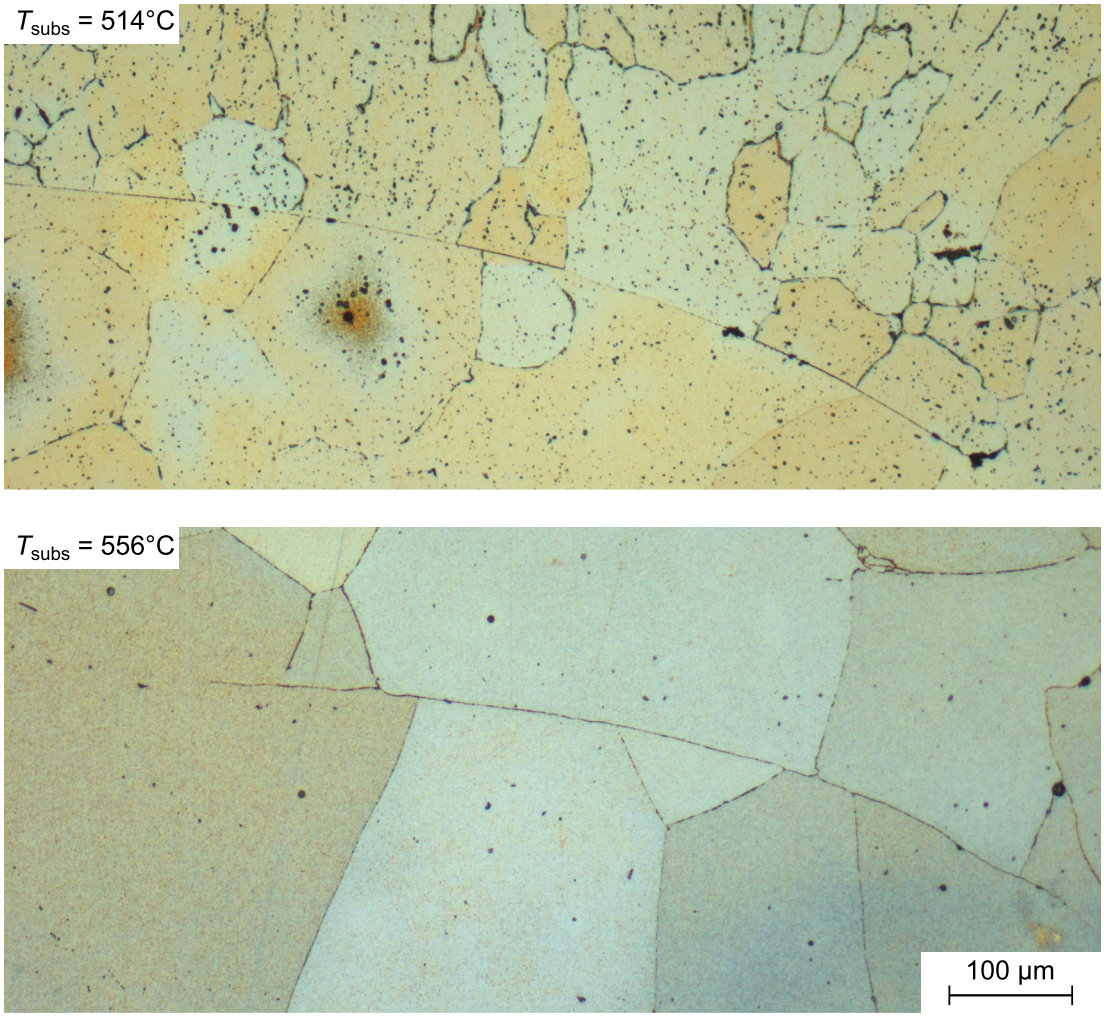

Figure 5.22: Micrographs of a droplet-droplet interface for AlCu5: At T_{subs} = 514 °C the interface is visible as a common grain boundary and a fine distributed phase is present inside the grains. At T_{subs} = 556 °C grains are bigger and extend over the interface. A smaller amount of a second phase appears inside the grains. T_{drop} = 750 °C

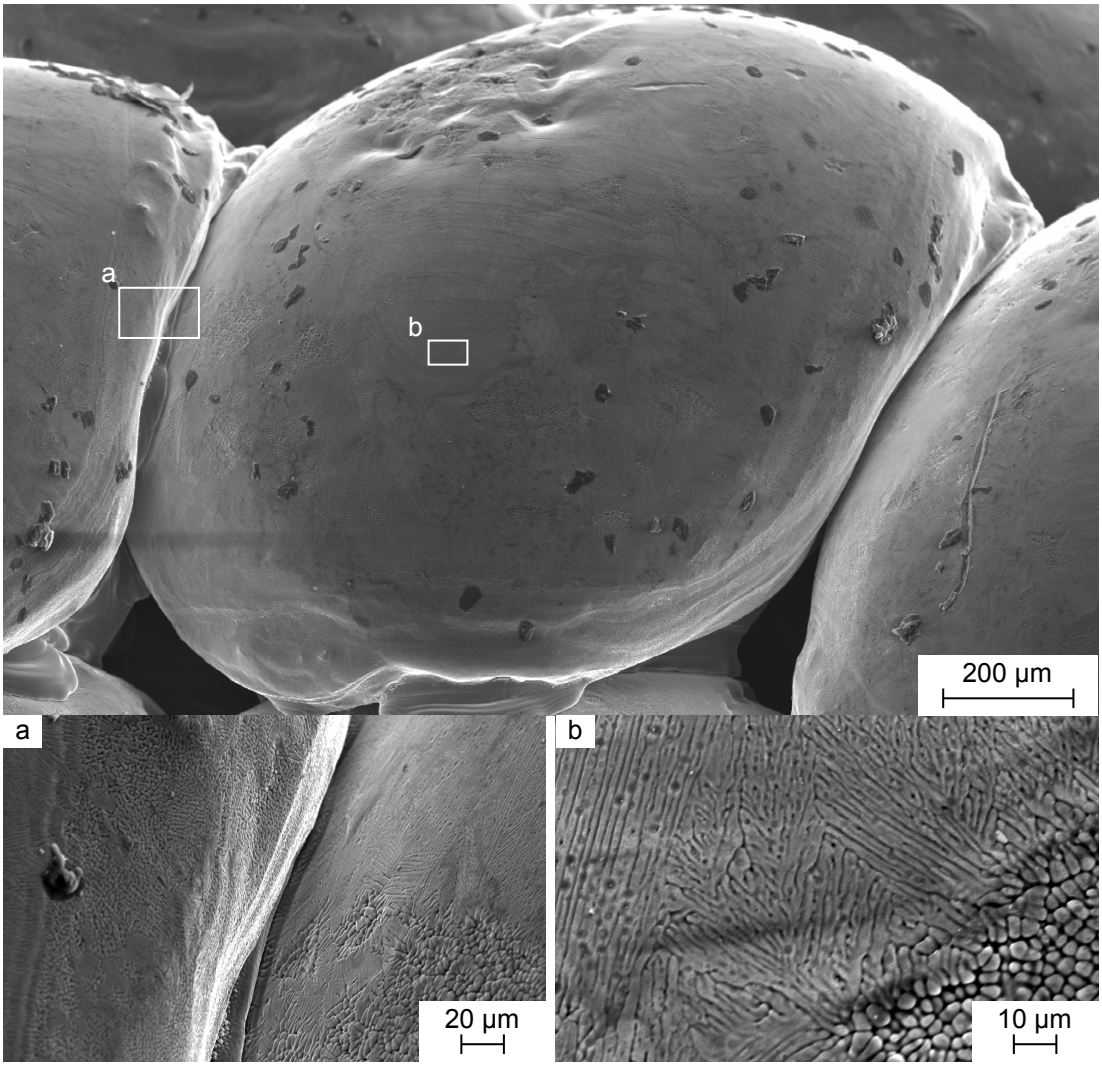

Figure 5.23: SEM images of an AlCu5 droplet at 514 °C substrate temperature: Droplet overview and magnifications of the contact area (a) and part of the surface (b). T_{drop} = 750 °C

The results of tensile tests for AlCu5 are shown in figure 5.24. Specimens printed at lower substrate temperatures than 514 °C failed during machining or while removing the cuboid from the nickle plate. For all properties the highest values are measured for a substrate temperature of 556 °C with about 8 % uniform elongation, 180 MPa 0.2% offset yield strength and 290 MPa ultimate tensile strength. While the elongation of the cast reference (8 %) is comparable to the maximal value of printed material, the yield strength (90 MPa) and the ultimate tensile strength (195 MPa) of the cast reference are lower than the maximum values of printed material. One outlier is visible at 514 °C.

Discussion

Interpreting the tensile tests for an aluminium-copper alloy is more complex than for an aluminium-silicon alloy, as it can be age hardened, so the thermal history of the blocks has to be considered.

Just as for AlSi12 and AlSi5, the relative density and uniform elongation increase with the substrate temperature. The density values are one or two percent lower than those of AlSi5 and have a comparable gradient. But here, unlike for aluminium-silicon alloys, the yield strength also increases with the substrate temperature. Consequently, the tensile strength increases steeply.

This behaviour can be explained by the form of the intermetallic Al_2Cu-phase: When the material is held at 514 °C the thermodynamic equilibrium state will be approached. At this temperature the solid solution contains about 3.2 wt.% copper. The remaining copper will form the stable and incoherent θ-phase inside the grains as well as at the grain boundary as it can be seen in figure 5.22. This phase is brittle and incoherent, so it weakens the material. After printing, the cuboids were air quenched and aged at room temperature during storage. The copper contained in the solid solution will form GP I-zones that harden the material to a certain grade.

In case of $T_{\mathrm{subs}} = 556$ °C the temperature is already 8 °C higher than $T_{\mathrm{sol}} = 548$ °C (binary Al-Cu phase diagram) so the copper is completely dissolved in the solid solution. There might also be some liquid fraction, but as the phase diagram is only valid for strictly binary compositions and the used alloy contains a plurality of impurities, it cannot clearly be stated if there is a liquid fraction. However, it can be ignore here. After quenching and cold ageing, a greater amount of GP I-zones will form as the copper concentration in solid solution was higher before quenching. Accordingly, the material will be hardened more by the precipitation and it is also free of the brittle θ-phase. These effects are stronger than the reduction of mechanical properties owing to coarser grains, which certainly form at higher substrate temperatures.

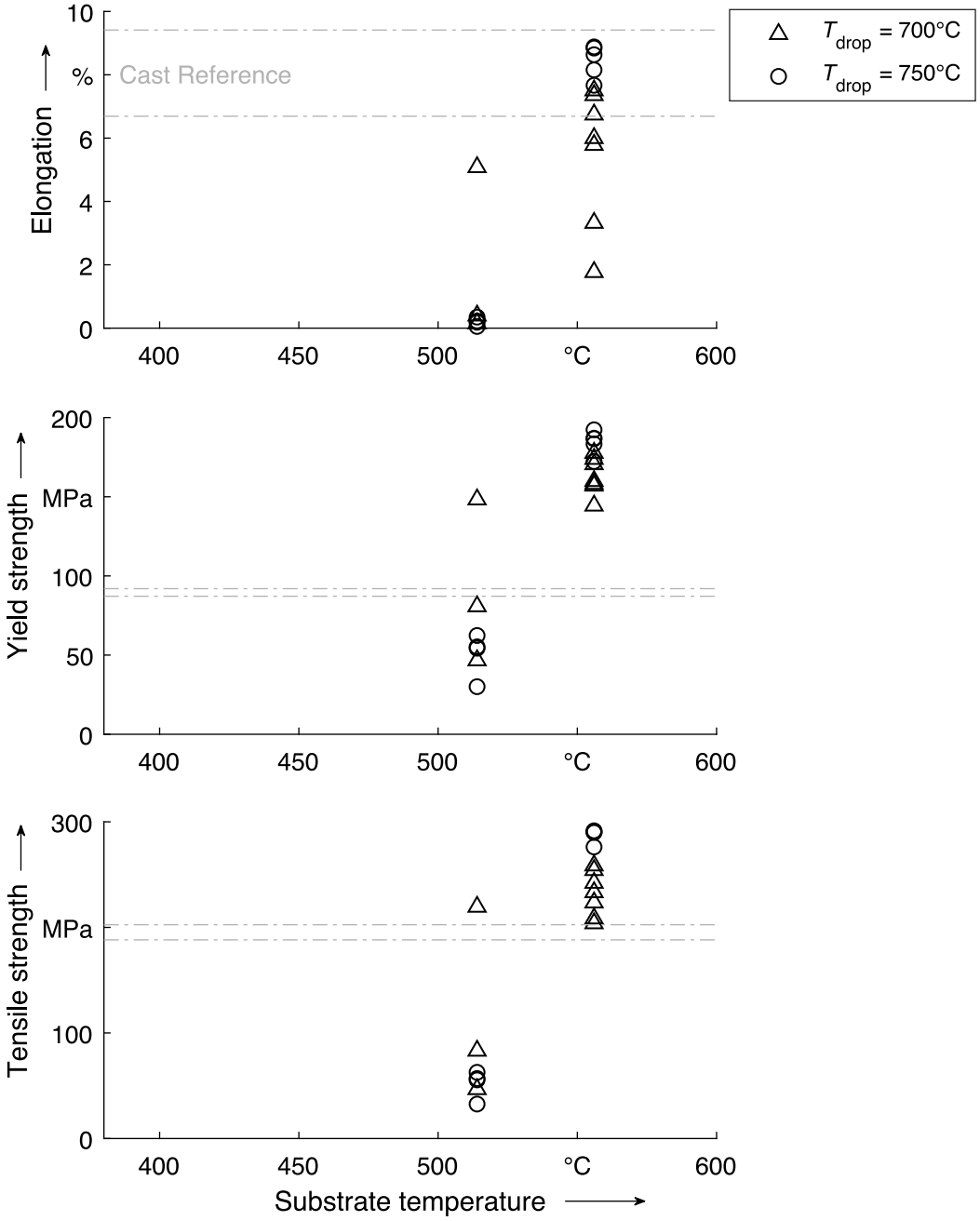

Figure 5.24: Tensile properties of printed AlCu5. The uniform elongation at T_{subs} = 556 °C is comparable to the cast reference. The highest value of 0.2% offset yield strength is measured for 556 °C and is twice the value of the cast reference. Also the ultimate tensile strength shows the highest value for 556 °C, which is 50 % higher than the cast reference. Cast reference shows the range of two standard deviations.

5.2.5 Al99.5Ti

For Al99.5Ti micrographs are not included, as they do not show any contrast at the interface between two droplets. SEM images, density and tensile test evaluation are presented and discussed according to the preceding sections.

Results

For Al99.5Ti relative density values are shown in figure 5.25. The density remains almost constant at 99 % over the substrate temperature range of 33 °C that enabled specimen evaluation.

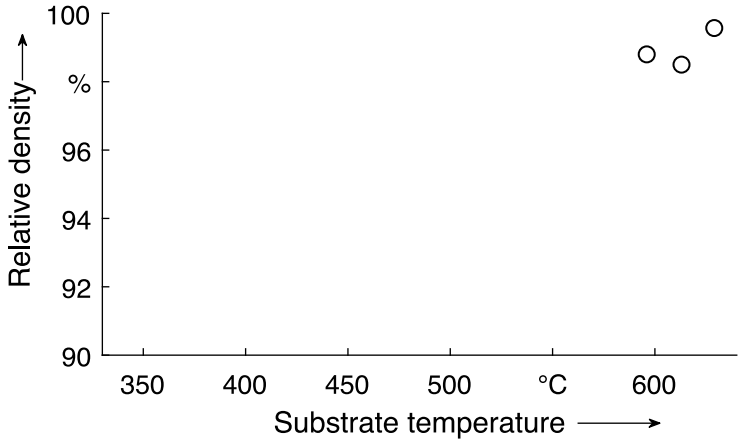

Figure 5.25: Relative density of printed Al99.5Ti against substrate temperature for a droplet temperature of 750 °C.

Figure 5.26 shows SEM images of a part made of Al99.5Ti. Like AlCu5, this technically pure aluminium shows a smooth surface in low magnification, but in the close-up of the surface a dendrite-like surface structure clearly becomes visible. This structure is significantly coarser than for all other alloys. The macroscopic contact angle is about 90° and only a small 'foot' with a contact angle just below 90° forms.

Tensile specimen for this alloys could not be produced for substrate temperatures below 613 °C as they fractured during machining. Tests were also conducted at T_{subs} = 659 °C, but those results had to be excluded, as at those temperatures an Al-Ni alloy forms with nickle from the substrate plate. The eutectic temperature of Al-Ni is 640 °C. Specimens fabricated at 596 °C could at least be removed from the nickle plate, so density measurements were conducted. Figure 5.27 presents the tensile properties of Al99.5Ti. Elongation increases slightly with the substrate temperature, but stays below the cast reference at 24 %. Yield strength decreases a small amount for higher substrate temperatures from values close to the cast reference at 50 MPa

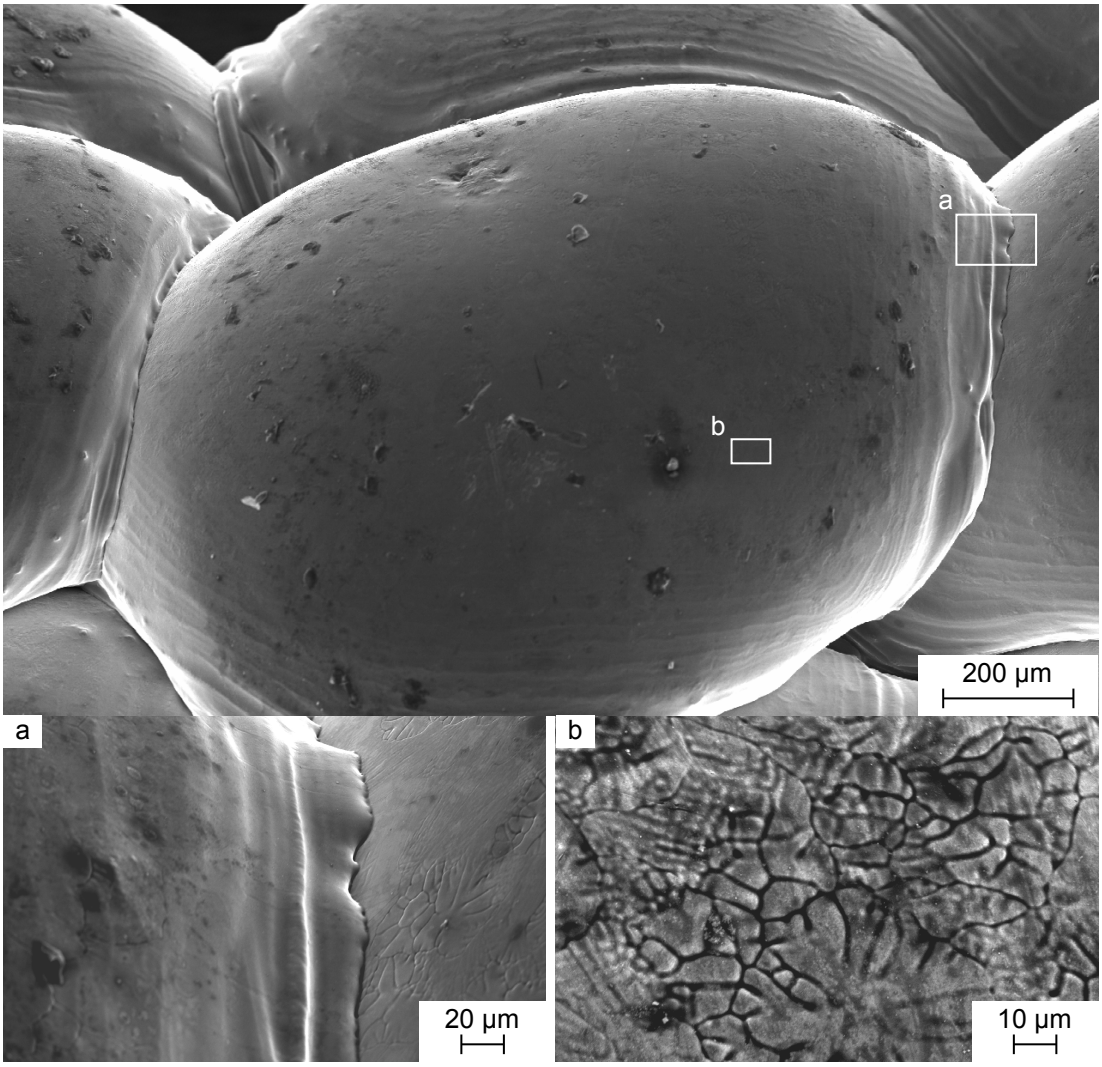

Figure 5.26: SEM images of an Al99.5Ti droplet at 613 °C substrate temperature: Droplet overview and magnifications of the contact area (a) and part of the surface (b). T_{drop} = 750 °C

to about 40 MPa. Same is true for the tensile strength, which decreases from values just below the cast reference at 73 MPa to about 62 MPa.

Discussion

For this technically pure aluminium a minimum substrate temperature of 596 °C is necessary to obtain enough strength to be able to remove cuboids from the substrate plate in one piece. For T_{subs} = 596 °C a relative density of 99 % could be evaluated, but despite the low porosity, those samples were not strong enough to be machined into tensile specimens. Clearly, droplet-droplet bonds form independent of the relative density.

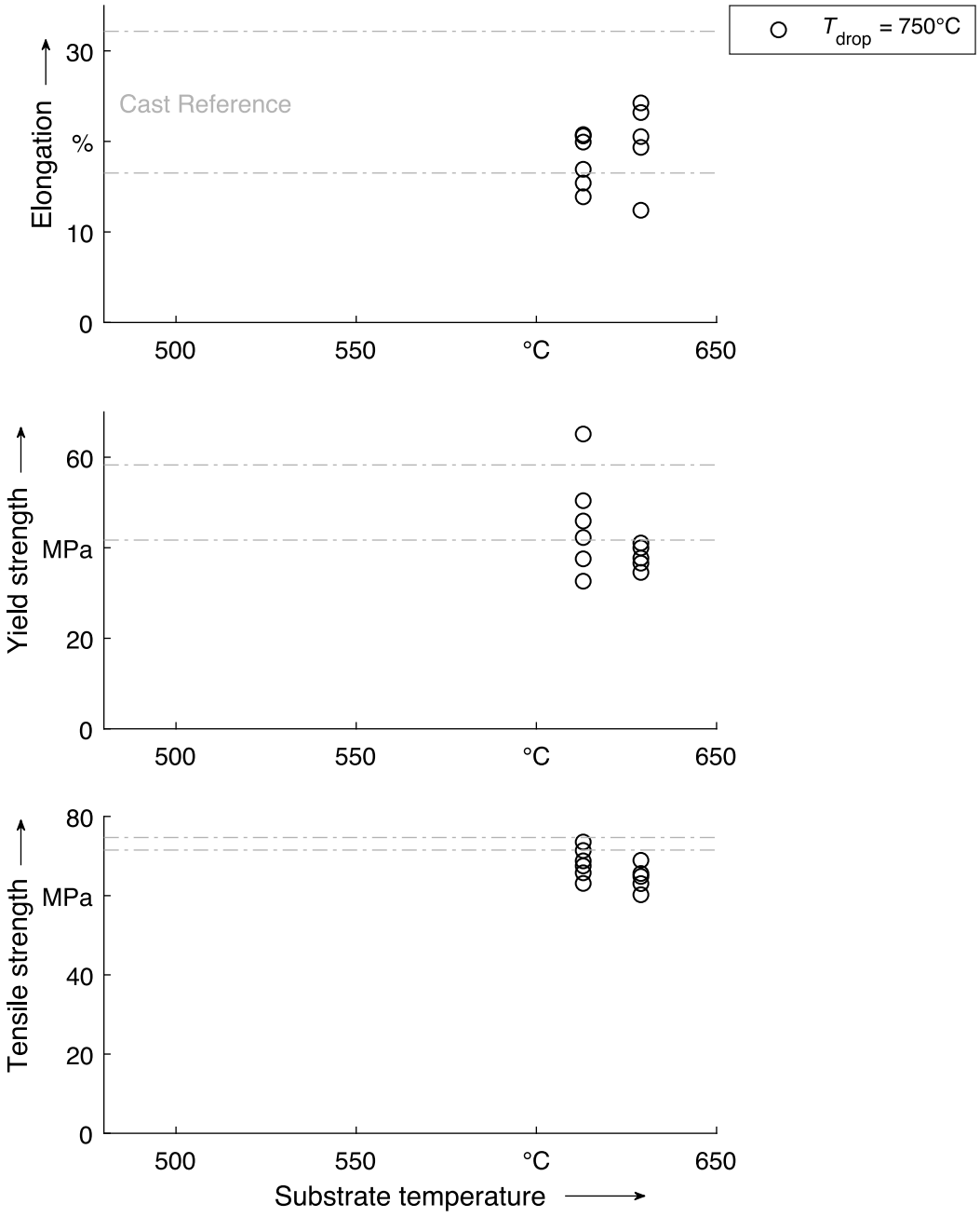

Figure 5.27: Tensile properties of printed Al99.5Ti: The uniform elongation increases with the substrate temperature, but stays below the cast reference. The 0.2% offset yield strength is comparable to the cast reference and decreases for a higher substrate temperature. The ultimate tensile strength decreases for a higher substrate temperature. All results are close to, but still below the cast reference. Cast reference shows the range of two standard deviations.

At a substrate temperature of 654 °C droplets almost completely spread and the shape of a cuboid was lost as can be seen in figure 5.28.

Figure 5.28: Images of an Al99.5Ti specimen printed at T_{subs} = 654 °C. Sharp corners and the overall shape are lost.

Therefore, tensile specimens were only evaluated for two substrate temperatures: 613 °C and 629 °C. While the uniform elongation slightly increases, the yield strength and ultimate tensile strength slightly decrease. This can be explained by the grain size, which is smaller for lower substrate temperatures and yields higher strength and lower elongation values.

5.3 Variation of Oxygen Concentration

Owing to the high oxygen affinity of aluminium, the concentration of remaining oxygen in the printing environment is crucial for the process. This section will first present a study on oxygen distribution in the printing chamber and close to the printing nozzle. Next, the influence of oxygen on mechanical properties and microstructure is shown and discussed.

5.3.1 Oxygen Distribution in Printing Chamber

In a separate test series, the oxygen concentration close to the print head's nozzle in comparison to the oxygen concentration in the printing chamber was measured by replacing the crucible with the oxygen sensor. Those tests were part of a student thesis by Alexander Hofmann.

Results

Figure 5.29 shows the concentrations measured at the nozzle in comparison to the concentrations measured in the printing chamber. The values close to the nozzle are about 600 ppm higher and increase linearly with the printing chamber concentration.

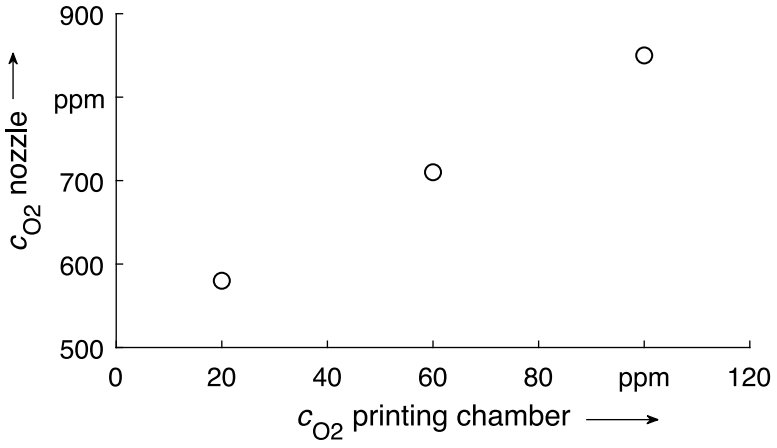

Figure 5.29: Oxygen concentration c_{O_2} close to the nozzle compared to the concentration in the printing chamber: Significantly higher amount of oxygen close to the nozzle with a linear dependency on the chamber concentration.

With the inert gas injection described in section 4.3.8 the oxygen concentration measured at the nozzle position is 0 ppm for an inert gas flow rate of $0.25\,m^3\,h^{-1}$ independent of the printing chamber concentration. Considering the accuracy of the oxygen sensor, the oxygen concentration is < 20 ppm.

Discussion

In the normal print head setup (without inert gas injection) the bottom plate is made from a porous calcium silicate ceramic. The open porosity is 58 % and contains air during downtime of the machine. When the ceramic is heated by the crucible during operation, the air in the pores expands and escapes to the small chamber between printing chamber lid and printing nozzle (see figure 5.30). As the heat diffusivity of the ceramic is low, no stationary conditions are achieved in acceptable times (one hour). To reduce the amount of oxygen close to the printing nozzle, an inert gas vent was machined in the bottom of the plate to allow inert gas from the printing chamber to flow upwards through the opening in the printing chamber lid and purge the volume close to the orifice. As oxygen concentration measurements close to the nozzle show, the supply with inert gas is insufficient to ensure comparable oxygen concentrations in the printing chamber and close to the nozzle. The situation close to the printing nozzle is depicted in figure 5.30. In the setup for oxygen concentration measurements the crucible is replaced by the sensor. Even though the sensor is heated to 350 °C it will still conduct less heat to the ceramic as the crucible and consequently the ceramic will release less oxygen. Thus, those measurements are only a rough estimation.

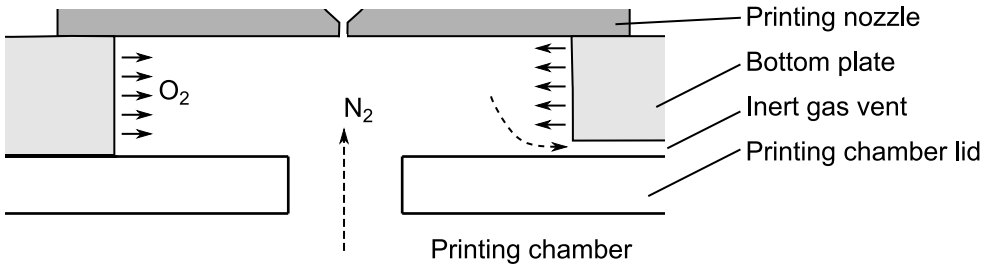

Figure 5.30: Gas flows close to the printing nozzle in normal setup. Oxygen is pressed out of the ceramics open porosity owing to heat expansion. A inert gas vent allows inert gas from the printing chamber to flow through the volume between printing chamber lid and printing nozzle.

5.3.2 Analysis of Specimens Printed at Different Oxygen Concentrations

Magnesium containing alloys showed a substantially different behaviour during the experiments compared to alloys without magnesium additions. This can be attributed to oxidation and the results in this chapter are therefore presented separately for alloys containing magnesium and for those without.

Results for AlMg alloys were obtained in the student thesis by Alexander Hofmann and results for AlSi12 in the master's thesis by Jakob Reif.

AlMg Alloys

With both tested AlMg alloys (AlMg3 and AlMg5Cr) it was not possible to print parts with a constant droplet size. For all test setups, the nozzle was clogged by oxides within one printing run (1200 droplets). Either it was clogged completely or the droplet sizes reduced significantly. Even though installing the inert gas injection improved the behaviour, it was still impossible to print specimen with a constant droplet size. Tests were performed with three different inert gases: standard N_2 with 99.999 % purity, high purity nitrogen with 99.9999 % and argon with 99.999 % purity. With higher purity, nozzle clogging was delayed, but still it appeared too fast, to print specimen for the evaluation of microstructure and tensile strength. Figure 5.31 shows a nozzle after a single test run with columnar crystals growing from the orifice rim inwards.

AlSi12

As already shown, the oxygen concentration in the printing chamber and close to the print head's nozzle are not necessarily equal. All results for the oxygen concentration presented here are labelled with the concentrations measured in the printing chamber.

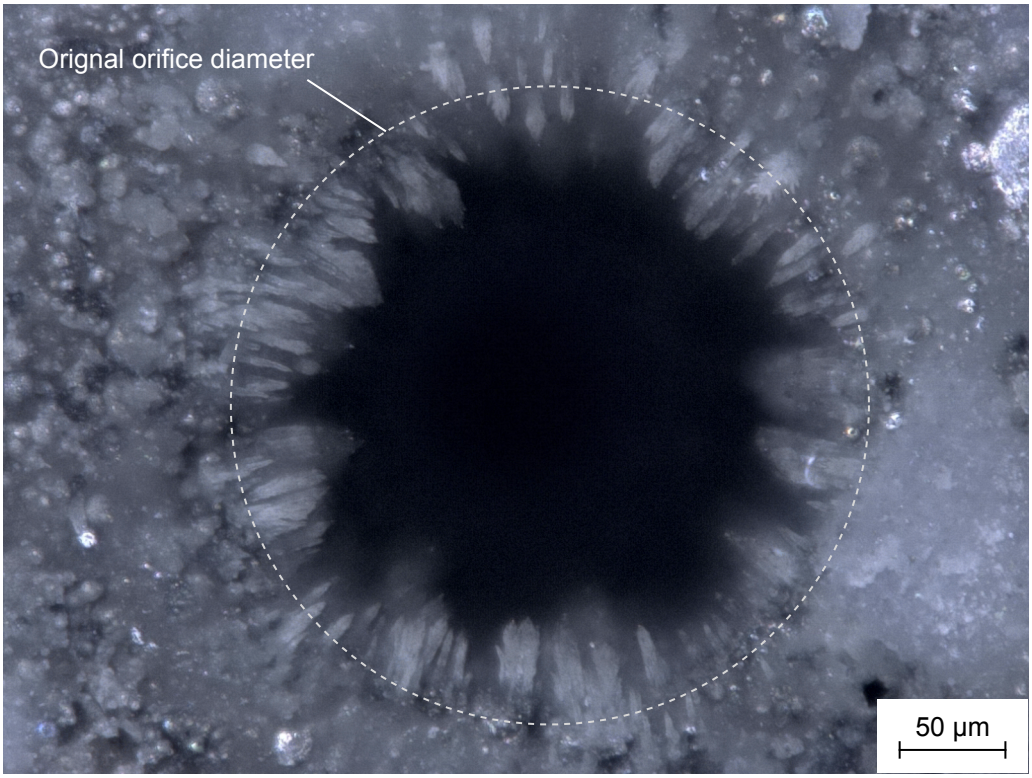

Figure 5.31: Image of a nozzle after printing with AlMg3. Crystals grow from the orifice rim inwards and clog the nozzle.

Figure 5.32 shows that no effect on the density of the printed parts can be measured. The amount of pores lies within the range of 1.5 to 4 %.

Figure 5.33 shows a droplet-droplet interface of a part printed with AlSi12 at $T_{\text{subs}} = 520\,°\text{C}$ and $T_{\text{drop}} = 650\,°\text{C}$ with an oxygen concentration in the build chamber of 20 ppm and 350 ppm.

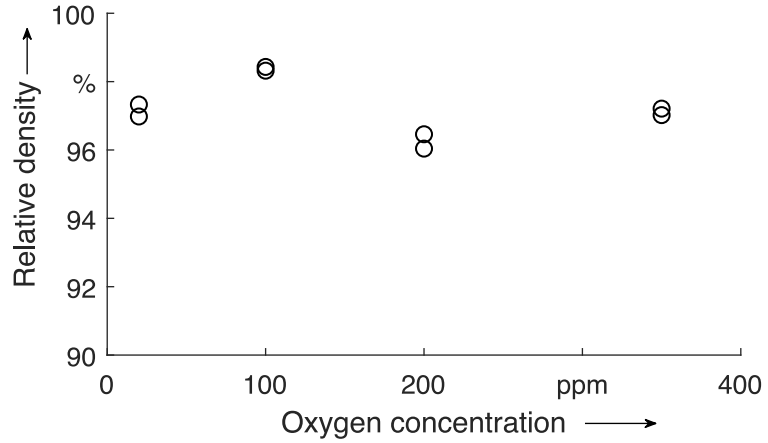

Figure 5.32: Relative density against oxygen concentration of printed AlSi12. No influence of oxygen on the resulting part density can be measured.

No changes in microstructure are visible, but the interface is partially interrupted for 350 ppm. As for the other results related to oxygen concentration, the interruptions in the interface appear abruptly at an oxygen concentration in the chamber between 100 and 200 ppm. The amount and size of interruption does not further increase between 200 and 350 ppm.

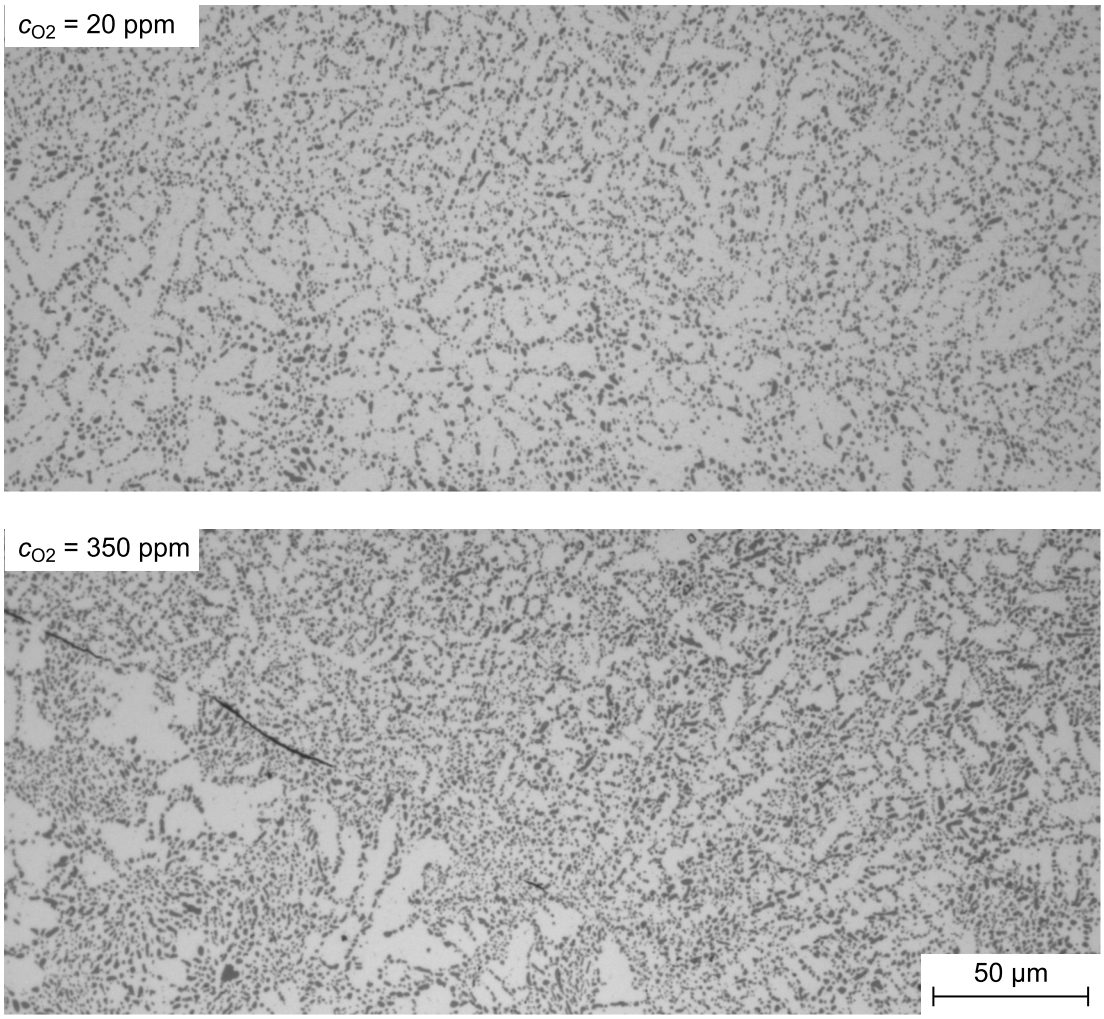

Figure 5.33: Influence of c_{O_2} on micrographs of a droplet-droplet interface for AlSi12: The interface at higher c_{O_2} is partially interrupted and the microstructure remains unchanged. c_{O_2} measured in the build chamber. T_{subs} = 520 °C

Figure 5.34 presents the dependence of uniform elongation, offset yield strength and ultimate tensile strength on the oxygen concentration. The scatter of elongation data is again high, as it was already observed and discussed for AlSi12 at T_{subs} = 520 °C. For concentrations below 100 ppm all tensile properties are independent of the oxygen content in the environment. At 140 ppm a sudden decrease is apparent, as some of the tested specimens show the high values of lower oxygen concentration and others the low values of higher concentrations. Values for yield

strength and tensile strength at 200 ppm and 350 ppm show only the results for those specimens that survived machining. In case of 200 ppm five of ten specimens could be machined and in case of 350 ppm only two of ten. For all other oxygen concentrations ten out of ten specimens were tested.

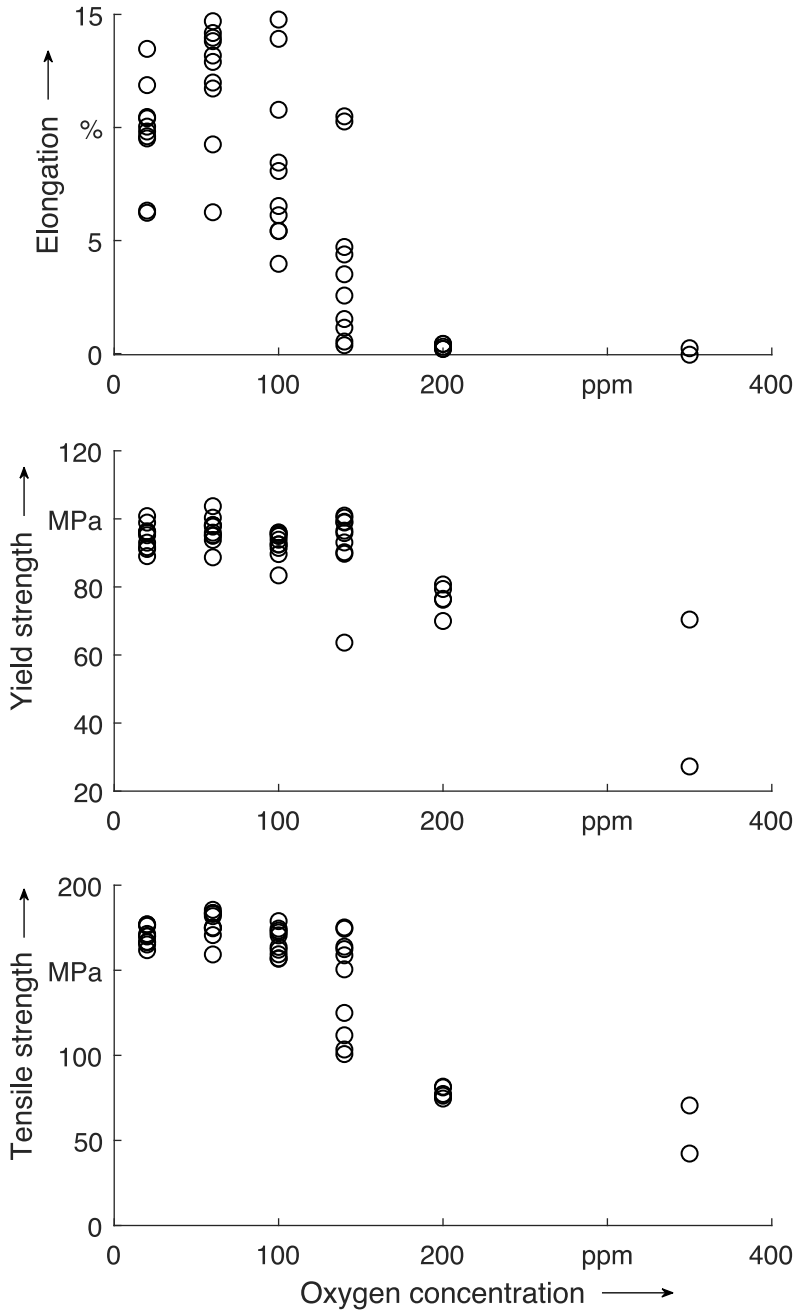

Figure 5.34: Tensile properties against oxygen concentration of printed AlSi12: All measured properties are constant below 100 ppm and reduce significantly for values higher than 140 ppm. $T_{\text{subs}} = 520\,°\text{C}$, $T_{\text{drop}} = 650\,°\text{C}$

5.3.3 Discussion on the Influence of Oxygen

To discuss the influence of surface oxidation on the MJT process aluminium-magnesium alloys will be compared to AlSi12, which is considered to be representative for all magnesium-free alloys. Magnesium is the only addition to aluminium in the used alloys that significantly effects the oxide skin behaviour (see figure 2.29). It is therefore valid to assume that all magnesium free alloys will behave as AlSi12.

Aluminium-Magnesium Alloys

Magnesium is one of the few elements that has a higher affinity to oxygen than aluminium. Hence, it will mainly appear at the surface of a molten AlMg alloy. MgO skins are less protective compared to Al_2O_3 as literature reports (Thiele, 1962). This is caused by the formation of MgO crystals. While an amorphous skin is protective, a crystalline skin is not. Especially when the surface is seeded with crystals of either MgO or even metal crystals in the mushy zone, the oxide skin of aluminium-magnesium alloys will soon form crystalline structures and become non-protective (Cochran et al., 1977; Silva and Talbot, 2016).

In the experimental setup used here, the formation of crystalline MgO is probably seeded by the printing nozzle material that is mainly consisting of aluminium nitride. This assumption is supported by the fact that the observed columnar crystals clogging the nozzle are always growing from the orifice rim inwards. Even though it was not proven that those crystals are MgO, the indication is strong as they were never observed when working with magnesium free alloys and the literature reports that oxides formed on AlMg alloys are essentially pure MgO for a Mg content in the alloy greater than 1.5 to 2 % (Cochran et al., 1977; Silva and Talbot, 2016). The alloys used in the experiments contain at least 3 % magnesium.

Magnesium Free Alloys

When the concentration of oxygen in the printing environment is increased, a sudden decrease in the mechanical properties – especially uniform elongation – is observed at about 140 ppm. The following will try to discuss, where, when and how aluminium oxide influences the printing process.

Generally, oxidation of aluminium can not be completely suppressed by means of a ‘normal’ technical process. As Stucki et al. (1987) have shown, a monolayer of Al_2O_3 forms on solid aluminium at room temperature after an exposure of 1.33×10^{-4} mbar s. Assuming the process

works at atmosphere pressure of 1 bar and an oxygen concentration of 20 ppm, the time t_{ml} that passes until an aluminium surface was exposed to 1.33×10^{-4} mbar s calculates to:

$$t_{ml} = \frac{1.33 \times 10^{-4}\,\text{mbar s}}{1000\,\text{mbar} \cdot 20 \times 10^{-6}} = 6.7\,\text{ms}$$

This time is significantly shorter than almost any time scale in the printing process. Therefore, any solid aluminium surface will be covered by aluminium oxide. Still it is possible to obtain a sound droplet-droplet bound, which means that either the oxide layer is destroyed upon impact of the droplet or it does not disturb the bonding. Yamaguchi (1974) reports that the oxide layer of Al_2O_3 is bound to the aluminium substrate over the suboxides Al_2O and AlO. As those compounds have free valence electrons and a similar lattice parameter, they can form bonds to the metal. Consequently, it is unlikely that the oxide layer can be destroyed by the liquid droplet upon impact, as long as the substrate is not remelted. In the example of AlSi12 it is possible to obtain sound mechanical properties without remelting as already shown.

For an elevated oxygen concentration a sudden decrease in bonding strength was measured. If the assumption of an indestructible oxide layer on the substrate is correct, then this oxide layer either changes in a way to disturb bonding or the oxide layer on the liquid droplet is critical. According to Thiele (1962) oxide layer growth – after the formation of a monolayer – is controlled by the diffusion of aluminium through the layer and therefore independent of the oxygen partial pressure. Consequently, it is improbable that the oxide layer thickness causes the decrease in mechanical properties. A sudden change in oxide layer morphology at a constant temperature was also not reported in literature. So it can be assumed, that the oxide layer on the solid substrate is not responsible for the loss of strength.

Heugenhauser (2018), on the other hand, shows that it is not possible to obtain a sound bonding in compound casting, if the oxide layer on the substrate is not removed during the process. In his work, the solid substrate is heated to temperatures above 500 °C over a time of 30 min without a protective environment before it comes into contact with the melt. During heating from room temperature to 500 °C, the oxide layer fractures by morphology changes and the substrate's thermal expansion (Pieczonka, 2017). In an oxidising environment this will lead to a significantly thicker oxide layer compared to MJT. This interpretation is also in line with the publication by Nerl et al. (2014), who create a compound by casting two aluminium alloys in immediate sequence without reheating the substrate and who do not report problems with oxide

layer formation. From the publication one needs to assume that also in their setup the substrate is covered with an oxide layer before the melt comes into contact with it.

In the case of MJT it will be assumed, that the oxide layer developing on the liquid droplet is critical for droplet-droplet bonding. Considering the knowledge on early oxidation presented in section 2.7 there are two options: Either the onset of oxidation on liquid aluminium at an oxygen exposure of 1.33×10^{-3} mbar s or the formation of a monolayer of aluminium oxide at 3.99×10^{-3} mbar s lead to the abrupt loss of mechanical strength (Stucki et al., 1987). For further understanding, the time for start of oxidation t_{so} and the time for monolayer formation t_{ml} on liquid aluminium at 140 ppm are calculated.

$$t_{\mathrm{so,max}} = \frac{1.33 \times 10^{-3}\,\mathrm{mbar\,s}}{1000\,\mathrm{mbar} \cdot 140 \times 10^{-6}} = 9.5\,\mathrm{ms}$$
$$t_{\mathrm{ml,max}} = \frac{3.99 \times 10^{-3}\,\mathrm{mbar\,s}}{1000\,\mathrm{mbar} \cdot 140 \times 10^{-6}} = 28.5\,\mathrm{ms}$$

As shown by experimental results (section 5.3.1), the oxygen concentration close to the nozzle is substantially higher than the value measured in the chamber. At 140 ppm in the chamber, the gas close to the nozzle has a concentration of $\approx$ 1000 ppm. Now the times calculate to:

$$t_{\mathrm{so,min}} = \frac{1.33 \times 10^{-3}\,\mathrm{mbar\,s}}{1000\,\mathrm{mbar} \cdot 1000 \times 10^{-6}} = 1.3\,\mathrm{ms}$$
$$t_{\mathrm{ml,min}} = \frac{3.99 \times 10^{-3}\,\mathrm{mbar\,s}}{1000\,\mathrm{mbar} \cdot 1000 \times 10^{-6}} = 4.0\,\mathrm{ms}$$

Those values can be compared with the time of flight t_{f} for a droplet between droplet ejection and deposition. With a distance between substrate and nozzle of approximately 8 mm and a droplet velocity of approximately $2\,\mathrm{m\,s^{-1}}$, the time of flight is $t_{\mathrm{f}} = 4$ ms. Even though all those values are rough estimations, the time of flight is the only time in the process that is in the same order of magnitude as the times for oxidation onset and monolayer formation at the given oxygen concentrations.

Figure 5.35 presents two SEM images of the fractured area after tensile tests of two specimens printed at 140 ppm: the sample with the highest and the one with the lowest measured tensile strength. The one with the highest tensile strength shows rough surfaces just as specimen produced at 20 ppm, with the characteristic appearance of a ductile fracture as it can be seen

in the enlarged image. The sample with the lowest tensile strength instead, shows great areas of a smooth surface. Occasionally, small spots with a fracture surface are situated inside the smooth area, like the one enlarged. Next to those spots the smooth area shows wrinkles. All samples printed at oxygen concentrations higher than 140 ppm show those large smooth areas with wrinkles.

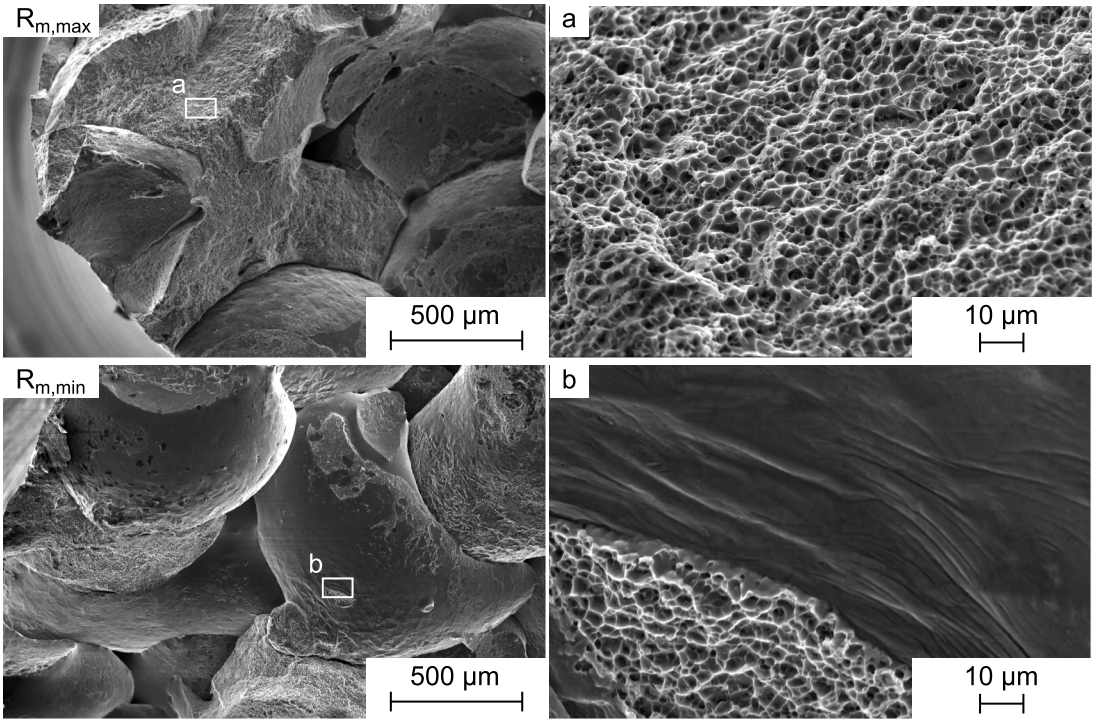

Figure 5.35: SEM images of fracture surfaces comparing the strongest and weakest specimen printed at 140 ppm. The strongest specimen shows rough surfaces, while the weak specimen shows great areas of smooth surface with small spots of sound bonding with adjacent wrinkles.

The smooth surfaces in the fractured area of the weak specimen can be interpreted as an oxide skin covering the whole droplet, which will not coalesce with the neighbour droplet. In some places, this skin is teared open by fluid dynamic forces during deposition and local coalescence is observed. Next to the 'holes' in the oxide layer, this skin is pushed together and forms wrinkles like a fabric would do. Those wrinkles are only observed close to areas with a fracture surface.

The samples in figure 5.35 were fabricated with identical process setups and owing only to process variations, they either show a completely rough surface without traces of an oxide skin or an almost completely smooth droplet surface that is assumed to be a result of an oxide skin. This allows the conclusion that the critical condition is not the onset of oxidation, but the formation of a coherent monolayer of aluminium oxide. As explained earlier, Al_2O_3 can create

bonds to the metal matrix. Two layers of Al_2O_3 cannot bond at the given conditions, as sintering temperatures of Al_2O_3 start at 1200 °C (Alper, 1970). The situation at the interfaces is therefore illustrated as shown in figure 5.36. If the arriving droplet is not covered by a coherent oxide layer, the oxide islands on the droplet surface can move freely and molten metal comes directly into contact with the existing oxide skin on the solid material. Bonds between metal and oxide can form via suboxides. But if the droplet is covered by a coherent oxide skin that only partly rips during impact, two separate oxide layers are present at the interface. As those layers can not form bonds in the solid state at the given conditions, they create gaps in the interface.

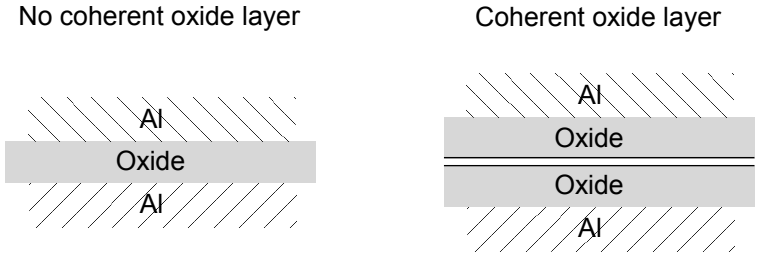

Figure 5.36: Illustration of the situation at oxidised droplet-droplet interfaces. When the arriving droplet is not covered by a coherent oxide skin, metal directly comes into contact with the oxide skin of solid aluminium and bonds to it. A coherent oxide skin on the droplet will not bond to the oxide skin on solid Al.

5.4 Variation of Weber Number

This section will present only the results from the variation of droplet velocity, which is here presented as the Weber number. The discussion is included in the next section.

Figure 5.37 shows two interfaces of cuboids printed with Weber numbers of 12 and 27 at a substrate temperature of 350 °C. Narrow corners that form between droplets are filled at higher Weber numbers. The microstructure in those corners is even finer than close to a 'normal' interface. Other than that, the microstructure of a droplet-droplet interface is not changed by the Weber number.

Figure 5.38 presents the effect of droplet velocity respectively the Weber number on the relative density of AlSi12. After an initial increase, the relative density stays constant with further increased Weber numbers. The maximum value depends on the substrate temperature. As figure 5.39 shows, the printed samples loose their cuboid geometry for higher Weber numbers. Compared to $We = 13$, the cuboid printed at $We = 27$ and $We = 70$ show rounded corners and rougher surfaces on the sides.

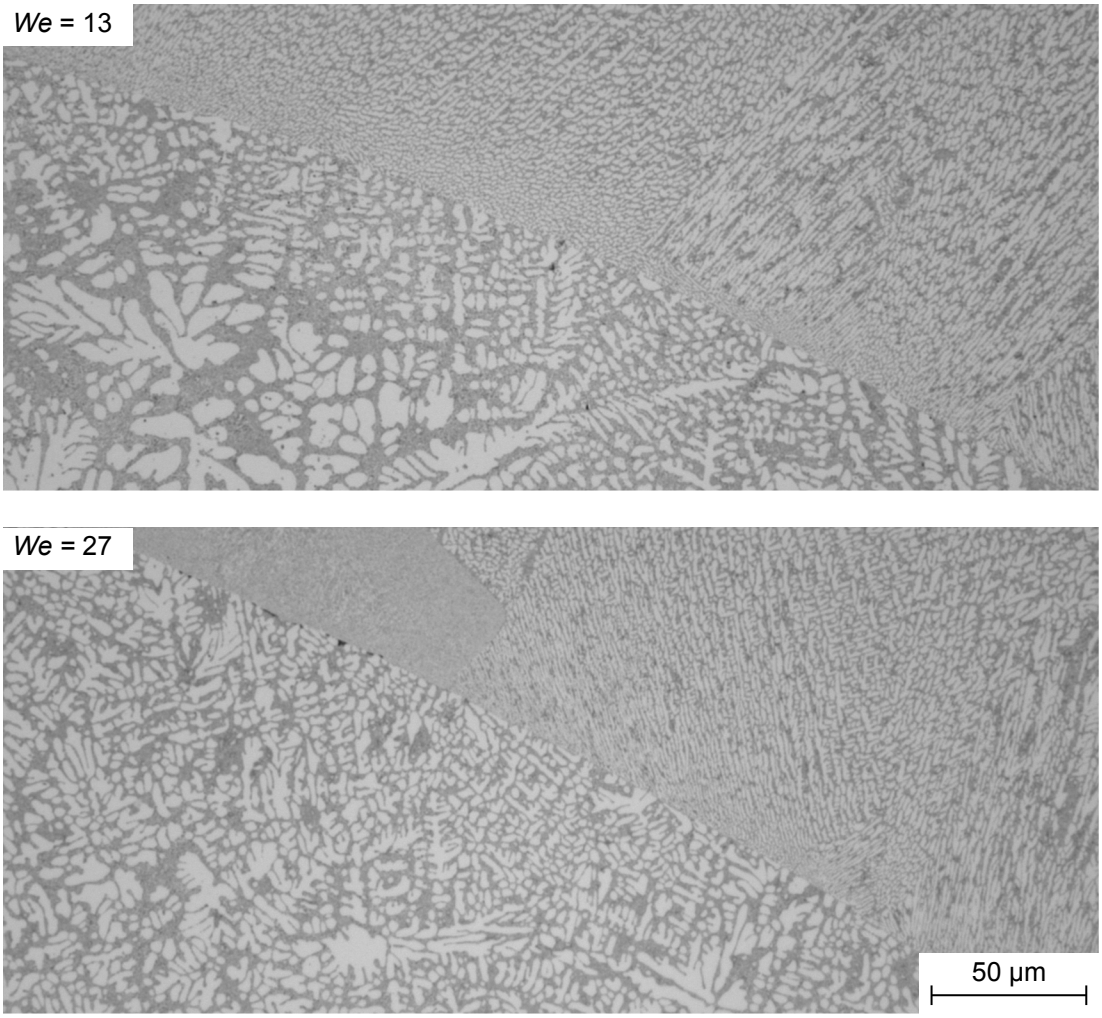

Figure 5.37: Micrographs of a droplet-droplet interface for AlSi12 at different Weber numbers. While the general appearance of the interface remains unchanged, more narrow corners are filled. $T_{\mathrm{subs}} = 350\,^{\circ}\mathrm{C}$

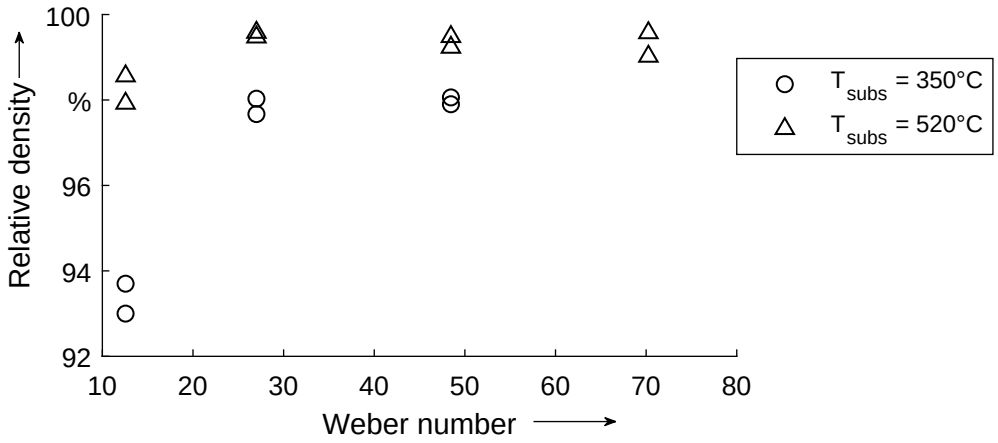

Figure 5.38: Relative density against Weber number of printed AlSi12. Initial increase of relative density with the Weber number to an afterwards constant value that depends on the substrate temperature. $T_{\mathrm{drop}} = 700\,^{\circ}\mathrm{C}$

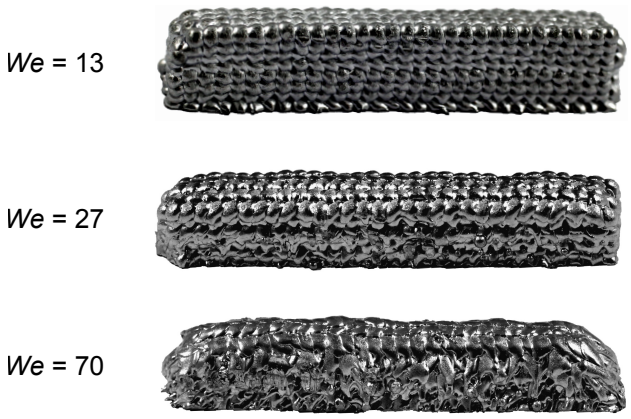

Figure 5.39: Images of cuboids printed at high Weber numbers with $T_{\mathrm{subs}} = 520\,^{\circ}\mathrm{C}$ *and* $T_{\mathrm{drop}} = 700\,^{\circ}\mathrm{C}$*. With increasing Weber number the outer shape of a cuboid is lost owing to droplets spreading over the sides of the previously printed material.*

5.5 Aspects of Droplet Deposition

This section describes the relevant processes during a single droplet impact, spreading and solidification. And it will compare the measured results from the test series of this work with the models given in the literature to judge their quality of predicting the behaviour of the analysed alloys.

5.5.1 Impact and Spreading

To characterise the impact and spreading this work mainly follows the assumptions and models stated by Schiaffino and Sonin (1997a). During isothermal impact and spreading of a droplet four forces can play a role: gravitation, inertia, viscosity and capillary forces. In the case of metal droplet printing, gravitational forces can generally be neglected as the Bond number is in the order of 10^{-2} (i.e. 7×10^{-3} for pure Al droplets with $d = 0.5\,\mathrm{mm}$). Same is true for viscous forces, as the Ohnesorge number, which measures the relation between viscosity and surface tension ($Oh = \eta/\sqrt{\rho\sigma d}$), is also small. In the case of pure Al $Oh = 1 \times 10^{-3}$. Accordingly, the relevant forces for droplet deposition are inertia and capillary forces, whose relation is measured by the Weber number: For higher Weber numbers the deposition process is controlled by inertia. That means, when a droplet hits the substrate, the dynamic pressure drives the fluid flow during spreading against the inertia. For low Weber numbers the process is controlled by capillary forces meaning that the droplet is 'drawn' onto the substrate after contact.

5.5.2 Solidification

Pasandideh-Fard et al. (1998) studied the impact of molten tin droplets on a steel substrate and conclude that the effects of solidification on the impact and spreading process can be neglected if $\sqrt{St/Pr} \ll 1$, with the Stefan number $St = c(T_{\mathrm{sol}} - T_{\mathrm{subs}})/L$ and the Prandtl number $Pr = \eta c/\lambda$. For aluminium and at reasonable substrate temperatures $\sqrt{St/Pr}$ is greater than unity and solidification is therefore effecting droplet spreading and the final droplet shape.

Schiaffino and Sonin (1997b) describe the model of the advancing contact line of a molten droplet spreading over a cold solid (see Figure 5.40). For MJT it is assumed that no thermal resistance exists at the interface and that no undercooling of the liquid occurs as nucleation sites

are plentiful on the surface of the substrate of the same kind.[1] Therefore, immediately upon contact a layer of solid will grow into the droplet. This layer has the angle θ_{sf} at the contact line. According to Schiaffino and Sonin (1997b) this angle is only a function of material properties and the Stefan number (see equation (Equation 2.6)). As long as the contact angle of the solidified layer is smaller than the current dynamic contact angle of the advancing contact line, the droplet will spread further. According to the Hoffman-Tanner-Voinov law (X. Wang et al., 2007), the dynamic contact angle of a moving contact line increases with contact line velocity[2]. The velocity of the contact line will decrease during spreading and the dynamic contact angle will therefore also decrease until it is equal to the solidification contact angle. At this point the contact line is arrested as no liquid material can be supplied to the contact line. Figure 5.41 shows the SEM images of an AlSi5 droplet printed at $T_{subs} = 516\,°C$ and $T_{drop} = 700\,°C$. One can clearly see the layer of rapid solidification close to the substrate (previously printed droplet) with a contact angle smaller than the apparent contact angle of the complete droplet.

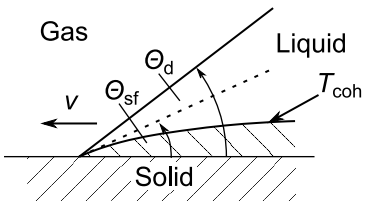

Figure 5.40: Contact line during molten droplet spreading: Close to the contact line a solid layer forms in the droplet with a constant angle θ_{sf}. Spreading continuous as long as the dynamic contact angle θ_d is greater than θ_{sf}. According to Schiaffino and Sonin (1997b)

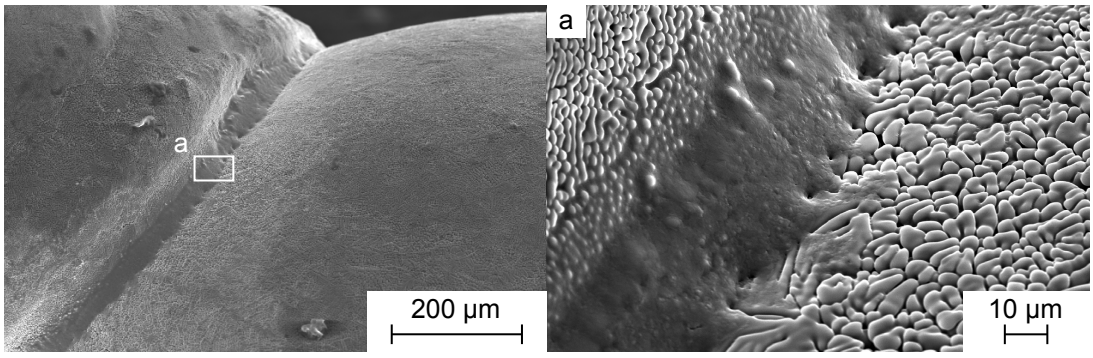

Figure 5.41: SEM image of an AlSi5 droplet with a foot at the contact line. The appearance of the droplets showing a rapid solidified layer with a 'foot' at the contact line agrees with the models by Schiaffino and Sonin (1997b)

[1] In this case undercooling only means undercooling owing to homogeneous nucleation. Undercooling owing to non-equilibrium solidification will still occur.

[2] This is only valid during spreading. Hoffman-Tanner-Voinov law: $\mu v/\sigma = k(\theta_a^3 - \theta_e^3)$. With θ_a the dynamic contact angle, θ_e the equilibrium contact angle and k a material constant.

One could argue that this is only true if no remelting of the substrate occurs. But in the early times of a droplet impacting on an infinite solid, the contact line of the droplet will keep advancing on 'fresh' solid. Therefore, it is valid to assume that close to the contact line there is always a solid layer growing inside the droplet, at least for a moderate melt superheat. The topic of remelting is discussed in more detail in section 5.5.3.

When looking at the results of different Weber numbers, it can first be said that all results were obtained for the inertia controlled regime as the lowest Weber number is 12. With an increasing Weber number the relative density initially increases, which is absolutely in agreement with the aforementioned. As a higher droplet velocity results in a higher spreading velocity, the droplet can spread further and fill smaller corners, before the spreading is arrested by solidification. On the other hand at high Weber numbers, the outer appearance of the samples is more chaotic, because surface tension can not ensure a mainly spherical droplet shape anymore. Instead, droplets spread over the sides of the cuboids and form a chaotic surface. So even at a Weber number of 50 the relative density is no higher than 98 % for $T_{\mathrm{subs}} = 350\,^{\circ}\mathrm{C}$.

All the aforementioned models and publications are related to pure materials with a melting point. But in the case of MJT of metals, one will generally work with alloys showing a broader solidification range. It is now necessary to find a way to compare different alloys and their results to find a more general approach. It is commonly assumed that a solidifying alloy will behave as a liquid as long as its temperature is above the temperature of dendritic coherency T_{DCP}. Therefore, figure 5.42 compares the results of relative density for substrate temperature variation by their distance to the coherency temperature $T_{\mathrm{subs}} - T_{\mathrm{DCP}}$. Values for T_{DCP} are taken from table 5.1. Independent of the bonding between droplets, the relative density should reflect the droplet spreading upon impact. The further the droplet spreads upon impact, the lower the solidification angle θ_{sf} becomes and the better this droplet will fill the corners to adjacent droplets as visualised in figure 5.43.

Independent of the solidus temperature, the highest density values for all alloys are obtained at substrate temperatures $\approx 50\,^{\circ}\mathrm{C}$ below the coherency temperature. When comparing AlSi5 and AlCu5, one can see that liquidus temperatures are equal (630 °C), coherency temperature of AlSi5 is 9 °C higher (621 °C vs. 612 °C) but the solidus temperature of AlCu5 is 29 °C lower (548 °C vs. 577 °C). If T_{sol} would be relevant for the droplet spreading and thus, the relative density, one would expect the density values of AlCu5 to be higher, but exactly the opposite is the case.

Another observation is that while the alloys AlSi5 and AlCu5 show a very steep gradient in the density against $T_{\mathrm{subs}} - T_{\mathrm{DCP}}$, the values for AlSi12 remain almost constant. Eutectic alloy

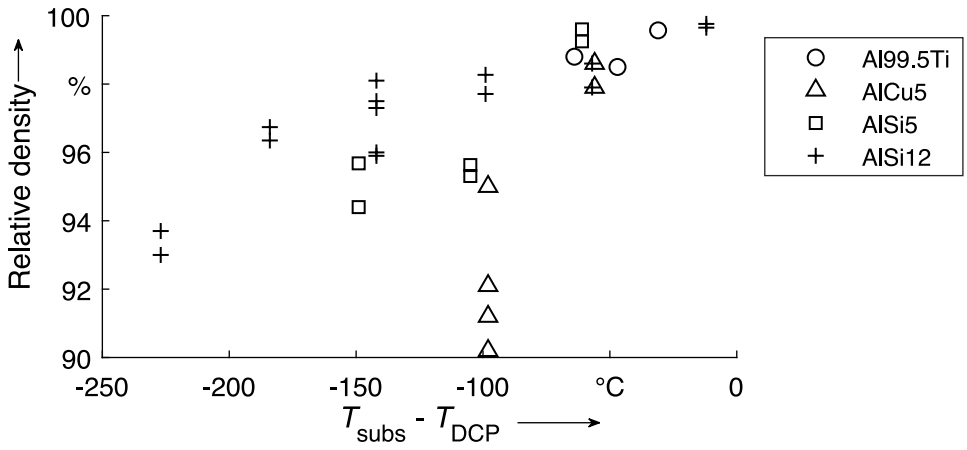

Figure 5.42: Relative density of different alloys compared to the coherency temperature.

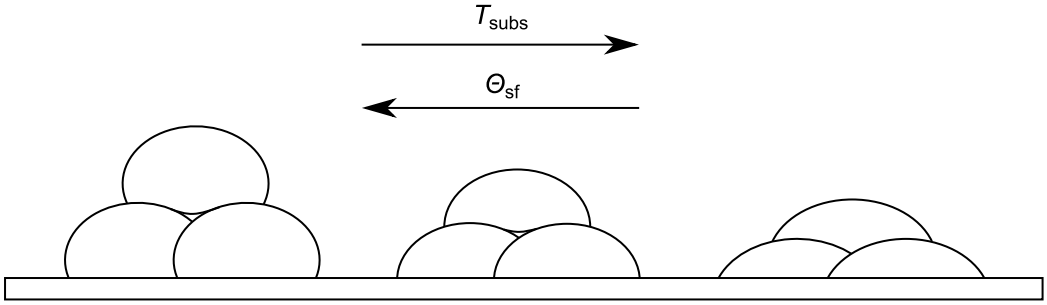

Figure 5.43: Illustration of the solidification angle's effect on the relative density: With an increasing substrate temperature, the solidification angle θ_{sf} decreases and corners between adjacent droplets can be filled better and the relative density therefore increases.

specimens with a constant density can be fabricated over a range of almost 150 °C. Note that values of AlSi12 at $T_{subs} - T_{DCP} = -27\,°C$ have to be judged differently, as in this case the droplets fuse to form lines during printing.

Following the model of Schiaffino and Sonin (1997b) (figure 5.40) it is assumed that the angle θ_{sf} is greater, when the 'solidified' layer at the bottom is thicker. If the heat flow to the substrate is comparable for different alloys, then the 'solidified' layer thickness in the droplet during spreading at a given time h_{DCP} is indirect proportional to the heat of fusion, which is released

by this layer. Note that a layer is assumed to be 'solidified' in terms of fluid motion, once it has reached the coherency point. Therefore:

$$\theta_{\mathrm{sf}} \propto h_{\mathrm{DCP}} \propto \frac{1}{fs_{\mathrm{DCP}} \cdot L} \qquad \text{(Equation 5.1)}$$

θ_{sf}: Solidification angle of spreading droplet
h_{DCP}: 'Solidified' layer inside spreading droplet
fs_{DCP}: Fraction solid at coherency point
L: Specific heat of fusion

It is common practice to estimate the fraction solid at a given temperature T inside the solidification range to $fs(T) = (T_{\mathrm{liq}} - T)/(T_{\mathrm{liq}} - T_{\mathrm{sol}})$. This can be used to estimate fraction solid at coherency points and to calculate $fs_{\mathrm{DCP}} \cdot L$, which is presented in table 5.1 for the alloys used. The difference in fs_{DCP} between AlSi5 and AlSi12 for example is caused by a different solidification morphology. While eutectic alloys show a planar solidification front, hypo-eutectic alloys solidify in a dendritic morphology. When solidifying in a dendritic morphology, the solidification can reach deep into the droplet and hinder fluid motion at a low fraction solid and thus, a low amount of released heat of fusion. Respectively, when the same amount of heat is transferred to the substrate, the 'solidified' layer of an alloy with dendritic solidification morphology is thicker than the layer of an alloy with planar solidification morphology. Figure 5.44 illustrates the situation at the molten contact line.

Table 5.1: Values of $fs_{\mathrm{DCP}} \cdot L$ for the alloys used in the studies. Values for AlSi5 and AlCu5 were taken from Chai et al. (1995) for a cooling rate of 1 K s^{-1}. Values for T_{DCP} were calculated by $T_{\mathrm{liq}} - fs_{\mathrm{DCP}}(T_{\mathrm{liq}} - T_{\mathrm{sol}})$.

Alloys	T_{DCP} in °C	fs_{DCP}	$fs_{\mathrm{DCP}} \cdot L$ in kJ kg^{-1}
Al99.5Ti	660	1	397
AlCu5	612	0.21	77
AlSi5	621	0.2	78
AlSi12	577	1	426

Those results and their interpretation are in line with the technological properties 'fluidity' of metal melts as used in conventional metal casting. Stefanescu (2002) describes fluidity by the length covered by melt during mould filling before the melt solidifies (flow length l_f). For pure metals and eutectic alloys, he gives the equation $l_f = v \cdot t_f$ and for dendritic single phase alloys $l_f = fs_{DCP} \cdot v \cdot t_f$ with the velocity of the melt v and the time until melt flow arrests t_f.

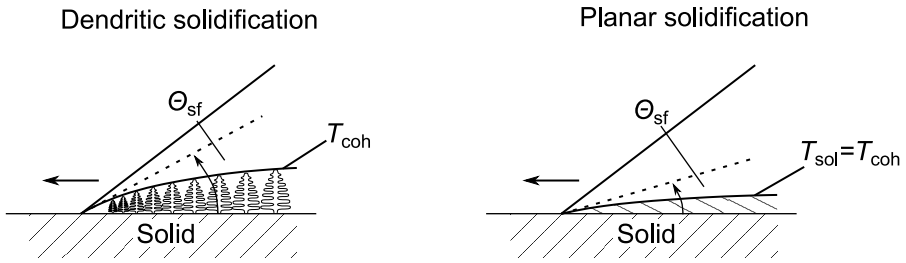

Figure 5.44: Illustration of the solidification morphology's influence on the behaviour of a molten contact line: For the same amount of fraction solid, an alloy with dendritic solidification will form a thicker layer of 'solidified' material compared to an alloy with planar solidification.

Figure 5.45 presents measured values for the fluidity of Al-Si melts depending on the Si content. In contrast to the results presented in this work, the fluidity improves with the melt superheat. This is probably caused by the difference in thermal resistance between melt and substrate. In conventional casting the fluidity is measured by the distance an alloy flows in a preheated steel mould that usually has the shape of a spiral. The heat transfer coefficient between liquid aluminium and steel mould is limited and in the range of 10^3 to 10^4 W m^{-2} K^{-1} (MEl-Mahallawy and Assar, 1991). In the case of droplet deposition, the thermal resistance between droplet and substrate is neglectable, as they are made of the same material and form a metallic bond. Therefore, the substrate temperature will completely dominate the processes close to the contact line. Another reason is that in conventional casting the first dendrites can move freely inside the melt where they mix with still overheated melt. So in this case a homogeneous distribution of fraction solid is assumed. During droplet deposition instead, the dendrites are connected to the substrate and can not move inside the liquid droplet, so a solid layer forms, which is part of the substrate and again dominated by the substrate temperature. Nevertheless, it is valid to say that an alloy with a high fluidity will form dense metal parts more easily and also over a wider range of substrate temperatures compared to an alloy with a low fluidity.

Conclusion

The droplet spreading is arrested by solidification at the interface to the substrate. For alloys with a low fraction solid at dendrite coherency the spreading is arrested earlier compared to alloy with a high fs_{DCP}. The technical property fluidity reflects fs_{DCP} and therefore droplets of an alloys with a high fluidity will spread further and hence, form parts with a high relative density.

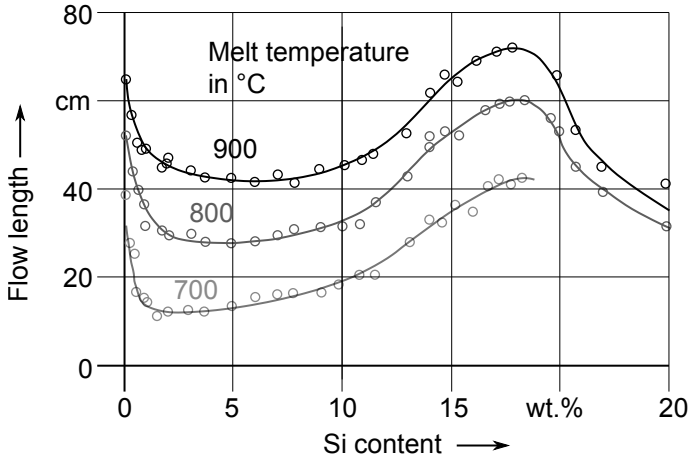

Figure 5.45: Fluidity of Al-Si alloys depending on the Si content. Values measured by fluidity spiral. According to Bundesverband der Deutschen Gießerei-Industrie (2013)

5.5.3 Contact Temperature and Remelting

In the literature of droplet-based metal printing as well as compound casting, several authors state that remelting of the substrate is an essential condition to achieve metallic bonds (Chao et al., 2013; Fang et al., 2009; Lange, 1998; S. P. Wang et al., 1998). To determine whether remelting occurs, most publications use the semi-infinite-bodies solution (Equation 2.1) and assume that a contact temperature T_{c1} higher than T_{sol} leads to remelting. Figure 5.46 plots the relative ultimate tensile strength for all tested alloys against $T_{c1} - T_{sol}$. Measured values are plotted relative to the maximum value of each alloy. Remember that except for AlSi12, specimens had insufficient strength to be machined for substrate temperature lower than lowest presented value. If the assumptions in the literature were correct, one would expect no significant strength below zero and successively increasing values above. That is approximately true for AlSi5 and Al99.5Ti but definitely not for AlCu5 and AlSi12. In case of AlSi12 it is possible to obtain tensile strengths comparable with cast material for contact temperatures 100 °C below solidus temperature. Whereas for AlCu5 no specimens could be machined until 40 °C above solidus. Furthermore, this model implies that the droplet temperature has a significant effect on the strength, which is not the case for the results presented in this thesis.

Irrespective of whether remelting is a necessity for metallic bonding, the model of semi-infinite bodies also fails to predict remelting or even the temperature during droplet deposition. Aziz and Chandra (2000) deposit tin droplets on a steel substrate and measure the temperature by a fast-response thermocouple. They find that T_{c1} (Equation 2.1) underestimates the measured temperatures. They conclude that the model does not account for the fluid convection in the droplet, which transports heat to the interface during spreading and propose to model the

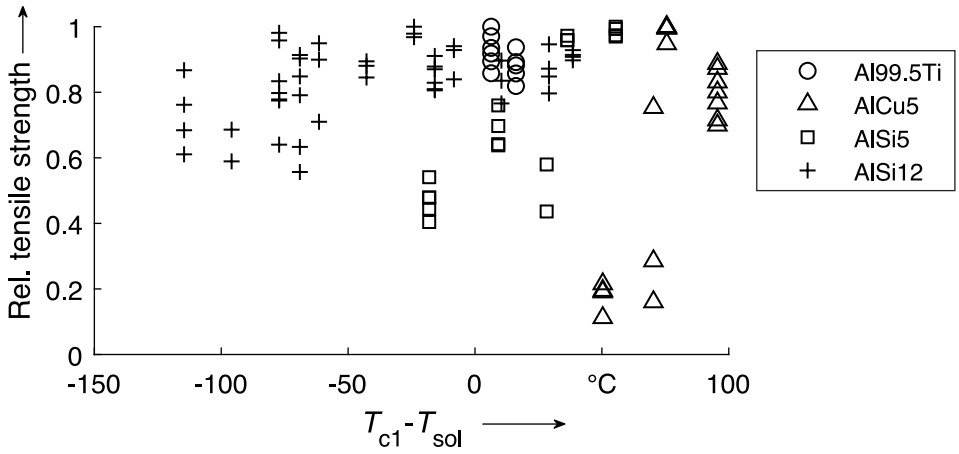

Figure 5.46: Relative ultimate tensile strength of all tested alloys against $T_{c1} - T_{sol}$. Values are given relative to the maximum value of each alloy. Measured data does not reflect the models cited in the literature.

temperature in the substrate by a semi-infinite body with a finite heat transfer coefficient to a constant temperature condition at the interface (Equation 2.2). Even though it is correct that the semi-infinite-bodies-solution does not account for fluid convection in the spreading droplet, this model does also not account for something far more important: heat of fusion. Say the thermal conditions are in a way that solid forms inside the droplet, which is certainly the case in the experiments by Aziz and Chandra (2000) and probably in all common cases as solidification will always occur close to the contact line of the spreading droplet, then the solidifying material will release its heat of fusion and maintain the solidus temperature until it has fully solidified. For pure aluminium, the latent heat of fusion releases the same energy as aluminium melt cooled by 336 °C without a phase change. Consequently, it is heavily effecting the thermal conditions and must not be neglected.

Moreover, the semi-infinite-bodies-solution is valid only for short times after impact, to satisfy the assumption of infinity. So heat transfer between the droplet and the substrate needs to happen without significant time delay. This is not possible for problems involving solidification as solidification is a time controlled process with a finite solidification rate. This rate is limited in metallic alloys by diffusion in the liquid state and is in the order of $3\,\mathrm{m\,s^{-1}}$ (MacDonald et al., 1989). Melting instead is not controlled by diffusion, the 'collision-limited model' can therefore be applied, which limits the maximum rate of phase change to the speed of sound (Tsao et al., 1986). In solid bodies the speed of sound for longitudinal waves is approximately $\sqrt{E/\rho}$. For aluminium at melting temperature the speed of sound is about $3500\,\mathrm{m\,s^{-1}}$.

S. P. Wang et al. (1998) model a finite splat of thickness b on an infinite substrate. They numerically solve the governing equation in one dimension and allow phase change with subcooling

of the liquid and overheating of the solid as a consequence of rapid phase change. The top of the splat is assumed to be adiabatic, which is a valid assumption for short times, as convection at the upper side of a droplet is small compared to heat conduction in the substrate. Under those assumptions they present an operational map shown in figure 2.14. When thermal resistance between substrate and droplet is assumed to be small, then $Bi \gg 1$ and for Al on Al one obtains $(T_{\mathrm{drop}} - T_{\mathrm{subs}})/(T_{\mathrm{melt}} - T_{\mathrm{subs}}) \approx 2.5$, where T_{melt} is the distinct melt temperature of a pure metal or eutectic alloy. This results in the same remelting condition as predicted by the semi-infinite-bodies-solution (Equation 2.1). By putting $T_{\mathrm{c1}} = T_{\mathrm{melt}}$ and rearranging, one obtains:

$$\frac{T_{\mathrm{drop}} - T_{\mathrm{subs}}}{T_{\mathrm{melt}} - T_{\mathrm{subs}}} = \frac{\sqrt{\rho_{\mathrm{drop}} c_{\mathrm{drop}} \lambda_{\mathrm{drop}}} + \sqrt{\rho_{\mathrm{subs}} c_{\mathrm{subs}} \lambda_{\mathrm{sub}}}}{\sqrt{\rho_{\mathrm{drop}} c_{\mathrm{drop}} \lambda_{\mathrm{drop}}}} \qquad \text{(Equation 5.2)}$$

With values for pure aluminium (Equation 5.2) gives $(T_{\mathrm{drop}} - T_{\mathrm{subs}})/(T_{\mathrm{melt}} - T_{\mathrm{subs}}) = 2.53$.

The elaborate model by S. P. Wang et al. (1998) accounting for latent heat and rapid phase change phenomena will predict the same onset of remelting as the overly simple model of semi-infinite-bodies. It was already assessed that the presented data is not consistent with the semi-infinite-body solution. Consequently, it is also not consistent with the model by S. P. Wang et al. (1998).

Conclusion
Remelting is not a necessary condition to form metallic bonds in the case of AlSi12 and it is also not sufficient to form metallic bonds in the case of AlCu5. One needs to find novel models to predict whether droplets in MJT will form a coherent material.

5.5.4 Rapid Solidification

Thermophysical data of solidifying alloys as liquidus, solidus and coherency temperature are dependent on the rate of solidification respectively the cooling rate. In most publications, the cooling rate is defined as the cooling rate before the onset of solidification.

The solidification time in the presented results is between 30 and 200 ms. The lower value was measured in section 5.2.1 and the upper value is a boundary, when individual droplet solidification is assumed at a printing frequency of 5 Hz. With an average droplet height of 0.6 mm, the average solidification rate is in the range of 3 to 20 $\mathrm{mm\,s^{-1}}$. Cooling rate can be

calculated from the solidification time to $\dot{T} = L/(c \cdot t_{sf})$, when it is assumed that the rate of heat transfer to the environment remains constant before and after the onset of solidification. In this case, the average cooling rate is between 2×10^3 and 12×10^3 K s^{-1}. At those conditions, the equilibrium phase diagram is not valid. Liquidus and solidus temperatures are shifted to lower temperatures and the eutectic point is shifted to a higher solute concentration. It is not possible to quantify those differences for the conducted experiments from published data.

For remelting, the solidus temperature during heating is relevant, which is not significantly effected by heating rates, as melting is not diffusion controlled. However, during spreading, solidification at the contact line and the fraction solid at DCP are controlling the droplet deposition. As described in section 2.6, the dendrite coherency depends on the cooling rate without a clear tendency. Therefore, reliable data on the DCP of the used alloys at high cooling rate is necessary to discuss the droplet spreading in more detail.

5.5.5 Surface Structure

The different surface structures apparent on the droplet surfaces of different alloys at different temperatures can also be explained by the solidification morphology. When the solidification is dendritic, two different behaviours can be observed: when the solute concentration is below the maximum solubility in solid solution, as it is the case for AlCu5, then dendrites will grow until coherency and then thicken until complete solidification. In this case, the surface is compact but bumpy, as two convex dendrite arms can never create a flat surface. When the solute concentration is above the maximum solubility in solid solution, as it is the case for AlSi5, dendrites will grow until the remaining melt reaches the eutectic composition. Now, this remaining melt will freeze in between the dendrite arms and the volume deficit can only be taken from the remaining liquid melt. This causes the melt to draw back from the surface leaving dendrite tips that reach out of the droplet surface with gaps in between. Figure 5.47 shows the SEM images of the surface of AlSi5 droplets compared to AlCu5 droplets. This microstructure also has the effect that AlSi5 parts appear matt while those made from AlCu5 and especially those made from AlSi12 and Al99.5 are shiny.

When the solidification front is planar, all material needed to feed the volume deficit during solidification is directly supplied by the liquid at the solidification front and the resulting surface is even. Droplets of AlSi12 show a smooth surface at the bottom and more and more dendrite tips to the top. Droplets printed on cold substrate show a greater amount of smooth surface, while droplets printed on a warmer substrate show more rough surface on the top.

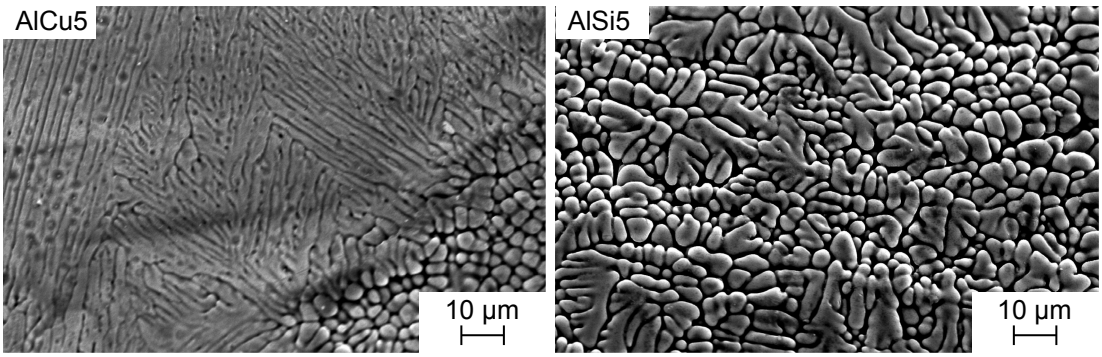

Figure 5.47: SEM images taken from the surface of AlCu5 droplets compared to AlSi5 droplets. While AlCu5 forms a dense but bumpy surface, AlSi5 shows dendrite tips with gaps in between.

This can be explained, taking the micrographs into account, by rapid solidification close to the interface. Here a high solidification rate results from the steep thermal gradient short times after contact. As the thermal gradient reduces, the solidification rate also reduces in the late time of solidification. High solidification rates will lead to a planar solidification front (see figure 2.27), while comparable lower rates lead to a dendritic morphology. The solidification rates are high enough in any case to shift the eutectic compositions to higher Si concentration, which makes AlSi12 behave like a hypo-eutectic alloy (see figure 2.26). Figure 5.48 shows images taken from AlSi12 droplets printed at $T_{\mathrm{subs}} = 350\,^{\circ}\mathrm{C}$ and $T_{\mathrm{subs}} = 520\,^{\circ}\mathrm{C}$.

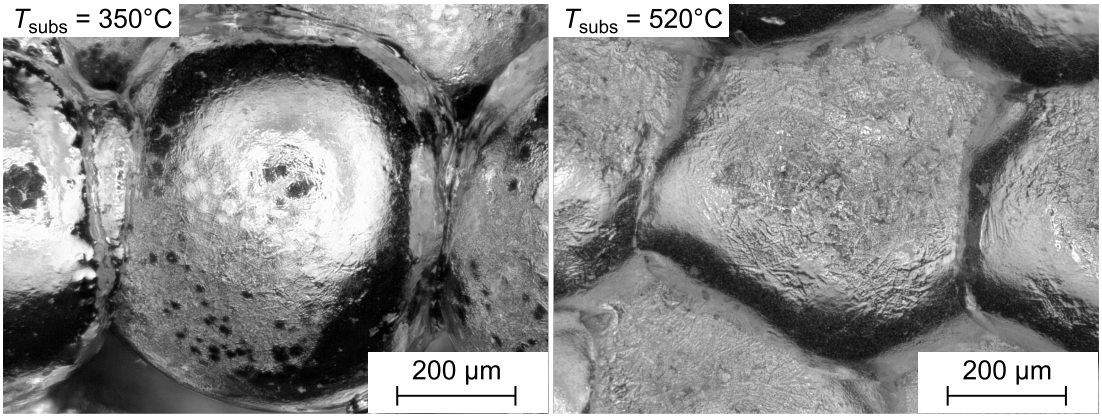

Figure 5.48: Images taken from the top surface of AlSi12 cuboids printed at $T_{\mathrm{subs}} = 350\,^{\circ}\mathrm{C}$ and $T_{\mathrm{subs}} = 520\,^{\circ}\mathrm{C}$. The amount of smooth surface is higher at lower substrate temperatures.

From the presented data, it is difficult to draw clear conclusions on the effects of surface structure. For the formation of metallic bonds, the melt of an arriving droplet needs to completely fill the gaps of a rough substrate surface. This will happen easier, when surface roughness is low. Solidified droplets from AlSi12 show a significantly lower surface roughness than all other

tested alloys. At the same time, AlSi12 specimens show a high tensile strength also at low substrate temperatures. Possibly, the smooth surfaces of AlSi12 droplets enable the formation of metallic bonds at low substrate temperatures.

6 Consequences for an Industrial Material Jetting Process of Aluminium

The scope of this chapter is to look beyond the limited possibilities of the experimental setup in this work and to extrapolate the knowledge already presented on an industrial printing process. Such a process needs to work with smaller droplets to be able to fabricate small corners and fine details. Moreover, a higher deposition rate is necessary to increase build rates.

For this purpose, the simulation model is extended and used to conduct a parameter study. Those results are interpreted and then combined with the experimental results, to discuss the consequences for an industrial material jetting process of aluminium.

6.1 Simulation Model of Industrial Setup

In order to get a basic understanding on how process parameters will influence local thermal conditions, the simulation model used for the laboratory setup was adapted: A shortcoming in the laboratory setup is the low heat transfer between carrier plate and build platform, which is especially critical at high deposition rates. For the industrial model it is assumed that the temperature in the carrier plate can be exactly controlled and therefore the boundary condition in negative z-direction is now a fixed temperature T_{plat} without a thermal resistance to the plate. Assuming that the motion stage in an industrial machine can achieve high accelerations and velocities, the pause times between lines and layers are neglected. The time between two droplet depositions is always t_{period}. For variations of the droplet diameter, the mesh size was adapted accordingly.

Two test plans were simulated: a screening plan, where one factor is varied at a time and a full factorial design. The factors platform temperature T_{plat}, droplet temperature T_{drop}, droplet diameter d_{drop} and printing frequency f are considered. Geometry of the part being printed will also have an influence on the local thermal field, especially when very thin features as single droplet towers or walls are build. Additionally, different printing paths can be used to build the same geometry and the printing path will also have an impact on the thermal field. The possibilities are infinite and the purpose of this study is to generate a basic understanding, so

path planning and geometry are not considered in this work. All variations will be performed with the familiar cuboid geometry.

6.1.1 Screening Design

The base of the screening design is a reference setup with $T_{plat} = 400\,°C$, $T_{drop} = 800\,°C$, $f = 50\,Hz$ and $d_{drop} = 0.8\,mm$. The printing frequency $f = 1/t_{period}$ will be used here instead of the time between two droplet ejections t_{period}. The droplet diameter d_{drop} is the diameter of a sphere with the same volume as the bricks used in the simulation. Based on the reference setup, each factor was varied independently.

Results

At higher volume flow rates, either by a bigger droplet diameter or by a higher printing frequency, a significant temperature difference between adjacent temperatures in x- and z-direction develops. Adjacent temperatures in y-direction are always between those in x- and z-direction. To account for that, the evaluation of the industrial model's results is different from those of the laboratory model: Each figure shows the mean adjacent temperature $T_{adj,m,x/z}$ in x- and z-direction separately on the left and the maximum spread $\Delta T_{adj,x/z}$ on the right. Again, the first layer and the first and last three droplets in each line are ignored. Figures 6.1 to 6.4 present the influences of T_{drop}, T_{plat}, d_{drop} and f.

The droplet temperature does not show any significant effect on the mean adjacent temperatures but it increases the variation within both adjacent temperatures. Those variations mainly occur within one layer, in most cases within one line.

The build platform temperature directly controls the adjacent temperatures in all directions. Apart from $T_{plat} = 500\,°C$ the maximal differences are unaffected by the platform temperature.

When more energy is brought into the system by either a bigger droplet or a higher deposition rate, $T_{adj,m,x}$ will deviate from $T_{adj,m,z}$ and $\Delta T_{adj,x}$ increases to a maximum before it rapidly decreases again. This behaviour can be observed in figure 6.1 at $d_{drop} = 1\,mm$ and in figure 6.4 at $f = 100\,Hz$.

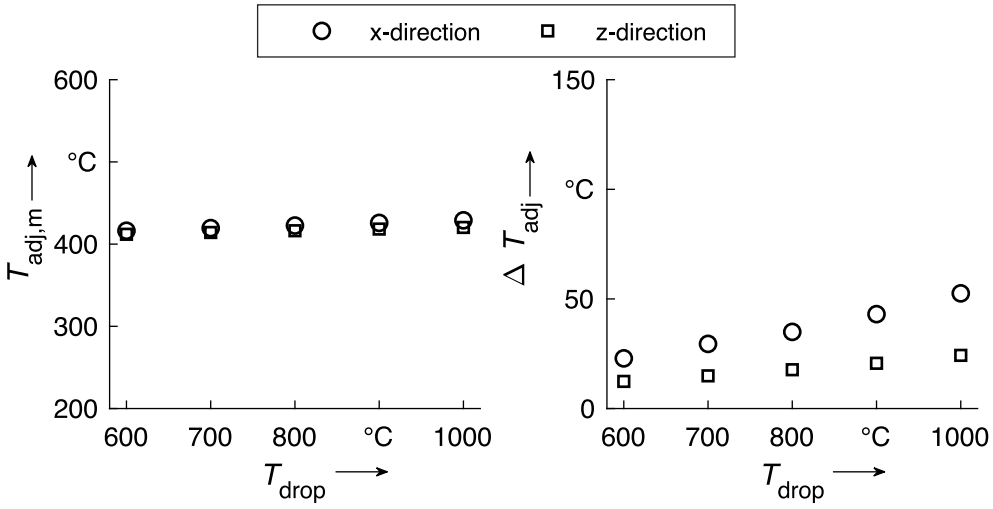

Figure 6.1: Effect of droplet temperature on mean adjacent temperatures in x- and z-direction and maximum adjacent temperature difference in both directions. While the droplet temperature does not affect the mean temperatures, it increases the maximum difference in each direction.

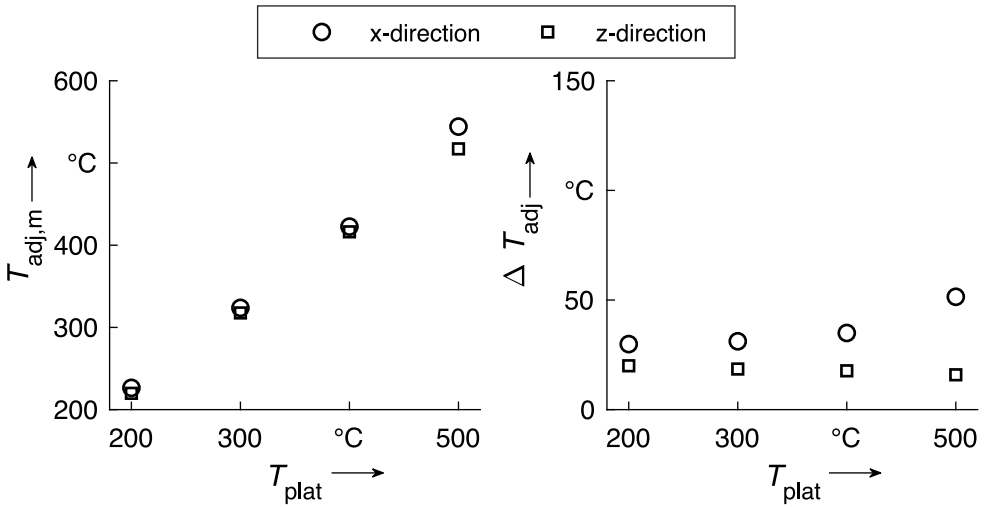

Figure 6.2: Effect of platform temperature on mean adjacent temperatures in x- and z-direction and maximum adjacent temperature difference in both directions. The platform temperature linearly increases $T_{adj,m,x/z}$ and slightly increases $\Delta T_{adj,x}$ for high platform temperatures.

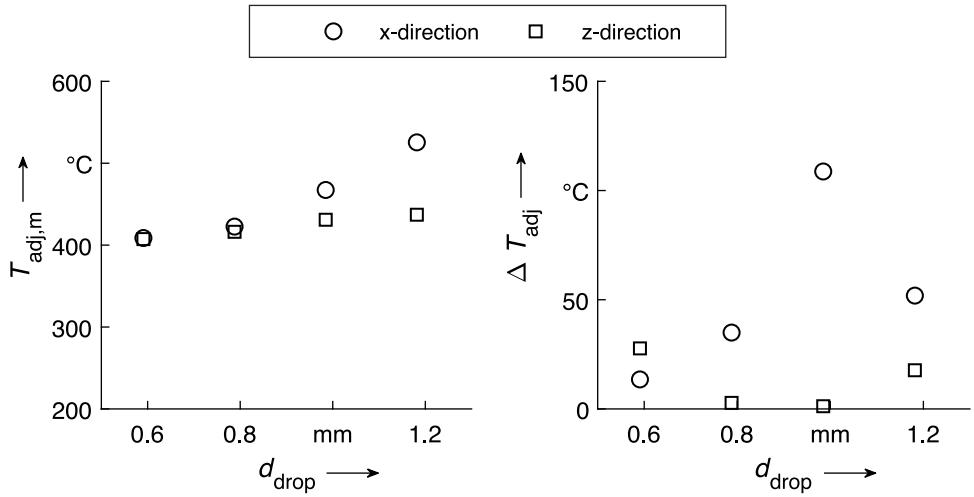

Figure 6.3: Effect of droplet diameter on mean adjacent temperatures in x- and z-direction and maximum adjacent temperature difference in both directions. The droplet diameter increases $T_{adj,m,x}$ and a maximum occurs for $\Delta T_{adj,x}$.

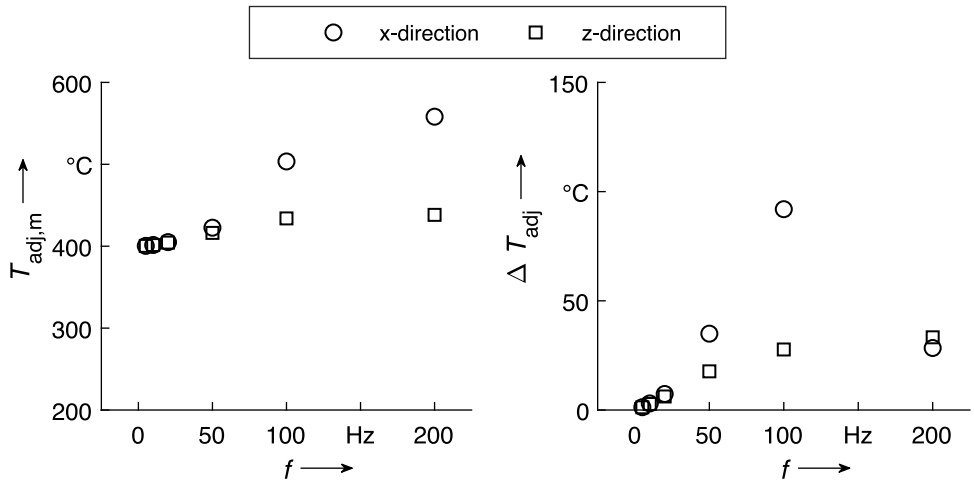

Figure 6.4: Effect of printing frequency on mean adjacent temperatures in x- and z-direction and maximum adjacent temperature difference in both directions. The printing frequency increases $T_{adj,m,x}$ and $\Delta T_{adj,z}$, while $\Delta T_{adj,x}$ shows a maximum.

Discussion

The main part of the droplets thermal energy is stored in the latent heat and not in the superheat, therefore the droplet temperature shows only small effects. As the build platform is the main heat sink, its temperature will directly control the cooling rate and consequently the adjacent temperatures.

The droplet diameter increases the volume of the droplet and consequently the energy brought into the system by the power of three, while the surface area grows by the power of two. Therefore, a bigger droplet cools less before the next droplet is deposited and consequently $T_{\mathrm{adj,m,x}}$ increases. Owing to the high heat conductivity of aluminium and a perfect heat sink at the lower z-boundary, $T_{\mathrm{adj,m,z}}$ only increases to a small amount.

The peak in $\Delta T_{\mathrm{adj,x}}$ observable for the variation of d_{drop} and f can be explained as follows: at high rates of energy deposition, droplets do not have sufficient time to cool to the bulk temperature before the next droplet is deposited and $T_{\mathrm{adj,m,x}}$ is therefore higher than $T_{\mathrm{adj,m,z}}$. A difference between $T_{\mathrm{adj,m,x}}$ and $T_{\mathrm{adj,m,z}}$ yields high thermal gradients. And when thermal gradients are high, small variations in the cooling conditions will lead to high variations in the temperature and so $\Delta T_{\mathrm{adj,x}}$ increases, when $T_{\mathrm{adj,m,x}}$ and $T_{\mathrm{adj,m,z}}$ deviate. As soon as droplets can not completely solidify during t_{period}, thermal gradients will be reduced owing to latent heat release and consequently $\Delta T_{\mathrm{adj,x}}$ decreases. In those cases, droplets will not solidify individually but as coherent lines, so properties of the printed part will be different in the spatial directions and also the outer occurrence changes accordingly. The onset of this line-wise solidification is at $d_{\mathrm{drop}} = 1\,\mathrm{mm}$ or at $f = 100\,\mathrm{Hz}$.

Note: $\Delta T_{\mathrm{adj,x}}$ and $\Delta T_{\mathrm{adj,z}}$ evaluate the spread only in one direction, whereas ΔT_{adj}, which was used in the presentation of the laboratory model, evaluates the maximum spread in all directions. Those two values develop in opposite directions at the onset of line-wise solidification: While $\Delta T_{\mathrm{adj,x}}$ decreases, because thermal gradients decrease, ΔT_{adj} will increase at the onset of line-wise solidification, because the difference between x- and z-directions increases.

6.1.2 Full Factorial Design

Based on the results of the screening design, a full factorial variation of the most significant factors d_{drop}, T_{plat} and f was performed. The platform temperature is varied between 200 and 500 °C, the frequency between 20 and 500 Hz and the droplet diameter on two stages: 0.6 and 1.2 mm.

Results

Figures 6.5 and 6.6 show contour line plots for the mean adjacent temperatures over platform temperature and printing frequency.

For a droplet diameter of 0.6 mm the adjacent temperatures in z-direction are almost constant over the printing frequency in the shown range, while adjacent temperatures in x-direction depend equally on platform temperature and printing frequency. The 550 °C contour line deviates from the otherwise constant pattern.

In the case of a droplet diameter of 1.2 mm, an influence of the printing frequency on $T_{\mathrm{adj,m,z}}$ is present but still small compared to the effect on $T_{\mathrm{adj,m,x}}$. At a higher droplet diameter, the adjacent temperature in x-direction is dominated by the printing frequency. Again, the contour lines greater or equal to 550 °C are more distant from their neighbours.

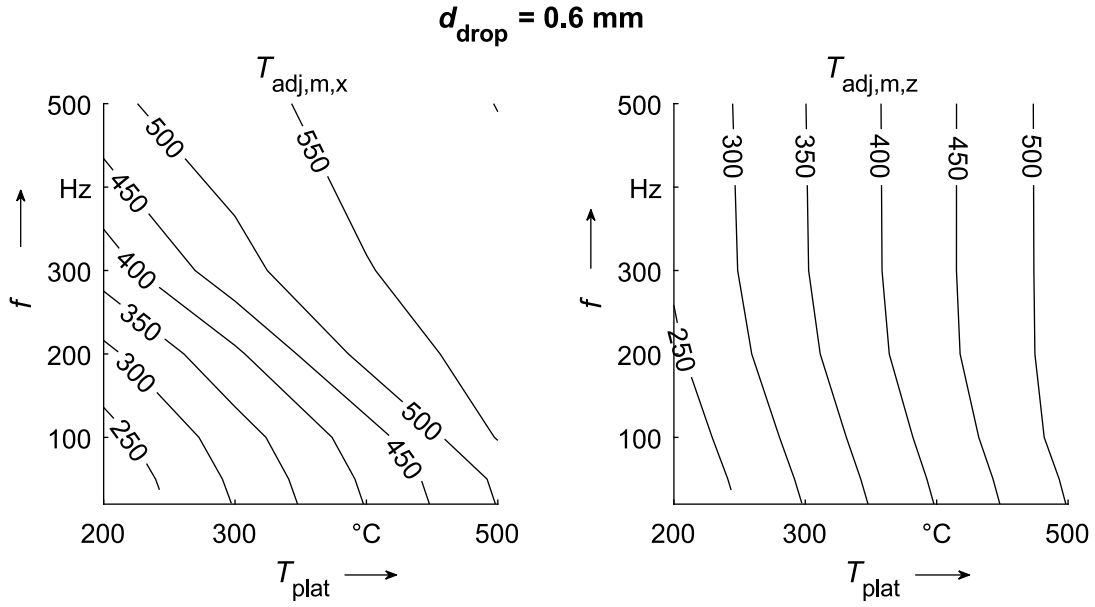

Figure 6.5: Effect of platform temperature and printing frequency on mean adjacent temperatures in x- and z-direction for a droplet diameter of 0.6 mm.

Discussion

Adjacent temperatures in z-direction show a weak dependency on the printing frequency, which means that preheating of the bulk material by the previously deposited droplet is small. Adjacent temperatures in x-direction on the other hand, are significantly dependent on the printing frequency, which implies that droplets cannot completely cool to the bulk temperature at high frequencies before the next droplet is deposited. Contour lines of 550 °C and above are more

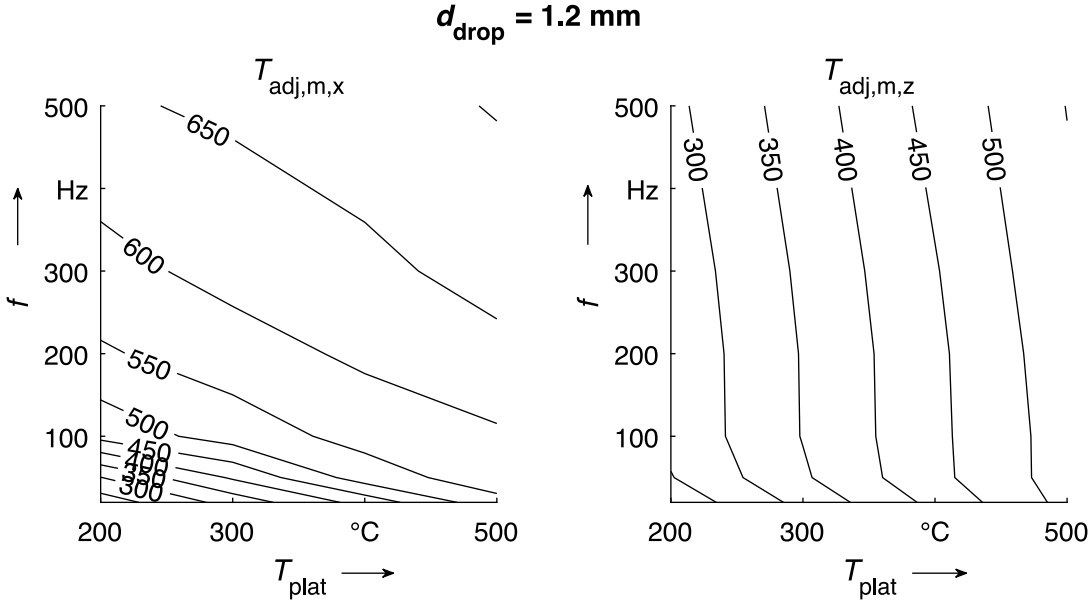

Figure 6.6: Effect of platform temperature and printing frequency on mean adjacent temperatures in x- and z-direction for a droplet diameter of 1.2 mm.

distant from their neighbours. This marks the onset of incomplete solidification of the previous droplet, as latent heat release will reduces cooling rates.

Droplets with $d_{\mathrm{drop}} = 1.2\,\mathrm{mm}$ have eight times the volume of droplets with $d_{\mathrm{drop}} = 0.6\,\mathrm{mm}$, the volume deposition rate is scaled by factor eight. Figure 6.7 compares $T_{\mathrm{adj,m,x}}$ for both droplet sizes at the same volume deposition rate. Even though the two contour plots have somewhat comparable patterns, they are shifted about 50 °C to lower temperatures in the case of $d_{\mathrm{drop}} = 1.2\,\mathrm{mm}$. This reflects the differences in contact area of each individual droplet and the differences in cooling time between volume deposition and measurement of the shown values.

6.2 Combining Experimental and Simulation Results

In this section the results gathered in the experimental part of this work are combined with the simulation results just shown to discuss the consequences for an industrial process.

Thermal Control

For being able to manufacture parts from arbitrary alloys it is necessary to maintain the substrate temperature close to or inside the alloy's solidification range. The simulation results for AlSi12 from the industrial model show that the temperature of the underlying layer (z-direction) needs

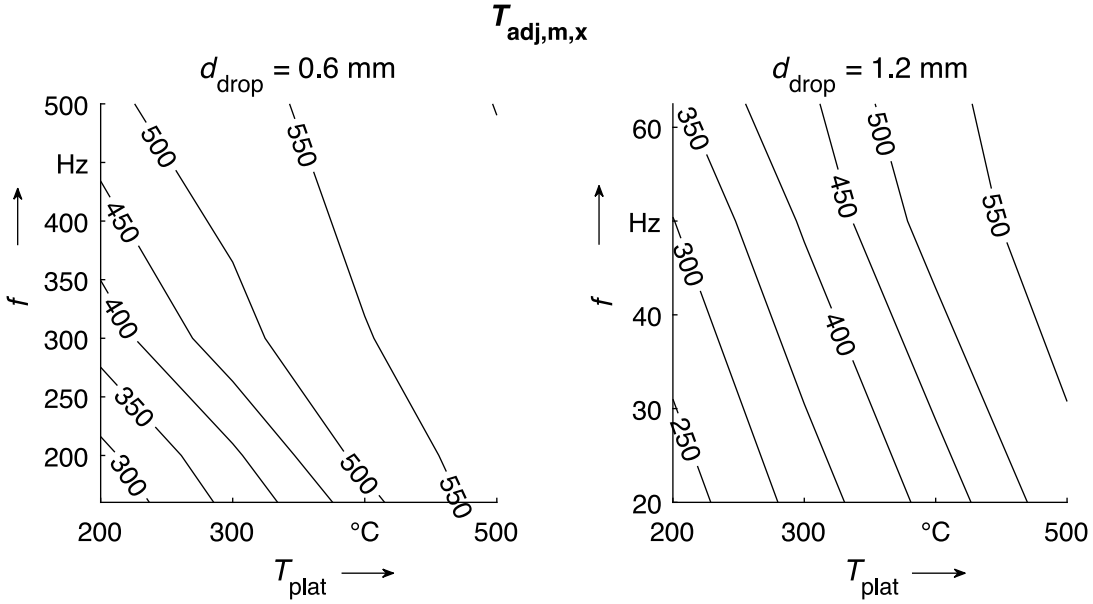

Figure 6.7: Comparison of effects on $T_{adj,m,x}$ for different droplet sizes. The ordinate is scaled to show the same volume rate for both droplet diameters. The pattern is comparable, but shifted about 50 °C.

to be controlled by the platform temperature, as all other parameters have little or no effect on it. Figure 6.8 presents an operational map for a droplet diameter of 0.6 mm based on the simulation results: To obtain sound droplet-droplet bonds that yield elongations in the range of the cast reference, an adjacent temperature of at least 500 °C is necessary. To ensure this condition in the z-direction, a minimal platform temperature of 470 °C is needed. At this platform temperature, adjacent temperatures in x-direction will reach 550 °C at 150 Hz printing frequency. As shown by the experimental results, for a mean substrate temperature just above 550 °C line-wise solidification will start. If line-wise solidification is acceptable or even desirable, a printing frequency of at least 200 Hz should be chosen, to avoid the transition zone, where individual and line-wise solidification will occur in a single layer. Finally, at very high printing frequencies, $T_{adj,m,x}$ will reach more than 600 °C, which means the previously printed material remains completely liquid and overheated for a certain period of time. This will probably lead to a loss of shape as it was observed in the experiments. As a result, for the given setup and a droplet size of 0.6 mm, accurate parts with homogeneous properties and appearance can only be printed at a frequency below 150 Hz with individual solidification or at a frequency between 200 and 500 Hz with line-wise solidification. To achieve higher deposition rates, additional technical equipment is needed, e.g. a print head with multiple nozzles or a local cooling device.

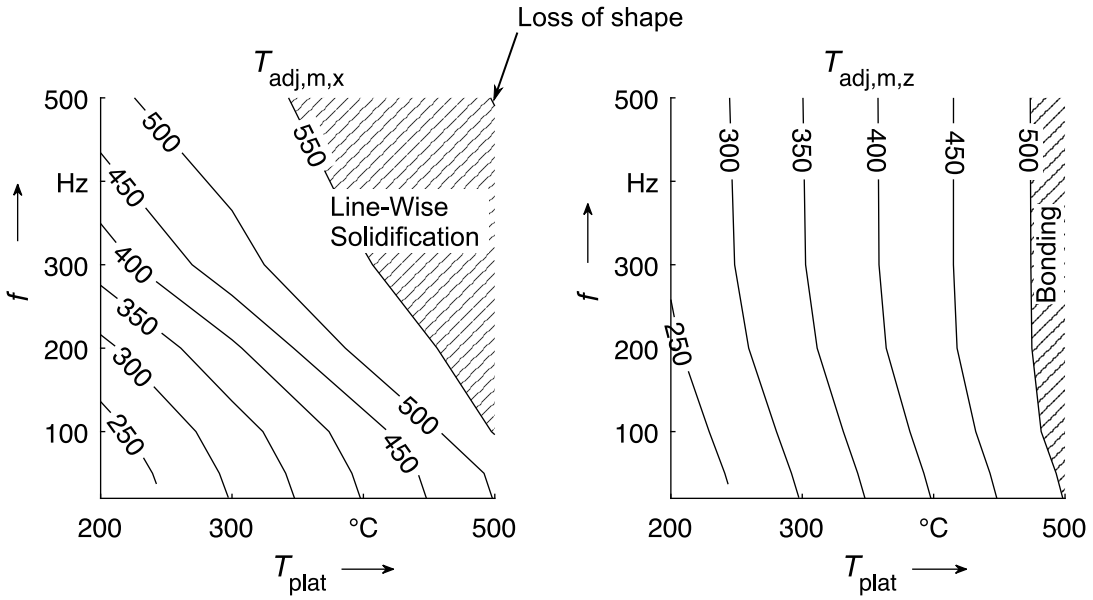

Figure 6.8: Operational Map for AlSi12 based on the simulation results. Conditions for sufficient bonding, line-wise solidification and loss of shape are marked. $d_{\mathrm{drop}} = 0.6\,\mathrm{mm}$

One needs to bear in mind that this data shows average values from the build-up of a simple cuboid with constant layer sizes and layer printing times. To find a process window to print an arbitrary geometry is a challenging task and will most probably need special process parameters for special parts of the geometry, like the first line in a layer or very thin features. The most dynamic process parameter that can be changed from droplet to droplet, is the printing frequency. It can be used to control adjacent temperatures for individual geometric features within one layer, but at the cost of a lower build rate. Hence, the task for an industrial printing process will be to find a good trade-off between high build rates and homogeneous part properties. Alternatively, to maintain high deposition rates, a dynamic local cooling device could be used to increase the solidification rate after deposition at a given substrate temperature.

By comparing the laboratory model with the industrial model, it is clear that the build platform is by far the main heat sink and therefore essential to control the temperature inside the part. Consequently, an industrial printing machine needs the ability to exactly control the build plate temperature close to the printed part. It needs to be heated to start a build job or at low deposition rates but for high deposition rates it will certainly need a cooling system as well.

Inert Environment

It will be impossible to completely suppress the oxidation of parts as well as droplets. If the assumptions are correct, one needs to focus on the oxygen concentration close to the printing

nozzle and during droplet flight. Here a lowest possible oxygen concentration should yield best results in terms of nozzle clogging and mechanical properties. Whereas the oxygen content in the printing chamber can be significantly higher.

To be able to fabricate parts of an aluminium alloy containing magnesium in a stable process, one has to come up with a different idea as it will not be possible to suppress oxidation completely. One option could be to use a nozzle material that does not act as a seed to the formation of crystalline MgO. Another option could be to work with the alloys composition. For example beryllium additions could help in reducing the oxidation.

Alloys

Industries most relevant aluminium alloys contain a certain amount of magnesium and are currently problematic to be printed due to the above mentioned oxidation issues. Apart from that also the alloy's solidification rate will affect its behaviour in the MJT process. Pure or eutectic alloys have the advantage of a high fraction solid at dendrite coherency and therefore, it is possible to produce parts with an acceptable density also on colder substrates. However, an alloy with a small solidification range will loose geometric accuracy quickly for temperatures above solidus. In contrast to that an alloy with a high solidification range can still create an accurate geometric shape at substrate temperatures greater than the solidus temperature, but relative density decreases rapidly for lower substrate temperatures.

Owing to the small droplet sizes, little or no porosity is formed by insufficient feeding during solidification. Therefore, even wrought alloys can be processed by material jetting, which can usually not be used for conventional form castings.

Also the droplet surface, which is directly correlated to the solidification behaviour, has an impact on the droplet-droplet bond formation. The data suggests, that a smooth surface as it is created by a planar solidification is beneficial to droplet-droplet bonding. Consequently, alloys that solidify with a planar solidification front will improve process stability in terms of droplet-droplet bonding.

7 Summary and Future Work

Material jetting of aluminium is a novel and promising additive manufacturing technology that can potentially fabricate parts from aluminium alloys at higher build rates and lower costs compared to current state-of-the-art processes. In MJT processes, a print head directly deposits molten material on a build platform to successively create parts. It is a single-step process defining basic shape and material properties during build-up, without the need for post processes like sintering. The deposition of a single droplet is mainly controlled by the temperature of adjacent material and the conditions of the droplet itself (velocity and size). The temperature of adjacent material develops during the process as it is a result of process parameters and layer geometries. It is therefore a major challenge of this technology to control the temperatures in a way that each droplet

- spreads out far enough to fill corners and form a dense part without enclosing pores,
- forms metallic bonds with adjacent material to create a sound metallic part and
- cools sufficiently fast, to maintain a desired and controllable shape.

For the experimental work in this thesis, a prototype MJT printer for aluminium alloys was developed. The pneumatic print head can be heated to maximal 750 °C, ejects droplets at a maximal rate of 50 Hz and a droplet size between 0.6 and 1.2 mm. The build platform can be heated to 650 °C and manipulated in three dimensions inside a build chamber. The oxygen concentration in the build chamber can be controlled between 20 and 1000 ppm in order to minimise oxidation.

This work contributes to the knowledge needed to control the MJT process by systematically examining the resulting part properties of specimens built under controlled thermal conditions from different aluminium alloys, namely Al99.5Ti, AlSi5, AlSi12 and AlCu5. Moreover, a novel method to simulate the temperature field that develops during build-up of arbitrary geometries is presented. Additionally, the influence of oxidation on macroscopic part properties is studied. The most important findings of this work are presented in the following paragraphs.

Findings on droplet spreading

When adjacent droplet temperatures are 50 °C below the temperature of dendrite coherency or higher, the relative density of printed specimens is greater than 98 %. At sufficiently high

substrate temperatures or printing frequencies, droplets will fuse to coherent lines in the printing direction, which leads to a further increase of relative density. The loss of relative density at lower adjacent droplet temperatures depends on the alloy composition. This is explained by the solid fraction at the coherency point. When the fraction is low, droplet spreading will soon be arrested by solidification, whereas alloys with a high fraction solid at DCP can spread further on a cold substrate. The explanation is in line with the property of melt fluidity used in casting practice. In other words, an alloy with a high fluidity will more likely form dense parts in MJT. The amount of spreading can also be increased by the droplet Weber number to a certain amount. However, at high Weber numbers the surface tension cannot prevent droplets from spreading over the sides of already printed material leading to a loss of shape.

Findings on droplet-droplet bonding

The formation of metallic bonds between droplets is independent of the creation of high relative densities. Samples with sufficiently high densities could be fabricated without any appreciable strength and others showed an ultimate tensile strength comparable to cast material at relative densities below 95 %. With increasing adjacent droplet temperatures, the relative density increases and microstructure's fineness decreases. While a dense part shows higher elongation values, a finer microstructure yields higher mechanical properties. According to published literature on metal droplet deposition and compound casting, it is necessary to remelt underlying material by the droplet's thermal energy, to enable the formation of metallic bonds. In this work, several analytic models are applied to predict the onset of remelting. The results of this work do not match the predictions by any of these models. It is therefore concluded – in contrast to other publications – that remelting is neither sufficient to form metallic bonds, nor is it necessary.

Findings on geometric shape

Analysing the effect on geometric shape was not in the scope of this work, but some results were gathered anyway: at a certain deposition rate, depending on droplet size and substrate temperature, droplets will start to fuse and form coherent lines in the printing direction. This is unavoidable, when high deposition rates are desired and will lead to inhomogeneous part properties. At high Weber numbers, droplets loose their sphere-like shape and the deposit geometry becomes uncontrollable. When adjacent droplet temperatures in the z-direction (towards the build platform) become too high, droplets will spread out and merge with the underlying layer to an extent, that the geometric shape is lost. Relative to the temperatures needed to form metallic bonds, this occurs at lower temperatures for alloys with a small solidification range. Hence, the process window between metallic bonds and loss of geometry is greater for alloys with a greater

solidification range. In the cases of individual droplet solidification at low Weber numbers the outer appearance of printed cuboids was not significantly effected by thermal conditions.

Findings for an industrial MJT process

The presented simulation method was used to perform simulations of high deposition frequencies and small droplets sizes, beyond the capabilities of the prototype printer. Together with the experimental results, basic information for the thermal process design of an industrial MJT can be given: To be able to print conventional aluminium alloys, the substrate needs to be heated to a temperature close to the alloy's solidus temperature. Adjacent droplet temperatures will always differ to a certain amount within one layer. Therefore, a transition zone between individual and line-wise solidification forms, where some droplets of a layer will solidify individually and others will fuse. That zone should be avoided as it will most probably cause uncontrollable inhomogeneities. At high printing frequencies, material is kept in the molten state over the period of several droplet depositions, creating a melt pool containing several droplets. Once the melt pool reaches a certain size, the defined geometric shape of the printed lines is lost.

As an industrial printing process will try to achieve highest possible deposition rates, additional technical solutions to the presented setup need to be found, to avoid the loss of geometric shape. A print head with multiple nozzles would increase deposition rate by the number of nozzles, without significantly changing the local thermal conditions, assuming that adjacent nozzles do not print simultaneously at the same position. Usually, the distance between two orifices is bigger than the diameter of one droplet. Another possibility to increase deposition rate with a single nozzle would be to cool the printed material immediately after deposition by e.g. a stream of cooling gas.

The droplet cooling rate differs significantly depending on the current local geometry, i.e. for lines with adjacent material in only one direction or adjacent material in two directions. Thus, for special geometric features like single line walls, one will need special process parameters (e.g. reduced printing frequency).

Findings on surface oxidation

Separate experiments for the influence of surface oxidation in the controlled environment were conducted with the following results: alloys containing a significant amount of magnesium (> 1 wt.%) will form magnesium oxides on the nozzle surface at a high rate causing the orifice diameter to reduce continuously even at very low oxygen concentrations (1 ppm). Therefore, it was not possible to print aluminium-magnesium alloys in the current setup. For Mg-free alloys

a limit in oxygen concentration exists. Below that limit, no effect of oxidation can be measured and for higher concentration, the material immediately looses its mechanical strength. This is attributed to the formation of a coherent monolayer of aluminium oxide on the droplet's surface during flight between ejection and deposition. Solid material will always be covered with Al_2O_3 ($c_{O_2} > 1$ ppm) and it is assumed that those thin oxide layers will stay inside the material without affecting the material properties, as metal will bond with those layers from both sides.

Future Work

All of these results contribute to the basic understanding of the printing process, but MJT of aluminium is still in its infancy. Based on the shown results future work should address several topics:

- Find a stable process for Mg-containing alloys.
- Develop an analytic model to predict whether metallic bonds form and to what extent, which is valid for all aluminium alloys.
- Establish support structures to enable three dimensional printing of overhanging structures.
- Design a print head with multiple nozzles to increase volume deposition rates.

Possibilities to suppress oxidation of magnesium in aluminium alloys are the addition of alloy elements that have a higher affinity to oxygen and form a protective layer. Amongst others, beryllium is a potential candidate. The literature describes breakaway oxidation of MgO caused by crystalline seeds on the melt's surface. Possibly, the nozzle material, which is in this case mainly aluminium nitride and boron nitride, acts as the seed for breakaway oxidation. Consequently, a different nozzle material or coating could avoid excessive oxidation.

To discuss the formation of metallic bonds further and to formulate a valid model it is necessary to obtain reliable non-equilibrium properties of the alloys. During MJT, droplets cool at extremely high rates and published thermophysical data, which is measured close to equilibrium solidification, is not valid and can only be a first estimation. One first needs to find a measurement method to determine solidus temperature, liquidus temperature and coherency point at very high cooling rates. Second, the amount of different alloys needs to be extended to AlMg, AlZn and commercial alloys. Then finally, by comparing reliable properties with more experimental data, one could derive a valid prediction for the formation of metallic bonds.

Even though it is possible to create overhanging structures by carefully choosing process parameters, it is still necessary to establish a support material to create an additive manufacturing

method able to build arbitrary geometries. An option would be to use a different material that can be removed chemically or mechanically after printing. Another option could be to manipulate the deposition of the build material in a way that only weak bonds form in the areas defined as support, i.e. by local oxidation or cooling.

Until today all publications focus on single nozzle print heads with a multitude of actuation methods. To fully use the capability of MJT, it will be necessary to design a compact print head with multiple independent nozzles.

Though different improvements are still to be found, the process material jetting of aluminium is capable of becoming an industrial additive manufacturing process, which can add new possibilities to the way parts are manufactured in the future.

A List of Figures

B List of Tables

C Bibliography

AGARWAL, K., D. MATHUR and R. SHIVPURI (2002). Evaluation of PROMETAL technique for Application to Dies for Short Run Forgings. In: *Solid Freeform Fabrication Proceedings 2002*. Austin, TX: University of Texas.

ALPER, A. M., ed. (1970). *High temperature oxides*. **v. 5**. New York: Academic Press.

ARNBERG, L., G. CHAI and L. BACKERUD (1993). Determination of dendritic coherency in solidifying melts by rheological measurements. In: *Materials Science and Engineering: A* **173**.1-2, 101–103.

ATWOOD, C., M. L. GRIFFITH, M. E. SCHLIENGER, L. D. HARWELL, M. T. ENSZ, D. M. KEICHER, J. A. ROMERO and J. E. SMUGERESKY (1998). Laser engineered net shaping (LENS): a tool for direct fabrication of metal parts. In: *Proceedings of ICALEO*. **98**, 16–19.

AZIZ, S. D. and S. CHANDRA (2000). Impact, recoil and splashing of molten metal droplets. In: *International Journal of Heat and Mass Transfer* **43**.16, 2841–2857.

BACHRACH, R. Z., S. A. FLODSTRÖM, R. S. BAUER, S. B. M. HASTRÖM and D. J. CHADI (1978). Surface resonances and the oxidation of single–crystal aluminum. In: *Journal of Vacuum Science and Technology* **15**.2, 488–493.

BAUMGARTNER, G. (2019). 'Das mikromechanische Verhalten von binären Aluminium-Silizium-Legierungen unter Last'. Dissertation. München: Technische Universität München.

BOBZIN, K. (2013). *Oberflächentechnik für den Maschinenbau*. 1. Aufl. Weinheim: Wiley-VCH.

BOSE, S. K. and R. KUMAR (1973). Structure of rapidly solidified aluminium-silicon alloys. In: *Journal of Materials Science* **8**.12, 1795–1799.

BÜHRIG-POLACZEK, A., W. MICHAELI and G. SPUR (2013). *Handbuch Urformen*. München: Carl Hanser.

BUNDESVERBAND DER DEUTSCHEN GIESSEREI-INDUSTRIE, ed. (2013). *Aluminium-Guss*. Düsseldorf: Gießerei-Verl.

CHAI, G., L. BÄCKERUD, T. RØLLAND and L. ARNBERG (1995). Dendrite coherency during equiaxed solidification in binary aluminum alloys. In: *Metallurgical and Materials Transactions A* **26**.4, 965–970.

CHAO, Y.-p., L.-h. QI and Z. BAI (2016). 3D Dynamic Simulation Analysis of Thermal-Mechanical Coupling during 7075 Aluminum Alloy Micro-droplet Deposition Manufacture. In: *Rare Metal Materials and Engineering* **45**.8, 1924–1930.

CHAO, Y.-p., L.-h. QI, Y. XIAO, J. LUO and J.-m. ZHOU (2012). Manufacturing of micro thin-walled metal parts by micro-droplet deposition. In: *Journal of Materials Processing Technology* **212**.2, 484–491.

CHAO, Y.-p., L.-h. QI, H.-s. ZUO, J. LUO, X.-h. HOU and H.-j. LI (2013). Remelting and bonding of deposited aluminum alloy droplets under different droplet and substrate temperatures in metal droplet deposition manufacture. In: *International Journal of Machine Tools and Manufacture* **69**.0, 38–47.

CHENG, S. X., T. LI and S. CHANDRA (2005). Producing molten metal droplets with a pneumatic droplet-on-demand generator. In: *Journal of Materials Processing Technology* **159**.3, 295–302.

CHIARAMONTE, F. P. and B. N. ROSENTHAL (1991). Wettability of Pyrolytic Boron Nitride by Aluminum. In: *Journal of the American Ceramic Society* **74**.3, 658–661.

COCHRAN, C. N., D. L. BELITSKUS and D. L. KINOSZ (1977). Oxidation of aluminum-magnesium melts in air, oxygen, flue gas, and carbon dioxide. In: *Metallurgical Transactions B* **8**.1, 323–332.

DAHLE, A. K., K. NOGITA, S. D. MCDONALD, C. DINNIS and L. LU (2005). Eutectic modification and microstructure development in Al–Si Alloys. In: *Materials Science and Engineering: A* **413-414**, 243–248.

DESKTOP METAL INC. (2018). Production | Desktop Metal. URL: https://www.desktopmetal.com/products/production/ (visited on 18/06/2018).

DJURDJEVIC, M. B., J. H. SOKOLOWSKI and Z. ODANOVIC (2012). Determination of dendrite coherency point characteristics using first derivative curve versus temperature. In: *Journal of Thermal Analysis and Calorimetry* **109**.2, 875–882.

DMG MORI (2018). Powder Nozzle - ADDITIVE MANUFACTURING Machines by DMG MORI. URL: https://uk.dmgmori.com/products/machines/advanced-technology/additive-manufacturing/powder-nozzle (visited on 19/06/2018).

ELLIOTT, R. and S. GLENISTER (1980). The growth temperature and interflake spacing in aluminium silicon eutectic alloys. In: *Acta Metallurgica* **28**.11, 1489–1494.

FANG, M., S. CHANDRA and C. B. PARK (2009). Heat transfer during deposition of molten aluminum alloy droplets to build vertical columns. In: *Journal of Heat Transfer* **131**.11, 1–7.

FINKE, S. and F. K. FEENSTRA (2002). Solid freeform fabrication by extrusion and deposition of semi-solid alloys. In: *Journal of Materials Science* **37**.15, 3101–3106.

FRANZ, H. (1957). *Über die Aushärtung von Aluminium-Kupfer-Legierungen*. Düsseldorf: Aluminium-Verl.

FRIEL, R. J. and R. A. HARRIS (2013). Ultrasonic Additive Manufacturing – A Hybrid Production Process for Novel Functional Products. In: *Procedia CIRP* **6**, 35–40.

GARTLAND, P. O. (1977). Adsorption of oxygen on clean single crystal faces of aluminium. In: *Surface Science* **62**.1, 183–196.

GEBHARDT, A. (2013). *Generative Fertigungsverfahren*. München: Carl Hanser.

GEIGER, M., W. STEGER, M. GREUL and M. SINDEL (1994). Multiphase Jet Solidification - a new process towards metal prototypes and a new data interface. In: *Proceedings of Solid Freeform Fabrication 1994*, 9–16.

GERDES, B., M. JEHLE, M. DOMKE, R. ZENGERLE, P. KOLTAY and L. RIEGGER (2017). Drop-on-demand generation of aluminum alloy microdroplets at 950 °C using the StarJet technology. In: *19th International Conference on Solid-State Sensors, Actuators and Microsystems (TRANSDUCERS)*, 690–693.

GHONCHEH, M. H. and S. G. SHABESTARI (2015). Effect of Cooling Rate on the Dendrite Coherency Point During Solidification of Al2024 Alloy. In: *Metallurgical and Materials Transactions A* **46**.3, 1287–1299.

GONZALEZ-GUTIERREZ, J., D. GODEC, C. KUKLA, T. SCHLAUF, C. BURKHARDT and C. HOLZER (2017). SHAPING, DEBINDING AND SINTERING OF STEEL COMPONENTS VIA FUSED FILAMENT FABRICATION. In: *Proceedings of the CIM 2017-16th International Scientific Conference on Production Engineering*. Ed. by E. ABELE, T. UDILJAK and D. CIGLAR.

GOTHAIT, H., E. KRITCHMAN, A. BENICHOU, T. SHMAL, G. EYTAN, W. SALALHA, Y. DAYAGI, O. KODINETS and L. LAIVD (2015). 'Methods and systems for printing 3d object by inkjet'. Pat. req. WO2015056230A1.

GOUMIRI, L. and J. C. JOUD (1982). Auger electron spectroscopy study of aluminium-tin liquid system. In: *Acta Metallurgica* **30**.7, 1397–1405.

HAENLEIN, A. (1931). Über den Zerfall eines Flüssigkeitsstrahles. In: *Forschung auf dem Gebiete des Ingenieurwesens* **2**.4, 139–149.

HAFERL, S. and D. POULIKAKOS (2002). Transport and solidification phenomena in molten microdroplet pileup. In: *Journal of Applied Physics* **92**.3, 1675–1689.

HAFERL, S. and D. POULIKAKOS (2003). Experimental investigation of the transient impact fluid dynamics and solidification of a molten microdroplet pile-up. In: *International Journal of Heat and Mass Transfer* **46**, 535–550.

HAO, L., S. MELLOR, O. SEAMAN, J. HENDERSON, N. SEWELL and M. SLOAN (2010). Material characterisation and process development for chocolate additive layer manufacturing. In: *Virtual and Physical Prototyping* **5**.2, 57–64.

HARNISCH, J. W. (2009). 'Aufbau und Untersuchung eines Drop-on-demand-Systems für den Hochtemperatureinsatz'. Dissertation. München: Technische Universität München.

HEINZL, J. and C. H. HERTZ (1958). Ink-Jet Printing. In: *Advances in electronics and electron physics*. Ed. by L. MARTON and P. W. HAWKES. **65**. Boston: Academic Press, 91–171.

HELLAWELL, A. (1970). The growth and structure of eutectics with silicon and germanium. In: *Progress in Materials Science* **15**.1, 3–78.

HEUGENHAUSER, S. (2018). 'Simulationsgestützte Entwicklung eines Gießverfahrens zur Herstellung von Schichtverbunden aus Aluminiumlegierungen'. Dissertation. Aachen: RWTH.

HIMMEL, B., D. RUMSCHOETTEL and W. VOLK (2019). Tensile properties of aluminium 4047A built in droplet-based metal printing. In: *Rapid Prototyping Journal* **25**.2, 427–432.

HIMMEL, B., D. RUMSCHÖTTEL and W. VOLK (2018). Thermal process simulation of droplet based metal printing with aluminium. In: *Production Engineering* **12**.3-4, 457–464.

HIRT, C. and B. NICHOLS (1981). Volume of fluid (VOF) method for the dynamics of free boundaries. In: *Journal of Computational Physics* **39**.1, 201–225.

HO, H.-N. and S.-T. WU (1998). The wettability of molten aluminum on sintered aluminum nitride substrate. In: *Materials Science and Engineering: A* **248**.1–2, 120–124.

IMPEY, S. A., D. J. STEPHENSON and J. R. NICHOLLS (1988). Mechanism of scale growth on liquid aluminium. In: *Materials Science and Technology* **4**.12, 1126–1132.

ISSLEIB, A., A. FRIEDEL and I. LUBOJANSKI (1995). Verbundgießen von Eisen-Kohlenstoff-Legierungen - grundlegende metallurgische Reaktionen an der Grenzfläche - Teil I. In: *Gießerei-Praxis* 15/16.

JOHN, H. (1981). 'Untersuchung von Einflussgrößen bei der Benetzung von Aluminiumoxid durch Aluminium'. Dissertation. Berlin: Technische Universität Berlin.

JUSTI, S. (1971). 'Untersuchung des Kristallisationsablaufs von Aluminium-Silizium-Legierungen im Hochtemperaturmikroskop'. Dissertation. Berlin: Technische Universität Berlin.

KAMMER, C. (2002). *Aluminium-Taschenbuch*. 16. Aufl. **1**. Düsseldorf: Aluminium-Verl.

KARAMPELAS, I., S. VADER, Z. VADER, V. SUKHOTSKIY, A. VERMA, G. GARG, M. TONG and E. FURLANI (2017). Drop-on-Demand 3D Metal Printing. In: *TechConnect briefs 2017*. Ed. by M. LAUDON and B. ROMANOWICZ. Danville, CA, U.S.A.: TechConnect.

KARUNAKARAN, K. P., P. V. SHANMUGANATHAN, S. J. JADHAV, P. BHADAURIA and A. PANDEY (2000). Rapid prototyping of metallic parts and moulds. In: *Journal of Materials Processing Technology* **105**.3, 371–381.

KHAN, S. and R. ELLIOTT (1996). Quench modification of aluminium-silicon eutectic alloys. In: *Journal of Materials Science* **31**.14, 3731–3737.

KURZ, W. and D. J. FISHER (1992). *Fundamentals of solidification*. 3. rev. ed., reprinted. Aedermannsdorf: Trans Tech Publ.

KURZ, W. and R. TRIVEDI (1991). Eutectic growth under rapid solidification conditions. In: *Metallurgical Transactions A* **22**.12, 3051–3057.

LANGE, A. (1998). 'Verbundgießen für Anwendungen in der Verschleißtechnik'. Dissertation. Magdeburg: Otto-von-Guericke-Universität.

LAX, E. and M. PIRANI (1929). *Temperaturstrahlung fester Körper*. Berlin, Heidelberg: Springe.

LEE, T.-M., K. TAE GOO, Y. JEONG-SOON, J. JEONGDAI, K. KWANG-YOUNG, C. BYUNG-OH and D.-S. KIM (2008). Drop-on-Demand Solder Droplet Jetting System for Fabricating Microstructure. In: *Electronics Packaging Manufacturing, IEEE Transactions on* **31**.3, 202–210.

LI, H.-p., H.-j. LI, L.-h. QI, J. LUO and H.-s. ZUO (2014). Simulation on deposition and solidification processes of 7075 Al alloy droplets in 3D printing technology. In: *Transactions of Nonferrous Metals Society of China* **24**.6, 1836–1843.

LI, H., P. WANG, L. QI, H. ZUO, S. ZHONG and X. HOU (2012). 3D numerical simulation of successive deposition of uniform molten Al droplets on a moving substrate and experimental validation. In: *Computational Materials Science* **65**.0, 291–301.

LIM, S., R. A. BUSWELL, T. T. LE, S. A. AUSTIN, A. GIBB and T. THORPE (2012). Developments in construction-scale additive manufacturing processes. In: *Automation in Construction* **21**, 262–268.

LIU, Q. and M. ORME (2001). On precision droplet-based net-form manufacturing technology. In: *Proceedings of the Institution of Mechanical Engineers, Part B: Journal of Engineering Manufacture* **215**.10, 1333–1355.

LUO, J., F. YANG, S. ZHONG and L. QI (2014). Modelling of Uniform Micron-sized Metal Particles Production Using Harmonic Mechanical Excitation. In: *Procedia Engineering* **81**, 1312–1317.

MACDONALD, C. A., A. M. MALVEZZI and F. SPAEPEN (1989). Picosecond time–resolved measurements of crystallization in noble metals. In: *Journal of Applied Physics* **65**.1, 129–136.

MAKHLOUF, M. M. and H. V. GUTHY (2001). The aluminum–silicon eutectic reaction: mechanisms and crystallography. In: *Journal of Light Metals* **1**.4, 199–218.

MALEKAN, M., S. NAGHDALI, S. ABRISHAMI and S. H. MIRGHADERI (2016). Effect of cooling rate on the solidification characteristics and dendrite coherency point of ADC12 aluminum die casting alloy using thermal analysis. In: *Journal of Thermal Analysis and Calorimetry* **124**.2, 601–609.

MALEKAN, M. and S. G. SHABESTARI (2009). Effect of Grain Refinement on the Dendrite Coherency Point during Solidification of the A319 Aluminum Alloy. In: *Metallurgical and Materials Transactions A* **40**.13, 3196–3203.

MATTHES, K. J., E. RICHTER and F. RIEDEL, eds. (2003). *Fügetechnik*. 1. Aufl. München: Carl Hanser.

MEINERS, W., K. WISSENBACH and A. GASSER (1998). 'Shaped body especially prototype or replacement part production'. German pat. DE19649865C1.

MELCHELS, F. P., M. A. DOMINGOS, T. J. KLEIN, J. MALDA, P. J. BARTOLO and D. W. HUTMACHER (2012). Additive manufacturing of tissues and organs. In: *Progress in Polymer Science* **37**.8, 1079–1104.

MEL-MAHALLAWY, N. A. and A. M. ASSAR (1991). Effect of melt superheat on heat transfer coefficient for aluminium solidifying against copper chill. In: *Journal of Materials Science* **26**.7, 1729–1733.

MILLS, K. C. (2002). *Recommended Values of Thermophysical Properties for Commercial Alloys*. Cambridge: Woodhead Pub.

MOLINA, J. M., R. VOYTOVYCH, E. LOUIS and N. EUSTATHOPOULOS (2007). The surface tension of liquid aluminium in high vacuum: The role of surface condition. In: *International Journal of Adhesion and Adhesives* **27**.5, 394–401.

MONDOLFO, L. F. (1976). *Aluminum alloys*. London: Butterworth.

MÜLLER, K. (1996). *Möglichkeiten der Gefügebeeinflussung eutektischer und naheutektischer Aluminium-Silizium-Gußlegierungen unter Berücksichtigung der mechanischen Eigenschaften*. Als Ms. gedr. **424**. Düsseldorf: VDI-Verl.

MURRAY, J. L. and A. J. MCALISTER (1984). The Al-Si (Aluminum-Silicon) system. In: *Bulletin of Alloy Phase Diagrams* **5**.1, 74–84.

MYERBERG, J. S., R. FULOP, R. CHIN and Y. MING-CHIANG (2017). 'Three-dimensional electrohydrodynamic printing of metallic objects'. Pat. req. US20170056966A1.

MYERBERG, J. S., T. K. NATCHURIVALAPIL RAPPAI JAMES, E. M. SACHS, P. A. HOISINGTON and K. M. LI (2017). 'Sediment controlling in pneumatic jetting of metal for additive manufacturing'. Pat. req. US20170252810A1.

NERL, C., M. WIMMER, H. HOFFMANN, E. KASCHNITZ, F. LANGBEIN and W. VOLK (2014). Development of a continuous composite casting process for theproduction of bilayer aluminium strips. In: *Journal of Materials Processing Technology* **214**, 1445–1455.

NGO, T. D., A. KASHANI, G. IMBALZANO, K. T. NGUYEN and D. HUI (2018). Additive manufacturing (3D printing): A review of materials, methods, applications and challenges. In: *Composites Part B: Engineering* **143**, 172–196.

ORME, M. and R. F. SMITH (1999). Enhanced Aluminum Properties by Means of Precise Droplet Deposition. In: *Journal of Manufacturing Science and Engineering* **122**.3, 484–493.

OSTERMANN, F. (2014). *Anwendungstechnologie Aluminium*. Berlin, Heidelberg: Springer.

PAPIS, K., B. HALLSTEDT, J. F. LÖFFLER and P. J. UGGOWITZER (2008). Interface formation in aluminium–aluminium compound casting. In: *Acta Materialia* **56**.13, 3036–3043.

PASANDIDEH-FARD, M., R. BHOLA, S. CHANDRA and J. MOSTAGHIMI (1998). Deposition of tin droplets on a steel plate. In: *International Journal of Heat and Mass Transfer* **41**.19, 2929–2945.

PASANDIDEH-FARD, M., S. CHANDRA and J. MOSTAGHIMI (2002). A three-dimensional model of droplet impact and solidification. In: *International Journal of Heat and Mass Transfer* **45**.11, 2229–2242.

PEK, P. (1987). 'Gefügemorphologie und Festigkeitseigenschaften binärer Aluminium-Silizium-Legierungen'. Dissertation. München: Technische Universität München.

PHAM, D. T. and R. S. GAULT (1998). A comparison of rapid prototyping technologies. In: *International Journal of Machine Tools and Manufacture* **38**.10–11, 1257–1287.

PIECZONKA, T. (2017). Disruption of an Alumina Layer During Sintering of Aluminium in Nitrogen. In: *Archives of Metallurgy and Materials* **62**.2, 987–992.

POLIFKE, W. and J. KOPITZ (2009). *Wärmeübertragung*. 2., aktualisierte Aufl. München and Boston: Pearson Studium.

RAYLEIGH (1878). On The Instability Of Jets. In: *Proceedings of the London Mathematical Society* **1-10**.1, 4–13.

REED, T. B. (1971). *Free energy of formation of binary compounds: an atlas of charts for high-temperature chemical calculations*. Cambridge Mass.: MIT Press.

RHEITER, H. J. H. and M. V. RASA (2015). 'Method for ejecting molten metals'. U.S. pat. US9593403B2.

RICE, C. S. (2000). *Semi-Solid Metal Freeform Fabrication - Phase I Final Report for Period September 4, 1999–June 14, 2000*.

RIDLER, T. W. and S. CALVARD (1978). Picture Thresholding Using an Iterative Selection Method. In: *IEEE Transactions on Systems, Man, and Cybernetics* **8**, 630–632.

RUMSCHOETTEL, D., B. GRIEBEL, F. IRLINGER and T. C. LUETH (2017). A fast pneumatic droplet generator for the ejection of molten aluminum. In: *2017 Pan Pacific Microelectronics Symposium (Pan Pacific)*. [Piscataway, NJ]: IEEE.

SACHS, E. M., M. G. GIBSON, P. A. HOISINGTON and R. R. FONTANA (2017). 'Magneto-hydrodynamic deposition of metal in manufacturing'. Pat. req. US20170252821A1.

SAHM, P. R., H. JONES and C. M. ADAM (1986). *Science and Technology of the Undercooled Melt*. Dordrecht: Springer Netherlands.

SAHM, P. R., ed. (1999). *Schmelze, Erstarrung, Grenzflächen*. Braunschweig: Vieweg.

ŠARLER, B. (1995). Stefan's work on solid-liquid phase changes. In: *Engineering Analysis with Boundary Elements* **16**.2, 83–92.

SCHIAFFINO, S. and A. A. SONIN (1997a). Molten droplet deposition and solidification at low Weber numbers. In: *Physics of Fluids* **9**.11, 3172–3187.

SCHIAFFINO, S. and A. A. SONIN (1997b). Motion and arrest of a molten contact line on a cold surface: An experimental study. In: *Physics of Fluids* **9**.8, 2217.

SCHIAFFINO, S. and A. A. SONIN (1997c). On the theory for the arrest of an advancing molten contact line on a cold solid of the same material. In: *Physics of Fluids* **9**.8, 2227.

SILVA, M. P. and D. E. J. TALBOT (2016). Oxidation of Liquid Aluminum — Magnesium Alloys. In: *Essential Readings in Light Metals*. Ed. by J. F. GRANDFIELD and D. G. ESKIN. **8**. Cham: Springer International Publishing, 137–142.

SOHN, H. and D. Y. YANG (2005). Drop-on-demand deposition of superheated metal droplets for selective infiltration manufacturing. In: *Materials Science and Engineering: A* **392**.1–2, 415–421.

SOVA, A., S. GRIGORIEV, A. OKUNKOVA and I. SMUROV (2013). Potential of cold gas dynamic spray as additive manufacturing technology. In: *The International Journal of Advanced Manufacturing Technology* **69**.9-12, 2269–2278.

STEENT, H. and A. HELLAWELL (1972). Structure and properties of aluminium-silicon eutectic alloys. In: *Acta Metallurgica* **20**.3, 363–370.

STEFANESCU, D. M. (2002). *Science and engineering of casting solidification*. New York: Kluwer Academic/Plenum Publishers.

STUCKI, F., M. ERBUDAK and G. KOSTORZ (1987). The initial oxidation of solid and liquid aluminium. In: *Applied Surface Science* **27**.4, 393–400.

SUKHOTSKIY, V., P. VISHNOI, I. KARAMPELAS, S. VADER, Z. VADER and E. FURLANI (2018). Magnetohydrodynamic Drop-on-Demand Liquid Metal Additive Manufacturing: System Overview and Modelling. In: *TechConnect briefs 2017*. Ed. by M. LAUDON and B. ROMANOWICZ. Danville, CA, U.S.A.: TechConnect.

SUTER, M., E. WEINGÄRTNER and K. WEGENER (2012). MHD printhead for additive manufacturing of metals. In: *Procedia CIRP* **2**.0, 102–106.

SUTER, M. (2012). 'Magnetohydrodynamischer (MHD) Druckkopf für die additive Fertigung von Metallbauteilen'. Dissertation. Eidgenössische Technische Hochschule ETH Zürich.

TAMINGER, K. M. B. and R. A. HAFLEY (2003). Electron beam freeform fabrication: A rapid metal deposition process. In: *Proceedings of 3rd Annual Automotive Composites Conference*. Ed. by SOCIETY OF PLASTICS ENGINEERS.

TAMINGER, K. M. B. and R. A. HAFLEY (2006). Electron beam freeform fabrication for cost effective near-net shape manufacturing. In: *NATO AVT* **139**.

THIELE, W. (1962). Die Oxydation von Aluminium- und Aluminiumlegierungs-Schmelzen. In: *Aluminium* **38**.11, 707–786.

TROPMANN, A., N. LASS, N. PAUST, T. METZ, C. ZIEGLER, R. ZENGERLE and P. KOLTAY (2012). Pneumatic dispensing of nano- to picoliter droplets of liquid metal with the StarJet method for rapid prototyping of metal microstructures. In: *Microfluidics and Nanofluidics* **12**.1-4, 75–84.

TSAO, J. Y., M. J. AZIZ, M. O. THOMPSON and P. S. PEERCY (1986). Asymmetric melting and freezing kinetics in silicon. In: *Physical review letters* **56**.25, 2712–2715.

UCHINO, K. (2017). *Advanced Piezoelectric Materials: Science and Technology*. Duxford, Cambridge and Kidlington: Woodhead Publishing.

VADER SYSTEMS (2018). Liquid Metal 3D Printing. URL: `https://vadersystems.com/` (visited on 22/06/2018).

VADER, S. and Z. VADER (2015). 'Conductive liquid three dimensional printer'. U.S. pat. US9616494B2.

VADER, S., Z. VADER, I. H. KARAMPELAS and E. P.-. FURLANI (2016). Advances in Magnetohydrodynamic Liquid Metal Jet Printing. In: *TechConnect briefs 2016*. Ed. by M. LAUDON and B. ROMANOWICZ. Danville, CA, U.S.A.: TechConnect.

VDI, ed. (2013). *VDI-Wärmeatlas*. Berlin, Heidelberg: Springer Berlin Heidelberg.

VOEHRINGER, P., S. HERBSTER, W. QI, U. RIEGLER and R. GIEZENDANNER-THOBEN (2017). 'Print head for the 3D printing of metals'. Pat. req. DE102015218375A1.

WANG, S. P., G. X. WANG and E. F. MATTHYS (1998). Melting and resolidification of a substrate in contact with a molten metal. In: *International Journal of Heat and Mass Transfer* **41**.10, 1177–1188.

WANG, X., X. PENG, Y. DUAN and B. WANG (2007). Dynamics of Spreading of Liquid on Solid Surface. In: *Chinese Journal of Chemical Engineering* **15**.5, 730–737.

WEBER, C. (1931). Zum Zerfall eines Flüssigkeitsstrahles. In: *ZAMM - Zeitschrift für Angewandte Mathematik und Mechanik* **11**.2, 136–154.

WEN, C.-D. and I. MUDAWAR (2006). Modeling the effects of surface roughness on the emissivity of aluminum alloys. In: *International Journal of Heat and Mass Transfer* **49**.23-24, 4279–4289.

WOHLERS, T. and R. I. CAMPBELL (2017). *Wohlers report 2017*. Fort Collins, Colo.: Wohlers Associates, Inc.

WU, G., N. A. LANGRANA, S. RANGARAJAN, R. MCCUISTON, R. SADANJI, S. DANFORTH and A. SAFARI (1999). Fabrication of Metal Components using FDMet: Fused Deposition of Metals. In: *Proceedings of Solid Freeform Fabrication Symposium*.

XJET (2018). Technology - Xjet. URL: `https://xjet3d.com/technology/` (visited on 20/06/2018).

YAMAGUCHI, S. (1974). Zur Oxidschicht von Aluminium. In: *Werkstoffe und Korrosion* **25**.5.

YI, S., F. LIU, J. ZHANG and S. XIONG (2004). Study of the key technologies of LOM for functional metal parts. In: *Journal of Materials Processing Technology* **150**.1-2, 175–181.

YOUNG, T. (1805). An essay on the cohesion of fluids. In: *Phil. Trans. R. Soc. Lond.* **95**, 65–87.

ZÄH, M. F. and S. LUTZMANN (2010). Modelling and simulation of electron beam melting. In: *Production Engineering* **4**.1, 15–23.

ZHANG, D., L. QI, J. LUO, H. YI and X. HOU (2017). Direct fabrication of unsupported inclined aluminum pillars based on uniform micro droplets deposition. In: *International Journal of Machine Tools and Manufacture* **116**, 18–24.

ZHAO, Z., D. POULIKAKOS and J. FUKAI (1996a). Heat transfer and fluid dynamics during the collision of a liquid droplet on a substrate—I. Modeling. In: *International Journal of Heat and Mass Transfer* **39**.13, 2771–2789.

ZHAO, Z., D. POULIKAKOS and J. FUKAI (1996b). Heat transfer and fluid dynamics during the collision of a liquid droplet on a substrate—II. Experiments. In: *International Journal of Heat and Mass Transfer* **39**.13, 2791–2802.

ZHONG, S., L. QI, Y. TANG and J. LUO (2014). Development and Experimental Research of Aluminium Alloy Droplet Generator based on Mechanical Vibration. In: *Procedia Engineering* **81**, 1583–1588.

ZUO, H.-s., H.-j. LI, L.-h. QI, J. LUO, S.-y. ZHONG and Y.-f. WU (2015). Effect of non-isothermal deposition on surface morphology and microstructure of uniform molten aluminum alloy droplets applied to three-dimensional printing. In: *Applied Physics A* **118**.1, 327–335.

D Norms

ISO 17296-2 (2015). *Additive manufacturing – General principles – Part 2: Overview of process categories and feedstock*.

ISO/ASTM 52900 (2018). *Additive manufacturing - General principles - Terminology*.

VDI 3405-2 (2013). *Additive manufacturing processes, rapid manufacturing - Beam melting of metallic parts - Qualification, quality assurance and post processing*.

ISO 6892-1 (2016). *Metallic materials - Tensile testing - Part 1*.

DIN 50125 (2016). *Prüfung metallischer Werkstoffe – Zugproben*.

ISO 857-2 (2005). *Welding and allied processes – Vocabulary – Part 2: Soldering and brazing processes and related terms*.

ISO 18273 (2016). *Welding consumables - Wire electrodes, wires and rods for welding of aluminium and aluminium alloys - Classification*.

E Appendix

Student Theses

Name	Type	Title (Year)
Wenig, F.	Bachelor's Thesis	Incremental Casting of Aluminum - Design of an Experimental Environment (2016)
Nudelis, N.	Student Thesis	Determination of the emission coefficient of aluminium alloys for process monitoring in additive manufacturing (2017)
Ojeda, E.	Student Thesis	Incremental Casting of Aluminum, Process Simulation with ANSYS
Geitner, C.	Bachelor's Thesis	Examination of the behaviour of a hypoeutectic Al-Si alloy compared to an eutectic Al-Si alloy in a droplet based additive manufacturing process (2018)
Reif, J.	Master's Thesis	Analysis of oxygen influence on droplet generation and component strength in droplet-based, direct metal printing with aluminum (2018)
Hofmann, A.	Student Thesis	Material jetting of aluminium magnesium alloys - reducing oxidation by implementing a coaxial inert gas nozzle (2019)

Dissertationen des Lehrstuhls für Umformtechnik und Gießereiwesen, Prof. Dr.-Ing. Wolfram Volk

01 *Felix Zimmermann*
Generierung von maßgeschneiderten Bauteileigenschaften in PHS-Bauteilen durch Anlassen mittels Flamme; 2014;
ISBN: 978-3-95884-007-2

02 *Christopher Joseph Thoma*
Simulationsgestützte Optimierung der Maßhaltigkeit in der Prozesskette Druckguss; 2015; ISBN: 978-3-73699-009-8

03 *Joung Sik Suh*
Verbesserung der Kaltumformbarkeit von AZ31 Mg-Blech durch Equal Channel Angular Pressing (ECAP); 2015;
Urn: http://nbn-resolving.de/urn/resolver.pl?urn:nbn:de:bvb:91-diss-20151215-1271570-1-8

04 *Robert Ramakrishnan*
3-D-Drucken mit einem anorganischen Formstoffsystem; 2016;
Urn: http://nbn-resolving.de/urn/resolver.pl?urn:nbn:de:bvb:91-diss-20160129-1276474-1-5

05 *Patrick Saal*
Quantitative Phasenanalyse von ausferritischem Gusseisen mithilfe der Neutronendiffraktometrie; 2017;
Urn: http://nbn-resolving.de/urn/resolver.pl?urn:nbn:de:bvb:91-diss-20170125-1304161-1-8

06 *Peter Sachnik*
Methodik für gratfreie Schnittflächen beim Scherschneiden; 2017;
Urn: http://nbn-resolving.de/urn/resolver.pl?urn:nbn:de:bvb:91-diss-20160406-1304184-1-8

07 *Thomas Martin Kopp*
Einfluss der Werkzeugsteifigkeit auf Scherschneidprozess und Werkzeugverschleiß beim offenen Schnitt; 2017;
Urn: http://nbn-resolving.de/urn/resolver.pl?urn:nbn:de:bvb:91-diss-20170426-1327352-1-7

08 *Simon Josef Maier*
Inline-Qualitätsprüfung im Presswerk durch intelligente Nachfolgewerkzeuge; 2018; ISBN: 978-3-95884-004-1

09 *David Jocham*
Bestimmung der lokalen Einschnürung nach linearer und nichtlinearer Umformhistorie sowie Ermittlung dehnungs- und geschwindigkeitsabhängiger Materialkennwerte; 2018;
ISBN: 978-3-95884-012-6

10 *Christoph Kaiser*
Effiziente Produkt- und Prozessabsicherung für
gefalzte Karosseriebauteile durch ein metamodellbasiertes
Assistenzsystem; 2018; ISBN: 978-3-95884-018-8

11 *Daniel Marian Opritescu*
Risikominimale Überbrückung von Kapazitätsengpässen
im Presswerksverbund der Automobilindustrie; 2018;
ISBN: 978-3-95884-020-1

12 *Maria Anna Hiller*
Fügen durch Clinchen mit rotierender Werkzeugbewegung;
2019; ISBN: 978-3-95884-024-9

13 *Hannes Alois Weiss*
Fertigung effizienter Elektromotoren; 2019;
Urn: http://nbn-resolving.de/urn/resolver.pl?urn:nbn:de:bvb:91-diss-20190516-1463362-1-3

14 *Wan-Gi Cha*
Formability Consideration in Bead Optimization to stiffen Deep
Drawn Parts; 2019;
Urn: http://nbn-resolving.de/urn/resolver.pl?urn:nbn:de:bvb:91-diss-20190717-1469833-1-2

15 *Sven Peter Jansen*
Methodik zur Auslegung konturnaher Temperiersysteme
in Druckgusswerkzeugen; 2019; ISBN: 978-3-95884-035-5

16 *Georg Baumgartner*
Das mikromechanische Verhalten von binären
Aluminium-Silizium-Legierungen unter Last;
2019; ISBN: 978-3-95884-032-4

17 *Simon Vogt*
Entwicklung eines Verfahrens zur Herstellung von
verpressten Spulen für effizientere E-Traktionsantriebe; 2019;
Urn: http://nbn-resolving.de/urn/resolver.pl?urn:nbn:de:bvb:91-diss-20191001-1483133-1-0

18 *Patrick Thomas Helmut Woisetschläger*
Beitrag zur Optimierung der Schichtanbindung bei
thermisch gespritzten Zylinderlaufflächen im Verbrennungsmotor;
2020; ISBN: 978-3-95884-042-3

19 *Michael Walter Krinninger*
Ansätze zur Reduzierung der prozessbedingten Flitterbildung
beim Scherschneiden von Aluminiumblechen im offenen Schnitt;
2020; ISBN: 978-3-95884-045-4

20 *Tim Benkert*
Blechradkörper für Leichtbauzahnräder – Eine Machbarkeitsstudie zur
Herstellung von tiefgezogenen und feingeschnittenen Innenteilen
mehrteiliger Zahnräder; 2020; ISBN: 978-3-95884-046-1

21 *Benjamin Himmel*
Material Jetting of Aluminium – Analysis of a Novel Additive Manufacturing Process; 2020; ISBN: 978-3-95884-049-2